Volume 25
Number 5
7 March 2025
Pages 731–1374

Lab on a Chip

Devices and applications at the micro- and nanoscale

rsc.li/loc

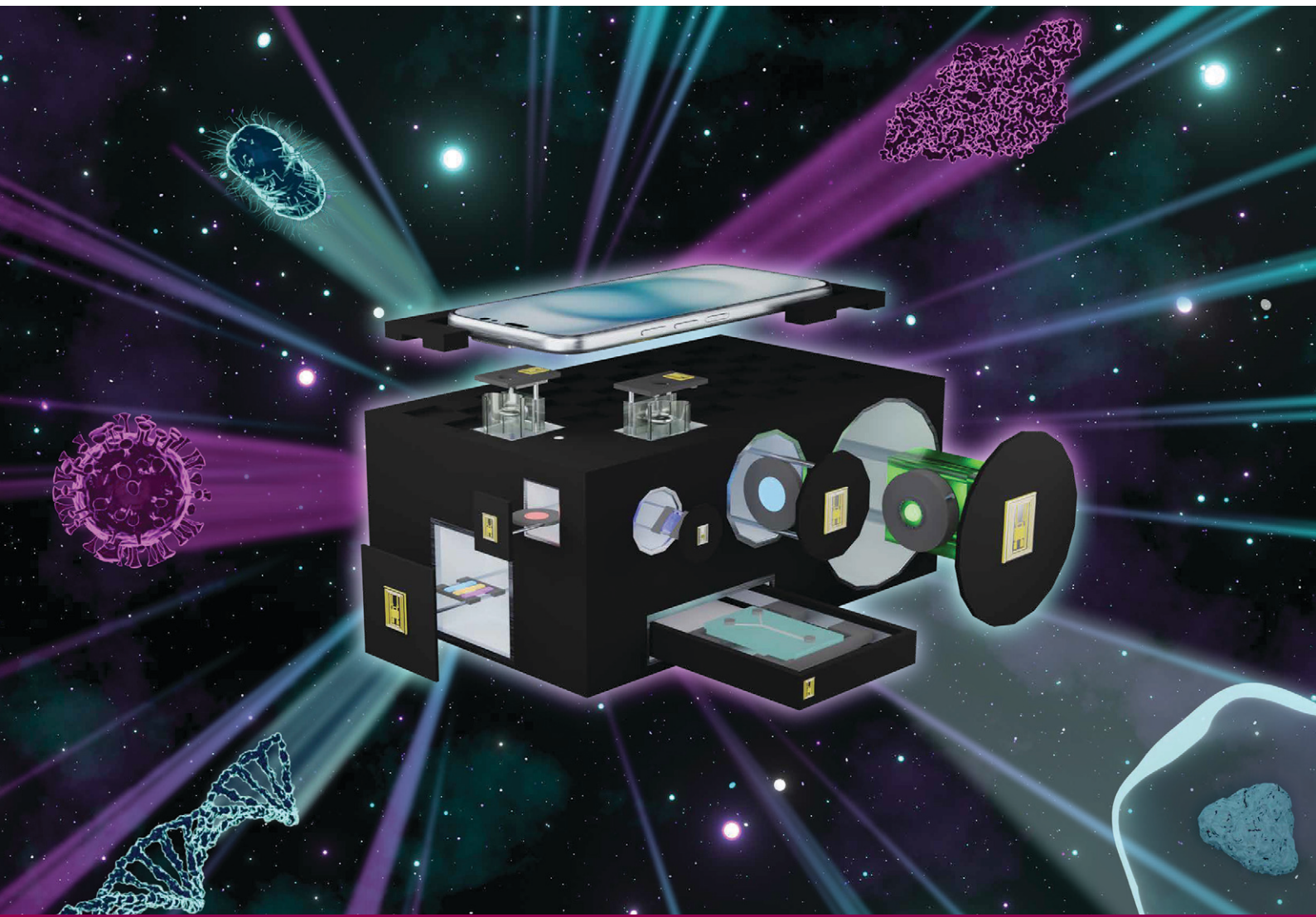

Themed issue: Lab on a Chip Reviews Issue 2025

ISSN 1473-0197

ROYAL SOCIETY OF CHEMISTRY

CRITICAL REVIEW
W. Russ Algar *et al.*
Smartphones as a platform for molecular analysis: concepts, methods, devices and future potential

Lab on a Chip

CRITICAL REVIEW

View Article Online
View Journal | View Issue

Open Access Article. Published on 07 February 2025. Downloaded on 19/4/2026 11:02:09 PM.
This article is licensed under a Creative Commons Attribution-NonCommercial 3.0 Unported Licence.

Check for updates

Cite this: *Lab Chip*, 2025, **25**, 884

Smartphones as a platform for molecular analysis: concepts, methods, devices and future potential†

Daina V. Baker, ‡ Jasmine Bernal-Escalante,‡ Christine Traaseth,‡ Yihao Wang, Michael V. Tran, Seth Keenan and W. Russ Algar *

Received 18th November 2024,
Accepted 27th January 2025

DOI: 10.1039/d4lc00966e

rsc.li/loc

Over the past 15 years, smartphones have had a transformative effect on everyday life. These devices also have the potential to transform molecular analysis over the next 15 years. The cameras of a smartphone, and its many additional onboard features, support optical detection and other aspects of engineering an analytical device. This article reviews the development of smartphones as platforms for portable chemical and biological analysis. It is equal parts conceptual overview, technical tutorial, critical summary of the state of the art, and outlook on how to advance smartphones as a tool for analysis. It further discusses the motivations for adopting smartphones as a portable platform, summarizes their enabling features and relevant optical detection methods, then highlights complementary technologies and materials such as 3D printing, microfluidics, optoelectronics, microelectronics, and nanoparticles. The broad scope of research and key advances from the past 7 years are reviewed as a prelude to a perspective on the challenges and opportunities for translating smartphone-based lab-on-a-chip devices from prototypes to authentic applications in health, food and water safety, environmental monitoring, and beyond. The convergence of smartphones with smart assays and smart apps powered by machine learning and artificial intelligence holds immense promise for realizing a future for molecular analysis that is powerful, versatile, democratized, and no longer just the stuff of science fiction.

1. Introduction

At their time of first release, many classic works of science fiction imagined ambitious and powerful technologies: computers that accepted commands and returned information verbally; handheld devices that processed reams of data on demand; wearable devices for long-range wireless communication; augmented reality eyewear; artificial intelligence that predicted needs and preferences; and portable scanners that measured electromagnetic radiation, vital signs, and molecular composition. Here and now, in the real world, most of these capabilities are genuine features of smartphones, smartphone-linked peripherals, and apps and online tools accessible *via* smartphone. A notable exception is the scanning of molecular composition, which is neither a capability nor a realistic near-future expectation for smartphones. Nevertheless, smartphones are increasingly useful as detection and readout platforms for assays and sensors that do provide molecular information.

Contemporary "lab on a chip" (LOC) devices[1–3] hold promise for a future with portable molecular analyses but are nonetheless more aspirational than realized. Microfluidics have done much to advance the LOC concept—including methods for the automation of fluid handling, reduction of sample and waste volumes, faster analyses, precision in mixing, and other benefits from miniaturization—but a key challenge lies beyond the chip, where many microfluidic systems require peripheral equipment for their operation and for the detection of analytes. Examples of such equipment include pumps, pressure generators, power supplies, voltage sequencers, temperature controllers, light sources, microscopes, photodetectors, potentiostats, and other hardware for optical and electrochemical detection. There is a push toward passive microfluidics that eliminate pumping,[4] and rapid progress in microelectronics has helped to scale down and lower the cost of hardware, but further reductions in the size, cost, and complexity of off-chip components are still needed.[5] LOC systems that require specialized laboratory equipment for their operation are not logistically different than a traditional benchtop analysis.

Laboratories and their specialized equipment are principally located in populous and well-resourced urban centres. These facilities tend to be poorly accessible or inaccessible to residents of rural and remote communities,

Department of Chemistry, University of British Columbia, 2036 Main Mall, Vancouver, BC, V6T 1Z1, Canada. E-mail: algar@chem.ubc.ca

† Electronic supplementary information (ESI) available. See DOI: https://doi.org/10.1039/d4lc00966e

‡ These authors contributed equally.

 This journal is © The Royal Society of Chemistry 2025

Open Access Article. Published on 07 February 2025. Downloaded on 19/4/2026 11:02:09 PM.
This article is licensed under a Creative Commons Attribution-NonCommercial 3.0 Unported Licence.

who represent an underserved 45% of the current global population.[6,7] Moreover, laboratory facilities either do not exist at field sites or, when pop-up infrastructure is possible, are necessarily limited in their resources. Examples of field sites where molecular information has high value include sites suspected of a disease outbreak, sites suspected of environmental contamination, farms for agriculture and aquaculture, biomanufacturing plants, workplaces with potential for unsafe conditions, and frontiers of scientific exploration such as the ocean depths and outer space. Even when lab facilities are available in urban centers, restrictions on budget and throughput may hinder the implementation of analyses at the desired scale or frequency—something that is often the case for personalized medicine, environmental surveillance, food and water testing, and process monitoring in manufacturing. Although largely beyond the scope of this review, science education also faces challenges with the costs and access limitations associated with sophisticated scientific instruments and facilities.[8,9] In short, there are numerous unmet needs for LOC technologies that offer rapid and quantitative chemical and biological analysis, straightforward and lab-free operation, multitasking between more than one type of analysis, and democratization in the form of being able to be built, distributed, maintained, and utilized without substantial financial or other barriers.

A convergence of microfluidics and many other technologies will be required to create LOC devices and assays that translate to society and industry with global impact. These enabling technologies will originate from electronics, materials science, biotechnology, electrochemistry, optics, photonics, data science, and other fields of research and development. Of course, such a scope is too broad for a single review. Instead, this review focuses on the emergence of smartphones as an enabler of LOC, point-of-care, point-of-need, and other portable devices for chemical and biological analyses. Smartphones already integrate numerous technologies and thereby represent a shortcut to the convergence needed for translatable LOC systems. The review begins by discussing the motivation for adopting smartphones as a portable analysis platform, summarizes their potentially useful features, and highlights technologies and materials that are complementary to those features. It then provides a short tutorial on optical detection methods with a singular focus on use of the smartphone camera. A meta-analysis is presented as a preamble to a categorical and critical summary of the recent literature, including examples of how microfluidic platforms have been advantageously paired with smartphone-based devices. The review closes with a perspective on challenges and opportunities for research and development that will advance the technology from prototypes to authentic tools for molecular analysis. When the global ubiquity and ease of use of smartphones are achievements that LOC technologies aspire to emulate, why not leverage the technology of smartphones to help reach that goal?

2. Why smartphones?

2.1 A global technology

Smartphones are ubiquitous in many parts of the world and global penetration is projected to increase. The number of mobile subscriptions is more than 8B and the number of smartphone users varies from >80% to ≤30% between countries, with greater penetration in wealthier nations.[10,11] An estimated 54% of the world's population owns a smartphone,[12] and this number increases to ~70% when basic mobile phones (sometimes called "dumbphones") are included. Mobile networks of varying technology level are available to 95% of the world's population, with 5G coverage available to 45%.[13] To a large extent, modern society has reorganized around the capabilities and pocket presence of smartphones. Middle-income countries are already poised to adopt and deploy mobile devices as alternatives to centralized and costly laboratory facilities.[14] There is a trajectory, capacity, and motivation for smartphones to be a truly global technology in the near future.

2.2 Market size

Mobile technologies and services generated 5% of the global gross domestic product (GDP) in 2022.[15] One of the reasons that smartphone technology advances so quickly is its economy of scale. Annual sales have exceeded 1.3 billion smartphones since 2015 and represent a $500 billion USD market.[16] This market size enables the cost of innovation to be amortized across many consumers. Device costs range from $100 to $1200 USD, which are far lower than would be possible with a small market size. Although some of the high purchase price for scientific instruments is attributable to sophistication, much of the price still arises from the need to recover development and manufacturing costs (and profit) from a small customer base. Chemical and biological analysis technologies that leverage mass-produced consumer electronics will be able to have lower purchase costs, more robust supply chains, and more accessible repair options than bespoke instruments.

2.3 Integrated package

Smartphones are built to be a complete and integrated technological package (Fig. 1) with seamless and intuitive utilization of their numerous features by users. That is not the case for two other technologies adopted for portable analytical device development: microcontroller units (MCUs; *e.g.* Arduino) and single-board computers (SBCs; *e.g.* Raspberry Pi).

For a similar set of capabilities, smartphones will better minimize size and weight than custom MCU or SBC devices. Of course, the cost for this benefit is a higher purchase price, a closed hardware system that limits customization, and barriers to replacing individual components rather than the whole device. It contrast, MCUs and SBCs are inexpensive and are designed to be modular and enable custom

Open Access Article. Published on 07 February 2025. Downloaded on 19/4/2026 11:02:09 PM.
This article is licensed under a Creative Commons Attribution-NonCommercial 3.0 Unported Licence.

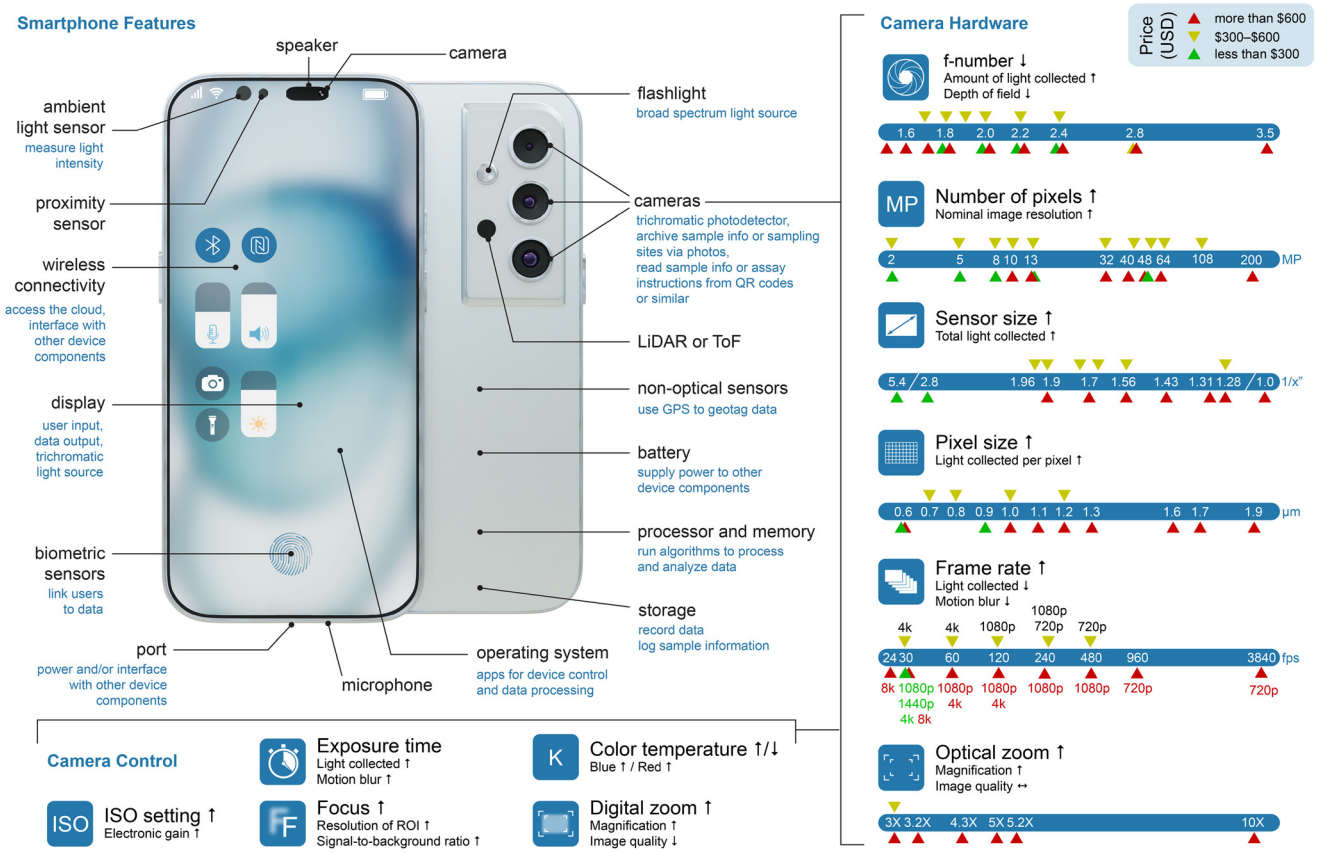

Fig. 1 Features of a modern smartphone and the potential utility of those features for developing devices for chemical and biological analysis. Aspects of the camera hardware and software-based camera control are also highlighted. The examples of hardware specifications for smartphones in three price ranges were collected from a sampling of 27 models released between 2022–2024. Specifications were from vendor websites and online consumer guides. Sensor size is expressed using the industry standard notation: a fraction of a one-inch video camera tube equivalent sensor size (*i.e.* 16 mm diagonal, 4 : 3 aspect ratio). A smaller value for x in $1/x$" is a larger sensor size. Pixel size was estimated from the sensor size and the total number of pixels: the dimension provided is the square root of the maximum possible area of each pixel.

applications. The open-source options for MCUs and SBCs are also beneficial for democratizing and advancing the technology,[17–25] albeit countered by the aforementioned global ubiquity of smartphones.

The technical features (*vide infra*) and form factors of smartphones are also unmatched. As such, common trade-offs for developing analytical devices around MCUs and SBCs include lower performance from lower-cost components, loss of benefits from the scale of the smartphone market, the need for external power and user interfaces, and the time, effort, expense, and learning curve of reengineering features that are already prepackaged in a smartphone. A smartphone is a more rugged and user-friendly platform, and its many integrated sensors are generally superior to the external options for MCUs and SBCs. Lastly, smartphones will best facilitate the integration of analytical devices and assay outcomes with electronic information systems. These systems are, for example, of ever-growing importance for the delivery of health care, and are a source of big data for gaining new health insights from machine learning (ML) and artificial intelligence (AI).

3. Technical features of smartphones

Smartphones have numerous components and features (Fig. 1) that are directly useful for measurements or otherwise support the operation of a portable analytical device.[26,27]

3.1 Cameras

Cameras are one of the most heavily marketed and fastest advancing optoelectronic components of a smartphone. Contemporary smartphone models feature multiple camera systems, where each system includes fit-for-purpose lenses, color filters, a CMOS image sensor, and a processing unit that amplifies, digitizes, and processes the sensor data into a digital image (Fig. 2A and B). The specifications that characterize the cameras are summarized in Fig. 1.

The CMOS image sensor generates data from an array of millions of photodetector elements, each corresponding to an individual pixel. More pixels per image sensor improves the nominal resolution, but does not necessarily improve image quality due to the smaller amount of light per pixel. Modern smartphones are now compensating with camera

 This journal is © The Royal Society of Chemistry 2025

Open Access Article. Published on 07 February 2025. Downloaded on 19/4/2026 11:02:09 PM.
This article is licensed under a Creative Commons Attribution-NonCommercial 3.0 Unported Licence.

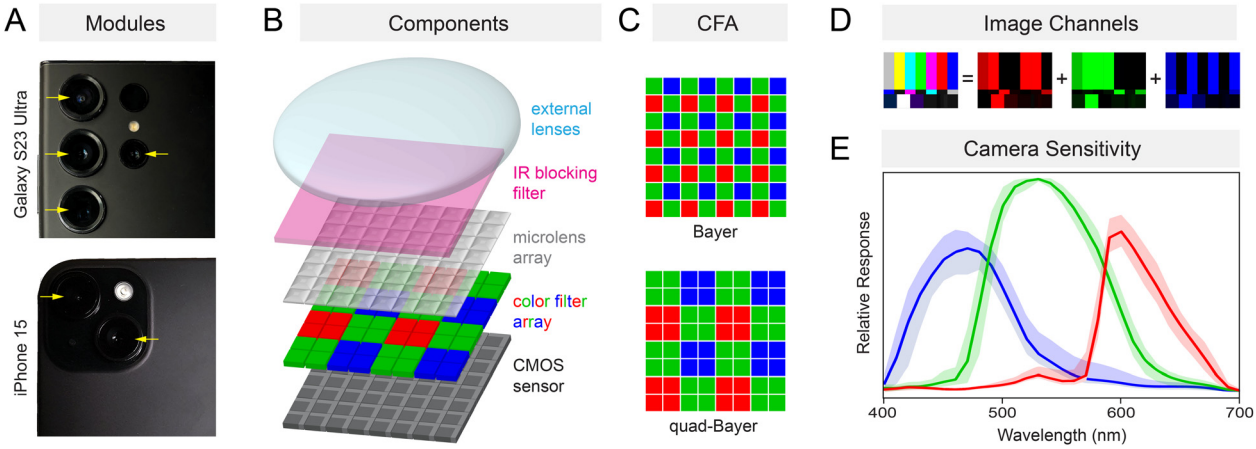

Fig. 2 Important technical components of a smartphone camera. (A) Examples of the exterior view of smartphone camera modules (marked with arrows). (B) Simplified general design of the camera module. (C) Typical arrangements of the Bayer and quad-Bayer color filter arrays (CFAs). (D) An RGB test image decomposed into the corresponding R, G, and B channel images. (E) Typical relative spectral responses of the smartphone camera's R, G, and B color channels. The solid lines in panel E represent the average response across 13 different models and 4 manufacturers of smartphones; the shaded regions reflect the highest and lowest responses at a given wavelength. The response data is from Tominaga *et al.*[28]

modules that offer pixel binning and one of the multiple camera modules having a larger sensor and pixels.

An infrared (IR)-blocking filter and a *Bayer mosaic* or similar color filter array (CFA) of red, green (×2), and blue (RGGB) filters are applied over the image sensor to enable color imaging (Fig. 2C and D). A few smartphone camera models were produced with modified CFAs that substituted yellow (Y) pixels for green pixels (*i.e.* RYYB), added non-selective white (W) pixels (*i.e.* RGBW), or were monochrome (no CFA), all with the goal of higher light capture in non-scientific photography. For otherwise similar sensor specifications, a study found that a monochrome sensor measured a fluorescence signal that was more than double the signal measured with a color sensor.[29] For many smartphones, a quad-Bayer array (Fig. 2C) improves performance at low light levels by supporting pixel binning. To date, the smartphones adopted for portable analyses have almost exclusively had RGB color filters. Most spectroscopists and microscopists would characterize these filters as poor by scientific standards because the transmission spectra overlap and lack a flat top (Fig. 2E). These limitations inform how to optimally use a smartphone camera for optical detection.

Video rates for smartphone cameras range from 24 fps (standard video rate) up to 3840 fps (see Fig. 1). Resolution typically decreases as frame rate increases, but high-end smartphones will support high-definition resolution (720 p or 1080 p) even at hundreds of frames per second. Light capture also decreases as frame rate increases.

3.2 Flashlight

The "flashlight" or "torch" associated with the smartphone camera is another useful component. It is approximately white-light emitting (Fig. 3) and is most often based on the combination of a blue-emitting LED and a phosphor.

The flashlight is a useful illumination source for spectroscopic and imaging applications. Peripheral devices with mirrors, optical fibers, and diffusers have been used to direct white light from the flashlight for a variety of brightfield measurements and imaging,[30–37] but direct illumination from the flashlight has also been satisfactory for many applications and devices. Other devices have used

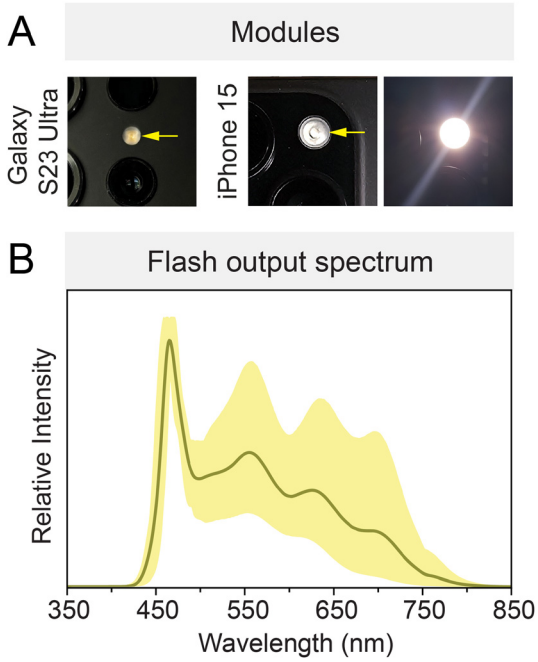

Fig. 3 Smartphone flashlight (or torch). (A) Examples of the exterior view of smartphone flashlight modules (marked with arrows). (B) Typical flashlight output spectrum. The solid line in panel B represents the average output spectrum from the flash across 18 different models and 3 manufacturers of smartphones; the shaded regions reflect the highest and lowest output at a given wavelength. The data in panel B was measured for this review.

Open Access Article. Published on 07 February 2025. Downloaded on 19/4/2026 11:02:09 PM.
This article is licensed under a Creative Commons Attribution-NonCommercial 3.0 Unported Licence.

optical filters to transmit only the blue light from the flashlight for excitation of fluorescence that is imaged in the R and G channels of the camera,[38–41] and transmit only red light for SPR measurements.[42–45]

3.3 Display

Almost every contemporary smartphone has a touchscreen display, where each display pixel comprises red, green, and blue (RGB) sub-pixels that emit that color of light (Fig. 4). As little as ten years ago, most smartphones had liquid crystal displays (LCD) displays. This technology is based on a white back light and each sub-pixel utilizes polarizers and a color filter to transmit only R, G, or B wavelengths with intensities controlled by voltage actuation of liquid crystals. At present and for the foreseeable future, organic light-emitting diode (OLED) displays are the predominant technology. Each pixel is made up of R, G, and B sub-pixels (*i.e.* OLEDs) that emit that color of light directly (Fig. 4B and C). Until recently, OLED displays also incorporated linear polarizers and quarter-wave plates to eliminate reflection of ambient light, but some contemporary displays no longer require these components and thus have better efficiency and higher maximum brightness.

In principle, the smartphone display is another source of light for spectroscopy and imaging experiments. The display has, for example, been used as a source of red light for surface plasmon resonance (SPR) measurements,[46] a source of blue light for excitation of fluorescence (albeit still in combination with a bandpass filter),[47] and as a source of white light for brightfield,[48] phase contrast,[49] and darkfield imaging.[47] A non-smartphone OLED display unit has also been used for multimodal imaging with a smartphone camera, suggesting similar capability for a smartphone display.[50] Potential drawbacks of the smartphone display as a light source include a lower intensity than other options and only three pseudo-monochromatic color choices. The spectrum of white light is also non-uniform, although this limitation equally applies to an external white-light LED. Benefits of the display as a light source include the elimination of a component external to the smartphone and the configurability of illumination, the latter of which has been leveraged to enable photochemistry in an array format.[51]

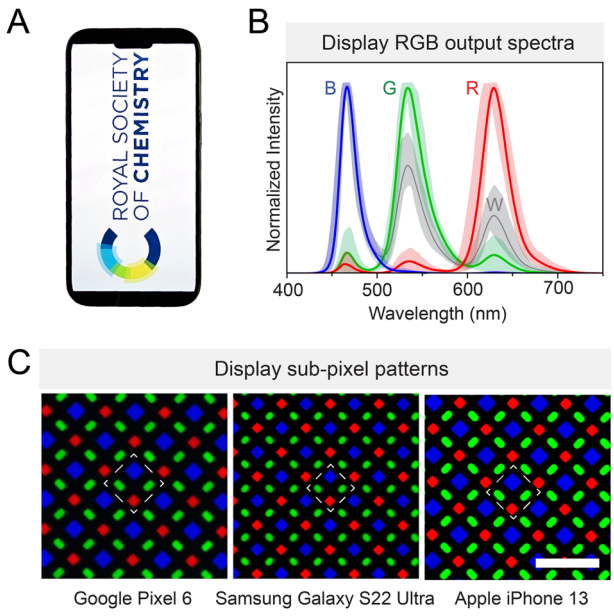

Fig. 4 Smartphone OLED displays. (A) Example of the exterior view of a smartphone display. (B) Typical output spectra of the R, G, and B sub-pixels of smartphone displays, and the combined "white light" output. The solid lines in panel C represents the average display output spectra across 18 different models and 3 manufacturers of smartphones. The shaded regions reflect the highest and lowest output at a given wavelength. (C) Micrographs of displays showing diamond sub-pixel patterns that are common with contemporary smartphone models. The dashed line marks one full pixel. The scale bar is 3.5 μm. The data in panels B and C were measured for this review.

3.4 Other light-based sensors

Most smartphones have proximity sensors, biometric sensors, and ambient light sensors (ALS), among other sensor types. Proximity sensors use reflected IR light to measure the distance from an object. This feature is used, for example, to turn off the smartphone display when held to a user's ear during a call. Some smartphones include sensors for light detection and ranging (LiDAR) or other time-of-flight (ToF) measurements based on reflected IR light. These features are for the purposes of facial recognition, distance measurements, and supporting augmented reality apps. Although largely untapped for molecular analysis, a study has shown that a smartphone LiDAR sensor is able to measure the viscosity of a liquid droplet, with the potential to analyze blood coagulation and the fat content in milk.[52] Smartphone LiDAR has also been proposed for monitoring patient movements.[53]

For biometrics, many smartphone-integrated fingerprint scanners operate based on capacitance or ultrasound imaging, whereas others use a combination of capacitive and optical readout *via* reflected IR light. Imaging reflected IR light is also the basis for iris recognition on some smartphones. These sensors are not anticipated to be directly useful for molecular analyses, but are a potential means of linking measurement data to relevant identifiers (*e.g.* patient, analyst) and for data security.

ALS have spectral responses that approximate the photopic response of the human eye. The sensor response is often used to automatically adjust display brightness and apps are available to measure light intensity quantitatively *via* the ALS. Although this sensor has some latent ability for imaging,[54] the capability is far from practical for molecular analyses. To date, the main analytical application of the ALS is non-imaging smartphone-based photometry, where the ALS has a larger dynamic range and bit depth than the smartphone camera. Cuvette-accommodating smartphone attachments have been developed to use the ALS to assess

 This journal is © The Royal Society of Chemistry 2025

Open Access Article. Published on 07 February 2025. Downloaded on 19/4/2026 11:02:09 PM.
This article is licensed under a Creative Commons Attribution-NonCommercial 3.0 Unported Licence.

bacterial growth *via* measurements of turbidity,[55] to measure enzyme activity and inhibition by heavy metals through a pH indicator dye,[34] and to quantify Cr^{6+} (aq) in water samples through a chromogenic chelator.[56] Smartphone ALS-based devices have also been developed for quantitative analysis of colorimetric dipstick[57] and lateral flow assays[58] for organophosphate pesticides, and for lateral flow tests of wild-type pseudorabies virus infection,[59] blood bilirubin levels,[60] prostate-specific antigen (PSA) in patient blood,[61] and ampicillin residue in animal milk.[61]

Multi-channel sensors that measure both the color and intensity of ambient light are the latest generation of ALS technology. These sensors enable automatic adjustment of color temperature for smartphone photography and device displays. This capability will support more robust colorimetric assays under ambient light and help minimize the number of peripheral components (*e.g.* box, specific light source) needed for reliable smartphone-based measurements.

3.5 Non-optical sensors

Most smartphones include non-optical sensors such as an accelerometer, gyroscope, other orientation and motion sensors, and a magnetometer/geomagnetic field sensor. Collectively, these components provide information about position and movement of a smartphone, and have roles in image stabilization, but are otherwise not anticipated to have direct application to molecular analyses. Every smartphone also has at least one built-in microphone, which is potentially useful for attaching verbal notes to measurement data, monitoring breathing,[62–64] and, speculatively, has latent potential for photoacoustic detection for assays. A database of smartphone sensors has been established to support the physical phone experiments (phyphox) education project.[65]

3.6 Battery

Smartphone batteries are lithium-ion technology and store up to 4000–6000 mAh of rechargeable energy. The batteries can power not only the phone but also peripheral components and devices. In most cases, up to 10 W of power (5.0 V DC potential and a current up to 2.0 A) can be drawn from the nominal charging port (*e.g.* USB-C) of the smartphone. This power is sufficient to operate many LEDs, laser diodes, and electric motors, meaning that smartphone-based devices do not necessarily need a separate power supply for components external to the phone. In principle, voltage and current can also be drawn from audio jacks (*e.g.* tip-ring-ring-sleeve, TRRS). These connectors are increasingly scarce with smartphones and may not reach the same voltage and current levels as a USB-C port. In addition, consumer demand for on-the-go charging of smartphones has led to the mass commercialization of portable power banks that are also useful as a power source in a portable device. Power banks have the potential to provide higher voltages (5–20 V) and currents (up to 5 A), and have longer operating capacities (≥10 000 mAh) than the batteries built into smartphones.

Despite the capability of the smartphone battery to power external components, most smartphone-based analytical devices still incorporate separate batteries (*e.g.* 1.5 V AA size, 9 V PP3 size) for this purpose. In some cases, these external batteries provide more direct access to a higher voltage (no need for a voltage converter in a circuit) or current, or might usefully extend the operating time of the smartphone device between recharges (*i.e.* less drain on the smartphone battery). In other cases, the use of external batteries is a preference for prototyping with no significant functional advantage over the smartphone battery. In both cases, downstream circuit components can modify the electrical output to what is required for an application.

3.7 Wireless connectivity

Most smartphones include technologies for medium-range and short-range (*e.g.* Bluetooth, near-field communication/NFC) connections and data transmission with other enabled devices in close proximity. These modalities have utility for connecting to and controlling device components external to the smartphone, helping to mitigate any limitations associated with the single physical port on a smartphone.

Smartphones also transmit data globally through Wi-Fi and cellular networks based on LTE (long term evolution) and other standards categorized as 3G, 4G, and 5G. For applications in some low resource settings, smartphone-based analytical devices will need to be fully functional in the absence of a network connection (although satellite connectivity for data transmission is reasonably anticipated for smartphones in the future). Connectivity adds processing and storage capacity *via* cloud services and makes support from human expertise accessible around the globe.

An on-board global positioning system (GPS) and other location services are available to tag data with geographical and temporal information—features that are especially useful for documenting field-based measurements. Most smartphones use assisted (or augmented) GPS (A-GPS) in normal operation, but do contain GPS receivers that function in the absence of cellular service or network connectivity.

3.8 Computation, memory and operating systems

Most contemporary smartphones have tens or hundreds of gigabytes of storage, gigabytes of memory (*i.e.* RAM), and gigahertz processors—technical specifications that are on par with or better than the minimum requirements that have operated laboratory instruments for decades. Even without considering opportunities for cloud computing, smartphone technology is capable of handling the data acquisition and processing needed for many spectroscopic and imaging applications, and some modest implementations of ML and AI algorithms for data analysis.

Smartphones run operating systems (OS) to connect hardware with apps. The two dominant OS are Android

Open Access Article. Published on 07 February 2025. Downloaded on 19/4/2026 11:02:09 PM.
This article is licensed under a Creative Commons Attribution-NonCommercial 3.0 Unported Licence.

(~71% of the global market) and iOS (~28%).[66] Most researchers adopt Android devices due to the larger market share, and for the more open and flexible ecosystem for app development and distribution. Nonetheless, there are concerns that Android is moving toward a more closed system with increasing reliance on proprietary software and a closed-source version of Android from Google. A closed system like iOS has potential advantages in terms of security and privacy, seamless integration with other devices (*e.g.* desktop and notebook computers, tablets), and a smaller number of smartphone models with which an app needs to be compatible. Although some researchers code their own apps for smartphone-based measurements, there are pre-existing apps that support research and development. Examples include native and third-party apps that provide users with substantial manual control over camera settings for photography (*vide infra*), mobile development apps for MATLAB and Python, and support for integration of these codes into custom Android or iOS apps written in Android Studio or Apple Xcode integrated development environments (IDEs).

4. Complementary technologies

On its own, a smartphone is sufficient hardware for only some assays—colorimetric detection being the most frequent example. For other assays, such as those based on fluorescence, a smartphone needs support from external components. There are several technologies that have a recurring role in supporting smartphone-based devices and assays.

4.1 3D printing

Three-dimensional (3D) printing fabricates objects through successive deposition of layers of material.[67–69] This rapidly proliferating technology is democratizing prototyping *via* simple-to-operate and consumer-affordable desktop printers. Although there are many classes of 3D printing, the two most relevant classes are fused deposition modelling (FDM)/fused filament fabrication (FFF) printers and photopolymerizable resin-based printers.

FDM/FFF printers are available at low to modest cost ($200–5000) and offer print resolution ≥0.2 mm, reasonable print speeds, potentially large build areas, and printing materials such as acrylonitrile butadiene styrene (ABS) and polylactic acid (PLA). These printers have been widely adopted for fabricating the housing of smartphone-based devices, as well as holders, mounts, and supports for optical components, circuit boards, and other peripheral components.

Photopolymerizable resin-based 3D printers are available in stereolithography (SLA), digital light processing (DLP), and masked stereolithography (MSLA; also known as LCD) varieties that use epoxy, acrylic and methacrylic monomers. The purchase prices are similar to FDM/FFF printers. Although post-processing such as UV curing and solvent washes are sometimes needed, the prints are macroscopically smooth, watertight, robust, and (for colorless resins) semi-transparent. The technology is suitable for the fabrication of watertight flow cells and making molds for the soft-lithographic preparation of microfluidic chips.[70–72] Lenses can also be fabricated but will tend to require post-print smoothing by sanding or coating procedures to obtain sufficient transparency for practical use.[73–75]

Collectively, a smartphone, an FDM/FFF 3D printer and filament, a photopolymerization 3D printer and resin, and some basic tools (*e.g.* sandpaper, knife, rotary tool and bits) have the potential to function as a near-complete kit for prototyping or maintaining a smartphone-based analytical device. Depending on the measurement modality and assay designs, some additional kit may also be warranted: light sources (*e.g.* LEDs), electronic components (*e.g.* wire, resistors, connectors, solder, soldering iron), simple optical components (*e.g.* lenses, mirrors, colored filters), mild solvents (*e.g.* isopropyl alcohol), and simple plasticware (*e.g.* tubing, syringes). Although these resources are not household items and not without cost, they are realistic and common for professional and at-home workshops to stock and utilize. Examples of LEGO®-based smartphone devices,[76,77] including with deep-learning-based computer vision, further show that analytical function is not predicated on sophisticated hardware external to the smartphone.

4.2 LEDs and laser diodes

Light-emitting diodes (LEDs) are ubiquitous in consumer electronic devices and have small sizes, low cost ($0.25–100 USD), and long operating lifetimes (≥10^4 h), making them an ideal peripheral light source for many smartphone-based

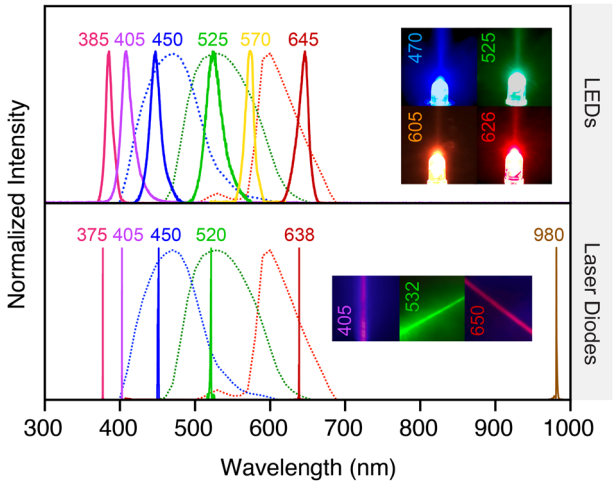

Fig. 5 LEDs and laser diodes. Examples of emission spectra of LEDs (top) and laser diodes (bottom) superimposed on the average spectral responses of the smartphone camera RGB color channels (dotted lines). The insets show images of LEDs and beams from laser diodes. Some digital adjustment of color was made to these images to mimic the appearance to the human eye. LED and laser diode spectra were plotted from publicly available vendor data (ThorLabs) for commercial products.

Open Access Article. Published on 07 February 2025. Downloaded on 19/4/2026 11:02:09 PM.
This article is licensed under a Creative Commons Attribution-NonCommercial 3.0 Unported Licence.

devices. LEDs with broad-spectrum "white light" emission (similar to a smartphone flashlight) and with nominally monochrome emission (FWHM of 20–70 nm; Fig. 5) from the UV through near-IR regions of the spectrum are available with milliwatt scale powers. With the exception of UV and some violet LEDs, the frequent trade-off for the lower cost of an LED is the loss of access to some or all of the bandwidth of an imaging RGB color channel due to the long-pass optical filter needed to block stray LED light. The inclusion of a narrow bandpass excitation filter in a design mitigates this disadvantage at the cost of lower excitation intensity.[78–80]

Laser diodes are also components in consumer devices (*e.g.* optical drives, laser pointers, barcode readers, 3D printers, laser printers) and are available at low to high cost ($10–1000) with small size, milliwatt powers, and wavelengths from the UV to the near-infrared. Although cost will generally favor the use of LEDs, the monochromatic output of laser diodes (FWHM ≤ 1 nm; Fig. 5) can be a technical advantage for photoluminescence (PL) measurements—the application where a majority of laser diodes[29,81–86] and non-white LEDs have been utilized—because a greater fraction of a smartphone camera RGB channel remains accessible.

Many LEDs and laser diodes are operable with the voltage and current output available from a smartphone USB-C connector, power bank, or common consumer batteries. A simple circuit can step voltage up or down as needed. LED wavelengths have ranged between 285 nm (UVB) and 625 nm (red). Laser diode wavelengths have ranged from 365 nm (UVA) to 638 nm (red), with powers ranging from 20 mW up to 180 mW. The notable exception has been measurements with upconversion materials, which utilize 808 nm or 980 nm wavelengths. For applications with non-trivial illumination requirements (*e.g.* PL measurements, microscopy, spectroscopy), laser diodes have been adopted as the excitation source about 15% of the time, whereas LEDs have been adopted about 65% of the time (or 70% when including the smartphone flashlight, *vide infra*).

4.3 Microcontrollers

SBCs such as Raspberry Pi compete with smartphones as a technology for operating portable analytical instruments. Certain models of SBC have some similar technical capability (GHz processors, up to 8 GB RAM, Bluetooth, Wi-Fi, Linux OS) but lack the display, user input, power, and sensor (*e.g.* camera) components that are built into a smartphone. Potential advantages of these SBCs over smartphones are their lower cost ($50–100 USD) and on-board pins for digital input/output (GPIO; 3.3 V, 16 mA) and power out (5 V, 1A), albeit that similarly functioning USB-C-connected external modules for GPIO can be connected to a smartphone. High-end external camera modules ($50 USD) for Raspberry Pi are available with adequate specifications and RAW support. The overall capabilities and features for smartphones and SBCs are generally too similar for both technologies to be logically used in tandem, and smartphones have an edge in several categories (Fig. 6).

In contrast to SBCs, MCUs have the potential to complement smartphones as a technology for operating portable analytical instruments. The open-source Arduino boards are popular for rapid prototyping,[87] and their combination with 3D printing has been reported to reduce costs by an order of magnitude for scientific technology.[88] Arduinos integrate features like a modest central processing unit (8–84 MHz), memory (up to 8 MB RAM), wireless communication (*e.g.* Wi-Fi, Bluetooth), and 5 V pins for

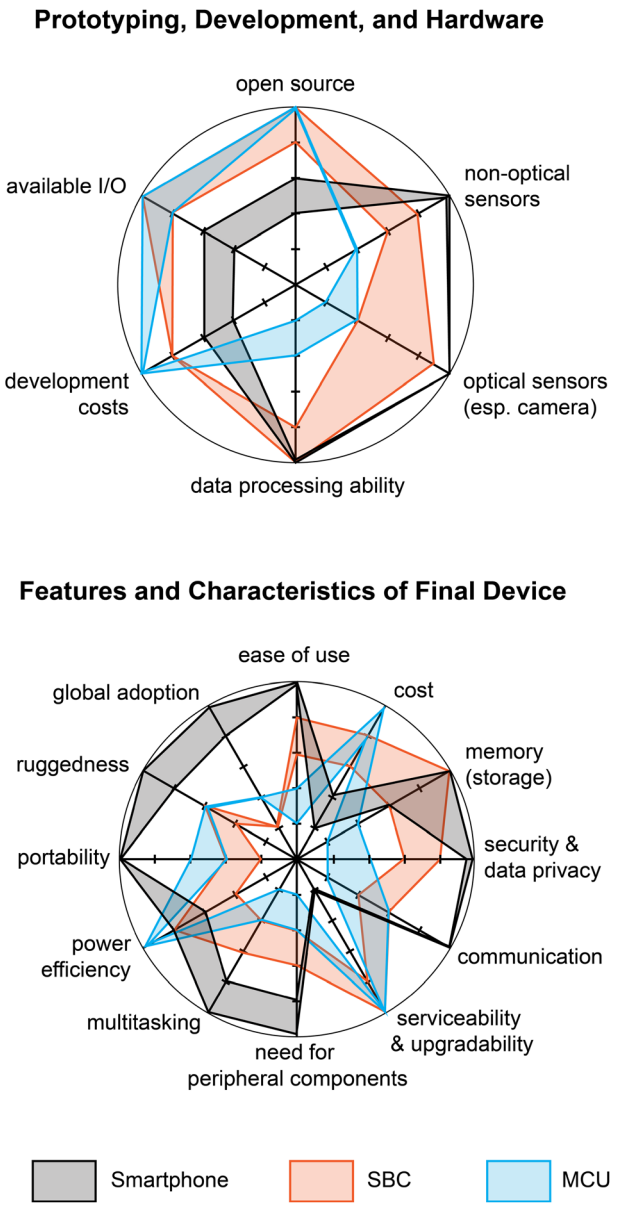

Fig. 6 Radar charts highlighting our perspective on some of the advantages and disadvantages of SBCs, MCUs, and smartphones as platforms for developing analytical devices. A further distance from the center indicates a more favorable rating. Ranges of ratings are shown in an effort to accommodate different specifications between different models and different application contexts.

Open Access Article. Published on 07 February 2025. Downloaded on 19/4/2026 11:02:09 PM.
This article is licensed under a Creative Commons Attribution-NonCommercial 3.0 Unported Licence.

digital input/output, analog output, and pulse-width modulation output (a digital means of mimicking analog output). These devices require external power, do not have built-in user interfaces, and do not utilize an OS, but there is software for writing and uploading code (*e.g.* Arduino IDE, based on C++, or MicroPython). The Arduino hardware catalog also includes external "shields" that interface with the main boards to provide additional features (*e.g.* motor drivers). Some non-Arduino MCUs, such as ESP32 and Teensy models, have higher processing power (up to 240 MHz and more RAM) but lower output voltage (3.3 V). With prices that range from $10–100 USD and minimal duplication of smartphone capability and features, MCUs add versatility by supplementing smartphone-to-peripheral connections with smartphone-to-MCU-to-peripheral connections. Several devices reported in the literature have paired smartphones with MCUs.[89–97]

4.4 Microfluidics

Microfluidic and nanofluidic devices manipulate small volumes (μL to pL) of fluid as continuous flows in channels and as discrete droplets in multiple formats. Fluid is transported *via* the application of pressure, electrowetting,[98,99] capillary forces, light,[100] and more.[101,102] Smartphone devices have the potential to interface with microfluidic devices as optical detectors, power supplies, controllers, data handlers, and user interfaces.[103] Ideally, the smartphone replaces a laboratory instrument for detection and the microfluidic chip replaces the benchtop sample preparation and assay steps done by a lab technician.

Common materials for microfluidic chips include glass, polymers, and even paper.[104] Although long associated with fabrication in clean rooms, channel microfluidics are now broadly accessible through commercially available glass capillaries, 3D printing of molds for polydimethylsiloxane (PDMS)-based soft lithography, and 3D printing of complete chips.[70–72] Do-it-yourself hardware is increasingly common: syringe pumps and peristaltic pumps that drive fluid flow have been built using 3D-printed components and low-cost motors that can be powered by batteries or spring loading,[105–112] and a low-cost 3D printer kit has been transformed into multiple syringe pumps.[113] Alternatively, microfluidic paper analytical devices (μPADs)[114] and capillaric chips[115] do not need pumps because flow is driven by capillary action—an operational simplicity that is ideal for portability. Paper also has the advantages of being lightweight, inexpensive, biodegradable, incinerable (*e.g.* if samples are biohazardous), and capable of sample cleanup *via* filtering action. Despite the discontinuation of commercial wax ink office printers, wax printing remains the most common method for patterning channels and zones on paper, but alternative methods of creating hydrophobic barriers have been developed.[116,117]

Beyond channels, digital microfluidics based on electrowetting are promising because of the complex operations that are possible in this format, and the potential to miniaturize the driving electronics and use optical actuation.[118–123]

For smartphone-based analyses, a microfluidic chip must have optical characteristics and a design that are suitable for the desired type of measurement. For example, reflection colorimetry often needs a white background, such as from a paper substrate or μPAD. PL detection benefits from transparent optical paths for emission and excitation light, avoidance of strong camera-directed reflections of excitation light, and low autofluorescence from the chip material. Nominally transparent polymers such as poly(methyl methacrylate),[124] polycarbonate, polyethylene terephthalate,[125–127] cyclic olefin copolymer,[128,129] and PDMS are useful materials for microfluidic chips.[130] These polymers transmit wavelengths longer than 400 nm, but transmission is usually lost between 300–400 nm, which has implications for excitation in PL measurements. The nominally transparent resins for photopolymerization 3D printing have a narrower range of transmission, with short-wavelength cut-offs nearer to *ca.* 430 nm, and often require polishing to be more transparent than translucent. Microfluidic chips made entirely of glass or with a glass face (*e.g.* PDMS-on-glass chips) typically provide the widest range of wavelength transmission. Autofluorescence and the scattering and reflection of light are sometimes challenging to address with smartphone-based devices, where considerations such as cost, robustness, and compact design may restrict the practical range of solutions to these problems.

5. Complementary materials

Smartphone cameras are capable imagers but nonetheless have technical limitations intrinsic to their design and intended use. The analytical performance of a smartphone-based device will almost always be less than what is possible with in-lab sample handling and a modern laboratory instrument, making it advantageous to adopt materials that help mitigate these limitations or otherwise simplify detection.

5.1 Indicator dyes

Indicator dyes undergo a spontaneous change or restriction in their molecular structure or conformation in response to an analyte, with a concomitant change in their visible color or fluorescence properties (*e.g.* brightness). Numerous indicator dyes exist for pH and the detection of ions, single-stranded DNA, double-stranded DNA, RNA, and more. These materials facilitate "mix-and-measure" assays that do not require washes or other signal development steps, and produce signals that can be followed in real time. The simplicity is ideal for a portable diagnostic test with smartphone-based readout. A potential drawback is that the typical absorption coefficients and fluorescence brightness for molecular dyes (10^4–10^5 M^{-1} cm^{-1}) are often modest compared to those for some nanomaterial chromophores and

 This journal is © The Royal Society of Chemistry 2025

Open Access Article. Published on 07 February 2025. Downloaded on 19/4/2026 11:02:09 PM.
This article is licensed under a Creative Commons Attribution-NonCommercial 3.0 Unported Licence.

fluorophores, potentially resulting in less favourable detection limits and sensitivity.[131] The excitation and emission spectra of many fluorescent dyes will also tend to restrict usage of one or more smartphone camera RGB color channels.

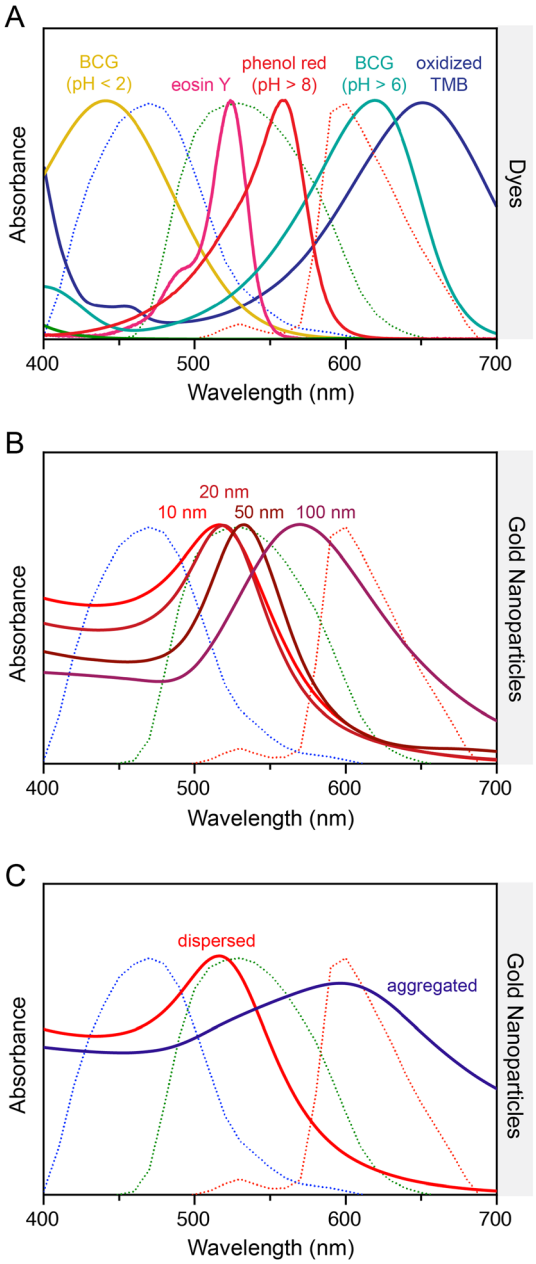

Fig. 7 Normalized extinction spectra of selected materials. (A) Examples of common dyes: oxidized TMB,[132] phenol red,[133] eosin Y,[133] bromocresol green (BCG). (B) Different diameters of AuNPs. (C) Dispersed and aggregated AuNPs. The spectra are superimposed on the typical RGB channel responses of a smartphone camera (dotted lines). Note: the spectrum for oxidized TMB is for its charge transfer complex with TMB, which is usually the first colored product from the catalyzed oxidation of TMB. Uncomplexed oxidized TMB has an absorption maximum at 450 nm (not shown) and is usually isolated by the addition of acid. The source data for dye spectra are cited. AuNP and BCG spectra were measured for this review.

Under approximate white-light illumination, molecular dyes produce color in smartphone images based on the wavelengths of light absorbed relative to the RGB color channel responses (Fig. 7A). In the dark, the imaged color of a fluorescent dye corresponds to the wavelengths of light emitted relative to the RGB channel responses (Fig. 8A).

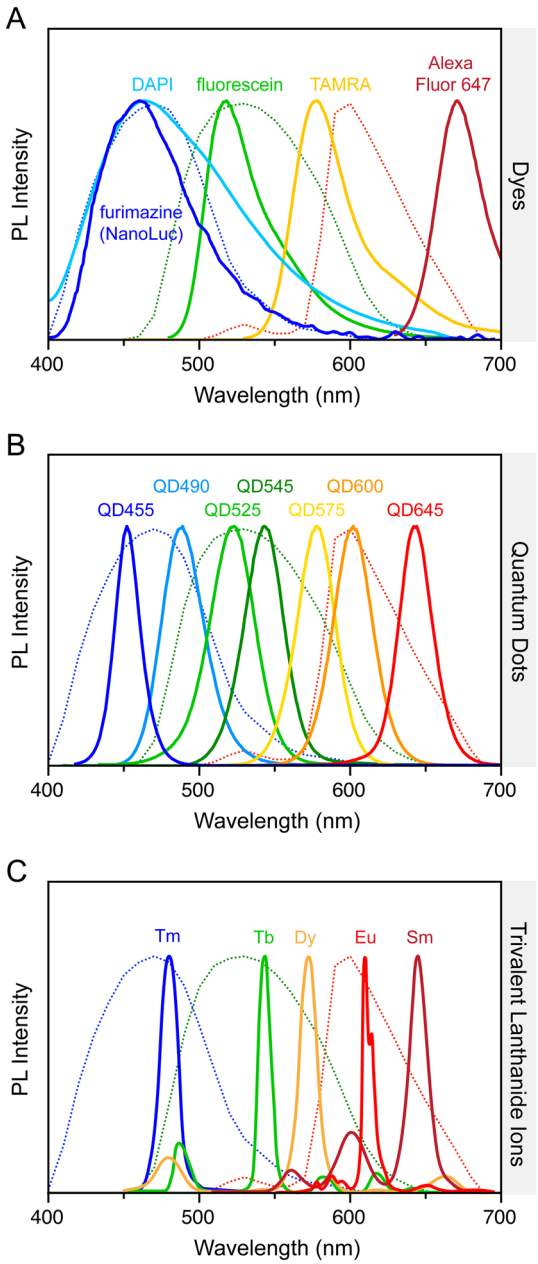

Fig. 8 PL emission spectra of selected materials: (A) common fluorescent dyes (DAPI = 4′,6-diamidino-2-phenylindole, fluorescein, TAMRA = carboxytetramethylrhodamine, Alexa Fluor 647, and the emissive product from turnover of furimazine by NanoLuc (dye spectral data from **http://FPbase.org**); (B) different sizes of QDs; and (C) some trivalent lanthanide ions (data replotted form ref. 134). These spectra are superimposed on the typical RGB channel responses of a smartphone camera (dotted lines).

Open Access Article. Published on 07 February 2025. Downloaded on 19/4/2026 11:02:09 PM.
This article is licensed under a Creative Commons Attribution-NonCommercial 3.0 Unported Licence.

5.2 Nanozymes

When sufficiently robust and selective, catalysts that are organic, inorganic, or biomolecular in nature are a useful means of producing amplified signals from individual binding events. Enzymatic amplification in molecular analysis is well-established in the form of enzyme-linked immunosorbent assays (ELISAs) and real-time polymerase chain reaction (PCR) to enhance detection limits with laboratory instruments. The catalytic amplification of chromogenic and fluorogenic reactions (typically using molecular dyes) has equal or greater value in mitigating the modest sensitivity of smartphone cameras compared to research-grade cameras and photodetectors. The potential trade-off is that these reactions add washing and signal development steps to assays, which conflicts with the oft-desired minimization of user actions.

Borrowing directly from classic ELISA methods, the enzyme-catalyzed (*e.g.* horseradish peroxidase, HRP) and nanomaterial-catalyzed oxidation of 3,3′,5,5′-tetramethylbenzidine (TMB) to yield a blue color has been the most widely adopted chromogenic reaction for smartphone-based assays. Peroxidase mimics and other nanoparticle (NP) catalysts that are able to turnover a chromogenic substrate under ambient conditions (*a.k.a.* nanozymes) are of interest because of their potentially greater robustness and shelf life, lower manufacturing cost, and ease of modification *versus* conventional enzymes.[135,136] Analogous to enzymes, nanozymes are not immune to inhibition by components of a sample matrix, and inhibitory effects are sometimes useful for the detection of certain analytes. Nanozyme-based amplification will benefit from the microfluidic automation of fluid handling to reduce multiple assay steps to a single user step.

5.3 Metal NPs

Gold nanoparticles (AuNPs; *ca.* 10–100 nm diameter) are a popular choice as a colorimetric label for smartphone-based assays. The plasmon resonance of these materials (Fig. 7B) generates a deep red color with very large per-particle extinction coefficients (10^7–10^{11} M^{-1} cm^{-1}), and there is a substantial spectral change in optical extinction between dispersed and aggregated states, with color turning from red (strong green absorption) to blue/purple (broad absorption from yellow to red; Fig. 7C). AuNPs are most frequently paired with smartphone cameras for brightfield imaging, and occasionally for darkfield imaging. The main advantage in both cases is the sensitivity boost from a high optical contrast per small amount of material. Unlike many other NPs, where light absorption is the dominant contribution to extinction, light scattering is also very strong for metal NPs. Moreover, metal NPs can be leveraged for metal-enhanced fluorescence. The robust chemical stability of AuNPs is why these materials are much more prevalent in assays than other metal NPs with similar plasmonic properties.

In most applications, AuNPs are adopted as a label for generating contrast in binding assays. Silver enhancement—the reductive growth of a thick layer of silver on AuNPs—has been used to generate even greater optical contrast, but the post-assay development steps are not ideal for a portable analysis without on-chip automation. The aggregative behavior of AuNPs also functions as a "mix-and-measure" sensor, but ensuring robust selectivity sometimes requires more careful and challenging design than for molecular indicator dyes.

5.4 Quantum dots

Quantum dots (QDs) are colloidal semiconductor nanocrystals (2–10 nm diameter[137]) that are brightly photoluminescent when prepared as high-quality core/shell materials.[138] The emission wavelength is tunable across the visible spectrum *via* nanocrystal size and composition. For monodisperse CdSe/ZnS, CdTe/ZnS and related QD materials, the emission is also symmetric and spectrally narrow (FWHM 25–35 nm; Fig. 8B). Other QD materials, such as InP/ZnS, have visible emission that is less narrow (FWHM 35–50 nm) but still symmetric. QDs are also characterized by spectrally broad absorption and higher brightness *versus* organic fluorophores. The latter arises from larger molar absorption coefficients (10^5–10^7 M^{-1} cm^{-1}), competitive emission quantum yields, and superior resistance to photobleaching. QDs have been shown to have a clear brightness advantage over fluorescent dyes and proteins, especially when blue light filtered from the smartphone flash is used for excitation.[38]

The PL properties of QDs are an ideal match to smartphone cameras: high brightness mitigates the modest sensitivity of the image sensor *versus* research-grade cameras and photodetectors; the resistance to photobleaching enables longer image exposure times to further enhance signals; the narrow PL emission can be aligned to one of the RGB color channels to maximize sensitivity while minimizing crosstalk with other channels; and the broad absorption enables all colors of QD to be optimally excited with violet or UV light, leaving all of the camera RGB channels available for PL emission measurements. Most organic fluorescent dyes do not offer the same capability. At present, QDs are the material that most readily enables up to three-color multiplexed detection with a smartphone camera.[139] QDs also function as "mix-and-measure" sensors for smartphone-based analyses through processes such as Förster resonance energy transfer (FRET),[139,140] where these sensors can be sufficiently bright for detection directly in whole blood.[141]

The main drawback of QDs is the frequent inclusion of cadmium in the best-in-class materials. This inclusion is often framed as a toxicity issue, but such framing is an oversimplification.[142–144] Toxicity has limited relevance to *in vitro* analyses, where measurements of biological samples are *ex vivo*, minute quantities of material are needed per test, and some assay formats will already include some level of containment for the sample. Rather, the more relevant

 This journal is © The Royal Society of Chemistry 2025

Open Access Article. Published on 07 February 2025. Downloaded on 19/4/2026 11:02:09 PM.
This article is licensed under a Creative Commons Attribution-NonCommercial 3.0 Unported Licence.

challenge is one of environmentally conscious or regulated disposal in low-resource settings and, ultimately, sustainability for use at a global scale.

5.5 Semiconducting polymer dots

Semiconducting polymer dots (Pdots) and conjugated polymer NPs are two classes of NP (20–100 nm diameter) with a high mass percentage (>50% w/w) of fluorescent semiconducting polymer in their composition. These materials have very large molar absorption coefficients for UV and blue light (10^6–10^9 M^{-1} cm^{-1}), competitive emission quantum yields, and photobleaching rates that are often slower than for fluorescent dyes. The semiconducting polymer emission is spectrally broad (FWHM 40–100 nm) but can be narrowed by incorporating suitable fluorophores into the polymer structure. The substantial advantage of Pdots is brightness that tends to be the highest per particle among the different types of fluorescent NPs. For example, Pdots have been shown to provide much lower detection limits than QDs in lateral flow-style binding assays, albeit outperformed by QDs for two-color multiplexing between the R and G smartphone camera channels.[145] The brightness was even sufficient to measure subcutaneous glucose and NADH in mouse models using red-fluorescent Pdot-based sensors with smartphone-based imaging under a UV lamp.[146,147]

5.6 Upconversion nanoparticles

Lanthanide-doped upconversion NPs (UCNPs; 20–150 nm diameter) leverage the electronic transitions that are possible within the 4f electron shells of lanthanide ions to generate visible luminescence from infrared excitation.[148,149] As is characteristic of trivalent lanthanide ions, the PL emission consists of narrow lines (FWHM 15–30 nm) at specific wavelengths and with relative intensities that depend on the composition of the UCNPs. Several lanthanide emitters have emission lines in the visible spectrum (Fig. 8C). Excitation of UCNP PL is *via* sequential two-photon absorption, typically using laser diode wavelengths of either 808 nm or 980 nm.

The main advantage of UCNPs with smartphone cameras is the near-IR excitation, which is a spectral region that is already blocked by the IR filter in the smartphone camera assembly and induces negligible autofluorescence from most samples and materials. UCNPs thereby enable imaging without an emission filter, with very low background, and with potentially less pre-processing of crude samples. For assay formats with short optical path lengths through samples, there is significant potential for the suppression of autofluorescence background from the assay vehicle (*e.g.* lateral flow membranes, paper test strips, microfluidic chips) to be a greater benefit than the suppression of autofluorescence from the sample itself.

A potential disadvantage of UCNPs is their modest brightness from relatively low absorption coefficients, modest upconversion quantum yields, and low emission rates. The emerging technology of organic-based triplet-triplet annihilation (TTA) upconversion NPs has the potential to provide higher brightness, but color multiplexing will typically be limited by the broad emission spectra.[131] Although some UCNP compositions have an narrow emission line that is well aligned with an RGB color channel, other compositions have lines that are detected in multiple color channels. Results with smartphone-based imaging of luminescent lanthanide complexes (LLCs) suggest that the combination of Tb(III) and Eu(III) emitters is effective for two-color multiplexing between the G and R channels,[150] and there is potential for Tm(III) to leverage the blue channel as well. With their typical UV excitation, molecular luminescent lanthanide complexes are arguably less appealing for smartphone imaging than UCNPs because of the technical need for a time-gated imaging mechanism to supress autofluorescence, which is more demanding than simple inclusion of a NIR laser diode. Otherwise, LLCs are expected to perform similarly to lanthanide-based UCNPs, with the possible added benefit of being directly substitutable for fluorescent dyes in assays.

5.7 Persistent-luminescence NPs

Persistent-luminescent NPs (PLNPs), also known as "afterglow" NPs, are materials that transiently trap and store energy from the absorption of UV-visible light or X-rays. This energy is gradually released as luminescence over a period of minutes, hours, or even days after the excitation source is turned off.[151] The emission centers tend to be lanthanide ions, transition metal ions, or main group/post-transition metal ions, with peak emission wavelength and bandwidths that correspond to these origins.

The primary advantage of PLNPs is the temporal separation of excitation and detection. An imaging camera is able to be turned off when the excitation light is turned on, and *vice versa*. This capability eliminates background from stray excitation light and sample autofluorescence. Persistent luminescence makes it possible for device designs to omit an optical filter (something that is essential for conventional fluorescence measurements) and to avoid background from autofluorescence. The potential drawbacks of PLNPs are concerns related to some of their metal-based compositions, the lower brightness that is an outcome of their slow emission rate, and additional parameters to keep constant for intensity-based calibration (*e.g.* excitation duration, time between the end of excitation and the start of imaging). In principle, the most suitable applications for PLNPs are those where the decrease in background more than offsets the decrease in signal compared to another type of luminescent material. In practice, it is difficult to fully benchmark the advantages and disadvantages of PLNPs because of the few studies with smartphone-based detection.

Open Access Article. Published on 07 February 2025. Downloaded on 19/4/2026 11:02:09 PM.
This article is licensed under a Creative Commons Attribution-NonCommercial 3.0 Unported Licence.

6. Measurement modalities and technical approaches

6.1 Role of the smartphone

Smartphones are utilized as components of portable analytical devices in three main ways: *linked*, *dongle*, and *integrated* (Fig. 9). Smartphone-linked devices are standalone devices in every way other than a wireless connection to a smartphone. Dongle devices require a physical connection to a smartphone, which is principally a user interface and power supply but is not directly active in analyte detection. Smartphone-integrated devices make direct use of the smartphone camera or another on-board feature (*e.g.* ALS, flashlight) for analyte detection. Integrated devices will frequently assemble dongle-like, wirelessly connected, and unconnected peripheral components around the smartphone to provide the full technical capability needed for a measurement.

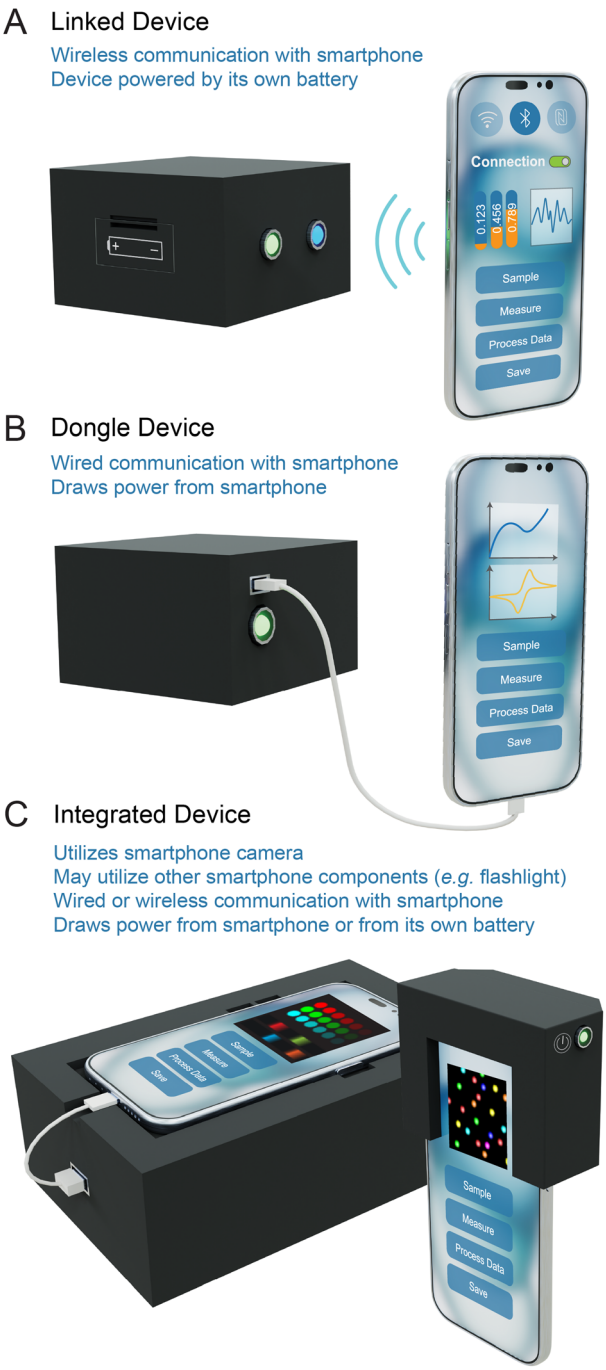

Fig. 9 Conceptualization and characteristic features of (A) linked, (B) dongle, and (C) integrated devices that utilize smartphones.

Linked and dongle devices are often bespoke and therefore adopt designs and components that are optimized for the analytical measurement and user context. The smartphone functions as a user interface and as a platform for data processing, storage, and sharing. Compared to other benchtop and portable instrument systems, linked and dongle devices benefit from offloading bulkier components (*e.g.* power, display, user input) to the phone. This approach decreases the size and cost of the analytical device when an analyst already has access to a smartphone. The anticipated worldwide standardization of smartphone charging ports to USB-C (already implemented in European Union[152]) will also enable linked and dongle devices to function independent of the make and model of smartphone. Indeed, dongle devices are an inevitable future for portable electrochemical analysis. The future for optical analysis is less certain because cameras and light sources are built into smartphones.

Given their bespoke designs and mere "connected" role for the smartphone, linked and dongle devices for molecular analysis are not discussed further in this review. Rather, the focus is on integrated devices that adopt, at minimum, the smartphone camera as an essential component. This approach requires fewer external components and less secondary engineering than linked and dongle devices, leading to simpler device prototyping (especially by non-engineers) and greater potential for democratization. The highly competitive consumer market also ensures that smartphones provide access to best-in-class image sensors, regularly upgraded technology, and opportunities to utilize non-imaging features to enhance measurements or data collection.

6.2 Colorimetry

This detection modality uses a smartphone camera to identify and quantitate changes in color, where both transmitted- and reflected-light configurations are useful for these measurements. Most measurements are under white light and the observed color is best predicted by subtractive color theory (Fig. 10A), with cyan (red absorbing), magenta (green absorbing), and yellow (blue absorbing) primary colors. Common signaling motifs include analyte-induced transitions between colorless and colored states, transitions between two different colors, and analyte-induced changes in color patterns for an array of chromophores. These signals most frequently originate from changes in the efficiency or dominant wavelength of light absorption associated with

This journal is © The Royal Society of Chemistry 2025

Open Access Article. Published on 07 February 2025. Downloaded on 19/4/2026 11:02:09 PM.
This article is licensed under a Creative Commons Attribution-NonCommercial 3.0 Unported Licence.

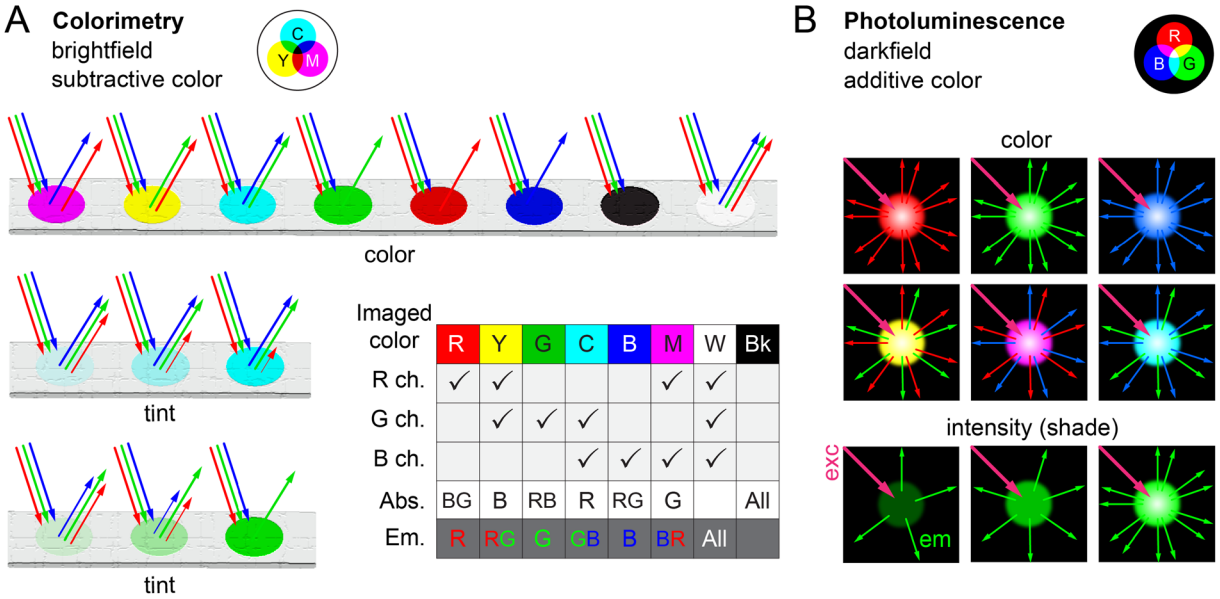

Fig. 10 Common designs and color relations for smartphone-based (A) colorimetry and (B) PL measurements. CL, BL, and ECL measurements are analogous to PL, notwithstanding the absence of excitation light. The color chart applies to both colorimetric and luminescence measurements—the difference is whether absorbance (brightfield) or emission (darkfield) is most relevant. Color abbreviations: R, red; Y, yellow; G, green; C, cyan; B, blue; M, magenta; W, white; Bk, black. Check marks indicate the light will be detected in the specified camera color channel. In panel A, the length and weight of the line indicates the relative intensity of the light. Examples of specific designs and configurations of smartphone-based devices are shown later in this review.

indicator dyes and chromogenic reactions, and from the retention of chromophores in binding assays (*vide infra* for examples). Changes in Bragg diffraction (*e.g.* photonic crystal sensors[153]) or thin film interference (*e.g.* etalon-based sensors[154]) would also produce analytically useful color changes but, to our knowledge, remain mostly unexplored with smartphone-based detection.

Potential advantages of colorimetric methods include operation in ambient light, simplification or elimination of hardware peripheral to the smartphone, and human vision as a redundancy and quality control measure for camera-obtained results—all of which contribute to the status of colorimetry as the most popular detection modality with smartphone-based devices. Potential disadvantages include less favorable detection limits than luminescence methods, interference from samples that are naturally colored, and a functional dependence on the color temperature or spectrum of the illumination. Approaches that have been used to address the last challenge are the use of a box[155–159] or an attachment[160] that excludes ambient light and provides reproducible and optimized illumination from a built-in source, and the use of color standards to calibrate ambient lighting.[161–165]

Most devices for colorimetric detection have been designed for use with cuvettes, lateral flow membranes, μPADs, and other test strips. Additionally, some devices for absorbance measurements have been designed for 96-well plates. One technical approach is to use an array of 96 optical fibers to deliver light transmitted through each well to a defined spatial position on the smartphone camera image. Examples of light sources for this type of configuration include an array of blue LEDs[166] and an electroluminescent plate as a white light source.[167] An alternate approach is to use a large-diameter convex lens for concurrent imaging of an 8 × 8 array of wells without significant optical distortion.[168]

6.3 Light scattering

Elastic light scattering assays measure light intensity at a position that is not along the optical axis of sample illumination or its reflection, with a dark field of view in the absence of scatter. The necessary optical arrangement is detection at an orthogonal or large oblique angle to a light beam through a cuvette or glass capillary. In practice, light scattering measurements also tend to differ from colorimetric measurements in their use of a light source that is monochromatic (*e.g.* laser diode) or pseudo-monochromatic (*e.g.* single-color LED) rather than white. Nonetheless, there are analyses that utilize AuNPs with white-light illumination and analyze the scattered light *via* a color ratio.[169] Light scattering assays require very efficient scatters and large analyte-induced changes in scattering efficiency to be practical and robust, such as in the case of analyte-dependent dissolution of NPs.[170,171]

6.4 Luminescence

This detection modality uses the smartphone camera to measure the intensity or color of light emitted against a dark background (Fig. 10B). The observed color is best predicted

Open Access Article. Published on 07 February 2025. Downloaded on 19/4/2026 11:02:09 PM.
This article is licensed under a Creative Commons Attribution-NonCommercial 3.0 Unported Licence.

by additive color theory, with blue, green, and red primary colors. Relevant mechanisms include photoluminescence (PL), chemiluminescence (CL), bioluminescence (BL), and electrochemiluminescence (ECL). The main advantages of luminescence detection are higher sensitivity and lower detection limits than other modalities, and capacity for color-based multiplexed detection within the same measurement volume. In some cases, luminescence methods will also better tolerate strong sample coloration.

The main drawback of luminescence detection is the additional components that are required for a functional device. A box or compartment is needed to exclude ambient light and provide a dark imaging environment. An excitation light source is also needed for PL measurements, along with an emission filter to prevent reflected or scattered excitation light from reaching the smartphone camera. External single-color LEDs and laser diodes are common excitation light sources. Violet and UV wavelengths enable full utilization of the camera's RGB channels, whereas longer wavelengths preclude imaging in one or more color channels. Excitation filters are needed to isolate a band of wavelengths when the smartphone flash or another white-light source is used for PL excitation.[38,41,145,172] Although infrequent, narrow bandpass filters have also been used with single-color LEDs to minimize the leakage of excitation light into the camera color channel to be used for detection.[173,174] This approach avoids reducing the range of wavelengths useful for PL detection, which can sometimes be a consequence of using an emission filter that blocks the full spectrum of an excitation LED. Such filtering also has the side-effect of reducing the excitation intensity. Monochromatic laser diodes do not pose the same challenge because long-pass and notch filters are able to block the excitation light from reaching the camera while maximizing the remaining wavelength range for PL detection.

Although of minimal importance for brightfield colorimetric imaging, the distance between the sample and the smartphone camera (or another primary imaging lens) is a relevant design consideration because PL, CL and BL exhibit isotropic emission. The measured intensity thus scales as the inverse square of this distance and greatly impacts assay sensitivity.

An additional consideration for PL detection is that components in the path of the excitation light and in the field of view of the camera must not be autofluorescent, and should be transparent to the excitation wavelength to maximize sensitivity. These requirements are sometimes more challenging than anticipated when working with violet and ultraviolet excitation: some paper,[175] plastic,[176,177] and (more rarely) glass materials generate significant levels of autofluorescence. Some low-cost colored glass filters will also exhibit autofluorescence when incident excitation light (*e.g.* from a reflection) is too intense.[178] Common clear plastics and glasses are transparent to NIR light (at 808 nm and 980 nm) and, as noted earlier, the use of UCNPs and PLNPs will avoid autofluorescence from samples and device materials alike. Nonetheless, UCNP users should also be cognizant of materials that could burn from extended exposure to the IR laser. UV light sources and NIR lasers suitable for upconversion PL both pose safety risks to skin and eyes that will need to be mitigated by suitable engineering of any device.

In contrast to PL detection, CL, BL, and ECL detection do not need an excitation source and optical filters. Nevertheless, there is intricacy associated with the temporal decay of CL and BL signals as a reaction progresses. In many cases, a greater number of reagents and assay steps are needed to generate signal. ECL provides a greater level of spatial and temporal control because the luminescence is restricted to an electrode interface and requires an applied

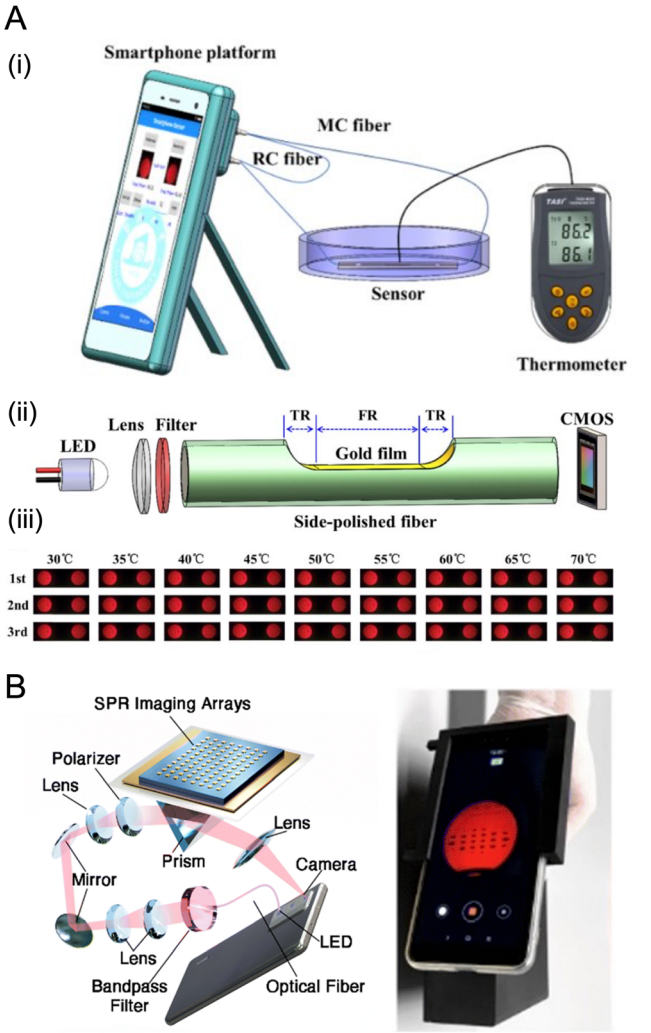

Fig. 11 Examples of the two main optical approaches for SPR with a smartphone. (A) An optical fiber format: (i) measurement setup; (ii) optical axis; (iii) examples of smartphone images of the reference (RC) and measurement (MC) fibers. Other abbreviations: TR, transition region; FR, flat region. Figure adapted with permission from ref. 44 Copyright 2019 Optical Society of America. (B) A Kretschmann configuration with a planar gold film on a chip in a flow cell (left) and an example of a smartphone-captured SPR image of the chip. Figure adapted from ref. 45 Copyright 2022 Royal Society of Chemistry.

Open Access Article. Published on 07 February 2025. Downloaded on 19/4/2026 11:02:09 PM.
This article is licensed under a Creative Commons Attribution-NonCommercial 3.0 Unported Licence.

voltage to be initiated.[179,180] ECL emitters can sometimes also be regenerated on the fly. In general, the emission rates for CL, BL, and ECL have a lower ceiling than with fluorescence, such that competitive detection limits are predicated on the background being darker than what is possible with PL, whether due to technical considerations or sample autofluorescence.

6.5 Surface Plasmon resonance

Two main optical approaches have been used to implement surface plasmon resonance (SPR) measurements with a smartphone camera. In an optical fiber format (Fig. 11A), one end of the fiber is coupled to a light source and the other end of the fiber is imaged by the camera. A segment along the length of the fiber is coated with a gold film and integrated into a flow cell, where the plasmon is excited by light coupled into the fiber by total internal reflection. The light source has been the flash on a smartphone (filtered to select red light)[42–45] or a standalone red LED.[44,181] The other common format is to use a non-fiber waveguide with a planar gold film in a flow cell. Examples have included a 3D-printed clear-plastic optical coupler that totally internally reflects red light from the phone display to the front-facing smartphone camera;[46,182] Kretschmann configurations that use the rear camera and a polarizer with either a red LED[183] or the phone flash (plus a red bandpass filter; Fig. 11B);[45] and a reverse Kretschmann configuration for SPR-coupled emission with a hemispherical prism.[184–187] Although a niche measurement modality at present, SPR has the prospective advantages of label-free and indicator-free detection of binding.

6.6 Microscopy

Devices for smartphone microscopy typically incorporate lenses that are external to the camera to achieve micron-scale image resolution. In practice, these external lenses are low-cost objective lenses or bespoke combinations of individual lenses that serve the same purpose. Magnification has also been increased with attachment of the lens from the laser pickup head of a CD player over the smartphone camera.[188] Ball lenses have also proven useful for magnification with simple and compact designs.[189,190] With some smartphone cameras now offering up to 10X optical zoom, some low-magnification applications may bypass the need for an external lens. Multiple camera units on the back of the smartphone will also support optics for stereomicroscopy.[191]

Beyond external magnification lenses, the components utilized for smartphone-based microscopy are similar to the components utilized for non-microscopy measurements. Devices for brightfield microscopy will incorporate a peripheral white LED source or redirect the smartphone flash for sample illumination because ambient light is not sufficiently intense for high magnification.[192] Although most

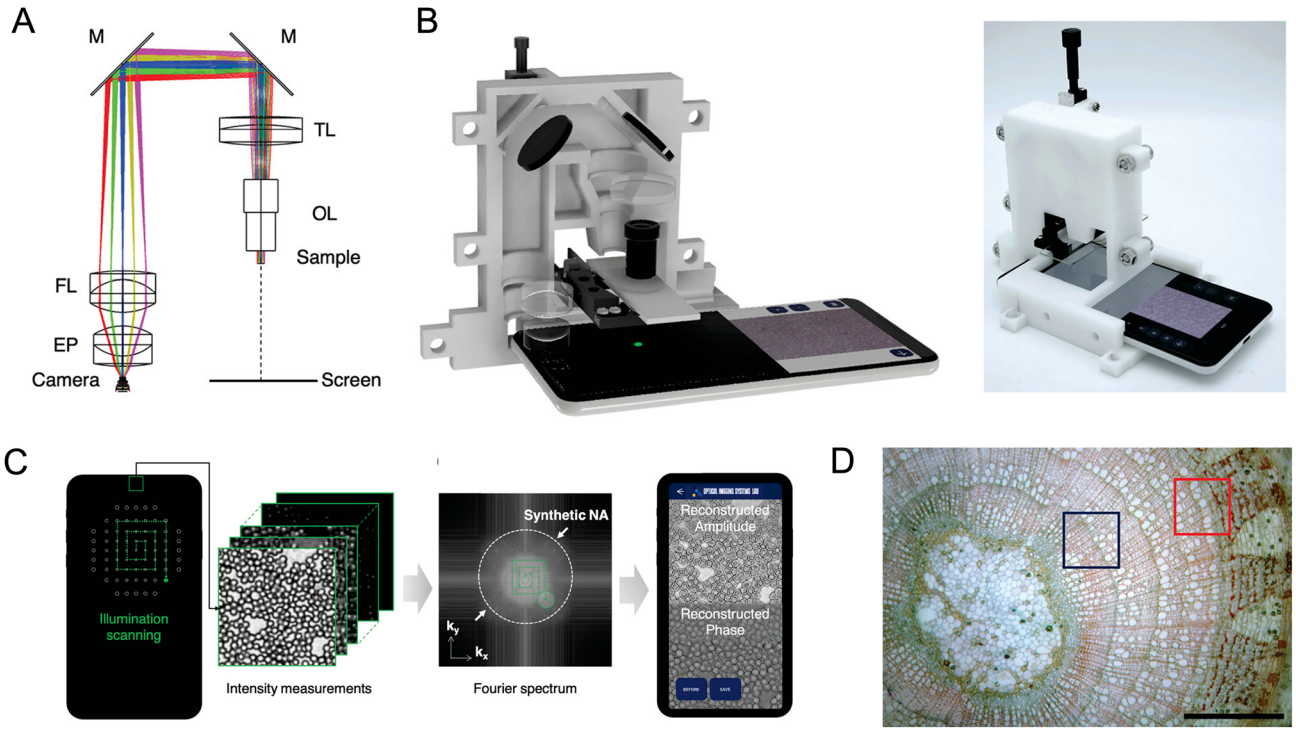

Fig. 12 A smartphone-based Fourier ptychographic microscope using the display screen for illumination. (A) Optical layout and (B) rendering and photograph of the microscope. Diagram abbreviations: OL, objective lens; TL, tube lens; M, mirror; FL, field lens, EP, eyepiece lens. (C) Working principle of the microscope. (D) Full field-of-view color reconstruction result of cross-section of a Tilia stem. (The blue and red boxes indicate image regions that are enlarged in the original publication). Figure adapted with permission from ref. 195 Copyright 2021 American Chemical Society.

Open Access Article. Published on 07 February 2025. Downloaded on 19/4/2026 11:02:09 PM.
This article is licensed under a Creative Commons Attribution-NonCommercial 3.0 Unported Licence.

microscope devices have been built around a single smartphone, there have been instances of using two smartphones—one for the flashlight to illuminate the sample and one for the camera to image the sample—to simplify optical design and avoid any circuits.[193]

Although uncommon, the smartphone display has been used as a light source for microscopy. Examples include the use of a liquid light guide to collect light from the display for downstream modulation by a digital micromirror device for hybrid illumination (HiLo) optical sectioning with 12 μm axial resolution,[194] and the use of the display as a dynamic and programmable light source to replace the typical two-dimensional LED array for Fourier ptychographic microscopy to obtain half-pitch resolution of 0.87 μm with a field of view of 3 mm^2 (Fig. 12).[195] An arguably simpler design used a separate OLED display, operated by a microcontroller, to act as a programmable light source for smartphone microscopy, demonstrating six different imaging modes: bright-field, dark-field, oblique illumination, Rheinberg, differential phase contrast, and fluorescence.[50] More commonly, single-color LEDs and laser diodes are used with appropriate optical filters for PL microscopy. Theater stage lighting gel films and acrylic films have been used as a low-cost alternative to conventional scientific-grade emission filters.[196,197] A related advance has been the development of colored polymer lenses that mount directly on a smartphone camera to concurrently magnify and block excitation light in PL imaging.[198] Another example of custom imaging is a tunable optofluidic design, based on hydraulic deformation of an elastomeric membrane, that offers an adjustable focus.[199] Simple mechanical approaches to focus adjustment have included spring-loaded screws to attach a phone cradle as the lid of a dark box,[84] and a screw-actuated 3D-printed seesaw mechanism that offers as small as 5 μm adjustments.[200]

6.7 Spectroscopy

Smartphone-based spectroscopy comprises absorbance, light scattering, luminescence, and SPR measurements with wavelength resolution. It is defined by the introduction of a dispersive element (*e.g.* prism, grating) as a peripheral component to the smartphone. The camera images the dispersion of the incoming light, obtaining wavelength-resolved intensity information (*i.e.* spectra) as a function of pixel address. The RGB color channels are inherent to the analysis but are secondary to the spatial encoding of wavelength. That said, the increasingly common presence of multiple rear cameras on smartphones may provide a technical solution to parallel spectral measurements and conventional imaging of the same sample.

Most smartphone-based absorption spectrometry devices have been designed to utilize cuvettes. A plurality of designs use a piece of a DVD[201–203] or CD[204,205] as a proxy for a made-for-purpose diffraction grating. The grating is typically used in a transmission format, although some reflection designs have been reported. Low-cost thin film gratings designed for classroom education have also been adopted,[206–208] as have research-grade transmission[209] and reflection gratings.[210] When reported, spectral resolutions have been <1 nm per pixel.[204,209,211] Although most devices have 3D-printed housing, some devices have been made with laminated paper,[201] cardboard and wood,[203] and Plexiglas.[202] The most common light source is a white LED external to the smartphone,[201] although some designs have utilized a tungsten halogen lamp (*i.e.* incandescent bulb),[203,209] a flashlight-sized xenon bulb,[212] and redirection of the phone flash *via* a light guide.[211,213] Two versatile designs implemented a bifurcated optical fiber to deliver light from the flash to the sample and to send reflected light back to the grating assembly and smartphone camera.[32,208] Other interesting device designs have included a double-beam system,[207] an eight-channel spectrometer based on a prism array for working with 96-well plates[212] and 8-well strips,[214] and endoscope designs.[213,215] Two designs have also omitted a light source, once for flexibility in source selection[216] and once for use with the Sun.[204] The Sun offers the advantage of a broader and more uniform spectrum than an LED or lamp, but poses challenges with ensuring consistent incident light intensity between samples and blanks, and with weather-dependent utility.

Regarding the smartphone, a study evaluated more than 60 models for spectral measurements and highlighted the importance of manual control over image acquisition and processing settings, the trade-off between higher signal-to-noise ratios from larger camera pixel sizes and higher wavelength resolution from more pixels, and the generally superior analytical performance of newer phones *versus* older phones.[211]

The advantage of smartphone-based spectroscopy over imaging is wavelength-resolved data that is more analogous to lab-based spectrometers. In principle, this resolution will support more robust or higher levels of spectral multiplexing and facilitate differentiation of analytical signals from background. In practice, smartphone spectrometers are often better suited to education and citizen science than for chemical and biomolecular analyses. The built-in RGB channels of the smartphone camera intrinsically provide some wavelength-related information, and few studies to date have demonstrated an application where the extra resolution from a grating provides essential new information.

6.8 Image processing and analysis

6.8.1 Processing and formats. Smartphone camera images are a three-dimensional array of pixel values: the first two dimensions are the horizontal and vertical spatial coordinates; the third dimension is the color data. Videos are image stacks, which add frame number (in practice, a time increment) as a fourth dimension to the array. In terms of the memory requirement, a picture (*ca.* 2–50 MB) is not actually worth a thousand words, but rather more than one hundred thousand words. To conserve memory and be more

 This journal is © The Royal Society of Chemistry 2025

Open Access Article. Published on 07 February 2025. Downloaded on 19/4/2026 11:02:09 PM.
This article is licensed under a Creative Commons Attribution-NonCommercial 3.0 Unported Licence.

efficient with processing power, the default for most smartphone users is storage of images in a compressed format such as HEIC (high efficiency image container) or JPEG (Joint Photographic Experts Group). These formats do not store the original image sensor data.

A full discussion of image compression algorithms are beyond the scope of the review and can be found elsewhere.[217–219] In brief, JPEG is a lossy format that simplifies the pixel data in the original image based, in part, on the limits of human vision and color perception. Nominally redundant data in the form of less perceivable detail is eliminated to conserve memory. Pixels in JPEG images can, in principle, adopt $2^8 = 256$ different (*i.e.* 8-bit) levels of red, green, and blue (R, G, and B), for a total of $2^{24} = 16\,777\,216$ (*i.e.* 24-bit) colors. Compared to the JPEG format, the HEIC format uses less memory to store higher quality images, with the potential for up to 16-bit depth for each RGB color channel.

For both JPEG and HEIC images, an acquired raw image is first processed by demosaicing. This process uses pixel interpolation and correlation algorithms to assign a full triplet of R, G, and B values to an image pixel, even though each image sensor pixel was sensitive to only one of these colors. Subsequent processing includes color space conversion, white balance or color temperature adjustment, and file compression steps. Notably, the color processing steps alter the quantitative data from the image sensor. Most image sensors have a linear response to light intensity and the pixel signals are typically digitized on 10-bit up to 14-bit scales. In addition to reducing the bit depth in a stored image, standard JPEG or HEIC conversion will also apply a gamma correction that transforms the original linear correlation between pixel value and light intensity to a non-linear one that better mimics human vision. Increasingly, there are also other behind-the-scenes actions by the smartphone camera app: various computational methods are used to further enhance and optimize image quality, thereby better mitigating the hardware compromises necessary for a small form factor, user friendliness, and versatility. Although these operations add value to the popular uses of smartphone cameras, autonomous image processing algorithms may not be well calibrated to scenarios encountered in scientific imaging and measurements. For example, many smartphone cameras and their default apps will attempt to make dim light brighter by altering both the hardware parameters for image capture and the downstream digital image processing. Such processing risks a low luminescence signal from a low concentration of analyte falsely appearing to be high signal from a high concentration of analyte. In short, undefined image processing algorithms are anathema to quantitative analysis and are to be avoided.

One strategy for avoiding non-quantitative data is to use smartphone camera apps that offer control over important settings used for image capture and processing. Examples of such settings include the focus, exposure, ISO level, and white balance/color temperature. Manual control provides a level of consistency between images and is sometimes adequate for quantitative analysis even when storing images or videos in compressed formats. An alternative to JPEG and HEIC is to store images in RAW format. The RAW format provides a digital image with the highest fidelity to what the image sensor recorded, including greater bit depth, with the trade-off of requiring more memory. RAW files ideally retain the linear response of the image sensor and are minimally processed. Acquiring RAW images will thus be the best approach to any quantitative analysis that is based on the light intensity measured in one or more of the camera's RGB color channels. Numerous apps are available to enable RAW image acquisition with manual control over the aforementioned camera settings, including the advanced or "pro" modes of some default camera apps for newer smartphones. Examples of non-default apps include Adobe Lightroom, OpenCamera, Camera FV5, Halide Mark II, and several apps that have "Pro Camera" (or similar) in their name. Apps capable of RAW video acquisition have been rare but do exist (*e.g.* MotionCam). There are also tools available for researchers to code their own custom camera apps using application programming interfaces (APIs) and software development kits (SDKs) that are available for smartphone operating systems such as Android, iOS, and HarmonyOS.

With smartphones, the precise details of the processing applied to the exported RAW image (*e.g.* digital negative, DNG, file format) depends on the device and app, but typically includes a demosaicing (*a.k.a.* debayering) process to obtain a full color image. Note that some image processing and analysis programs may require that the bit depth of an imported RAW image (*e.g.* 10-bit) be downscaled or upscaled to a supported value (*e.g.* 8-, 16-, 32-bit). Downscaling will reduce image detail and dynamic range, and add quantization noise. Upscaling will add gaps in the pixel intensity histogram of an image but otherwise retains the original quality of the data. Upscaling cannot undo the effects of a prior downscaling.

Color Spaces. The additive RBG color space is the natural default for smartphone camera images because both the camera and the smartphone display model color as a combination of red, green, and blue values. These primary colors combine in pairs to make yellow, cyan, and magenta. A full contribution from all three primary colors approximates white light and the full absence of all three colors produces black. When each primary color is plotted on an orthogonal axis, the result is a cubic color space (Fig. 13A). For data analysis, the RGB color space is intuitive in how it mimics the operational principles of the smartphone camera. It is arguably non-intuitive in that, from a visual perspective, the identity of a color (*i.e.* hue) and its tint (for brightfield imaging with a white background) or shade (for darkfield imaging) are not independent parameters. This aspect of the RGB model sometimes motivates the use of other color models.

The hue-saturation-value color space (HSV; also called hue-saturation-brightness, HSB; Fig. 13B) is an alternative

Open Access Article. Published on 07 February 2025. Downloaded on 19/4/2026 11:02:09 PM.
This article is licensed under a Creative Commons Attribution-NonCommercial 3.0 Unported Licence.

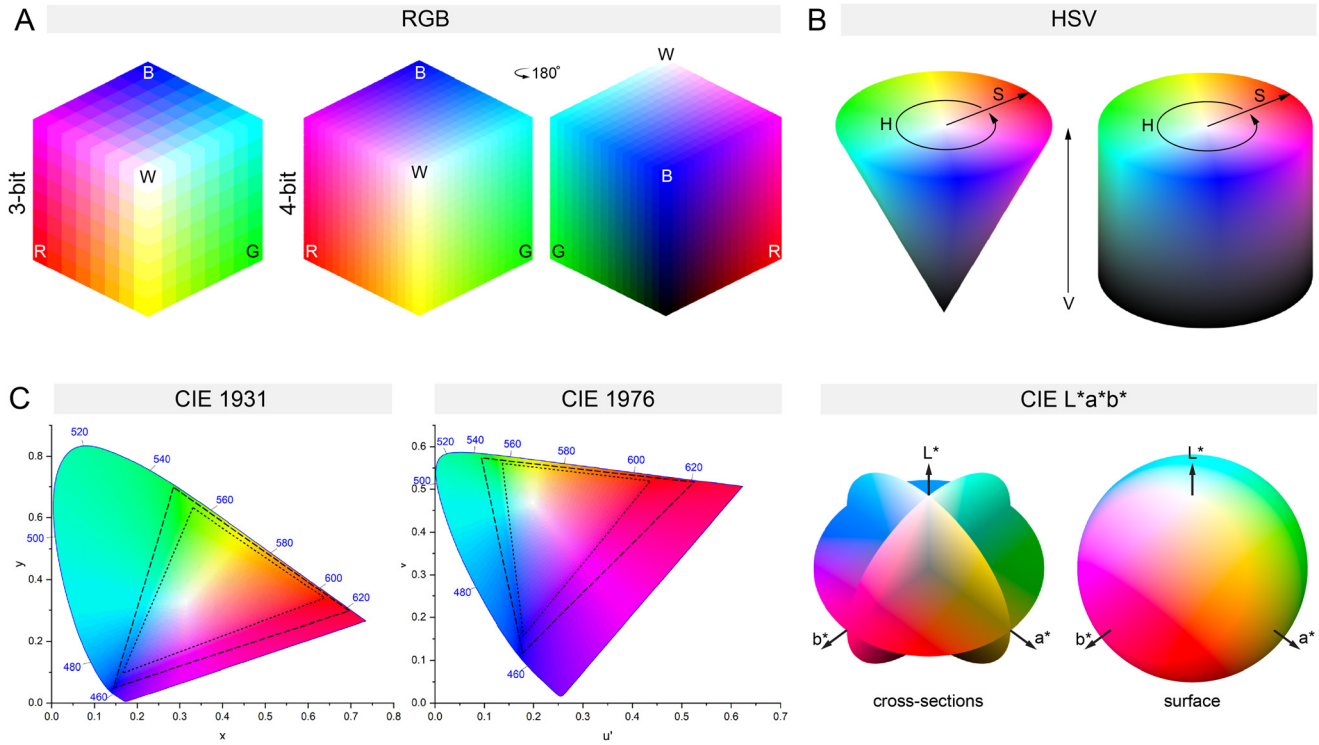

Fig. 13 Color spaces. (A) RGB color space at two different bit depths. Low bit depths are shown to illustrate the effect of bit depth on the number of possible colors. The R, G, and B coordinate values are plotted on orthogonal axes. Front and back views are shown for the 4-bit RGB cube. (B) The HSV/HSB color space represented as a cone and a cylinder. The vertical and radial coordinates are *V* and *S*, and the angular coordinate is *H*. (C) Two-dimensional projections of the CIE1931 (*xy*) and CIE1976 (*u′v′*) color spaces, and the RGB-compatible three-dimensional representation of the CIE Lab color space. All three spaces are derived from the *XYZ* tristimulus values. The triangles qualitatively illustrate the color gamut accessible to spectrally narrow RGB emitters (dashed triangles) and spectrally broad emitters (dotted triangles).

model to the RGB color space. HSV space uses a single coordinate, hue (*H*), to identify colors, where *H* is expressed in degrees (0–360°) on a cone or cylinder. For example, the RGB hues of red (255, 0, 0; 8-bit RGB coordinates), yellow (255, 255, 0), green (0, 255, 0), cyan (0, 255, 255), blue (0, 0, 255), and magenta (255, 0, 255) are at 60° intervals starting at 0° for red and ending at 300° for magenta, with brightness and saturation at 100%. The saturation (*S*) is expressed as a radial coordinate (0–100%) and quantifies the amount of a given hue *versus* a neutral white. The value (*V*) is expressed as the axial coordinate (0–100%) and is a measure of the perceived brightness of the hue. White has 8-bit RGB coordinates of (255, 255, 255) and HSV coordinates of (*H*, 0%, 100%). The corresponding coordinates for black are (0, 0, 0) and (*H*, *S*, 0%). There are defined equations for converting between the RGB and HSV color spaces.

Other examples of color spaces are the International Commission on Illumination (CIE) Lab model, its still-common predecessor, the CIE XYZ model, and two-dimensional representations commonly referred to as CIE 1931 (*xy*) and CIE 1976 (*u′v′*) (Fig. 13C). These models are perhaps less intuitive than the HSV color space, but are better mimics of the human perception of color. The CIE *XYZ* model defines *X*, *Y*, and *Z* coordinates as tristimulus values that nominally reflect the degree to which different wavelengths of light stimulate the three types of cone cells in an average human eye. Equations are defined to convert RGB coordinates to *XYZ* coordinates. In turn, equations are defined to convert the *XYZ* coordinates to the (*x*, *y*) and (*u′*, *v′*) coordinates for two-dimensional representation, and to convert *XYZ* to the *L**a**b** coordinates of the CIE Lab model. This latter and newer model aligns with how the average human actually experiences four pure color stimuli (red, green, blue, yellow) due to cone-opponent neurons that combine signals from the three types of cone cells. The *L** coordinate is the lightness of a color. The *a** and *b** coordinates reflect the redness-greenness and yellowness-blueness of a color, respectively, where a positive value indicates a predominance of the first color in a pair and a negative value indicates a predominance of the second color.

6.8.2 Data analysis. Once smartphone images are acquired, the next step is extraction of the relevant data. Many analyses will fall into the categories of quantifying a transition between low and high contrast states, quantifying a transition between two extremes of color, and color matching. The question is then how to best utilize the data to correlate optical signal with analyte.

RGB is the natural color space for smartphone image analysis and has been adopted in close to half of published studies (*vide infra*). Many studies have also used *HSV* and

Open Access Article. Published on 07 February 2025. Downloaded on 19/4/2026 11:02:09 PM.
This article is licensed under a Creative Commons Attribution-NonCommercial 3.0 Unported Licence.

*L*a*b** coordinates, where a few of these studies have advanced a notion that these color spaces have the potential to enhance the data. This idea is a misconception: the *HSV* and *L*a*b** coordinates are calculated directly from the original RGB values and thus cannot improve the quality of the data. Rather, conversion to these alternate color spaces has the potential to function as a form of data reduction, enabling fewer coordinates to reflect trends in the data and better correlating data with human perception. Grayscale conversion is likewise a data reduction mechanism because it is a weighted average of the RGB triplet values. *Ad hoc* color space conversions are not a substitute for knowledge of the optical spectroscopy relevant to a smartphone-based assay. The optimum approach to data analysis will emerge from careful consideration of the sources of signal, background and noise in an experiment, the sensitivity of the camera's RGB pixels to each source, and the contributions of each source to the coordinates of an image color space. Coordinates that maximize signal-to-background and signal-to-noise ratios will maximize analytical performance.

Signaling between low and high contrast states usually takes the form of a colorless to colored transition for colorimetric measurements, or a transition from dark to bright for luminescence measurements. For luminescence assays with a single luminophore, the transition is simply and effectively quantified *via* changes in the magnitude of the RGB channel values. The relevant channels will be determined by the overlap between the emission spectrum of the luminophore and the RGB channel responses, where the channel that provides the highest signal-to-background ratio will most often provide the highest quality data. Image analysis programs and coded scripts will output RGB coordinate values for pixels of interest and will split a color image into a separate monochrome image for each of the three channels. Background subtraction is important and should not be neglected.

Despite being adopted for data analysis in almost one quarter of studies (*vide infra*), the best-case scenario is that grayscale conversion has a neutral effect on data quality for colorimetric and luminescence measurements. It is equally likely to have a detrimental effect from averaging in color channels with inferior signal-to-background ratios. It should also be noted that data from an image is unreliable for quantitative analysis if a significant number of pixels are saturated in a color channel (*i.e.* an 8-bit value close to 255). Gross saturation is frequently observed as a white-hot glow for an imaged color of luminescence, but pixel data can be adversely affected before this effect is visually apparent.

For a transition between a colorless and colored state under approximate white light, the relevant color coordinate will be determined by the overlap between the absorbance spectrum of the chromophore and the RGB channel responses. The RGB channel that covers the largest fraction of the area of the absorbance spectrum will be most sensitive to the color transitions. Unlike in darkfield luminescence imaging, where, for primary colors, the visual color tends to match the optimum RGB channel, the visual color for brightfield imaging under approximate white light will tend to be complementary to the color of the optimum RGB channel. For example, red luminescence is best quantified in the R channel, whereas a red color in brightfield imaging is often best quantified in the G channel. The *S* value in HSV space is also an intuitive and suitable parameter for quantifying colorless to colored transitions, with the caveat that there is still potential for some of the data variance to be captured by the *H* and *V* coordinates. The data reduction from grayscale conversion has the potential to increase dynamic range from its averaging in of less-responsive RGB color channels, but risks a reduction in sensitivity for vivid colors.

Another common scenario is quantifying the degree of a transition between two color extremes, such as a blue-to-yellow transition or a green-to-red transition. A ratio of values between two RGB channels will often suffice to produce a monotonic trend in both darkfield luminescence and brightfield color imaging. The specific RGB channels will be those that align with the majority of the absorbance or emission that produces the two colors. A ratio between the sum of two channels and the third channel (or the mathematical inverse) also has the potential to be useful in the case of color changes associated with large shifts in broad spectra. Alternatively, the *H* coordinate of the HSV color space is a good conceptual match to this scenario and often utilized for this purpose. Although sometimes utilized, ML methods are generally unnecessary for quantifying a simple transition between two colors. Rather, the value of ML in this situation is accounting for significant variation in the illumination or in the optical properties of sample matrices (*i.e.* inconsistent background and noise). ML methods have similar utility when applied to colorless to colored transitions or dark to bright transitions in luminescence.

The last common scenarios for data analysis are color recognition and color pattern recognition, and it is here that ML methods are excellent for signal processing. When illumination is not well controlled, ML will have the dual role of color identification and correction for variation in conditions. Examples of ML for color recognition include support vector machines (SVM) for brightfield[220–222] and luminescence[85,223] imaging, and neural networks (NNs) for brightfield.[165,224,225] NNs, hierarchical cluster analysis (HCA), and linear discriminant analysis (LDA), and principle components analysis (PCA) have been used to discriminate between color patterns from array-based assays.[226–232] The data processing usually requires a calibration or training data set that spans a broad scope of possible assay inputs, color outcomes, and imaging conditions. Since most of these ML methods intrinsically perform a data reduction or transformation, there is little or no value to a prior conversion from RGB to another color space.

For research and development, an offboard approach is common for the implementation of data analysis methods.

Open Access Article. Published on 07 February 2025. Downloaded on 19/4/2026 11:02:09 PM.
This article is licensed under a Creative Commons Attribution-NonCommercial 3.0 Unported Licence.

Familiar computer-based tools (*e.g.* ImageJ/Fiji, Adobe Photoshop, Icy) and programming tools (*e.g.* MATLAB, Python) are utilized for extraction and processing of data from smartphone-acquired images. For onboard analysis,

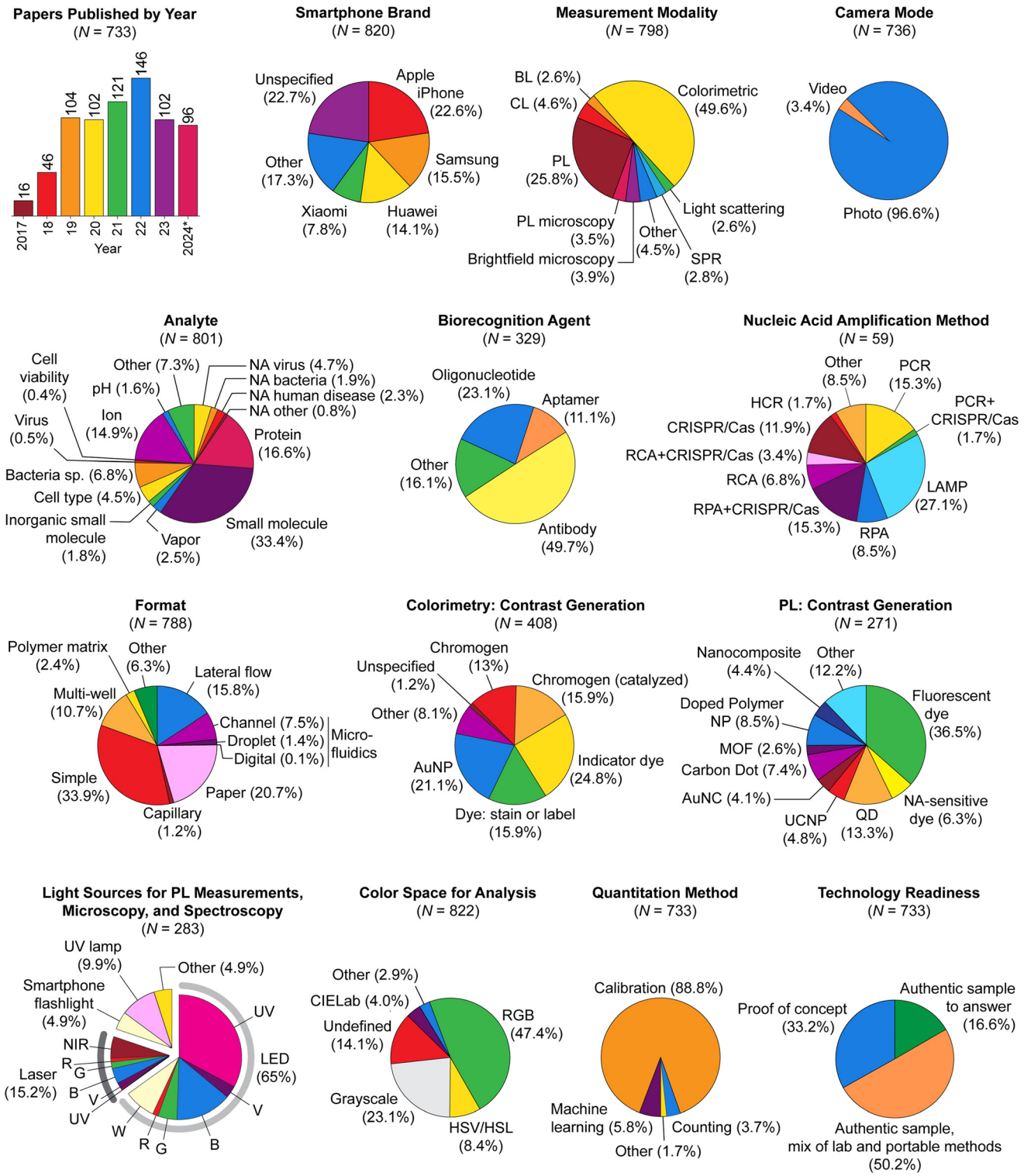

Fig. 14 Meta-analysis of the literature on smartphone-based analyses that use the smartphone camera for detection (2017–08/2024). Statistics are approximate. Not every publication disclosed all of the information needed for this analysis. Categories with a sample size (*N*) larger than the number of published papers are an outcome of papers that reported more than one item relevant to that category. Nucleic acid analytes are denoted as "NA". The "Format" pie chart divides microfluidics into three sub-categories: channel microfluidics with a continuous and single phase, channel-based droplet microfluidics, and digital droplet microfluidics. A "simple" format refers to a cuvette, single well, single chamber, or similar.

Open Access Article. Published on 07 February 2025. Downloaded on 19/4/2026 11:02:09 PM.
This article is licensed under a Creative Commons Attribution-NonCommercial 3.0 Unported Licence.

whether for prototype development or downstream applications and end-users, the norm is development of a custom smartphone app. There are numerous online resources to assist novices in coding smartphone apps, inclusive of leveraging code already generated in, for example, MATLAB and Python.

7. Analytes and assays

7.1 Metanalysis

Fig. 14 categorizes and summarizes some of the recent trends in the literature on smartphone-based detection and devices. This analysis surely did not capture the totality of studies published over the past 7 years, but is enough of a sampling to identify trends. Prevalent trends include colorimetric assays, static imaging, the use of antibodies as biorecognition agents for analytes, standard calibration, and portable detection without fully portable sample processing. Although some of these trends are likely to continue over the next several years, the implementation of ML and AI methods is rapidly increasing. We anticipate that the percentage of studies using these tools will be notably larger even within a year or two.

An opportunity for improvement in the field is for more studies to provide full technical details about the components of their smartphone-based device, which are sometimes lacking in full or in part. Common examples of omissions include the power of light sources and wavelength information beyond a nominal color (*e.g.* peak and bandwidth), specifications for lenses and other optical components, the name of the app and full imaging settings (*e.g.* exposure time/shutter speed, ISO value, color temperature), and details around the extraction of quantitative data from images. Nevertheless, the meta-analysis data highlights the prevalence of some of the technical approaches discussed in the preceding sections and the diversity of the assay designs discussed in the following sections.

7.2 Colorimetric analyses

Smartphone cameras have led to renewed interest in methods of analysis based on color changes. The RGB image from the camera enables color identification to be quantitative rather than qualitative, and for analyte quantity to be determined by calibration rather than titration to an end point. Almost 400 papers published in past 7 years have reported different variations on the colorimetric detection of analytes, making it the most popular detection modality with a smartphone camera. Collectively, indicator dyes, stains, and other molecular chromogens have been used for color generation in about two thirds of published studies, with AuNP adopted in about one in five studies (Fig. 14).

7.2.1 Molecular chromogens: indicators. Dyes that change color in response to analyte are a simple approach to colorimetric signaling. Examples of analytes detected *via* a smartphone camera and an indicator dye include aqueous metal ions (*e.g.* Th^{4+},[233] Hg^{2+},[234,235] Bi^{3+},[236] Cu^{2+},[235,237,238] Fe^{3+},[238,239] Ni^{2+},[233] Ca^{2+},[158,240] Mg^{2+}),[158] amplified SARS-CoV-2 nucleic acid (using SYBR green I; Fig. 15),[241] and volatile basic nitrogen compounds (*e.g.* headspace analysis of ammonia, dimethylamine, and trimethyl amine using pH indicator dyes for the assessment of food freshness).[242,243] In addition to synthetic dyes, anthocyanins extracted from red cabbage and butterfly pea flower, from red beats, and from red radish have been adopted for the measurement of pH,[244] Cu^{2+} (aq),[245] and volatile basic nitrogen compounds,[246] respectively. Starch indicator has been used for measuring aqueous iodine species in seaweed[247] and vegetable oil[248] samples. Vegetable dyes have potential benefits for sustainability and disposal.

7.2.2 Molecular chromogens: reactions. Chromogenic reactions are another approach to analysis by smartphone camera. Several analytes have been detected *via* their direct color-changing reaction with a dye: nitrite[249] and residual chlorine in drinking water,[250] aqueous cyanide,[251,252] biogenic amines in wine,[253] chemical oxygen demand in a waste solution,[254] hydrogen sulfide gas,[255] diethyl

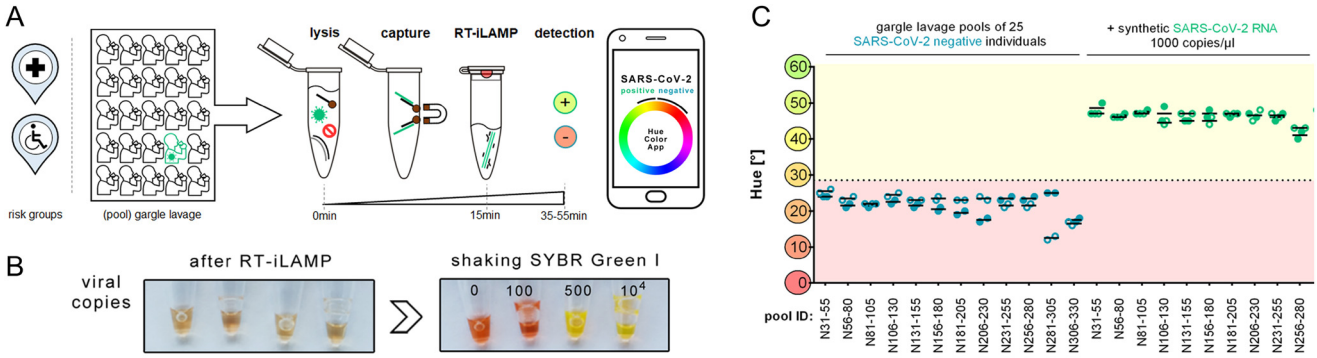

Fig. 15 Colorimetric RT-LAMP assay with an indicator dye and smartphone-based color measurement. (A) Assay work flow. (B) Color change induced by mixing a drop of SYBR green I in the lid of the tube after iLAMP reaction with different copy numbers of synthetic viral RNA. (C) Hue measurement of different sample pools after amplification. Samples from healthy individuals are marked in blue; samples for SARS-CoV-2-positive patients are marked in green. Adapted from ref. 241 under a Creative Commons Attribution 4.0 International License.

Open Access Article. Published on 07 February 2025. Downloaded on 19/4/2026 11:02:09 PM.
This article is licensed under a Creative Commons Attribution-NonCommercial 3.0 Unported Licence.

chlorophosphate as a proxy for sarin nerve gas,[256] and boron trifluoride gas.[257]

In other cases, analytes have reacted with colorless reagents to form a new colored species. Examples include the reactions of 2,4,6-trinitrotoluene with an amine to generate a brown Meisenheimer complex,[258] formaldehyde with acetylacetone and ammonium to generate a yellow product,[259] furfural vapour from gasoline with aromatic amines to generate a pink product,[260] and phenolics (*e.g.* capsaicinoid analytes[261]) with Gibbs reagent and with Folin–Ciocalteu assay reagents to generate a blue color.[262] Further examples include the detection of creatinine in urine *via* its reaction with picric acid (Jaffé method; orange color),[263] nitrite *via* its reaction with Griess reagents (pink color),[264] a cannabinoid *via* its reaction with Ehrlich reagent (pink color),[265] and gamma-hydroxybutyrate (a recreational drug) *via* its reaction with hydroxylamine and complexation of aqueous Fe^{3+} (purple color).[266]

Clearly, there is no shortage of chromogenic reactions that a smartphone camera is equipped to measure; however, their practicality for portable detection depends on the degree to which reagents must be handled by a user and the associated hazards. Most of the procedures for the detection of the solution-phase analytes noted above were at small scale and used a smartphone for quantitative readout, but were otherwise not substantially different from a standard benchtop laboratory protocol. This aspect is a potential barrier to successful translation to non-laboratory settings.

7.2.3 Molecular chromogens: enzyme substrates. Enzyme-catalyzed reactions are a third approach to generating smartphone-readable color in response to an analyte. Salivary,[267] urinary,[268] and ocular glucose[155] levels have been analyzed through coupled activity of glucose oxidase and horseradish peroxidase (HRP) to induce oxidative color changes of dyes such as *o*-dianisidine and TMB. The lactate level in sweat has been analyzed in the same manner by substituting glucose oxidase with lactate oxidase.[269] Atropine (an alkaloid) in baby food was analyzed through color conversion of iodonitrotetrazolium dye *via* the coupled activity of tropinone reductase and diaphorase,[270] and creatinine was detected *via* a trio of reactions catalyzed by creatininase, creatinase, and sarcosine oxidase, with a final peroxide-dependent chromogenic reaction.[271] As is classic, pesticides have been detected *via* their inhibitory effects on enzymes: profenofos and methomyl *via* inhibition of the conversion of 5,5′-dithio-bis-(2-nitrobenzoic acid) by acetylcholine esterase;[272] and ziram by inhibition of the conversion of a catechol dye by tyrosinase.[273]

When an analyte is neither a substrate nor an inhibitor of an enzyme, then HRP-conjugates are frequently adopted to

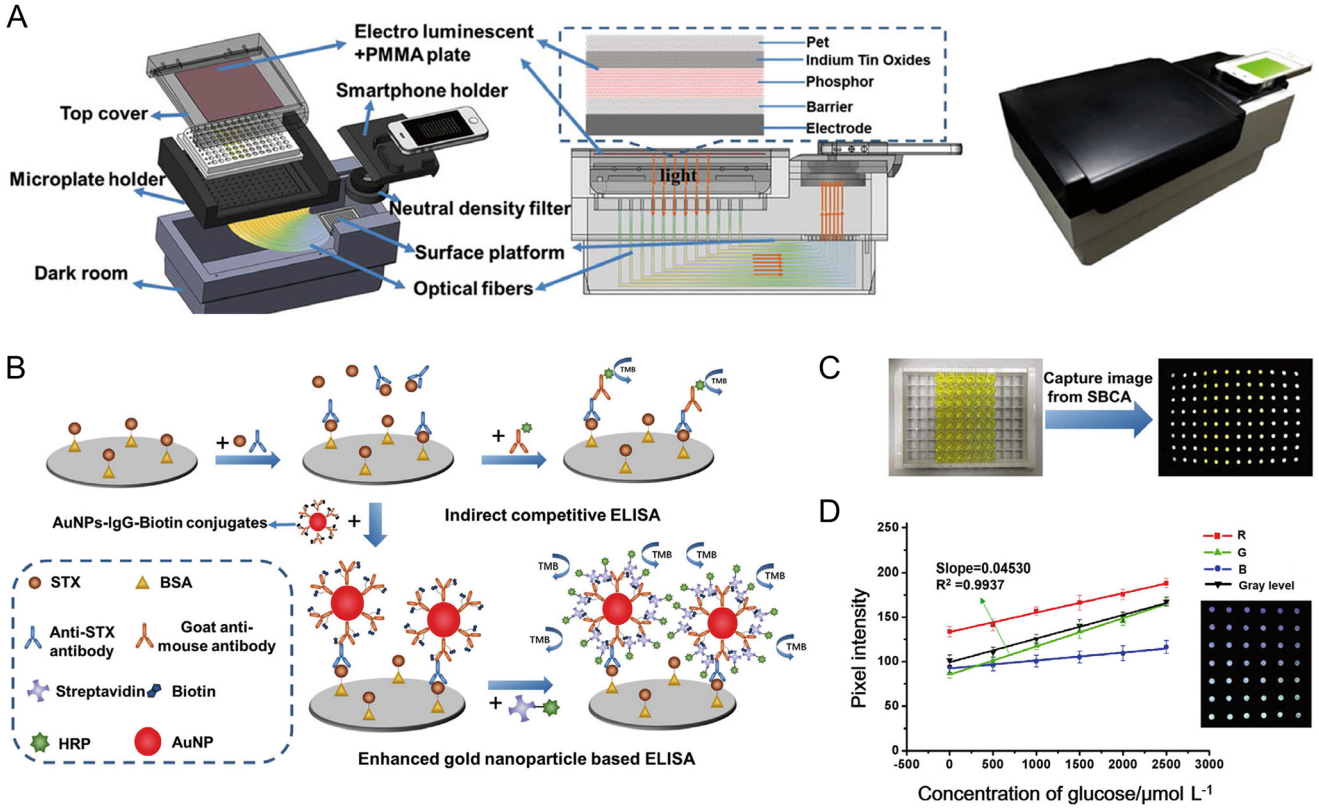

Fig. 16 Smartphone-based colorimetric analyzer for an AuNP-enhanced ELISA. (A) Device design. (B) Assay method. (C) Smartphone image (right) derived from the multi-well plate (left). (D) Plot of pixel intensity *versus* glucose concentration from RGB and grayscale image analysis. Abbreviations: STX, saxitoxin; BSA, bovine serum albumin. Also refer to the Abbreviations list. Adapted with permission from ref. 278 Copyright 2019 Springer Nature.

Open Access Article. Published on 07 February 2025. Downloaded on 19/4/2026 11:02:09 PM.
This article is licensed under a Creative Commons Attribution-NonCommercial 3.0 Unported Licence.

enable chromogenic detection. Examples of blot-style assays include the aptamer-based detection of *Mycobacterium tuberculosis* with TMB chromogen,[274] and the immunodetection of the SARS-CoV-2 spike and nucleocapsid antigens (LOD 2 pM) *via* a chromogenic HRP-induced silver metallization reaction.[275] Competitive enzyme-linked immunosorbent assays (ELISAs) have been ported to paper substrates for the smartphone-based detection of tetracycline (LOD 0.5 ng mL^{-1}) and chloramphenicol (0.05 ng mL^{-1}),[276] and ketamine in clinical oral samples (0.3 ng mL^{-1}).[277] Color generation in ELISAs has been enhanced by NP scaffolds that carry multiple copies of HRP, as in the cases of AuNPs in an assay for saxitoxin (0.4 ng mL^{-1}; Fig. 16)[278] and graphene oxide in an assay for okadaic acid (0.02 ng mL^{-1}).[279] To make the ELISA more user friendly for portable detection, capture antibodies were immobilized on microbeads within wells that had a membrane bottom with pores smaller than the microbead diameter. The wells were placed on top of an adsorbent pad to facilitate washing through the pores while retaining the microbeads for detection for SARS-CoV-2 nucleocapsid protein (LOD 7.5 pg mL^{-1}).[167] As another example of a strategy for simpler execution of an ELISA, capture antibodies for FXYD3 (a urothelial cancer biomarker) were immobilized on the inner surface of the lid of a glass vial.[280] The lid was moved stepwise between vials with the different assay reagents and shook, while also adopting AuNP-HRP conjugates for extra amplification per binding event.

Although colorimetric detection of nucleic acids is rare, one study leveraged the decrease in pH from polymerase activity during LAMP amplification to detect a SARS-CoV-2 gene (LOD < 50 copies/reaction) using the color change of phenol red pH indicator.[281] Another study combined RT-LAMP, CRISPR/Cas9, and a DNAzyme-catalyzed chromogenic reaction for the detection of SARS-CoV-2 in clinical samples.[282]

7.2.4 Molecular chromogens: NP catalysts. NPs are an alternative to enzymes for the catalysis of chromogenic reactions for smartphone-based detection. For the oxidation of TMB dye, Pd@Au NPs replaced HRP as the partner for glucose oxidase in the detection of glucose (LOD 9 μM),[283] and various NPs have also replaced HRP in immunoassays for the detection of *Salmonella* (MnO_2 NPs; LOD 44 CFU mL^{-1}),[284] omethoate insecticide (Au@Pt NPs; LOD 0.01 μg mL^{-1}),[285] and cyanotoxins (AuNPs; LODs < 0.7 μg L^{-1}).[286] Other examples of NP-catalyzed chromogenic reactions include the use of Cu-based NPs in a sandwich immunoassay for α-lactalbumin (reaction between 2,4-dichlorophenol and 4-aminoantipyrine to produce a red color)[287] and a paper-based test for phenolics (reaction with 4-aminoantipyrine to produce an orange color).[288]

Other colorimetric assays with NPs have been special cases where an analyte modulates the catalytic activity of the NP. For example, serum glutathione (LOD 0.3 μM) was detected through its inhibition of the oxidation of TMB by zeolitic imidazolate framework (ZIF-8)/AuNP materials.[289] Conversely, aqueous Hg^{2+} (LOD < 8 ng mL^{-1})[290] and Cr^{6+} (LOD 0.05 nM)[291] were detected *via* their enhancement of the catalytic activity of AuNPs toward oxidation of TMB and methylene blue, respectively.

7.2.5 Molecular chromogens: array-based detection. Colorimetric assays have been deployed in array formats for two purposes: the discrimination of different analytes and the parallel detection or screening of multiple analytes. In the former case, the chromogens have differential but non-specific responses to the analytes. Examples include the identification of volatile organic carbon compounds (*i.e.* solvent vapours) *via* unique color quartets with an on-paper array of four polydiacetylenes,[292] and an array of seven pH indicator dyes to distinguish between three different amine gases.[293] The four-color patterns were matched to a database of calibrated solvent responses, whereas PCA and HCA were used to match the amine to the seven-color patterns.

For the parallel detection of multiple analytes, each chromogen nominally responds to only one analyte. For example, a wearable patch was developed for detecting pH, urea, and Ca^{2+} (aq) in human sweat *via* separate spots with a cocktail of three pH indicator dyes, *p*-dimethylaminobenzaldehyde (Ehrlich reaction with urea), and *o*-methyl phenolphthalein indicator (Fig. 17).[164] Another wearable patch was reported for the AI-assisted analysis of pH, vitamin C, Ca^{2+} (aq), and protein levels in tears using a

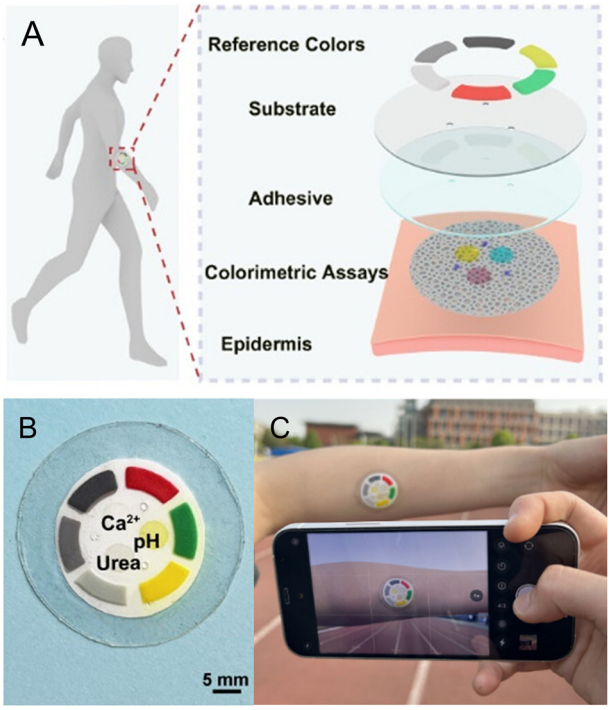

Fig. 17 Stretchable patch for colorimetric sweat sensing directly from skin. (A) Design of the patch. (B) Photograph of the patch with six reference colors and indicator spots for detecting pH, urea, and Ca^{2+} (aq). (C) Smartphone imaging of the patch for *in situ* colorimetric analysis. Adapted with permission from ref. 164 Copyright 2024 American Chemical Society.

Open Access Article. Published on 07 February 2025. Downloaded on 19/4/2026 11:02:09 PM.
This article is licensed under a Creative Commons Attribution-NonCommercial 3.0 Unported Licence.

cocktail of indicator dyes and three chromogenic systems.[230] A trio of indicator dyes was used on a paper substrate for the detection of gaseous ammonia, formaldehyde, and hydrogen sulfide,[294] and chromogenic inks were printed in a QR code pattern for dosimeter-like response to relative humidity, temperature, and gaseous H_2S, NH_3, and CO_2.[295] NO_3^- (aq), Mg^{2+} (aq), Ca^{2+} (aq), and NH_4^+ (aq) were detected as macronutrients of interest through a μPAD with a combination of the Greiss method, three indicator dyes, and the salicylate method.[296] A conceptually similar mix of indicator dyes and chromogenic reactions was used to develop a μPAD for the detection of Fe^{3+}, Ni^{2+}, Cr^{6+}, Cu^{2+}, Al^{3+}, and Zn^{2+} (aq).[297] NNs enabled an array of five chromogenic reactions to distinguish between seven illicit drugs,[231] and enabled a linear barcode of 20 different compositions of a halochromic dye, chitosan NPs, and cellulose acetate to predict meat freshness from its volatile amines.[229]

Enzyme-catalyzed chromogenic reactions have also been multiplexed. One example is a plate-based assay for the detection of glucose, uric acid, cholesterol, and triglycerides *via* oxidase-peroxidase coupled reactions ending in the chromogenic oxidation of 4-aminophenazone, supplemented with a classic biuret reaction and indicator dye for the additional detection of total protein and albumin (Fig. 18).[298] A related example is an injectable "ink" for pH measurement (*via* a cocktail of three indicator dyes), glucose (*via* the glucose oxidase–peroxidase-TMB chromogenic system), and albumin (*via* a protein-binding indicator dye).[299]

7.2.6 AuNPs: assembly. Plasmonic coupling between AuNPs has been exploited for colorimetric detection through both aggregative and assembly mechanisms.

In aggregative detection mechanisms, an analyte compromises the colloidal stability of the AuNPs. However, loss of colloidal stability is also a potential outcome from

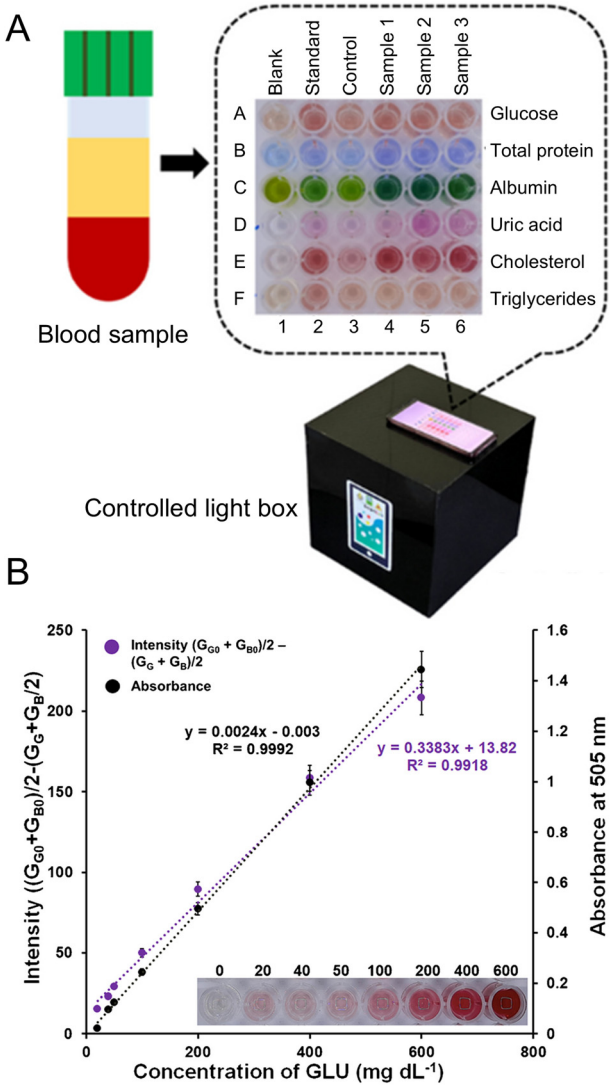

Fig. 18 Colorimetric assay for the simultaneous determination of glucose (GLU), total protein, human serum albumin, uric acid, total cholesterol, and triglycerides in plasma samples. (A) Smartphone image of the multi-well layout of the colorimetric array (each row) and its response to different samples (each column). (B) Comparison of calibration curves for glucose measured by smartphone (left *y*-axis) and by conventional spectrophotometry (right *y*-axis). Adapted with permission from ref. 298 Copyright 2024 Springer Nature.

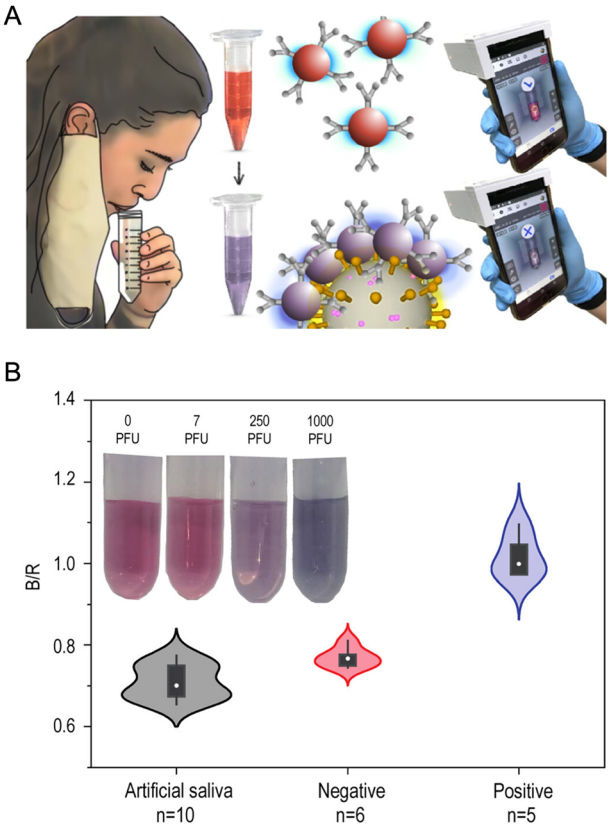

Fig. 19 Colorimetric detection of SARS-CoV-2 analysis in saliva samples using a smartphone. (A) Assay concept. (B) Change in color, measured *via* a B/R ratio, for samples with and without SARS-CoV-2 virus. The inset shows the change in the color of solutions with different amounts of virus (measured in plaque-forming units). Adapted with permission from ref. 302 Copyright 2022 American Chemical Society.

Open Access Article. Published on 07 February 2025. Downloaded on 19/4/2026 11:02:09 PM.
This article is licensed under a Creative Commons Attribution-NonCommercial 3.0 Unported Licence.

changes in temperature, ionic strength, and pH, as well as from non-specific binding interactions with molecules in a complex sample matrix. Although some aggregative mechanisms have been functional with authentic samples, a majority of studies have used lab-prepared solutions of analyte for proof of concept or relied on substantial dilution of authentic samples. Many of these approaches lack a defined and robust mechanism for selectivity and are not discussed in this review. Nevertheless, there have been examples of aggregative detection with a selective component: the nominal trypsin activity in pancreatitis samples was detected *via* a color change when the bovine serum albumin molecules stabilizing AuNPs were hydrolyzed to cause particle aggregation;[300] and a five-material array of AuNPs synthesized with different ligands and reducing agents was able to discriminate between eight different pesticides in washes of fruit samples.[301] In the latter case, the color changes were related to aggregation dependent on the level of inhibition of acetylcholine esterase activity by the pesticide.

Assembly-based assays incorporate a component for selective recognition of analyte that induces or disrupts a close proximity between AuNPs. As a simple and elegant example of this approach, AuNP–antibody conjugates bound to the spike protein on SARS-CoV-2 virus with sufficient density to generate a color change from red to blue (LOD 0.3 PFU mL^{-1}; Fig. 19).[302] Analogous detection of *Listeria monocytogenes* was also demonstrated,[303] and the concept was extended to the detection of a nucleic acid reporter sequence from a magnetic pull-down immunoassay for creatine kinase-MB (CK-MB; LOD 0.8 pM).[304] In the later example, the reporter was amplified by rolling circle amplification (RCA) and the proximity needed for a color change arose from binding of AuNPs (less sensitive) and AuNP-tetrahedra (more sensitive) along the repeating sequence of the linear product.[304] In another case, hybridization-mediated assembly between AuNP–oligonucleotide conjugates generated signal in a proteolysis-responsive transcription assay for matrix metalloproteinase-2 activity (LOD 5.7 pM) in serum, which distinguished between healthy persons and cancer patients.[305] Conversely, the *trans*-nuclease activity of CRISPR/Cas12a was used to prevent the assembly of AuNP–oligonucleotide conjugates for the detection of SARS-CoV-2 (LOD 1 copy per μL).[306]

7.2.7 Metal NPs: reactivity. Colorimetric detection with a smartphone camera has also been based on the reactivity (not catalysis) of various metal NPs. For example, metal NPs have been useful for headspace analysis of gaseous analytes: hydrogen sulfide (LOD 65 nM) *via* its color-fading etching action on Ag@Au core@shell nanoprisms;[307] formaldehyde (LOD 30 nM) through its color-changing reduction of Tollen's reagent complex to a silver layer on a gold nanoprism;[308] and bromine, iodine, and mercury vapour by their oxidative etching or amalgamation with Au nanorods (NR).[309] Whereas each of the foregoing examples used a hanging drop of NP dispersion on a hydrophobic cellulose substrate to detect a single analyte, a notable study demonstrated the headspace discrimination of multiple analytes using an array of nanomaterials and three dyes on a nitrocellulose substrate (Fig. 20).[310] The two sizes of AuNP and three sizes of AuNR were functionalized with cysteine, which reacted with

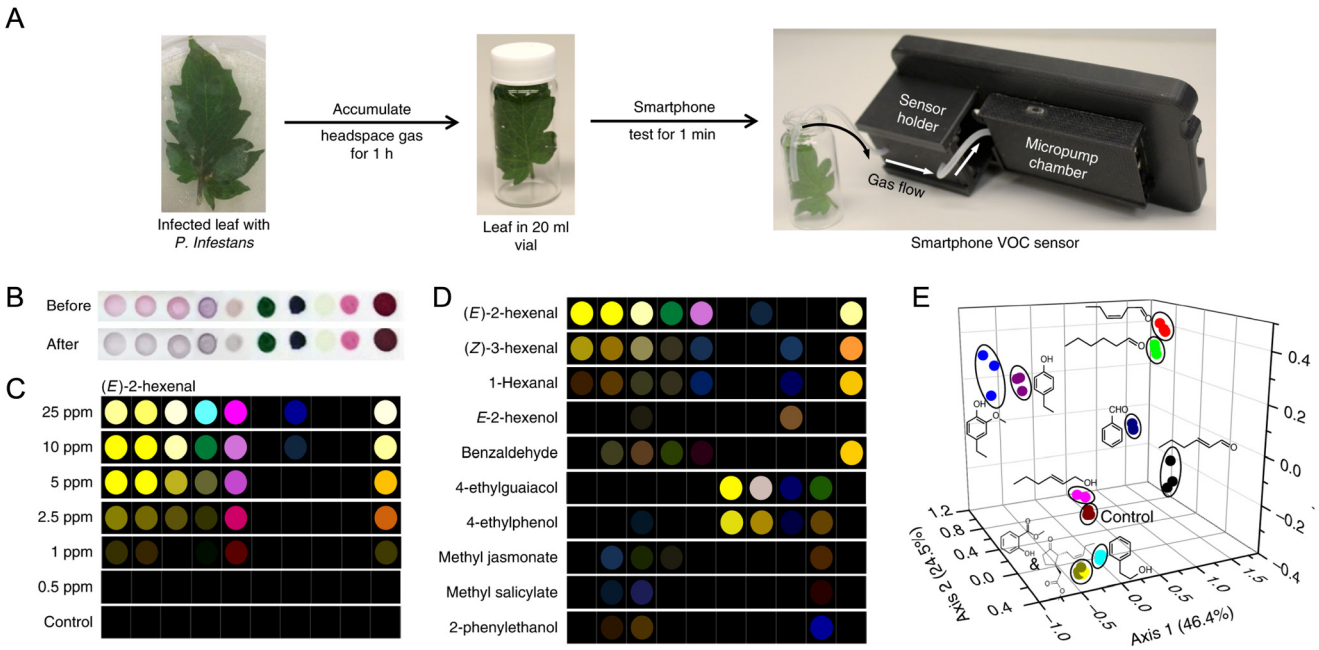

Fig. 20 Analysis of plant volatiles using a portable smartphone-based device and colorimetric array. (A) Assay work flow and photograph of the device. (B) Smartphone image of the colorimetric array before and after exposure to headspace gases. (C) RGB difference profiles for the array exposed to different concentrations of (*E*)-2-hexenal (0.5–25 ppm). (D) RGB difference profiles of ten representative plant volatiles at 10 ppm. (E) PCA score plot showing differentiation between multiple volatiles. Adapted with permission from ref. 310 Copyright 2019 Springer Nature Limited.

Open Access Article. Published on 07 February 2025. Downloaded on 19/4/2026 11:02:09 PM.
This article is licensed under a Creative Commons Attribution-NonCommercial 3.0 Unported Licence.

aliphatic α,β-unsaturated aldehydes such as (*E*)-2-hexenal through a 1,4-Michael addition reaction, stripping the ligand from the gold surface and causing aggregation with a color change. Measurements were made *via* a smartphone attachment with a diaphragm micropump and a windowed chamber for the test strip, where the collective changes in RGB colors and PCA were used to identify ten different plant volatiles and detect *P. infestans* infection from whole plant leaves.[310]

The reactivity of NPs has also been leveraged for the detection of solution-phase analytes. Bromide (LOD 0.5 mg dL^{-1}) and glucose (LOD 1 mg dL^{-1}) were detected *via* their direct and indirect (H_2O_2 production by glucose oxidase) etching of silver triangular nanoprisms;[225] Hg^{2+} (LOD 50 μM) was detected in tap water *via* its color-fading amalgamation with AgNPs;[311] and the activity of acid phosphatase (LOD of 0.97 U L^{-1}) in human serum was quantified through a set of coupled reactions that ultimately produced triiodide to etch gold nanorods (AuNRs).[312] As another example, cyanide was detected by its ability to etch Au@Au–Ag NPs, where three different sizes of the NPs (and thus starting colors) were used in an array format for greater quantitative reliability.[313]

A more exotic approach to detection has been the growth of NPs to generate color as the readout of immunoassays. A competitive immunoassay for tyramine utilized an alkaline phosphatase conjugate of the antibody to convert ascorbic acid phosphate to ascorbic acid to enable the formation of gold nanostars from gold salt.[314] A similar approach grew silver on AuNR seeds for the detection of acrylamide, albeit requiring chemical derivatization of the analyte as the first step in the immunoassay.[315]

7.2.8 Lateral flow immunochromatographic assays. LFIAs are one of the most widely reported formats for the detection of protein analytes and small-molecule analytes. Typically, the former are detected *via* sandwich immunoassays, whereas the latter are detected *via* competitive immunoassays. Examples with smartphone readout have used both commercial LFIA kits and custom-made LFIAs, where analytes have included human chorionic gonadotropin (LOD 3 ng mL^{-1}) in urine,[316] brain-derived neurotrophic factor (a biomarker for glaucoma; LOD 14 pg mL^{-1}) in artificial tears,[317] non-structural 1 secretory protein of Japanese Encephalitis (LOD 10 pg mL^{-1}) in clinically infected pig serum samples,[318] IgA specific to SARS-CoV-2 in serum and saliva,[319] 8-hydroxy-2′-deoxyguanosine in patient urine samples to screen for diabetic retinopathy,[320] and many more. Nearly all LFIAs have had the standard format of adjacent test and control lines on a horizontal membrane, but there have been embellishments such as designing the test and control lines to integrate into a barcode to facilitate readout.[321] Although far less common, dipstick[322] and vertical flow immunoassays[323] have also been adopted, where the latter provided an 80-fold improvement in the detection limit *versus* a standard LFIA but required disassembly for readout.

The principal motivation for smartphone-based imaging of LFIAs is quantitation based on the color intensity of the test line. Whereas qualitative LFIAs are useful for binary scenarios (*e.g.* pregnant or not, infected with virus or not), quantitative LFIAs enable assays of analytes that are naturally present in a sample to determine if levels are too high or too low. Quantitative smartphone readout of LFIA test lines has been shown to be well correlated with lab-based CL immunoassays.[324] When applied with LFIAs with multiple test lines for the same analyte—a configuration that nominally renders the assays pseudo-quantitative by visual inspection—smartphone readout provided a modest improvement in detection limit.[325]

In general, any strategy that improves LFIA sensitivity by visual inspection also benefits readout by smartphone. Examples of strategies include compression of a zone of the membrane to slow flow at the test line,[326] narrowing of the membrane at the test line to increase the density of analyte binding,[327] and electrokinetic preconcentration based on ion concentration polarization with a commercial 9 V battery (2.7-fold improvement in LOD).[328] Assembly of a cluster-like network of AuNPs, without a change in their plasmon resonance (*i.e.* red color), decreased the detection limit for an LFIA for enrofloxacin (LOD 10–1 μg L^{-1}) by three orders of magnitude compared to single AuNPs.[329]

Peripheral hardware for smartphone-based colorimetric LFIAs has been wide ranging. At the extreme of simplicity, hardware is absent and the assay relies on ambient light and manual positioning for image acquisition. In other cases, there are attachments and boxes to position the smartphone and LFIA strip and provide consistent illumination *via* an internal light source, whether the source is the smartphone flash[77,330] or LEDs external to the phone.[31,316,331,332] It is also possible to combine a box with ambient lighting for readout.[317] At the technical extreme, a multi-step LFIA was semi-automated by means of a device with a motorized rotor (Fig. 21).[333] The rotor had four diametric pairs of sample pads (for adding chromogenic signal development reagents) and absorbent pads (for driving fluid flow) that moved in sequence to bracket a central test zone membrane. A less technical approach for two-step development of signal in an LFIA was a two-tiered LFA with a slow-dissolving polymer barrier to delay the arrival of reagents for amplification (by NP growth) until after the initial binding of analyte and AuNP-antibody conjugates at the test line.[332]

Image processing for LFIAs have been as straightforward as color analysis of regions of interest in the RGB, HSV, and CIE spaces discussed earlier, as well as grayscale, but has also incorporated computer vision and ML for the recognition of test cartridge and line positions, and for image calibration.[334,335] Examples include the application of statistical image analysis,[336] support vector machines,[337,338] convolutional NNs,[339,340] and other deep NNs.[341]

Smartphone cameras have also benefited multiplexing with LFIAs. Some approaches, like bifurcated membranes, derive only the aforementioned quantitation advantage.[342]

Open Access Article. Published on 07 February 2025. Downloaded on 19/4/2026 11:02:09 PM.
This article is licensed under a Creative Commons Attribution-NonCommercial 3.0 Unported Licence.

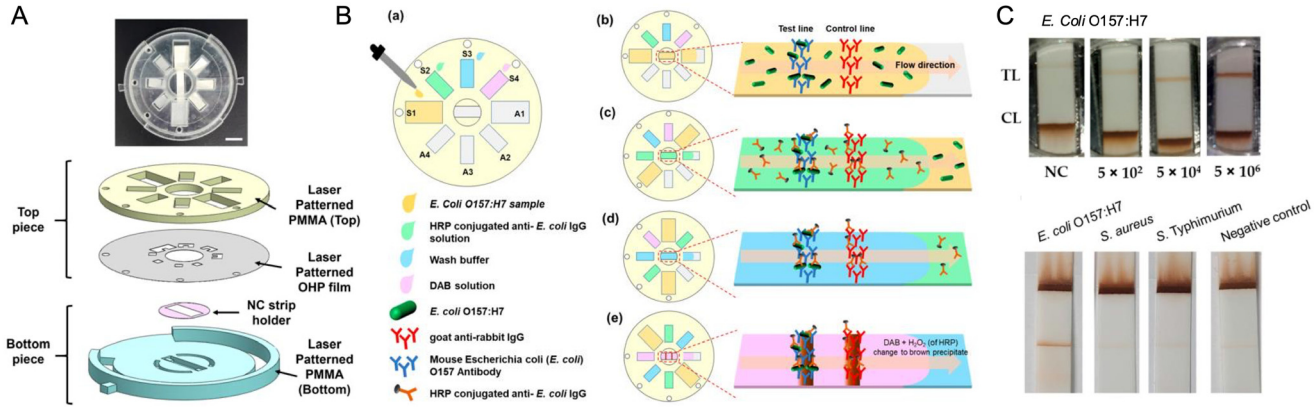

Fig. 21 Rotary device for an enzyme-linked LFIA with a colorimetric detection. (A) A photograph and illustration of the rotary device containing the nitrocellulose (NC) membrane, the sample pads and absorbent pads. The top layer is rotated *via* a motor controlled by the smartphone *via* Bluetooth. (B) Assay steps (a–e). Each step takes 5–10 min. (C) Smartphone images showing (top) the signal generation from the chromogenic turnover of 3,3′-diaminobenzidine (DAB) with increasing concentrations of the target *E. coli* bacteria, and (bottom) the selectivity for *E. coli* over other bacteria species. Figure adapted from ref. 333 under a Creative Commons CC BY 4.0 license.

Other multicolor approaches leverage the RGB information available. In one case, a single competitive LFIA was able to distinguish between food contamination with one of two different types of mycotoxin (aflatoxin B1 and type-B fumonisins; LODs of 1 and 50 ng mL^{-1}) through a pair of AuNP–antibody conjugates that roughly corresponded to red (30 nm diameter) and blue (75 nm) colors.[343] In another case, a sandwich LFIA featured a combination of two test lines, each with two co-immobilized capture antibodies, plus two different reporter antibody conjugates of each of blue and red latex microparticles, to detect and discriminate between serogroups of *Salmonella* (Fig. 22).[344] The position (first or second line) and color (blue or red) of test-line binding indicated the specific serogroup. In both cases, the camera provided a non-subjective means of color recognition. Another approach utilized an LFIA with three test lines for three mycotoxins and red, green, and blue colors of reporter antibody–latex microsphere conjugates.[345] Here, the color and line location provided a level of redundancy.

The vast majority of LFIAs have, to date, utilized AuNPs to generate contrast at test and control lines, and smartphone-based approaches are no exception. As noted above, dyed latex microparticles—another classic contrast label for LFIAs—have also been utilized with smartphone readout.[331,344] Nevertheless, numerous papers have evaluated alternative materials: blue-colored iridium (VI) oxide NPs,[346] which provided approximately double the contrast compared to AuNPs; rhodamine B-labeled polymersomes;[347] polydopamine NPs;[334] composite materials derived from hyperbranched AuNPs and polydopamine;[348] carbon black NPs;[349] and NPs

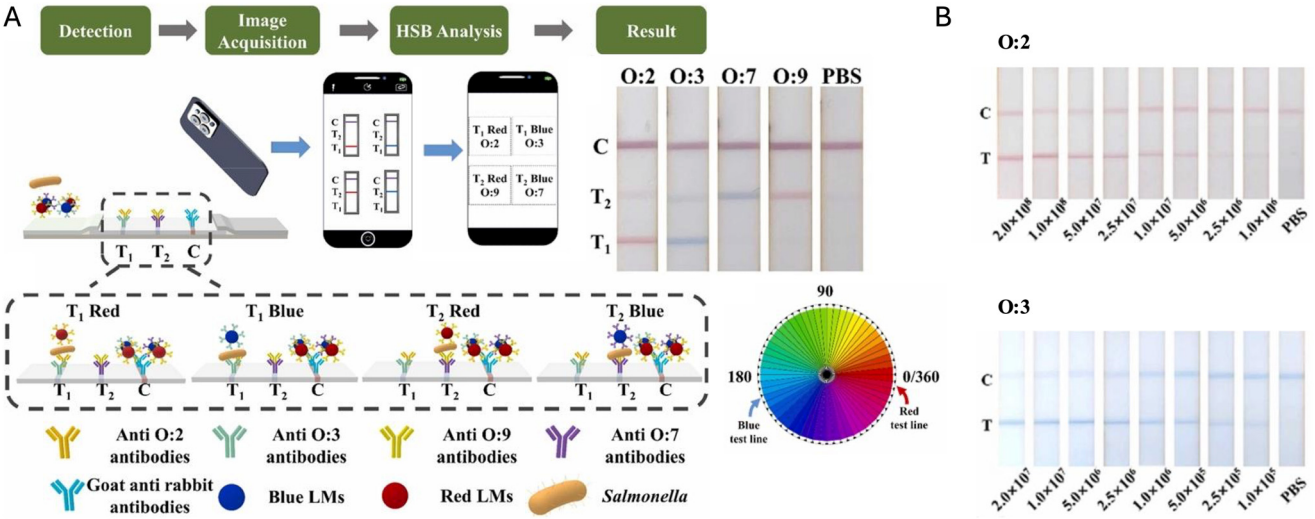

Fig. 22 Two-line two-color LFIA for serotyping *Salmonella*. (A) Assay design (left), smartphone images of LFIA results for four different serotypes (O:2, O:3, O:7, O:9, top-right), and position of the blue and red latex microspheres (LMs) on an HSB color space projection. (B) Smartphone images of LFIA test strip response to different concentrations of O:2 standard strain and O:3 standard strain. Adapted from ref. 344 with permission. Copyright 2023 Elsevier.

Open Access Article. Published on 07 February 2025. Downloaded on 19/4/2026 11:02:09 PM.
This article is licensed under a Creative Commons Attribution-NonCommercial 3.0 Unported Licence.

derived from cuttlefish ink.[350] A caveat in comparing the contrast from different NP materials is that extinction coefficients tend to increase with increasing size. It is therefore necessary to consider both the type and size of a material when choosing a colorimetric label. Size is also a potential consideration in so far as it affects NP transport on the LFIA membrane, non-specific binding, and blocking of membrane and pads.

Other LFIAs have adopted nanozymes and other NPs that catalyze chromogenic reactions for signal amplification with LFIAs. Examples of such materials include PtPd NPs with DTNB chromogen;[58] Au@Pt NPs,[351] CuCo NPs,[352] Rh NPs (50-fold improvement in LOD *versus* standard AuNP usage),[353] Au@PtPd NPs with TMB and peroxide;[31] and cerium oxide NPs with TMB (no peroxide; two-fold improvement in sensitivity *versus* AuNPs).[354] The gain in signal comes at the cost of an extra processing step and additional reagents.

Although not very common, the lateral flow assay format with smartphone readout has been adapted to the detection of nucleic acids. A simple adaptation utilized a test line with streptavidin, a control line with an oligonucleotide probe, and AuNP–oligonucleotide conjugates to detect biotinylated amplicons from recombinase polymerase amplification (RPA) of a *Salmonella* gene (LOD 19 CFU mL^{-1}).[355] Biotinylated and fluorescein-labeled LAMP amplicons for SARS-CoV-2 detection (LOD 4000 copies per mL) were likewise detected with a streptavidin test line and AuNP–anti-fluorescein–antibody conjugates.[356] Tilapia lake virus RNA was detected through RT-RPA amplification followed by CRISPR/Cas12a amplification with a biotin–oligonucleotide–fluorescein reporter and AuNP–anti-fluorescein conjugates (LOD 200 copies/reaction).[357] A similar approach was adopted to screen for six genes of *Bacillus cereus* in milk and rice samples (LOD 10^{-4} ng mL^{-1}),[358] and the CaMV35S promoter sequence relevant to genetically modified organisms was detected (LOD 10 aM) with substitution of RCA for RPA.[359] A lateral flow assay for detection of a *Salmonella* gene (LOD 1 CFU mL^{-1}) in food samples used a combination of RPA, CRISPR/Cas12a, and chromogenic oxidation of TMB.[360] Assays of this nature have notably compromised simplicity and portability for enhancement of detection in an LFIA format.

7.2.9 Cytometry and microscopy. Several smartphone-based methods have been reported for counting cells and bacteria. The most common approach is to quantify color changes associated with a change in dye structure from cellular metabolic processes, which avoids the need to image individual cells. Combinations of assay formats, dyes, and cell types have included microcapillary arrays with resazurin dye (blue to pink from reduction) for counting *E. coli* (gram-negative) and *S. saprophyticus* (gram-positive) bacteria (LOD of 10 CFU mL^{-1});[361] a microcentrifuge tube with a cocktail of bromothymol blue dye, tartrazine, Direct Red 80 dye, and polyvinylpyrrolidone (black to orange with changes in medium pH) for counting HeLa cells (LOD 51 000 cells);[362] a paper substrate with WST-8 dye (colorless to orange from reduction) for screening MCF-7, L-02, and HepG2 cells responses to cytotoxic drugs;[363] and a gel-filled poly(methyl methacrylate) through-hole array with resazurin (Alamar blue) for screening HeLa cell response to drugs.[364] Calibration relates viable cell count to color, where image analysis for these measurements has utilized both the RGB and HSV color spaces (analyzing specific color channels and saturation values) and grayscale conversion.

Other approaches for smartphone-based cell counting rely on the direct imaging of cells. As a unique example of bulk imaging, L929 cells were counted with the assistance of a trained convolutional NN through brightfield imaging of a centrifuged pellet of cells in a plastic tube.[365] However, most approaches resolve individual cells to generate counts. Stains have sometimes been used to enhance image contrast or to help identify target cells, as in the cases of counting red blood cells in a Leishman-stained blood sample,[366] and counting *Cryptosporidium* and *Giardia* (oo)cysts in vegetable wash water and river water samples with Lugol's iodine-staining.[367]

Some cell-counting approaches have also bypassed staining. A method of counting $CD4^+$ T cells for HIV monitoring relied on immunocapture of the target cells (from whole blood) within a microfluidic chip.[368] A battery-powered clip-on device utilized a broadband LED for illumination and a pair of lenses from a DVD drive to supplement the smartphone camera for brightfield imaging. Individual cells counted in the field of view were converted to a sample cell count. A similar technical approach was used to count sickled cells (*i.e.* monitor sickle cell disease) from whole blood samples.[369] The main difference was that immunocapture was not necessary since the image analysis algorithm distinguished round (healthy) cells from misshapen (sickle) cells.

Whereas most cell counting approaches have utilized a sample preparation with static cells, a smartphone-based brightfield imaging flow cytometer has been reported. The device used a high-power LED illumination source, a simple PDMS-on-glass microfluidic chip, and objective and eyepiece lenses borrowed from a conventional microscope.[370] The prototype sacrificed some portability for performance, requiring an outlet-connected power supply for the LED source, but was able to image cells with <700 nm spatial resolution at real-time rates up to 100 cells per second and post-processing rates of 67 000 cells per second. The high-power LED was necessary to produce sufficient illumination intensity for imaging the fast-flowing cells at a high frame rate to avoid motion blur. A convolutional NN analyzed cell size and morphological features to distinguish Jurkat and EL4 cells.

Tissue specimens have also been analyzed by smartphone microscopy. The assessment of nonalcoholic fatty liver disease lesions from hematoxylin-and-eosin-stained liver allograft biopsies,[371] and the evaluation of allograft kidney biopsy specimens,[372] are two examples of applications. A growing trend in smartphone microscopy is the use of deep learning (*i.e.* NNs) for the analysis of acquired images.

Open Access Article. Published on 07 February 2025. Downloaded on 19/4/2026 11:02:09 PM.
This article is licensed under a Creative Commons Attribution-NonCommercial 3.0 Unported Licence.

Benefits of this approach include automation, elimination of the need for a trained expert for image interpretation, mitigation of potential limitations in image quality, and additional informing power that avoids the need for further analysis (*e.g.* immunohistochemistry). Examples of deep-learning-supported imaging have included screening for sickle cell disease from patient blood smears (Fig. 23),[89] screening for cervical cancer from liquid cytology samples,[373,374] classification of skin lesions as malignant or benign,[375] identification of five species of an invasive insect (genus *Liriomyza*),[376] early detection of mold on bread,[377] and prediction of the presence of asbestos in building materials.[378]

In general, the above methods utilized clip-on attachments for a smartphone to enable brightfield microscopy with suitable magnification, or had 3D printed a small smartphone-based microscope device for the benchtop. One noteworthy clip-on attachment was only 0.15 cm^3 in volume, 0.5 g in weight, and $10 in cost, with a reported order of magnitude improvement in depth of field compared to a conventional microscope. It was combined with deep learning for classifying skin moisture levels.[379] At the other extreme of device design, microscopy has been approached by mounting a smartphone on a scientific benchtop microscope that would otherwise not be equipped with a digital camera. This approach has been implemented with deep learning for determining the risk of malignancy for thyroid fine-needle aspiration biopsy samples,[380] for subtyping of cancer cells and detecting lymph node metastasis from hematoxylin-and-eosin-stained pathology tissue slices,[381] and for evaluating the morphology of embryos for *in vitro* fertilization.[382] A third viable platform for smartphone microscopy has been the low-cost, commercially-available "foldscope" paper microscope, which was adopted to screen antifungal agents for their effect on the *C. albicans* pathogen,[383] and for imaging prepared slides of mammalian endocrine glands in a classroom setting.[384]

As a brightfield microscopic approach to molecular detection, polystyrene microspheres were combined with magnetic NPs to enable a digital competitive immunoassay for aflatoxin B1.[385] To report on a plate-based immunoassay, the secondary antibody for detection was conjugated with alkaline phosphatase to produce ascorbic acid, which then initiated an azide-alkyne click reaction that coupled magnetic nanoparticles to microspheres in the assay supernatant. The analyte was quantified through magnetic capture and AI-assisted counting of the microspheres. In principle, this strategy is adaptable to a variety of immunoassays and coupling or ligation reactions.

7.2.10 Spectrometry. Most of the assays implemented with smartphone-based spectrometers have been colorimetric. Examples of bioanalysis include commercial urine dipstick colorimetric tests,[32] and ELISAs for avian influenza virus H7N9 and porcine circovirus type 2 antibodies,[210] human interleukin-6 and two peanut allergens (Ara h1, Ara h2),[209] and four types of autoantibodies.[214] Examples of chemical analysis include the detection of atenolol (a drug) through its inhibition of a de-diazotization reaction,[205] sodium hypochlorite from its degradation of a colored dye,[206] and total dissolved copper in water samples *via* a bicinchoninate assay.[386] Chromogenic reactions have also been utilized for the spectrometric detection of ascorbic acid in beverages,[204] nitrite in tap and river water samples,[202] and bisphenol A (BPA) in water.[208]

As described, all of the assays noted above would have been possible with conventional RGB imaging with a

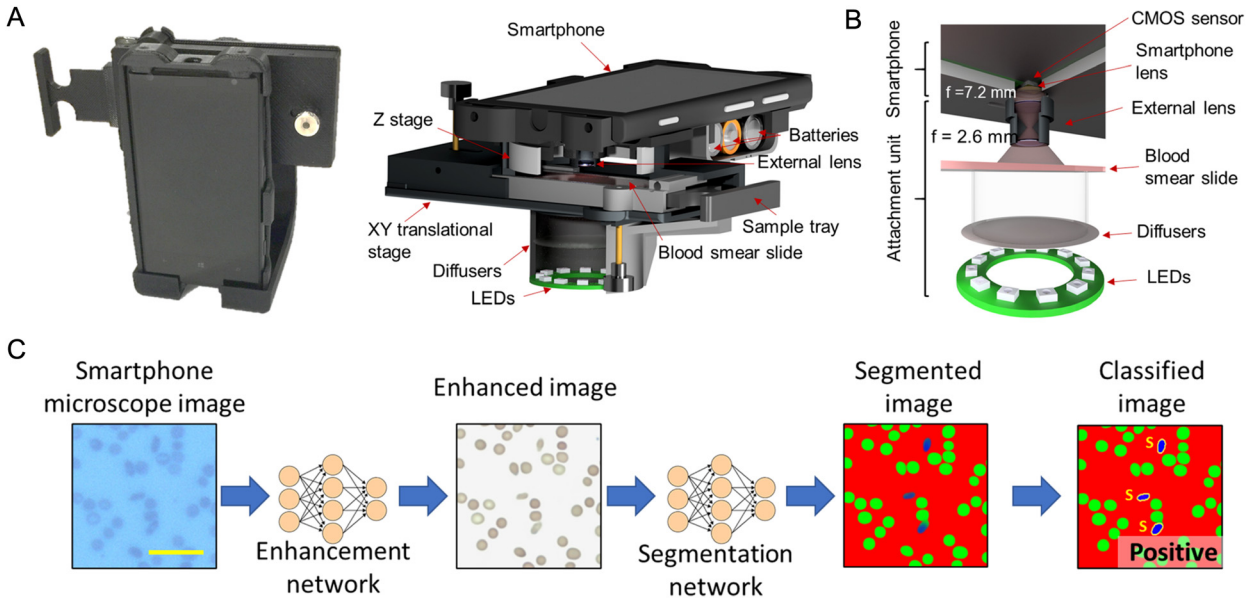

Fig. 23 Smartphone-based brightfield microscope for sickle cell identification. (A) Photograph (left) and design (right) of the microscope device. (B) Close-up of the optical path. (C) Workflow from image acquisition to identification of sickle cells. Adapted from ref. 89 under a Creative Commons Attribution 4.0 International License.

Open Access Article. Published on 07 February 2025. Downloaded on 19/4/2026 11:02:09 PM.
This article is licensed under a Creative Commons Attribution-NonCommercial 3.0 Unported Licence.

smartphone camera. Equivalent analytical performance would also be anticipated for conventional imaging, particularly when aided by modern ML methods. A smartphone spectrometer will be most useful when there is a need for detailed or continuous spectral data over color information, such as when two signals to be unmixed do not make significantly different contributions to two different RGB channels. This scenario is rare and thus the spectral resolution will often not be worth the technical costs.

7.3 Light scattering analyses

A variety of smartphone assays have been developed around imaging of light orthogonally scattered from the beam of a red laser by NPs. In each case, analyte directly or indirectly induces the aggregation or formation of metal NPs (*e.g.* gold, silver) to increase light scatter, or induces the dissolution of the NPs for a decrease in light scatter. Analytes have included cocaine and a protein biomarker,[387] creatinine,[388] glyphosphate,[389] and aqueous metal ions (Fe^{3+}, Hg^{2+}, Ag^{+}, Cu^{2+}).[390–395] A conceptually similar light scattering assay with AuNPs and aptamers utilized illumination with a green LED for the detection of certain antibiotics (tobramycin, kanamycin, alternariol; LODs < 200 ng mL^{-1}).[396]

In addition to metal NPs, materials such as metal–organic frameworks and cobalt oxyhydroxide nanoflakes have been used as scattering reporters. Scattering assays without synthetic reporters are also possible in certain cases: bacteria were detected in suspension through the loss of light scattering as a bacteriophage lysed the cells (and provides selectivity);[397] and SARS-CoV-2 genes (LOD 1 copy per μL) were detected using a water-in-oil emulsion implementation of LAMP, where the production of amplicons decreased the interfacial tension, decreasing the droplet size and scattering intensity as the amplification progressed.[398]

Smartphone imaging formats have also been developed around light scattering. In one example, a smartphone-based device with built-in polarizers and a green laser imaged backscattered light from bacterial colonies in a petri dish (Fig. 24).[399] Images features were algorithmically extracted, and the type of bacteria was identified through a support vector machine learning analysis of the colony morphology. A related example is the application of ML to count "DNA colonies" that were formed by LAMP reactions confined within a polyacrylamide hydrogel (Fig. 25).[400] The production of pyrophosphates during the amplification led to the formation of magnesium pyrophosphate precipitates, which scattered light and were highly visible by reflection imaging (LOD 1 copy/reaction). A darkfield configuration based on total internal reflection of white-light was used to image light scattered from metal precipitates to identify Pb^{2+} and Hg^{2+} in drinking water, where the color of the precipitate provided information about the identity of the metal.[401]

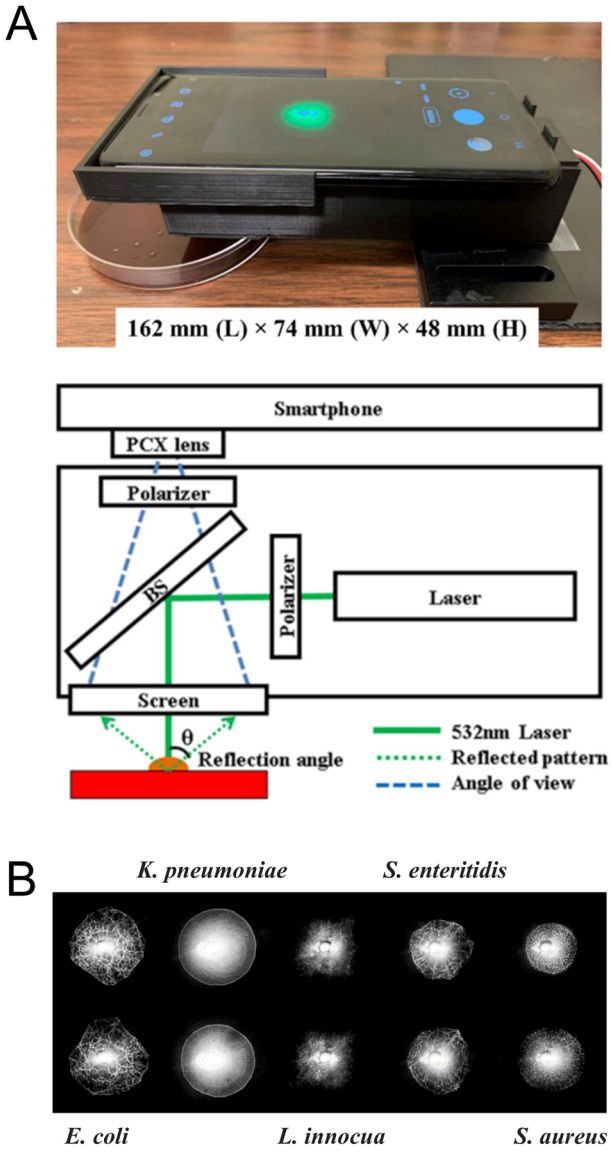

Fig. 24 Smartphone imaging and identification of bacterial colonies *via* elastic light scattering and machine learning. (A) Design of the smartphone-based device. (B) Examples of backscatter patterns from colonies of several species of bacteria. Abbreviations: BS, beam splitter; PCX, Plano-convex. Figure reproduced from ref. 399 under a Creative Commons CC BY 4.0 licence.

7.4 PL analyses

PL-based assays are the second most abundant class of assay after colorimetric assays. Molecular dyes are the most popular source of fluorescence, but there is significant adoption of luminescent NPs. LEDs are the most common excitation source, and there is frequent use of laser diodes and UV lamps, but only limited adoption of the light sources on-board the smartphone (Fig. 14).

7.4.1 Indicator dyes and Fluorogens. Dyes that become fluorescent or change their color of fluorescence in response to an analyte are very amenable to smartphone-based detection. DNA-sensitive dyes are the most frequent examples of such a dye, and are discussed later in the

Open Access Article. Published on 07 February 2025. Downloaded on 19/4/2026 11:02:09 PM.
This article is licensed under a Creative Commons Attribution-NonCommercial 3.0 Unported Licence.

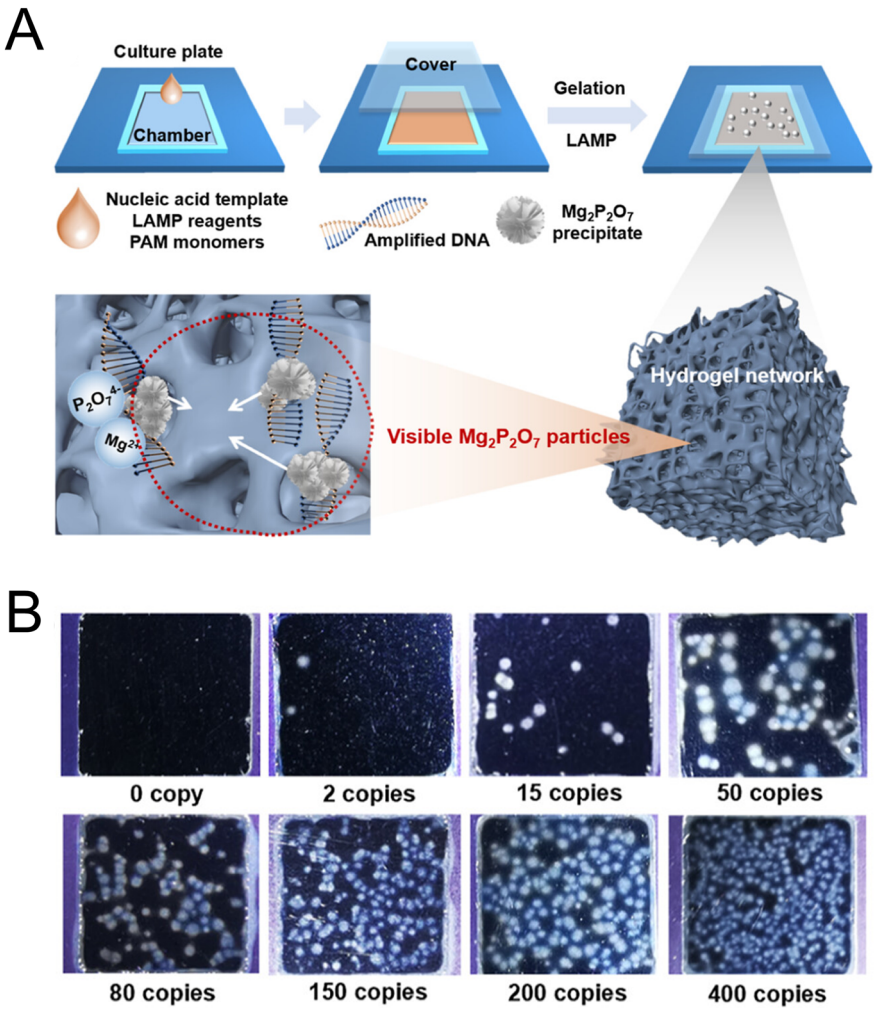

Fig. 25 Label-free detection of DNA *via* light scattering. (A) Assay methodology (PAM = polyacrylamide monomers). (B) Smartphone images of "DNA colonies" (precipitates of magnesium pyrophosphate) in a hydrogel. The colonies are ultimately counted by a machine learning algorithm. Adapted with permission from ref. 400 Copyright 2024 American Chemical Society.

context of nucleic acid amplification tests. In special cases, these dyes can also be used to detect non-nucleic acid analytes that have selective affinity for oligonucleotides, such as in the case of RCA detection of Pb^{2+} (aq, LOD 1 nM) in lake water using a metal-dependent DNAzyme.[402]

Fluorescent dyes have also been developed for interaction or reaction with an analyte, including dyes applied to the smartphone-based detection of malononitrile[403] (a cyanogen) and biogenic amines[404] (for assessing food freshness) through changes in emission color, and the detection of gamma-hydroxybutyric acid (the date rape drug) in carbonated and alcoholic drinks through an increase in emission intensity.[405] A thiol-responsive AIEgen (a dye that undergoes aggregation induced emission) was developed for the detection of an organophosphorous pesticide in hydrolyzed leaf extracts.[406] Dipicolinic acid (an anthrax biomarker) was detected through a competitive coordination interaction that activated the fluorescence from Tb^{3+} ion.[407] Volatile amines have also been identified through a combined analysis of the absorbance color and fluorescence color of a specially synthesized BODIPY dye.[408]

Examples of smartphone-based PL assays with enzyme-catalyzed fluorogenic reactions include measurement of the activity of β-glucosidase using a fluorogenic substrate,[409] and the detection of glucose in wound exudate through the coupled reactions of glucose oxidase and HRP to convert dichlorofluorescein-diacetate to its fluorescent form.[410]

Arrays of fluorophores have also been used to detect and identify analytes. A paper-based array of poly(arylene ethynylene) fluorophores identified 10 different polyaromatic hydrocarbons through changes in the RGB emission color of the polymers combined with principal component analysis and discriminant analysis.[226] Similarly, an array of six different fluorescent dyes distinguished between five types of amyloid fibrils, including with diluted plasma and artificial cerebrospinal fluid samples, through ML analysis of changes in fluorescence intensity and RGB color.[232]

7.4.2 Fluorescence quenching. Analyte-induced quenching of PL is a common mechanism for laboratory assays and has

Open Access Article. Published on 07 February 2025. Downloaded on 19/4/2026 11:02:09 PM.
This article is licensed under a Creative Commons Attribution-NonCommercial 3.0 Unported Licence.

been adapted to smartphone-based assays. Paraquat (a herbicide) has been detected in authentic water samples through its selective quenching effect on three common and low-cost fluorescent dyes (PTSA, HPTS, or Eosin Y).[411] The implementation was a test cartridge with a handheld UV lamp. Smartphone attachments for cuvettes were developed for an assay based on the quenching of Rhodamine 6G by Hg^{2+} (aq) in field-collected water samples,[412] and for an assay based on the quenching of citrate-cysteine-derived fluorophore by chloride in patient sweat (relevant to cystic fibrosis).[413]

The reactivity of NP materials has also been exploited for the detection of analytes. Examples include the quenching effects of Cu^{2+} (aq) on carbon dots,[414] Hg^{2+} (aq) and S^{2-} (aq) on CdZnTe QDs,[415] Hg^{2+} (aq) on gold nanoclusters,[416] and water in ethanol on perovskite QDs.[417] Quenching of luminescent metal organic frameworks have also been utilized for detection of chlortetracycline in seafood homogenate.[418]

7.4.3 Inner filter effects. Some smartphone-based assays have been developed around inducing or alleviating inner filter effects. These effects do not formally quench fluorescence but rather attenuate the ability of the light source to excite fluorescence and attenuate the ability of the emission to reach the detector. For example, the fluorescence of boron carbon oxynitride QDs was diminished by an inner filter effect from MnO_2 nanosheets, where the production of thiocholine by acetylcholine esterase reductively etched the nanosheets to alleviate the infer filter effect.[419] This format was useful for developing test strips for organophosphorus pesticides (which inhibit the esterase) in soil and water samples. Another approach to minimizing sample interference is headspace analysis, which was implemented with a smartphone-based device for detection of arsenic in well water *via* hydride generation.[420] The gaseous arsenic hydride reacted with Ag^{+} ion impregnated in paper to form AgNPs, which induced an inner filter effect with fluorescent carbon dots deposited on the same paper.

7.4.4 Lateral flow immunochromatographic assays. Analogous to colorimetric LFIAs, PL-based LFIAs have generally adopted competitive formats for small-molecule analytes and sandwich formats for protein analytes. The two main differences are the substitution of AuNPs and other color-only labels by fluorescent materials, and the concomitant increase in technical requirements for readout. Studies have shown that the return on this modest technical investment can be a 10^1–10^2-fold (or more) improvement in the detection limit *versus* an LFIA with AuNPs.[421–424]

Various photoluminescent NPs have been adopted for smartphone-based readout of LFIAs. QDs are one of the more popular materials and have been utilized for the detection of Influenza A nucleoprotein in simulated nasal matrix (LOD ≤ 3 fmol),[421] ciliary neurotrophic factor (biomarker for glaucoma; LOD 6 pg mL^{-1}),[425] and antibodies toward the *Taenia solium* rT24H antigen with samples from patients with neurocysticercosis.[426] Other LFIAs have amplified test-line signals by using silica or polymer particles doped with many QDs. Examples include the detection of PSA in human serum samples (LOD 0.14 ng mL^{-1});[427] interleukin-6,[428] ciprofloxacin (LOD 0.05 ng mL^{-1}),[429] and Zika virus non-structural protein 1 in serum (LOD 0.15 ng mL^{-1}).[430]

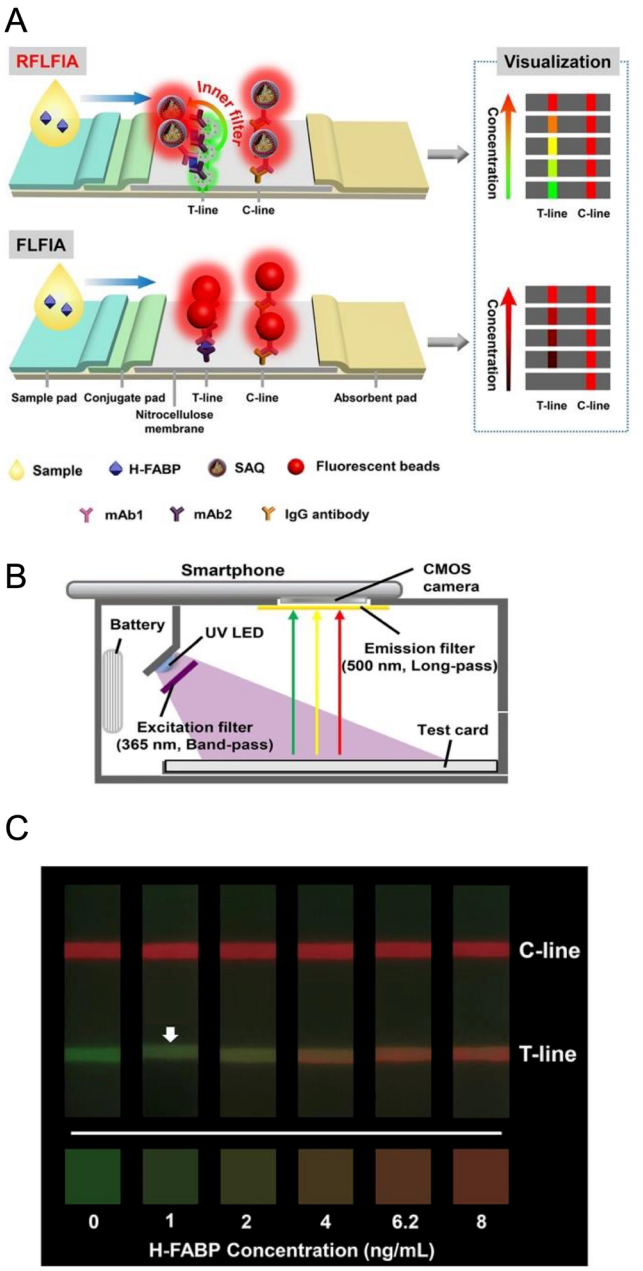

Fig. 26 A ratiometric fluorescence LFIA (RFLFIA). (A) Assay design and comparison to a conventional non-ratiometric fluorescence LFIA (FLFIA). Abbreviations: H-FABP, heart-type fatty acid binding protein; SAQ, silica nanosphere loaded with AuNPs and red-light emitting CdSe/CdS/ZnS QDs; mAb, monoclonal antibody. (B) Smartphone-based device for imaging the RFLFIA. (C) Examples of smartphone images of the RFLFIAs with increasing concentration of the heart-type fatty acid binding protein analyte. Adapted from ref. 432 with permission. Copyright 2021 John Wiley and Sons.

Open Access Article. Published on 07 February 2025. Downloaded on 19/4/2026 11:02:09 PM.
This article is licensed under a Creative Commons Attribution-NonCommercial 3.0 Unported Licence.

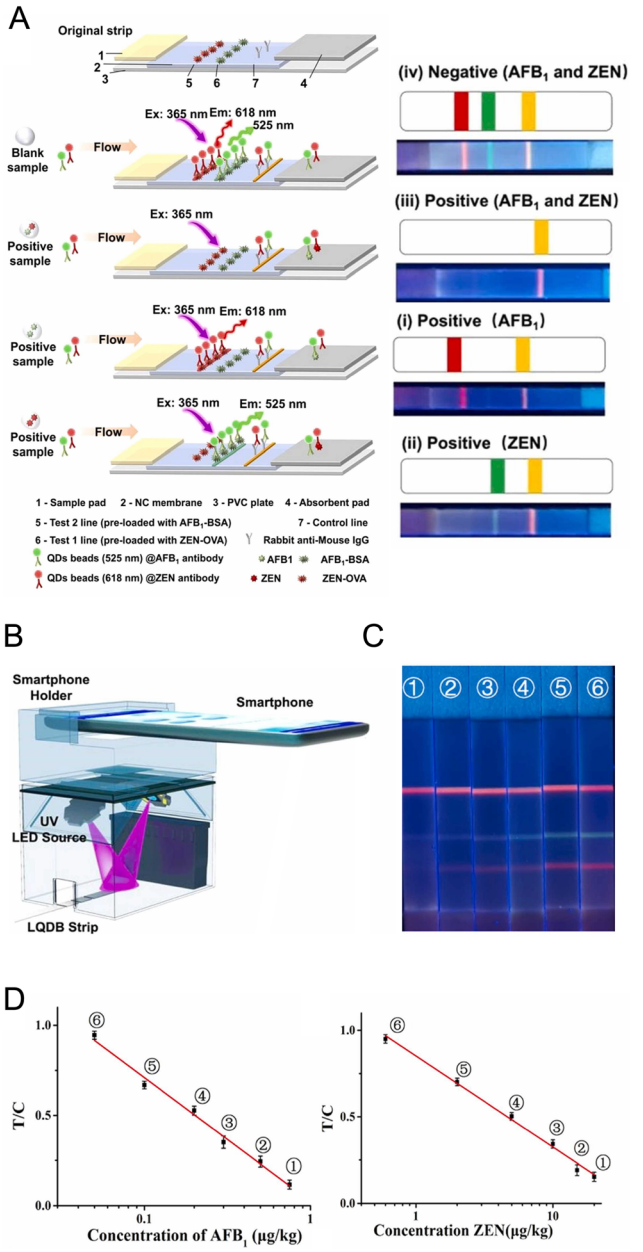

Fig. 27 Two-color, two-line multiplexed competitive LFIA with fluorescence detection. (A) Assay design and smartphone images of assay outcomes. (B) Design of the smartphone-based device used to image the LFIAs. (C) Smartphone images of LFIAs and (D) the corresponding calibration curves for each analyte, aflatoxin B1 (AFB1) and zearalenone (ZEN). The *y*-axis in panel D is the ratio of signal between the test and control lines. Adapted from ref. 78 with permission from Elsevier.

In addition to their high brightness, the spectrally narrow emission of QDs has enabled a novel detection approach for LFIAs: signaling of analyte through a change in the color of the test line rather than a change in its single-color fluorescence intensity. The analyte-induced transition is from green to red QD PL at the test line, with intermediate hues of yellow and orange. This color-changing approach is less dependent on illumination conditions and has better interpretability to the naked eye. It has been adopted for competitive assays of aflatoxin M1 (LOD 1 pg mL^{-1})[423] and benzothiostrobin (LOD < 1 ng mL^{-1}),[431] and for sandwich assays for heart-type fatty acid binding protein (LOD 0.21 ng mL^{-1}; Fig. 26)[432] and the SARS-CoV-2 nucleocapsid protein (LOD 0.1 ng mL^{-1}).[433] Beyond QDs, there is also an example of this strategy with red-fluorescent ruthenium(II)-complex doped NPs and green-fluorescent gold nanoclusters.[434]

The PL colors of QDs also have potential for multiplexed LFIAs. One strategy has been to use LFIAs with two test lines, either on the same strip (Fig. 27)[78] or on separate arms of a bifurcated membrane,[435] where immunoconjugates of green and red QDs (or QD assemblies) bind to separate lines for capture of each analyte. Because of the spatial separation of the two test lines, two different immunoconjugates of a single color of QDs would still be useful for these assays, albeit that the potential benefit from two colors is redundancy to guard against non-specific binding to the wrong test line. A format where the two analytes are captured on the same test line requires the two distinct colors of QD and a color-based analysis, as was the case for an LFIA of free and complexed forms of PSA.[436]

Many other luminescent NPs have been adopted in LFIAs. Polymer microspheres and nanoparticles doped with Eu(III) complexes were used as labels to detect thyroid stimulating hormone in diluted serum (LOD 0.02 μIU mL^{-1});[422] lung-cancer relevant plasma extracellular vesicles (LOD 10^5 mL^{-1});[437] ochratoxin A in wheat samples (LOD 0.32 μg kg^{-1});[438] Hepatitis B virus in serum samples;[439] and five different classes of mycotoxin, spanning 20 individual compounds, with a five-line LFIA.[440] Latex NPs conjugated with phycocyanobilin have also been utilized for LFIAs,[80] and lanthanide-doped UCNPs were labels to detect ochratoxin A, Hg^{2+} (aq), *Salmonella*, hepatitis B virus nucleic acids, and protein ST-2,[441] as well as C-reactive protein (LOD 0.05 ng mL^{-1}).[442] Two-color two-test-line LFIAs have also been demonstrated with Er^{3+} (green) and Tm^{3+} (blue) emitters for PSA and ephrin type-A receptor 2 (EphA2),[443] and for brain natriuretic peptide and suppression of tumorigenicity 2 antigen in serum.[444] PLNPs have been adopted for LFIAs of hCG (LOD 45 pg mL^{-1}),[35] 17β-estradiol in milk,[445] and T-2 toxins (0.025 ng mL^{-1}) in food samples,[446] plus two-test-line LFIA with green and blue colors for PSA and hCG.[447] Other examples of materials include a red-emitting gold nanocluster-doped zeolitic imidazolate framework as a label in an LFIA of olaquindox (LOD 2.5 μg L^{-1}),[448] and AIEgen-doped MOF as a label in an LFIA of aflatoxin B1.[449]

Any comparisons of analytical performance between different luminescent NPs will need to account for differences in excitation intensity and detection efficiencies between different smartphone-based devices. The most reliable comparisons will be head-to-head with the same device, and there are few instances of such studies in the literature.

7.4.5 Nucleic acid amplification tests. The measurement of nucleic acid targets (*e.g.* DNA and RNA) is of great interest for diagnostic testing because of the specificity. The overhead

Open Access Article. Published on 07 February 2025. Downloaded on 19/4/2026 11:02:09 PM.
This article is licensed under a Creative Commons Attribution-NonCommercial 3.0 Unported Licence.

to access this advantage is an amplification method to convert low amounts of endogenous nucleic acid in a sample into a detectable amount. In some cases, this amplification also requires a nucleic acid isolation step.

To date, the majority of published studies on smartphone-based detection of nucleic acids have focused on amplification of the target sequence and detection and quantification of the amplified targets. As such, sample preparation has tended to follow standard laboratory protocols using commercial kits for nucleic acid extraction, and mixing of sample with the reagent cocktails required for reverse transcription (for RNA targets) and the amplification method of choice. Only a few studies have streamlined the sample processing steps alongside smartphone-based detection. One unique approach used a patch-like microneedle array (made from polyvinyl alcohol) to extract RNA by pressing it onto a plant leaf and releasing the RNA by simple rinsing of the array with buffer.[450] The extracted RNA was ultimately used to detect plant infections, including *Phytophthora infestans* and tomato wilt virus (LOD of 1 pg; Fig. 28). With similar simplicity, hepatitis C viral DNA (LOD 5 pmol) was detected in clinical samples without an amplification step using a folded paper test square with immobilized peptide nucleic acid probes and an absorbent pad underneath.[451] Sample was added, washed, and fluorescently stained in successive steps that consisted of dropping microliters of solution onto the test square. These examples highlight how user actions can be simplified and minimized, to various degrees, despite the frequent requirement for numerous reagents and multiple steps in a nucleic acid analysis that goes from sample to answer.

With respect to amplification, polymerase chain reaction (PCR) coupled with a fluorescence detection method is the gold standard for nucleic acid diagnostics. This amplification method requires that thermocycling be implemented in a portable device. One approach to both conventional and digital PCR with smartphone-based fluorescence detection is reproduction of the classic temperature programming of PCR *via* a Peltier (*i.e.* thermoelectric) module, as done for the detection of the CD147 gene and cancer biomarker.[94] Convective thermocycling PCR, whether separate[435,452] or interfaced[453] with the detection device, has been an alternative approach that enables a heating element to be maintained at a constant temperature. It has been utilized with smartphone-based devices to detect lambda DNA (LOD 3000 copies),[452] genes diagnostic of methicillin-sensitive and methicillin-resistant *Staphylococcus aureus* (LOD 5000 copies),[435] and influenza A (H1N1) virus (LOD of 1 tissue culture infectious dose per mL).[453]

Another implementation that utilizes a heater at fixed temperature is continuous flow PCR, where, for example, one face of a trigonal helix of sample-carrying tubing was in contact with a constant-temperature heater to produce alternating hot and warm temperature zones that functioned for thermocycling.[454] Another example doped the PDMS of a microfluidic chip with gold nanorods for photothermal heating under illumination from an 808 nm laser.[91] Thermocycling arose from a circular geometry from a serpentine channel that moved in and out of the hot zone produced from the radial intensity profile of the laser spot. In these two examples, the analytes were H7N9 avian influenza DNA (LOD 10^4 copies per μL) and hepatitis B virus DNA (LOD 12 copies per μL, 40 min assay time).[91] From the

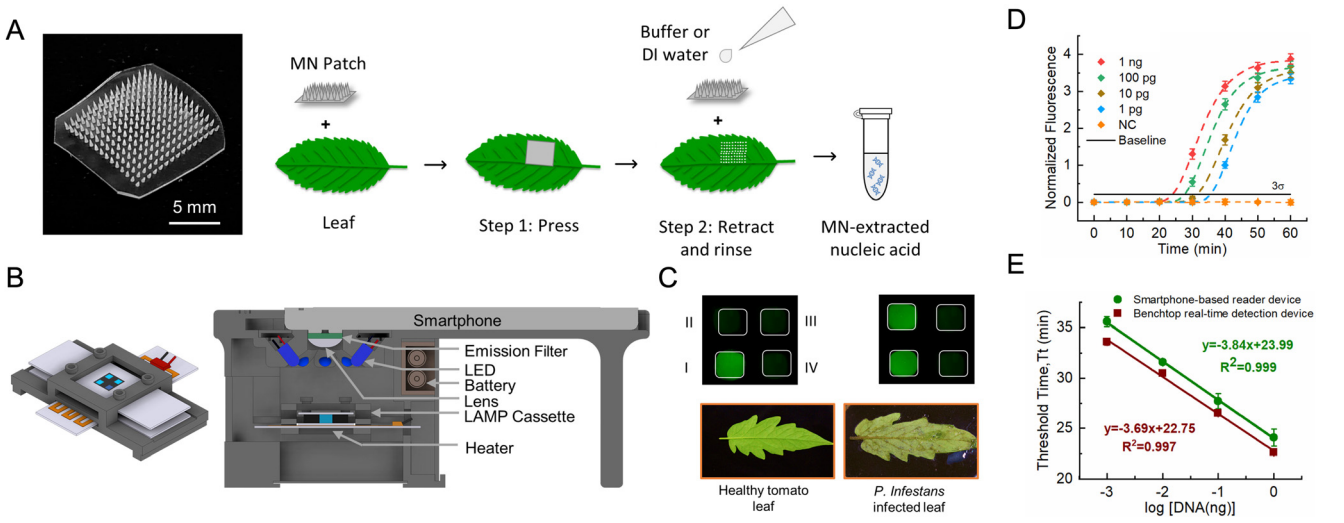

Fig. 28 Microneedle extraction of nucleic acid and on-chip LAMP with smartphone-based detection. (A) Photograph of a microneedle (MN) patch and work flow for the nucleic acid extraction. (B) Schematic of the LAMP sample cassette and cross-sectional view of smartphone-based reader device. (C) Representative smartphone fluorescence images of the parallel LAMP assay chip (top) for different nucleic acid sequences (I–IV) and photographs of healthy and infected leaf samples (bottom). (D) Real time amplification curves for *P. infestans* DNA obtained *via* the smartphone-based LAMP platform. (E) Comparison between the smartphone device and a conventional laboratory instrument. Adapted with permission from ref. 450 Copyright 2021 Elsevier B.V.

Open Access Article. Published on 07 February 2025. Downloaded on 19/4/2026 11:02:09 PM.
This article is licensed under a Creative Commons Attribution-NonCommercial 3.0 Unported Licence.

standpoint of device engineering, the difference between temperature programming and oscillating sample along a temperature gradient is minimal. Both formats regulate temperature using feedback from an integrated temperature sensor. Temperature programming devices more frequently add a cooling fan, but more readily accommodate array-based multiplexing since samples can be compartmentalized in a small area.

As an alternative to the thermocycling of PCR, loop-mediated isothermal amplification (LAMP) methods are frequently paired with smartphone-based detection. Some reported smartphone-based devices have had integrated heaters to obtain the 60–65 °C typical of the method,[450,455] another device had a distinct compartment dedicated to the heating step of the assay,[456,457] and some assays have relied upon benchtop heating instruments.[456–458] Analytes were lambda DNA (LOD 1 copy per μL),[458] SARS-CoV-2 RNA (LOD 10 copies per μL, 60 min assay time),[456] and human papillomavirus (HPV; 30 min assay time).[457] Another common isothermal method (normally 37–42 °C, less efficient at room temperature) is recombinase polymerase amplification (RPA). Examples of targets amplified by RPA have included HIV-1 RNA (LOD 67 copies), where a consumer coffee warming device was used as the heater,[459] and HIV and hepatitis B genes (LOD 1000 copies per mL).[81] The latter example was a small-scale suspension array that used the smartphone camera to recognize QD-doped bead colors corresponding to specific nucleic acid targets. Many other targets have also been measured through pairing of RPA with CRISPR/Cas signal amplification (*vide infra*).

Nearly all smartphone-based PL assays for nucleic acid detection have used fluorescent dyes for signal generation. Fluorescein is widely used as a dye label on oligonucleotide primers and reporters, likely due to is combination of low cost and high brightness relative to other dyes, optimal excitation by widely available blue LEDs, and green emission that overlaps well with the G channel response of smartphone cameras. Alexa Fluor 647 has also been utilized for its compatibility with orthogonal interrogation with QD-based microbead barcodes for optically multiplexed detection of DNA associated with infectious diseases such as human immunodeficiency virus (HIV) and hepatitis B and C (Fig. 29).[81] Alternatively,

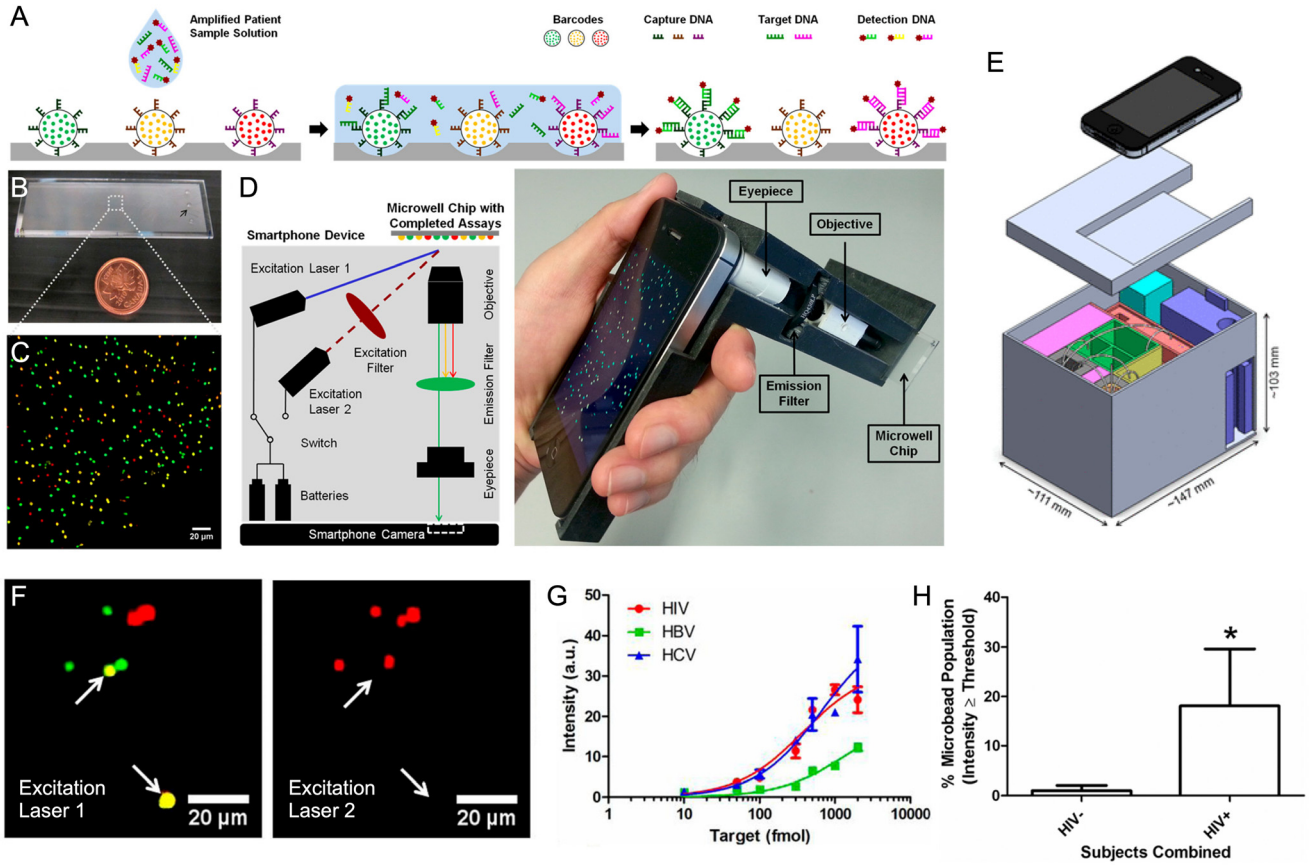

Fig. 29 Portable device for amplification and suspension-array-based detection of nucleic acid sequences. (A) Barcode detection of target DNA from patient samples by quantum dots. (B) Typical microwell chip containing different barcodes in each well. (C) Smartphone camera captures the image of four different quantum dot barcodes arrayed on the surface of the chip. (D) Schematic and real images of the smartphone device. (E) Visual representation of the envisioned final device, with the different compartments. (F) Yellow, green, and red barcodes are deposited on the chip and imaged using the device. (G) Sensitivity curves for genetic biomarkers for the blood-borne viruses human immunodeficiency virus (HIV), hepatitis B virus (HBV), and hepatitis C virus (HCV). (H) Comparison between the average combined statistics of all subjects of the HIV-negative group (3 subjects) and HIV-positive group (10 patients). Adapted with permission from ref. 81 Copyright 2015 American Chemical Society.

Open Access Article. Published on 07 February 2025. Downloaded on 19/4/2026 11:02:09 PM.
This article is licensed under a Creative Commons Attribution-NonCommercial 3.0 Unported Licence.

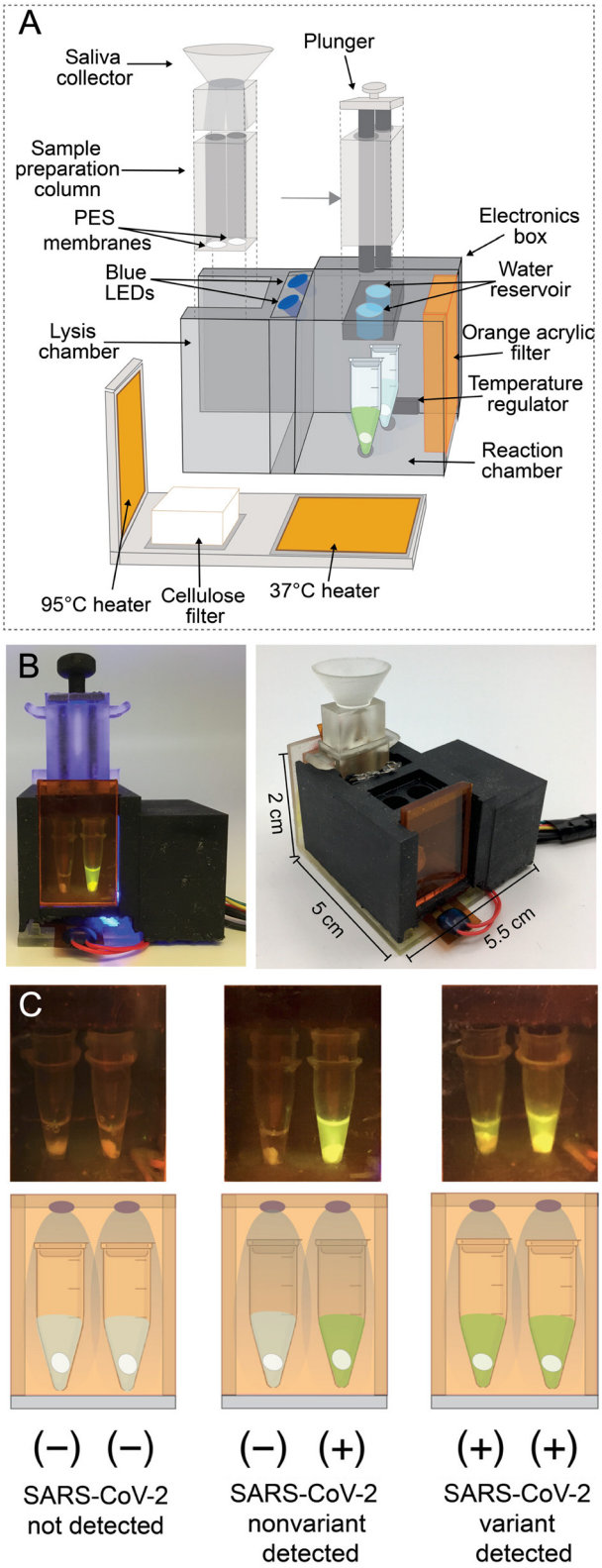

Fig. 30 Sample-to-answer device for CRISPR-based detection SARS-CoV-2 and variant nucleic acids. (A) Design of the device, including sample processing (left) and assay (right) modules. (B) Photographs of the device, which is capable of two-plex detection. (C) Smartphone-acquired fluorescence images of samples. Figure reproduced from ref. 470 under a Creative Commons CC BY 4.0 license.

intercalators and DNA-binding dyes (*e.g.* TB green, EvaGreen, SYBR Green) that switch from dark to bright PL upon interaction with double-stranded DNA have been utilized for readout from both PCR and LAMP amplifications.[450,454,455,460,461]

The smartphone-implemented fluorescence detection methods paired with nucleic acid amplification methods have included commercial TaqMan probes,[94,453] molecular beacons,[462] magnetic pull-down binding assays (PCR, fluorescein, phycoerythtrin),[452,463] and lateral flow binding assays (QDs with PCR;[435] QDs with RCA amp;[41] QDs with RTF-EXPAR, 10 aM, for multiple QDs per target;[464] UCNPs with PCR amplicons[465]). A smartphone-based microchip capillary electrophoresis unit has even been proposed for the detection of fluorescently labeled PCR amplicons.[124]

In several other studies, the target nucleic acid sequence triggers the *trans* cleavage activity of CRISPR/Cas12a or CRISPR/Cas13a to hydrolyze the reporter with loss of FRET and recovery of the dye fluorescence. Fluorescein is by far the most common dye in such fluorophore-quencher reporter systems, although carboxyrhodamine (ROX), carboxytetramethylrhodamine (TAMRA), and cyanine 5 (Cy5) have also been adopted. Examples of assays have included the detection of genes diagnostic of African Swine fever virus (LODs of 8 copies per μL),[466,467] Frog virus 3 (LOD 10 aM),[468] and SARS-CoV-2 (LOD 100 copies per μL).[469] Although these examples utilized a standard lab-based nucleic acid extraction, another study reported a small and low-cost device for simple isolation of RNA from saliva samples in one step and detection in a second step (Fig. 30).[470] The first step isolated RNA on a polyethersulfone (PES) membrane disc with pre-loaded lysis reagents and provided 95 °C heat for inactivation of nucleases. The second step transferred the membranes to a reaction chamber that was pre-loaded with freeze-dried assay reagents and provided 37 °C heat for RPA and Cas-mediated detection (LOD 1000 cp per mL; 60 min assay time).[470] Alternatively, multiple CRISPR/Cas methods reported for the detection of SARS-CoV-2 have returned results without extraction from patient samples, with assay detection limits in range of 100–1000 copies per mL with assay times of 15–50 min.[82,471,472] One such method used a laser-based smartphone device for readout of fluorescence from fluorophore-quencher reporter oligonucleotides (Fig. 31).[82]

Whereas the foregoing studies combined CRISPR/Cas12a with RPA, another approach has relied only on the signal amplification intrinsic to the multiple turnover capability of Cas12a for the detection of genes diagnostic of hepatitis B virus and HPV (LODs of 200 pM for a conventional assay and 5 fM as a digital assay).[473] Other signal amplification approaches for smartphone-based assays have included the hybridization chain reaction for detection of cancer relevant miRNA-224 from plasma,[474] Exo-III-assisted amplification for detection of miRNA-155 (LOD 42 aM), 16S rRNA of *S. aureus* (LOD 18 CFU mL^{-1}), and a gene from COVID-19 pseudovirus RNA (LOD 87 copies per μL).[475]

This journal is © The Royal Society of Chemistry 2025

Open Access Article. Published on 07 February 2025. Downloaded on 19/4/2026 11:02:09 PM.
This article is licensed under a Creative Commons Attribution-NonCommercial 3.0 Unported Licence.

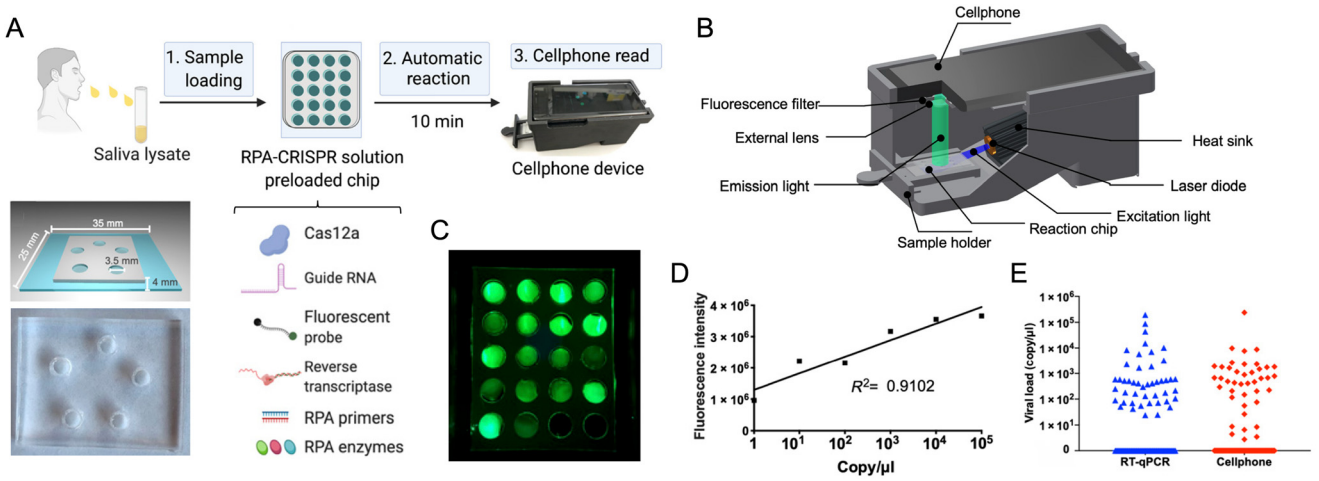

Fig. 31 CRISPR/Cas method for detection of viral RNA from SARS-CoV-2. (A) Workflow of the assay. (B) Design of a smartphone-based fluorescence reader. (C) Smartphone-acquired image of fluorescence from a multi-well chip preloaded with assay reagents. (D) Calibration curve for measured fluorescence intensity *versus* the copy number of viral RNA. (E) Comparison of results between the smartphone-based device and RT-qPCR as a standard laboratory method. Figure reproduced from ref. 82 under a Creative Commons CC BY 4.0 license.

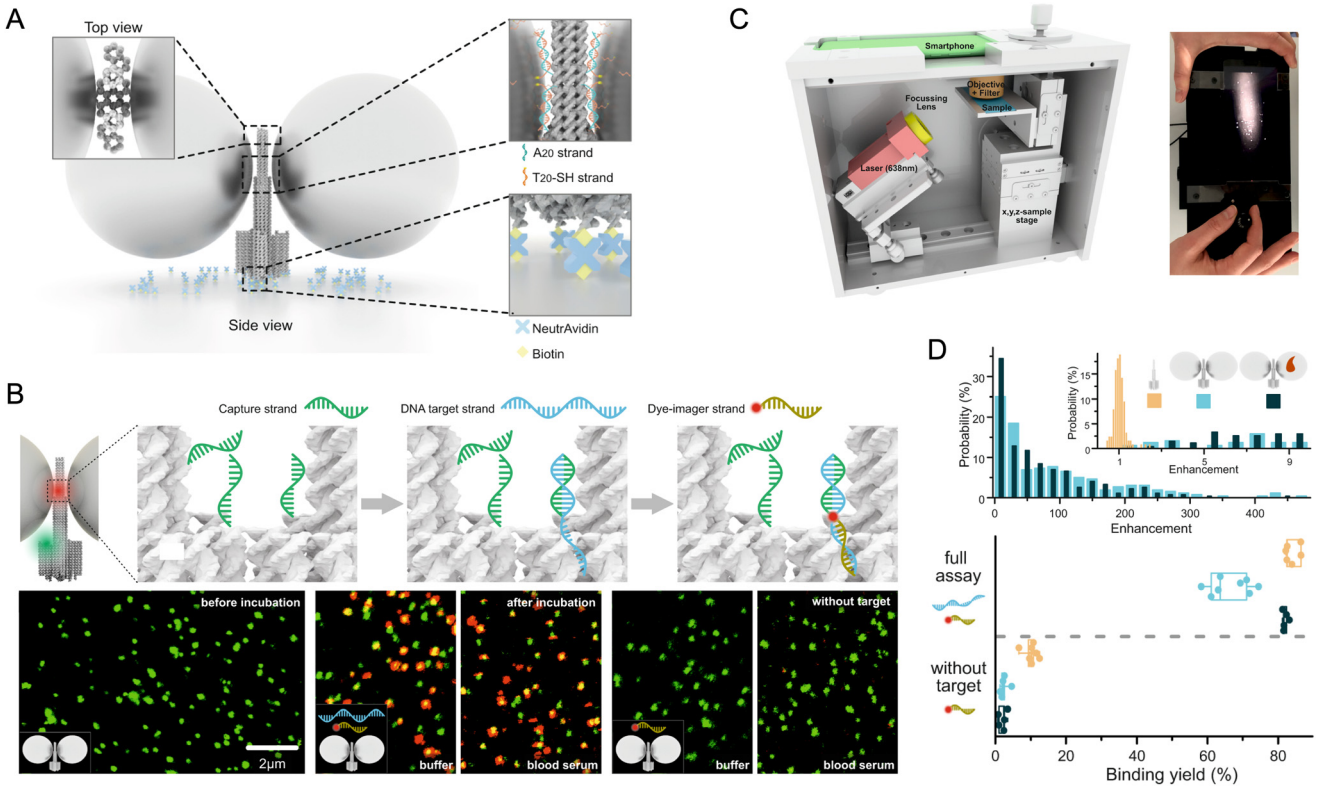

Fig. 32 Single-molecule fluorescence detection on a smartphone using plasmonic nanostructures for metal-enhanced fluorescence. (A) Schematic of the DNA–silver NP nano antennas with cleared hot spots (NACHOS). (B) Diagram (top) and confocal fluorescence images (bottom) images of the NACHOS with three capture strands in the hotspot and a green-fluorescent reference dye for labeling of the DNA origami. (C) Diagram of the portable smartphone-based microscope (left) and a photograph of the display during imaging (right). (D) Top: Fluorescence enhancement histogram of the sandwich assay in buffer solution (light blue) and in serum (dark blue). Bottom: Binding yield obtained for the full sandwich assay with and without added DNA target. Figure reproduced from ref. 83 under a Creative Commons CC BY 4.0 license.

The predominant use of fluorescent dyes for detection likely arises from four considerations: the widespread commercial availability of dye-labeled oligonucleotides; status as the gold-standard class of material for fluorescent labeling in lab-based nucleic acid assays; tolerance of dye labels by the enzymes leveraged for nucleic acid amplification and hydrolysis; and, in some cases, intrinsic sensitivity of dye fluorescence to nucleic acid structure.

Open Access Article. Published on 07 February 2025. Downloaded on 19/4/2026 11:02:09 PM.
This article is licensed under a Creative Commons Attribution-NonCommercial 3.0 Unported Licence.

Likewise, these considerations almost certainly underlie the almost uniform adoption of homogeneous solution-phase assay formats. Alternative fluorescent materials such as QDs have a higher ceiling for sensitive detection, but their productive combination with relevant enzymes—though possible, including in the context of smartphone-based nucleic acid detection[476] (amplification-free LOD of 50–100 pM)—is not as turnkey as it is for dyes. Nucleic acid assays with QDs are therefore more likely to be in the form of post-amplification binding assays that require wash steps, albeit avoidable with a lateral flow format, as demonstrated for the detection of DNA from methicillin-resistant *S. aureus* (LOD 4700 copies post-convective PCR).[435] Perhaps the best aspiration for ultra-bright fluorescent NPs is the amplification-free detection of clinically-relevant amounts of target nucleic acid with a smartphone device. A study has already demonstrated that plasmonic DNA nanostructures with silver NPs—in conjunction with a high numerical aperture objective and an atypically powerful (180 mW) laser diode—enable single-molecule fluorescence detection in DNA hybridization assays with a smartphone camera (Fig. 32).[83] Fluorescent NPs have the opportunity to lower the technical requirements for such performance.

7.4.6 Cytometry and microscopy. As with colorimetric detection, methods have been developed for quantifying bacteria *via* their metabolic activity without direct imaging of individual cells. Resazurin dye will change from weakly fluorescent to red fluorescent with cell metabolism, enabling digital detection with limiting dilution of a sample and imaging of a microcapillary array (LOD 10 CFU mL^{-1}).[361] Similarly, the intensity of blue fluorescence from methylumbelliferone, which is the product from the turnover of methylumbelliferyl-beta-D-glucuronide by the beta-D-glucuronidase (GUD) enzyme secreted by multiple strains of *E. coli*, has been used to quantify these bacteria.[477] In another example, fluorescent derivatives of alanine (blue-emitting coumarin dye), *N*-acetylglucosamine (green-emitting fluorescein), and *N*-acetylgalactosamine (orange-emitting Rhodamine B) were prepared for metabolic incorporation into growing bacteria.[478] Unique RGB fluorescent fingerprints were obtained for different bacterial species. The method was applied to the analysis of pus from a mouse model of skin infection (LOD 10^5 CFU per mouse) and, *via* the connection with mouth microbiota, distinguishing oral squamous cell carcinoma from precancerous and healthy cases from human clinical saliva samples.

Fluorescence detection has also been used for the imaging and counting of individual cells. Unlike brightfield microscopy, cell staining is a requirement for these measurements. Nuclear (*i.e.* DNA) stains are one of the most common methods for generating fluorescence contrast from cells. Examples include the use of SYTO16 for imaging (with[174] and without[479] ML analysis) of leukocytes extracted from human blood, and acridine staining for both total and differential white blood cell counts from blood samples (where the differential count used an R/G ratio in image analysis to distinguish between granulocytes and agranulocytes).[480] Other fluorescent stains have included Calcofluor White M2R and Solophenyl Flavine 7GFE 500 for the selective staining of *Nosema* spores in honey bee midgut samples (LOD 5×10^5 spores per bee),[481] Calcofluor White or Blankophor for proof-of-concept imaging of cultured dermatophytes,[482] and a newly-synthesized dye for staining microplastic particles.[97]

Fluorescent immunolabeling is also a viable approach to cell detection with smartphone-based microscopy. A compact clip-on device was designed for smartphone microscopy *via* ultraviolet surface excitation, demonstrating two-color imaging of brain tissue slices using an Alexa Fluor 488-labeled antibody (green fluorescence) and propidium iodide nuclear stain (red fluorescence), and was also suitable for imaging a combination of DAPI (blue) and Rhodamine B (orange) staining of tissue (Fig. 33).[483] A much larger 3D-printed benchtop microscope was used for imaging *T. cruzi* parasites stained with fluorescein-conjugated antibodies.[484]

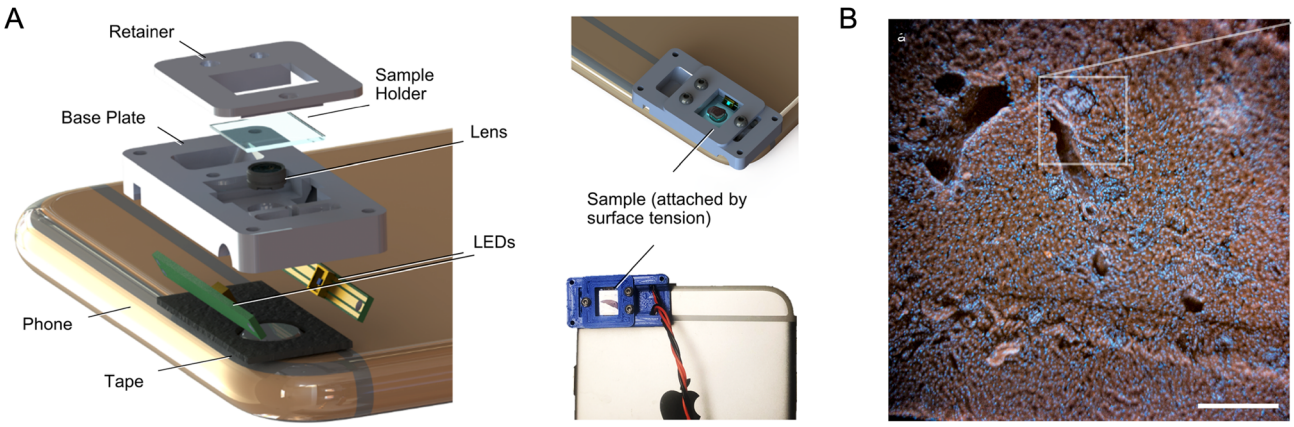

Fig. 33 Compact smartphone mounted microscope. (A) Design of the microscope attachment, which uses ultraviolet surface excitation. (B) Fluorescence image of a mouse kidney section stained with rhodamine B and DAPI dyes. Figure adapted from ref. 483 under a Creative Commons CC BY 4.0 license.

Open Access Article. Published on 07 February 2025. Downloaded on 19/4/2026 11:02:09 PM.
This article is licensed under a Creative Commons Attribution-NonCommercial 3.0 Unported Licence.

As much as QDs have been superior labels *versus* dyes for smartphone imaging, nanoscale assemblies of many QDs have outperformed individual QDs. For example, immunoconjugates of both supra- and super-particle assemblies of QDs have been developed for cell detection and imaging with smartphone-based devices. In one study, assemblies of magnetic particles and QDs were used for immunomagnetic isolation and fluorescent labeling of a target breast cancer cell line, which was then imaged and counted in a simple plastic chamber slide (Fig. 34).[84] Supra-QD assemblies with a silica NP scaffold have also been used for cell immunolabeling and imaging, providing an order of magnitude signal enhancement over conventional QDs with smartphone-based devices (Fig. 35A–D).[485] All these materials also utilized tetrameric antibody complexes, which enabled spontaneous immunoconjugation with speed and efficiency suitable for chemistry-free on-demand preparation. The supra-QD materials were further adopted for immunofluorescent flow cytometry (Fig. 36).[85] The high brightness of the materials provided the sensitivity necessary for the detection of cell-surface antigens with video rate imaging. A subsequent study showed that designer colors of supra-QD were able to be prepared from mixtures of R-, G-, and B-emitting QDs, with the potential for machine-learning-assisted detection of up to 14 colors with a smartphone camera (Fig. 35E).[223] The next generation of labels are super-particle assemblies, which may provide even larger signal enhancements than supra-QDs (Fig. 35F).[486]

Many of the devices used for cytometry and microscopy have been custom designs made *via* 3D printing with simple lens sets or conventional microscope objectives for magnification. Alternatively, there are several examples of smartphone imaging with commercially available microscope attachments for a smartphone. In each case, commercial dye-doped polymer nanoparticles were used for imaging assays of analytes such as cellular CD56 antigen expression,[487] bacteria (non-selective),[488] norovirus,[172,489] ROR1-antigen-positive cancer cells,[490] SARS-CoV-2,[491] α-amanitin mushroom toxin,[492] tetrahydrocannabinol,[493] and *B. burgdorferi* antigen (the marker for Lyme disease).[494] The assay format and details of the measurement and analysis varied between analytes, but generally involved a simple wax-patterned paper substrate and direct or indirect counting of cells labeled with the polymer nanoparticles, analyte-induced aggregates of the polymer nanoparticles, or particles bound in a test zone.

Time-gated imaging leverages luminophores with long PL lifetimes to insert a time delay between an excitation pulse and imaging. It differs from persistent luminescence in that the timescale is only microseconds to milliseconds, but has the same effect of eliminating background from excitation light and autofluorescence. Time-gated imaging has been implemented with smartphones using motor-driven choppers. One design used a single chopper, an optical switch component, and other electronics to enable excitation pulses and time-gated imaging, including proof-of-concept imaging of a Eu(III) chelate on a mouse tissue section (using the smartphone in tandem with an FPGA),[495] and for

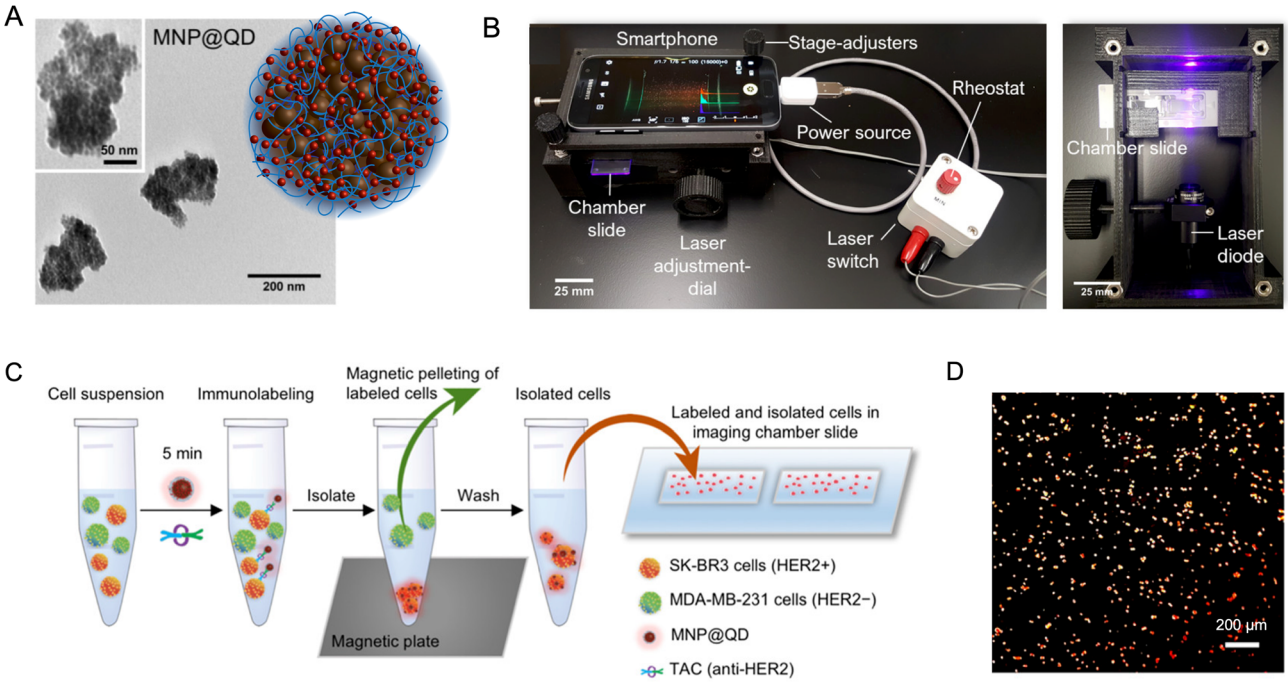

Fig. 34 Magnetic NP-QD assemblies for cellular isolation, imaging and enumeration with a smartphone-based device. (A) Cartoon and TEM of cluster-like assemblies of iron oxide magnetic NPs and QDs (MNP@QD). (B) Exterior and interior photographs of the smartphone-based device used for cell imaging. The laser diode is powered by the smartphone battery. (C) Workflow for cell isolation. (D) Processed smartphone PL image of isolated target cells for counting. Figure adapted with permission from ref. 84 Copyright 2019 American Chemical Society.

Open Access Article. Published on 07 February 2025. Downloaded on 19/4/2026 11:02:09 PM.
This article is licensed under a Creative Commons Attribution-NonCommercial 3.0 Unported Licence.

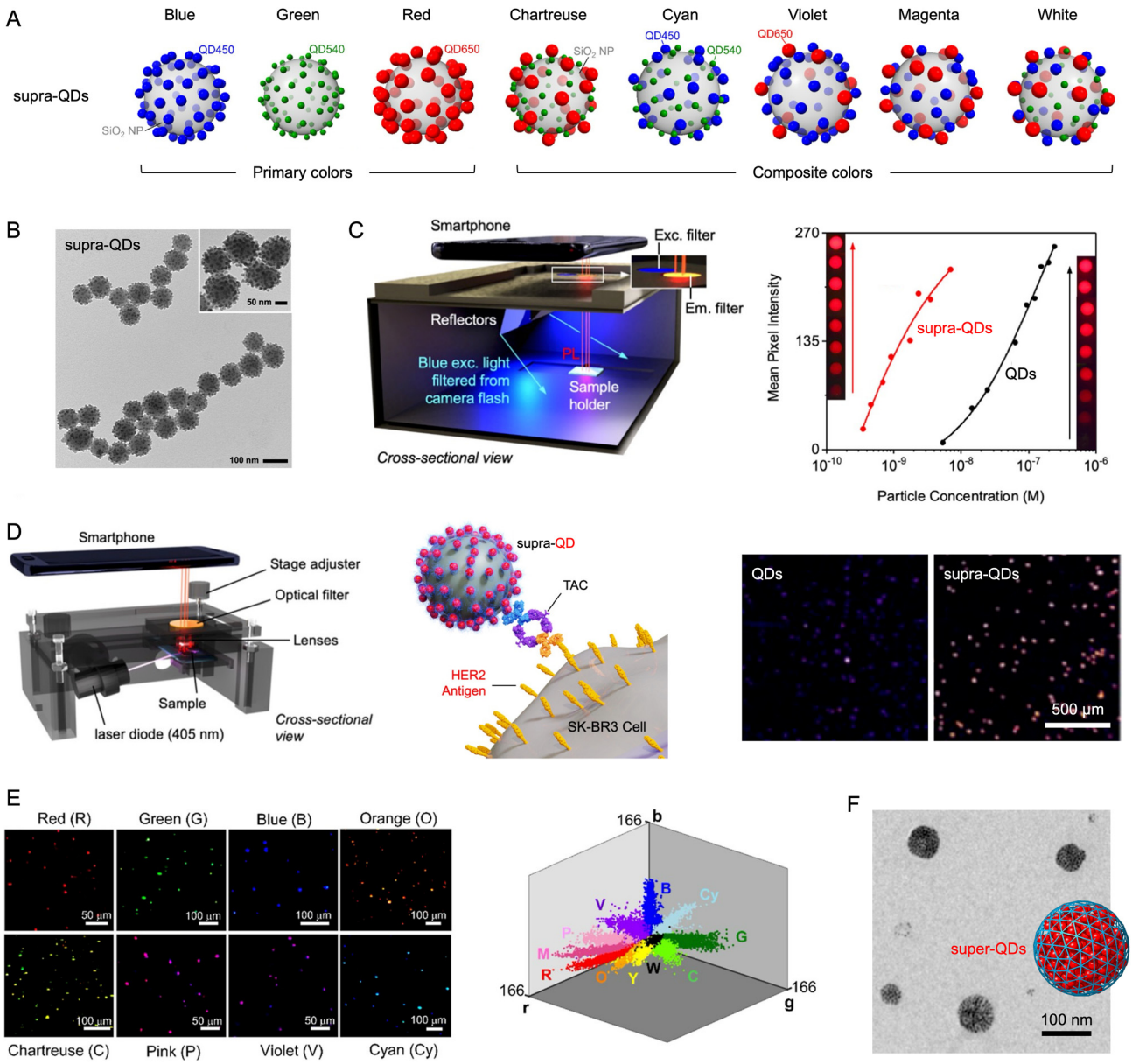

Fig. 35 QD-based assemblies for cellular imaging and enumeration with smartphone-based devices. (A) Illustrations of supra-QD assemblies prepared with QDs that emitted primary colors of PL (RGB). Supra-QDs with composite colors of PL are prepared with mixtures of primary-color emitting QDs on the same silica NP scaffold. (B) TEM image of supra-QDs. (C) Rendering (left) of a smartphone-based device that uses blue light filtered from the smartphone flashlight to excite PL. With this device, the supra-QDs provide an order of magnitude increase in detection limit (right). (D) Smartphone-based device with laser-diode excitation of PL from labeled cells in a plastic chamber slide (left). Diagram of TAC-based immunolabeling of the cells (middle). Cells labeled by supra-QDs are far brighter in smartphone images than the cells labeled with QDs. (E) Smartphone images of cell-sized objects labeled with primary and composite colors of supra-QD (left). Each color maps out a trajectory in the RGB color space (right). (F) TEM image and diagram of super-QDs, which are recently developed as potentially brighter successor material to supra-QDs. The internal volume of super-QDs is made up of many individual QDs. Panels A and E are adapted with permission from ref. 223 Copyright 2023 American Chemical Society. Panels B–D are adapted with permission from ref. 485 Copyright 2020 American Chemical Society. Panel F is adapted with permission from ref. 486 Copyright 2023 American Chemical Society.

detection of tetracycline directly in 50% milk samples (using an analog circuit).[496] As a fully mechanical alternative, two coaxial and out-of-phase choppers, with timing controlled by the rotation speed, were used for time-gated imaging of cells non-specifically stained with a Tb(III) complex, and for proof-of-concept of a time-gated FRET sensor for a target DNA oligonucleotide (Fig. 37).[150] The same study demonstrated that nanomolar and picomolar levels of detection of Tb(III) complexes and Eu(III)-doped NPs were possible in serum, and that quantitative two-color multiplexing of Tb(III) and Eu(III) complexes was possible using both the RGB color channels of the smartphone and two different chopper rotation speeds that exploited the difference in PL lifetime between the two complexes.

Open Access Article. Published on 07 February 2025. Downloaded on 19/4/2026 11:02:09 PM.
This article is licensed under a Creative Commons Attribution-NonCommercial 3.0 Unported Licence.

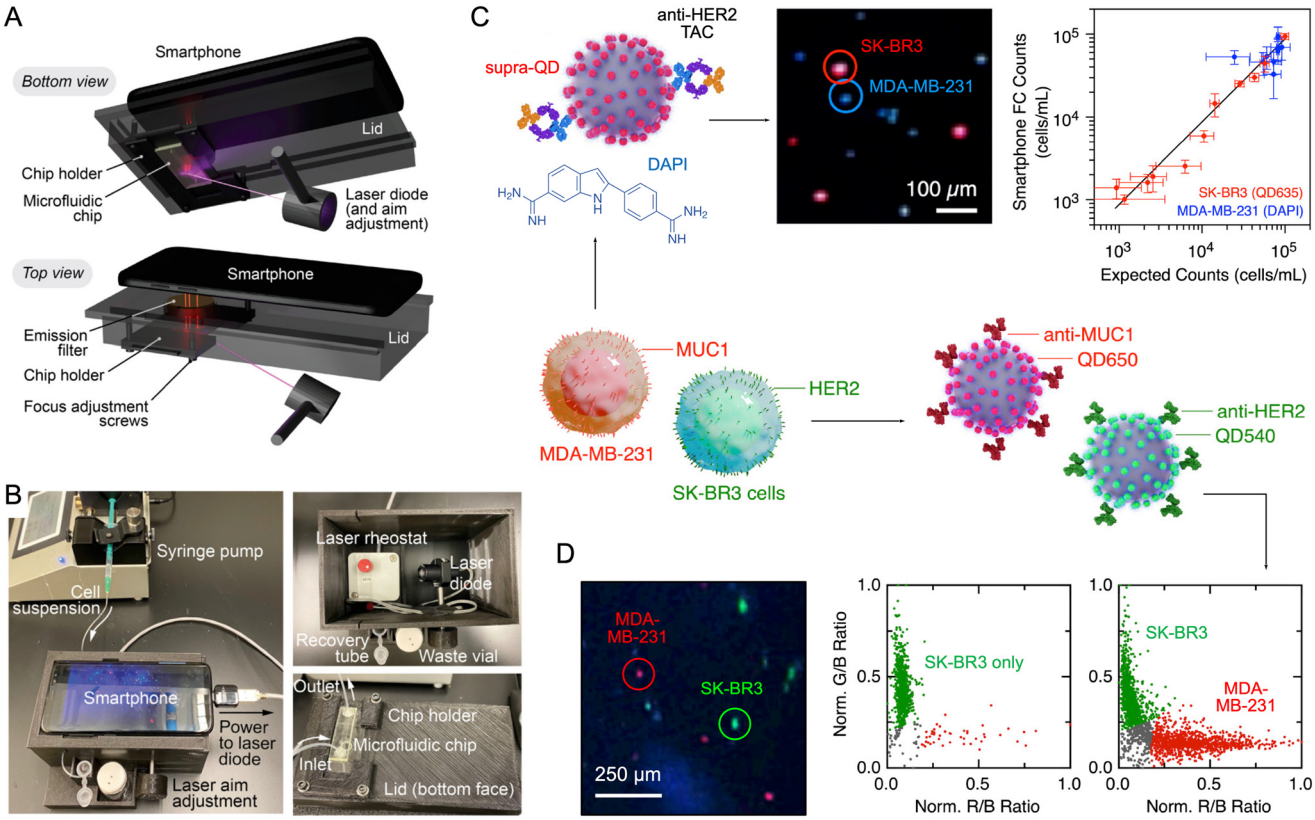

Fig. 36 Smartphone-based flow cytometry with immunofluorescent detection *via* supra-QDs. (A) Design and (B) photographs of the device. (C) Non-selective labeling of all cells (including non-target MDA-MB-231) with DAPI nuclear stain and immunolabeling of target cells (SK-BR3) with supra-QDs. An example of a zoomed smartphone image (left) is shown alongside validation of cell counting data (right). (D) Two-color immunolabeling of two cell lines (SK-BR3 and MDA-MB-231) using two different colors of supra-QD immunoconjugates. A zoomed smartphone image (left) is shown alongside flow cytometry data (right) for samples with a constant quantity of SK-BR3 cells, without and with MDA-MB-231 cells. Figure adapted from ref. 85 under a Creative Commons CC BY 4.0 license.

Non-mechanical approaches to time-gating with smartphones have been developed as well. One platform used an Arduino MCU to control the timing of excitation pulses and image acquisition with a smartphone camera.[497] An extra layer of background suppression was implemented through the use of upconversion PL excited by a NIR laser. A mixture of UCNP-antibody conjugates (anti-EpCAM, anti-CD44, and anti-Trop2) were used to stratify clinical cervical cell samples into high-risk, low-risk, and benign categories. In another study, a virtual chopper design (*i.e.* no physical chopper) for time-gated imaging with a smartphone was reported.[498] An LED was pulsed while a video was recorded by the phone, after which a convolutional NN reconstructed the video frames into an order that represented the PL decay of Eu(III) phosphors.

7.4.7 Spectrometers. Smartphone-based fluorescence spectrometers have generally been designed to accommodate cuvettes and have many similarities to their absorption spectrometer counterparts.[499–502] Indeed, some devices are able to do both types of measurements through orthogonal illumination axes, using the camera (in sequence) for both types of measurements.[499,502] Another design utilized the smartphone camera for fluorescence spectra and the smartphone ALS for non-spectral photometric of sample absorbance.[503] For fluorescence, the excitation axis is orthogonal to the light collection axis, where the excitation source has been a UV (long-wave, 355–375 nm peak)[499,500,502] or blue (450 nm)[502] LED, or a laser pointer (*e.g.* green, 532 nm).[501] Dispersive elements have been DVD fragments as transmission gratings, higher-grade transmission[500,501,504] and reflection gratings,[505] and G-Fresnel transmission gratings that also function as a lens.[215] Time-gated luminescence spectra from a Eu(III) chelate have also been measured using the aforementioned single chopper and electronic optical switch design.[505]

Smartphone fluorescence spectrometers are most likely to be useful in situations where spectral information is valuable, such as analyzing tissue autofluorescence, separating background autofluorescence from analytical signal, and multiplexing with more than three spectrally narrow emitters. Cuvette-based assays with a single dye, such as proof-of-concept detection of a miR-21 target as a potential biomarker for cardiovascular disease, are interesting but do not practically need a spectrometer.[501] In contrast, a smartphone-based endoscope for analyzing the auto-fluorescence of cervical tissue did require spectral resolution.

Open Access Article. Published on 07 February 2025. Downloaded on 19/4/2026 11:02:09 PM.
This article is licensed under a Creative Commons Attribution-NonCommercial 3.0 Unported Licence.

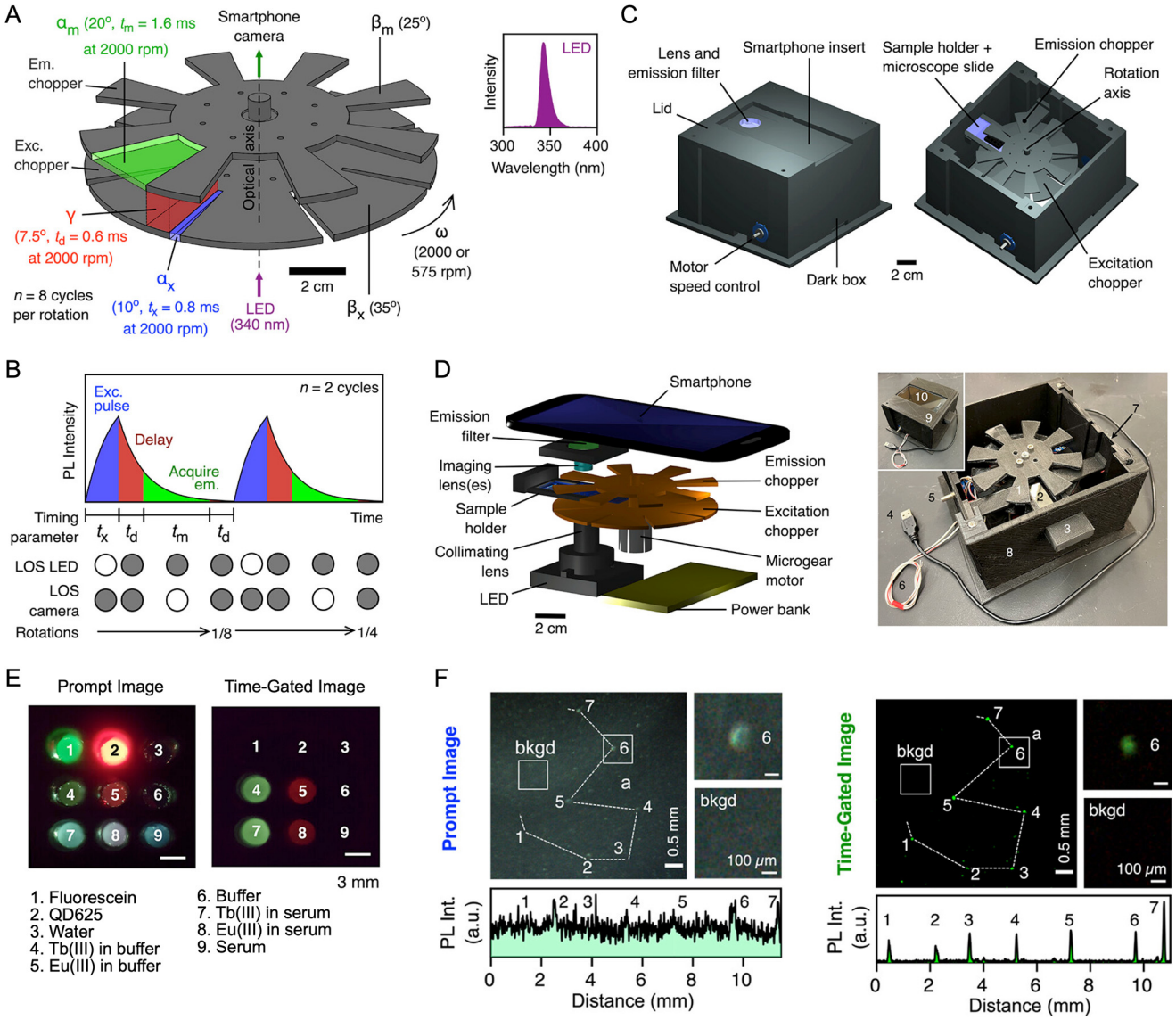

Fig. 37 Smartphone-based time-gated imaging with a dual chopper system. (A) Design of the dual chopper and features that control (B) the timing of excitation pulses, the gate delay, and PL signal acquisition. (C and D) diagrams and photograph of the device abbreviations: exc = excitation; em = emission; LOS = line of sight. (E) Comparison of prompt and time-gated smartphone images of samples with short PL lifetimes (1, 2) and long PL lifetimes (4, 5), and without (3–6) and with (7–9) autofluorescent sample matrices. (F) Prompt and time-gated images of cells stained with a Tb(III) complex with an autofluorescent tissue phantom matrix. Figure adapted with permission from ref. 150 Copyright 2023 American Chemical Society.

The endoscope design was capable of both reflectance-based absorption spectrometry and fluorescence spectrometry, incorporating beam splitters so that two light sources (a white LED and 405 nm laser diode) were able to utilize the same light paths to the sample and camera. Deep learning algorithms with spectral data were used to classify different grades of cervical cancer.[506] A similar design measured diffuse reflectance spectra alongside fluorescence imaging of oral tissues (Fig. 38).[215]

7.5 CL, BL, and ECL analyses

Collectively, CL and BL are the third most common modality for the detection. Mirroring the broader literature on CL assays, the majority of smartphone-based assays utilize luminol and its blue emission. A simple dark box tends to be the only peripheral component of the smartphone-based device. Analytes have included microRNA,[507–510] oligonucleotides and DNA amplicons,[511,512] protein biomarkers,[128,513–518] pathogenic bacteria,[519–521] alkaline phosphatase,[522] drugs,[523] pesticides,[524,525] an explosive,[526] phenolics,[527] mycotoxins,[528,529] catechols,[530] and sugars and other metabolites.[531–533] For the most part, the selective detection mechanism in these assays are nucleic acid hybridization, immunocomplexation, or inhibition or catalysis of the CL reaction.

Many published reports represent proof of concept for smartphone-based CL detection, but have not yet simplified

Open Access Article. Published on 07 February 2025. Downloaded on 19/4/2026 11:02:09 PM.
This article is licensed under a Creative Commons Attribution-NonCommercial 3.0 Unported Licence.

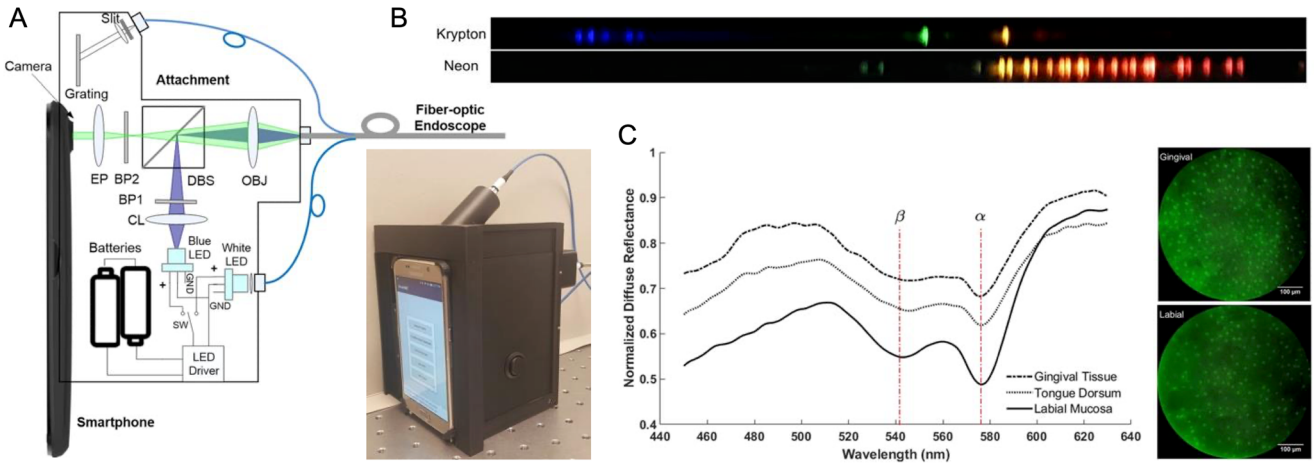

Fig. 38 Smartphone-based spectroscopic endoscope. (A) Diagram and photograph of the endoscope, which is capable of both diffuse reflectance spectroscopy and high-resolution fluorescence imaging. (B) Smartphone images of lamps for wavelength calibration. (C) Reflectance spectra from an *in vivo* study of healthy oral tissue (left) and corresponding fluorescence images (right). Abbreviations: BP, bandpass filter; CL, condenser lens; DBS, dichroic beam-splitter; EP, eyepiece; OBJ, objective lens. Figure adapted from ref. 215 under a Creative Commons CC BY 4.0 license.

the CL assay procedure to a level that is optimal for non-laboratory settings, still requiring users to execute multiple wet chemical or wash steps. One approach to reducing steps has been the adoption of the LFIA format, which ideally reduces the assays to two steps: addition of sample to the sample pad and subsequent addition of a CL or BL reagent to the test line zone. Such LFIAs have been developed for the detection of SARS-CoV-2 with bis(2,4,6-trichlorophenyl) oxalate "glowstick" chemistry with dye-doped NPs,[534] and luminol with a peroxidase enzyme[535] or mimic.[514] A CRISPR/Cas13a-coupled lateral flow nucleic acid assay has also been reported with a luminol system and chemiluminescence resonance energy transfer (CRET) to an AuNP.[521]

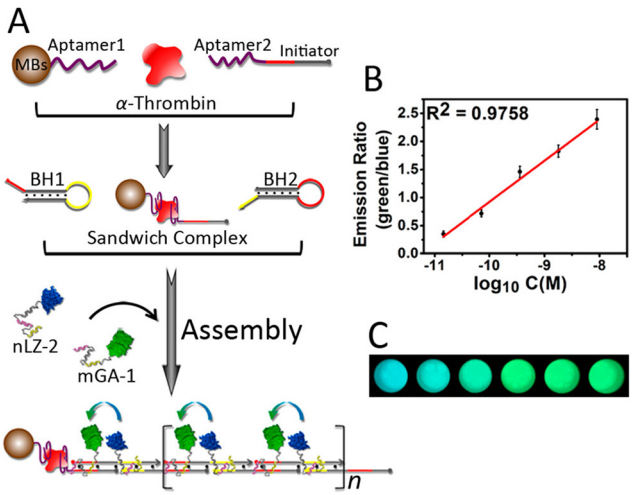

Fig. 39 BRET-based detection *via* smartphone. (A) Binding of aptameric probes to thrombin triggers, *via* two kinetically trapped DNA hairpins (BH1, BH2), the assembly of a DNA-templated BRET construct with luciferase (nLZ-2) and green fluorescent protein (MGA-1). (B) Linear relationship between the G and B smartphone image channels and the thrombin concentration. (C) Smartphone image of the bioluminescent response to various concentrations of human thrombin. Adapted with permission from ref. 540 Copyright 2018 American Chemical Society.

BL assays with smartphone detection have, to some degree, followed the same trends as CL assays. The most commonly utilized enzyme is the NanoLuc luciferase, which generates blue emission, usually from either furimazine or coelenterazine as the substrate. As with CL, smartphone-based devices are potentially as simple as a dark box. Analytes have included microRNA,[536–538] thrombin (Fig. 39) and other protein biomarkers,[539–542] pesticides,[543] disinfectant,[544] drugs,[545,546] other small molecules,[547,548] Hg^{2+} (aq) (Fig. 40) and other metal ions.[549,550] Immuno-complexation and nucleic acid hybridization remain common mechanisms for selective detection, and there have been several instances of detection that leverage bioluminescence resonance energy transfer (BRET)[536,539–541,547] and cells or bacteria encoded with reporter genes to express analyte-sensitive bioluminescent proteins.[545,549,551,552] An LFIA for imidaclothiz (an insecticide) has also been reported with NanoLuc as a BL system.[543]

Both BRET and engineered cells are strategies that avoid wash steps in assays and thus minimize user actions. Signaling in the BRET assay is generally a color change of the emission from blue to green, where tracking of the change in the B or G signal, or the G/B ratio, is useful for quantitation. Signaling with reporter-encoded cells is based on analyte-induced luciferase expression and more intense BL from higher analyte levels. Some of these systems use NanoLuc, whereas others use luciferases that generate green or red emission from their substrate. There are two consequences to the functional requirement for the cells to be alive: the assays must incorporate analyte-insensitive bioluminescent cells as viability controls, and the scope of possible field applications is more limited.

Similar to CL assays, efforts have been made to simplify assay procedures by drying reagents onto paper. For example,

Open Access Article. Published on 07 February 2025. Downloaded on 19/4/2026 11:02:09 PM.
This article is licensed under a Creative Commons Attribution-NonCommercial 3.0 Unported Licence.

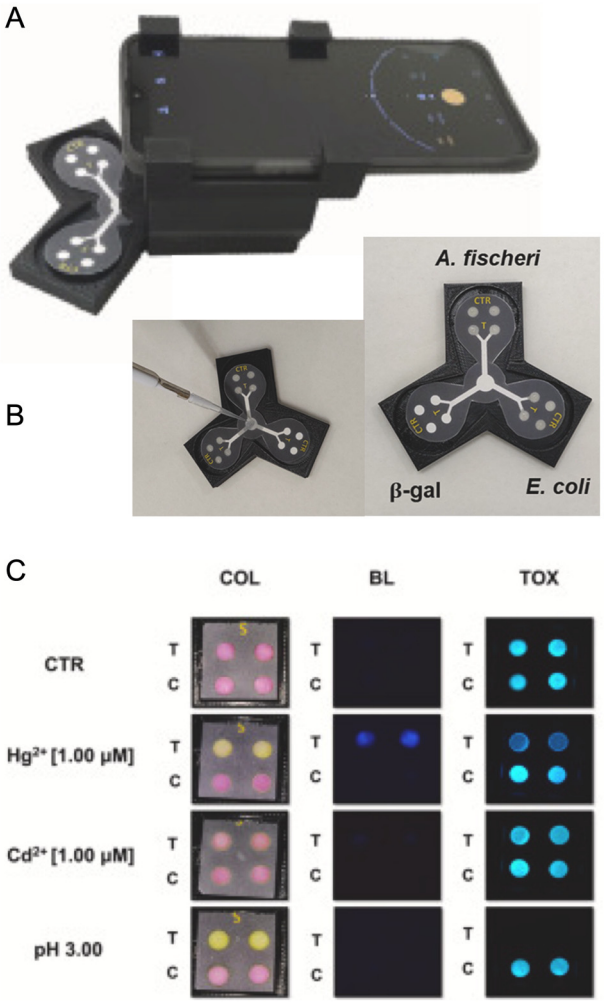

Fig. 40 Smartphone-based device for a dual colorimetric and bioluminescent detection of Hg^{2+} (aq). Photographs of (A) the device and (B) the three-leaf test strip system. The test used a chromogenic reaction catalyzed by β-galactosidase and two bioluminescent bacterial strain reporters (*E. coli* and *A. fisheri*). (C) Brightfield (COL) and BL images of the test strip responses to Hg^{2+}, Cd^{2+} and low pH. Adapted with permission from ref. 549 Copyright 2021 Elsevier B.V.

a chip was developed to contain spheroids encoded with green- and red-emitting luciferases.[551] The green emission was a viability control and the red emission increased with the concentration of tumor necrosis factor (TNFα; LOD 0.2 ng mL^{-1}). The assay had simple but separate steps for the addition of luciferase substrate. Another study developed a bioluminescent reporter-encoded *E. coli* system to detect mercuric ion (parts per billion LOD).[549] The bacteria were pre-loaded on a paper layer on which sample was added, and luciferase substrate was pre-lyophilized on a second paper layer that was applied to the first layer at a defined time after sample addition. Similarly, for a BRET-based microRNA assay (LOD of 2 fM), dried reagents for rolling circle nucleic acid amplification and BRET sensing were split between two paper discs that were added sequentially with sample in a microplate well.[536] In another case, a paper stack was designed to have two twisted-together threads sewn into one of the layers (Fig. 41).[541] One thread contained dried-on luciferase substrate and the other thread contained dried-on BRET sensor, where the latter was a fusion of NanoLuc and mNeonGreen fluorescent protein with an epitope-containing linker to detect target antibody biomarkers (LODs from 2–15 nM). The addition of sample and hydration of the threads reconstituted and mixed the sensors and luciferase substrate.

Although CL and BL methods are logical for the detection of analytes that are reactants or inhibitors of these mechanisms, the selection of CL or BL for many other assays is less intuitive. To date, we have not encountered a study with a head-to-head comparison of either CL or BL with PL. It is thus an open question as to whether the anticipated lower backgrounds of CL and BL methods ultimately provide better signal-to-background ratio than the anticipated greater signal of PL methods. The outcome of such a comparison will likely be very dependent on the nature of the sample and the fluorophore selection.

Examples of ECL detection with smartphones include proof-of-concept assays for glucose *via* a glucose oxidase-mediated ECL reaction with luminol and peroxide,[553,554] an analogous assay for choline *via* choline oxidase,[553] and an immunoassay for *E. coli* using the classic tris(2,2′-bipyridyl) ruthenium(II) and tripropylamine ECL reaction.[555] These and other smartphone-based devices have utilized different strategies to apply potential without a bulky potentiostat: 1.5 V AA batteries,[554] drawing energy from NFC,[556] and drawing energy from the USB port of the phone.[553,555]

7.6 SPR assays

There have been very few smartphone-based SPR assays reported to date. Examples include an array-format magnetic NP-enhanced sandwich immunoassay on a gold chip for the detection of multiple protein biomarkers for acute kidney injury (LODs in the range of 0.2–0.7 ng mL^{-1}),[45] a label-free immunoassay for CA125 and CA15-3 cancer biomarkers using an array of microfluidic channels with a surface layer of AuNPs at high density and a smartphone spectrometer,[557] and a label-free binding assay on a gold nanoplasmonic chip for measuring autoantibody levels for diagnosis of rheumatoid arthritis.[558] The latter approach also developed a solar-powered mini-centrifuge to pair with the smartphone device to isolate plasma from whole blood.

8. Microfluidic devices

8.1 Chip-based microfluidics

Microfluidic-like chips are a popular format for sample containment with smartphone-based measurements and devices. Discrete wells, simple channels, and inlets to chambers are common designs with PDMS-on-glass chips and hard polymer chips. Many assays that use these designs derive little or no benefit from fluid flow. Rather, these formats are adopted for reasons such as simplicity, compact size, relatively low cost, small sample volumes, confinement of sample within the focal plane for imaging, and prevention

Open Access Article. Published on 07 February 2025. Downloaded on 19/4/2026 11:02:09 PM.
This article is licensed under a Creative Commons Attribution-NonCommercial 3.0 Unported Licence.

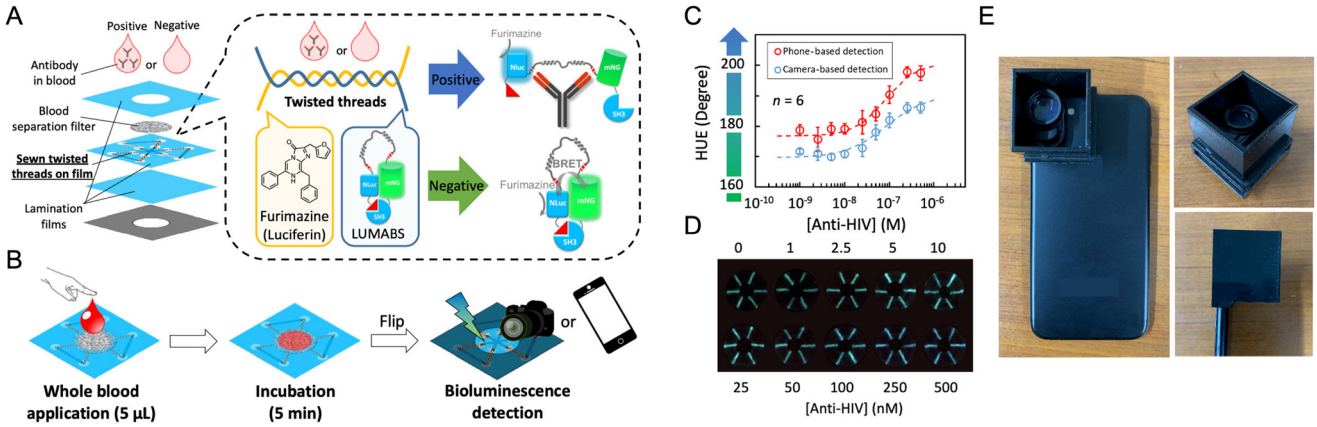

Fig. 41 Thread-based BRET detection of target antibodies to avoid user steps after the addition of sample. (A) Design of the threaded paper stack, with luciferase and its substrate dried on separate threads. (B) Assay workflow. (C) Plot of smartphone-measured luminescence hue *versus* analyte concentration. (D) Smartphone-acquired BL images for different concentrations of the anti-HIV antibody analyte. (E) Photographs of the smartphone-based imaging device. Figure adapted with permission from ref. 541 Copyright 2020 American Chemical Society.

of spills. Several of the smartphone-based assays highlighted in the preceding sections utilized sample containment of this nature. Here, in this section, the focus is on examples of smartphone-based assays where a microfluidic chip provided benefits or functions beyond simple sample containment.

8.1.1 Channel microfluidics. One simple but very practical benefit of microfluidic chips is automated distribution of sample to more than one measurement zone from a single user addition. For example, a polymethyl methacrylate (PMMA) chip with a channel that automatically filled four test zones was used for parallel smartphone-based fluorescence detection of glucose, total cholesterol, uric acid, and triglycerides, where the necessary enzymes were preloaded into the test zones.[559] More sophisticated chips have directly sampled sweat from skin and directed the fluid to different test zones for fluorimetric detection of Zn^{2+}, Cl^{-}, and Na^{+} (aq) *via* a smartphone-based device (Fig. 42).[40]

Another motivation for adopting a microfluidic chip is facilitating isolation of an analyte. For example, a spiral microfluidic channel with a herringbone structure was adopted to improve influenza virus capture efficiency by antibodies immobilized on the channel walls.[560] Subsequent steps completed a silver-enhanced colorimetric sandwich assay with AuNPs. In some cases, such as the detection of *Schistosoma haematobium* eggs in urine samples,[561] channel dimensions can be tapered to trap large-sized analytes with dimensions greater than about 20 µm. A benefit of this approach is concentration of analyte in the defined imaging zone, but it does not provide molecular specificity. The immunocapture of cells (plus a wash step) within a microfluidic chip provides this specificity. For example, a microfluidic channel with antibody-conjugated pillars was used to assess CD64 expression on neutrophils (Fig. 43).[173] With the effect of flow, cells with higher expression levels were captured earlier in the pillar channel, enabling both counting of the cells (*via* a fluorescent nuclear stain) and an estimate of the distribution of relative CD64 levels.

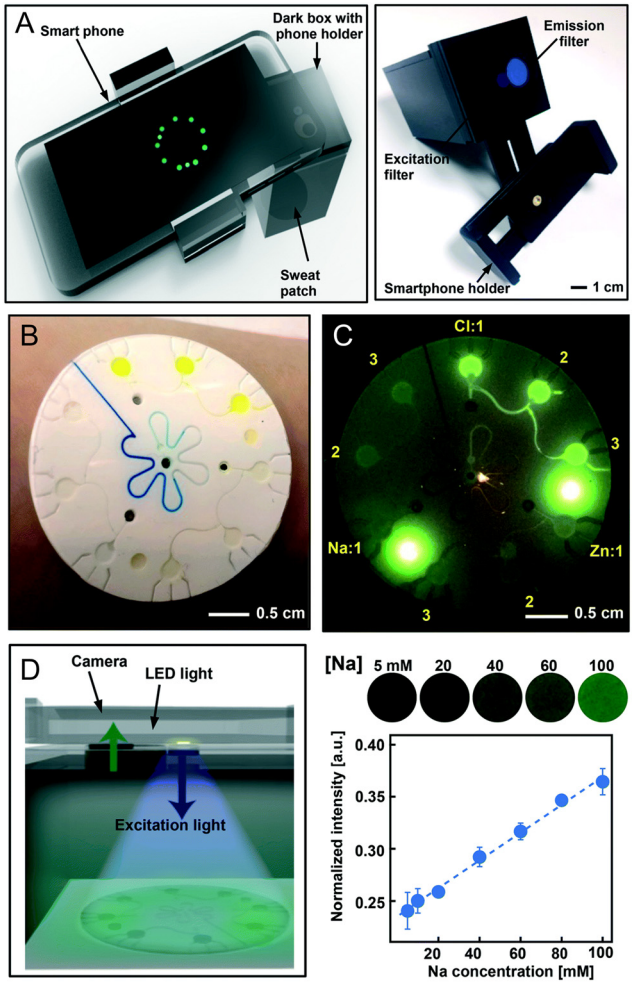

Fig. 42 Wearable fluorescent sensor for the detection of Zn^{2+}, Cl^{-}, and Na^{+} (aq) in sweat. (A) Smartphone device and optics module for visualizing the microfluidic patch. Visualization of the patch under (B) ambient illumination and (C) blue light illumination. (D) The blue light is filtered from the phone flashlight (left) and the green emission is linear with respect to analyte concentration (right). Adapted with permission from ref. 40 Copyright (2018) Royal Society of Chemistry.

Open Access Article. Published on 07 February 2025. Downloaded on 19/4/2026 11:02:09 PM.
This article is licensed under a Creative Commons Attribution-NonCommercial 3.0 Unported Licence.

The above examples of single-channel microfluidic immunoassays are multi-step and therefore require multiple volumes (*e.g.* sample followed by washes and reagents or immunoconjugates) to be introduced to the chip by the user. Other assays have pseudo-automated multiple steps through multi-channel microfluidic chips and multiple syringe pumps. Examples include a colorimetric enzyme-linked assay for miRNA pre-extracted from serum,[562] and an AuNP-based colorimetric assay for *Salmonella*.[563] Alternatively, solutions for a colorimetric sandwich ELISA have been added in sequence, *via* micropipette, to microfluidic channels and discharged *via* centrifugal flow with a portable device.[564] A low-tech approach reported for a multistep fluorogenic ELISA of Dengue fever NS1 antigen was self-priming siphon fluidics (Fig. 44).[565] Capture antibodies were immobilized within capillaries, and separate reservoirs for the sequences of reagents and washes were needed for the assay. Each of these approaches still requires multiple user actions, which is sub-optimal, but gains precision *versus* the manual introduction of solutions.

Other microfluidic approaches have housed reagents on-chip. Examples of varying complexity include a PDMS chip with two reagent reservoirs, a mixing channel, and micromechanical actuation for chromogenic detection of gaseous formaldehyde;[566] a five-stage and valved microfluidic chip with pre-loaded reagents for an immunomagnetic bead-based colorimetric ELISA;[567] and colorimetric ELISA using an AI-controlled chip with a micropump and valve, and process monitoring *via* the smartphone camera to initiate conditional actions, such as bubble removal and starting and stopping filling of the assay chamber (Fig. 45).[90]

Another technique that smartphone-based assays have borrowed from benchtop assays and general lab-on-a-chip development is magnetic capture. A few examples highlighted Sections 7.2, 7.4, and 7.6 have referred to immunomagnetic methods, which frequently use a fixed or actuated permanent magnet to hold analyte-linked magnetic particles in place for washing steps. One example not mentioned so far is an on-chip colorimetric ELISA for Zika virus antigen with a Arduino-controlled, motor-actuated magnet system.[93] A more exotic particle trapping method that has been reported is contour-mode acoustic streaming tweezers, which enabled multiple sequential steps within a single channel for a microparticle-supported sandwich immunoassay with CL detection of PSA (LOD of 0.2 ng mL^{-1}).[513]

Despite the greater number of proof-of-concept studies, there is good potential for simplification and utility of these assays beyond a lab. For example, an LFIA was developed for ochratoxin A in wine and coffee (LODs of 0.1–0.3 ng mL^{-1}), where sample was injected into an analytical cartridge with the LFIA-ready membrane and a fluidic component that dispensed the required reagents *via* "button pushing" with in-cartridge reagent pouches and "switch flipping" with on-cartridge flow control valves (Fig. 46).[528]

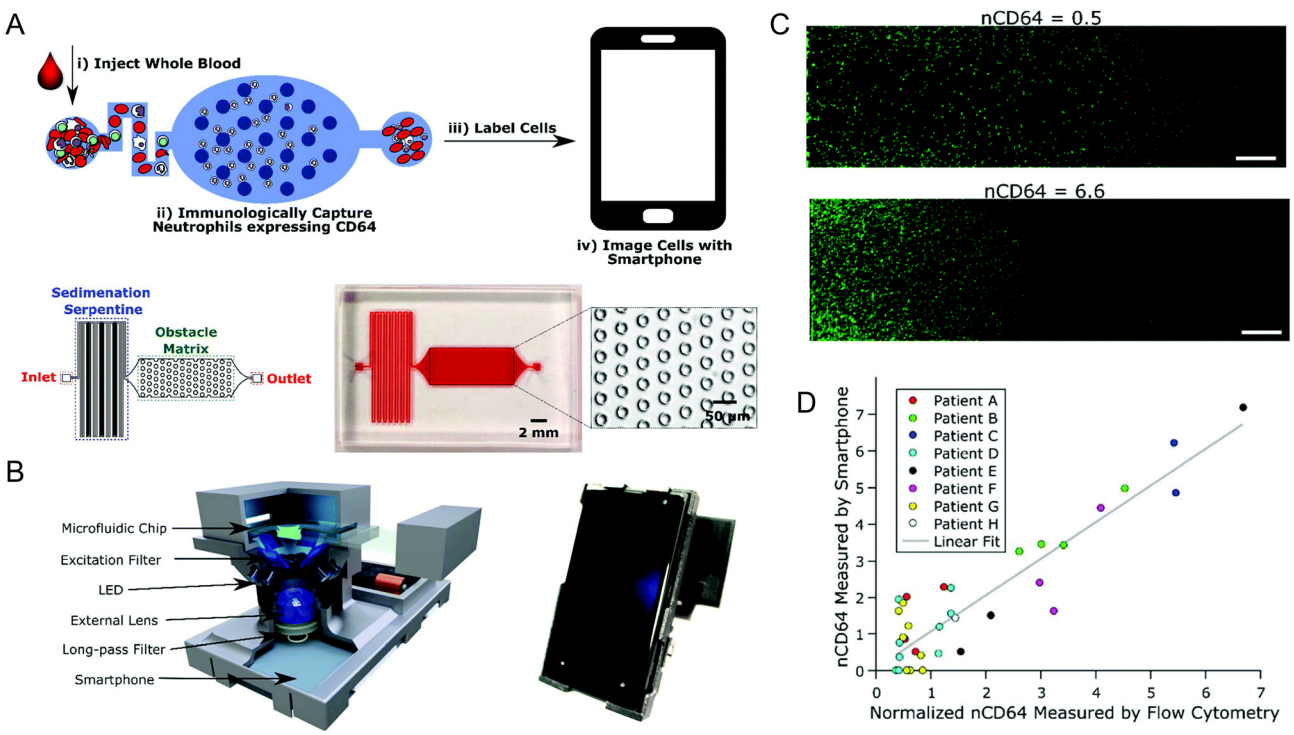

Fig. 43 Isolation of neutrophils based on CD64 expression. (A) Schematic of the microfluidic chip and summary of the workflow for the analysis (top), and schematic and photograph of the chip (bottom). (B) Design and photograph of the smartphone-based imaging device. (C) Examples of smartphone fluorescence images of captured cells. High-expression results in cells being captured earlier in the chip (bottom image). The scale bars are 1 mm. (D) Correlation between flow cytometry measurements and smartphone measurements. Adapted from ref. 173 Copyright (2019) Royal Society of Chemistry.

Open Access Article. Published on 07 February 2025. Downloaded on 19/4/2026 11:02:09 PM.
This article is licensed under a Creative Commons Attribution-NonCommercial 3.0 Unported Licence.

8.1.2 Droplet microfluidics. Although most examples of on-chip sample and assay processing for smartphone-based detection have featured channel microfluidics, droplet microfluidics have also been useful for this purpose. A sessile droplet microfluidic device used an aqueous two-phase system to isolate Cd^{2+} (aq) from a mixture of other metal ions for colorimetric detection.[36] As with several microchannel examples, this approach required the user to execute multiple steps. In contrast, an optoelectrowetting device automated the processing of marine water samples for fluorescent staining and counting of algae cells (Fig. 47).[568] The programmable nature of the smartphone display was leveraged to drive the optoelectrowetting and its camera was used for detection, highlighting remarkable technical synergy in this approach.

8.1.3 Nucleic acid amplification testing. Nucleic acid diagnostics are an application that stands to greatly benefit from smartphone portability and has substantial need for lab-on-a-chip support. For authentic samples, a multi-step and multi-reagent combination of nucleic acid isolation and amplification is required. Microfluidic chips designed for smartphone-based nucleic acid detection have addressed these requirements to different degrees and with different strategies.

A subset of microfluidic approaches have only addressed nucleic acid amplification and detection. Examples include a chamber-based microfluidic chip for digital PCR with a portable device for thermocycling;[94] digital droplet LAMP, using both channel-based droplet generation[462,569] and a pump-free open droplet array;[458] and a non-digital silicon microfluidic chip with multiple channels in which LAMP primers and a dsDNA-sensitive dye were pre-loaded.[570] The silicon chip was paired with a portable smartphone-based device for heating and fluorescence detection of up to five different equine respiratory viruses (one genetic sequence per channel) from pre-processed horse nasal swab samples.[570]

A subsequent study bridged the gap between sample and detection by devising a microfluidic cartridge for processing whole blood for Zika virus detection (LOD of 270 copies per μL; Fig. 48).[460] Reagent solutions for chemical lysis of the virus particles to release RNA, and for reverse transcription and isothermal amplification, were transported in multiple stages to different regions of the chip to execute the processing steps. The user manually rotated a built-in threaded screw syringe and actuated two "keys" to move sliding valves into the proper positions. The processed sample was ultimately transferred to a multichannel silicon microfluidic chip for LAMP and detection with a smartphone-based device.[460] Another example was a PMDS microfluidic chip with integrated chitosan-modified capillaries to pre-concentrate RNA for PCR amplification and detection.[461] The device had a Peltier chip and valves operated by an air-pump and a vacuum generator. In combination with negative pressure manually applied by a syringe draw, the valves enabled on-chip lysis, nucleic acid isolation, and PCR amplification. The device was relatively large and plugged into a mains socket. A third example of a

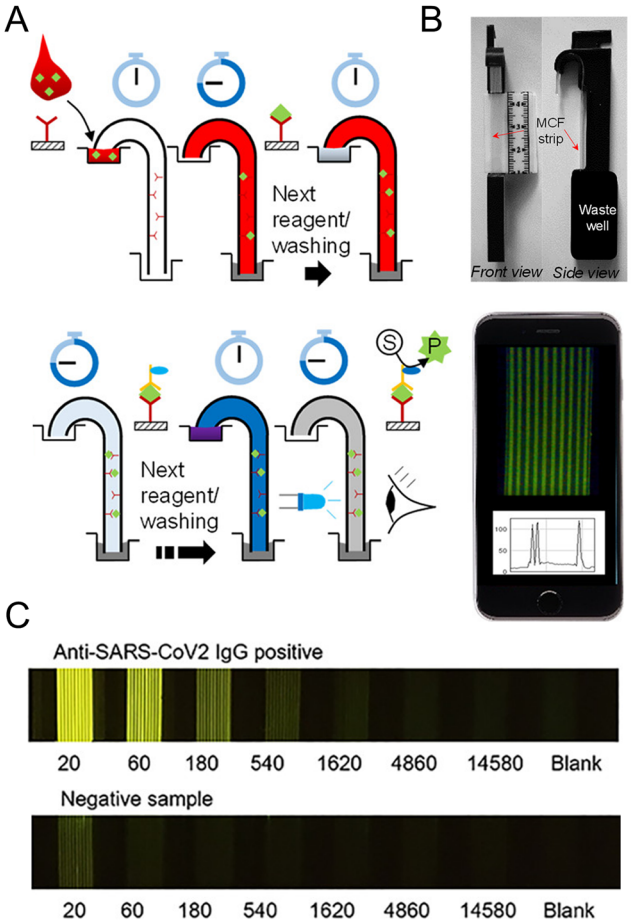

Fig. 44 Gravity-driven self-priming siphon microfluidics for fluorogenic ELISA-based detection of dengue fever NS1 antigen and quantification of anti-SARS-CoV-2 IgG in serum spiked samples. (A) Workflow for the assay. (B) Photograph of the siphon device with a microcapillary film (MCF) strip (top) and example of a smartphone-captured fluorescence image (bottom). (C) Detection of IgG anti-viral antibodies in positive and negative samples at various dilution factors. Figure adapted from ref. 565 Copyright 2021 American Chemical Society. This publication is licensed under CC-BY 4.0.

user-driven two-stage approach combined a basket with a DNA extraction disc at the bottom, a block module with a wash chamber for DNA purification, a reaction chamber with a rotary valve for target DNA amplification *via* RPA, and a microfluidic channel with immobilized oligonucleotide probes for capture of amplified targets (Fig. 49).[571] AuNPs and silver enhancement were used for labeling and colorimetric signal enhancement for detection of genes isolated from bacteria in milk samples and urine, human genes isolated from blood samples, and more. This example was also notable because it used heat generated by the smartphone to reach the 37 °C needed for amplification.

A single chip design for both isolation and amplification is also possible. One such example was a finger-actuated microfluidic chip with four buttons, each of which was pushed repeatedly by the user to dispense and flow buffers

Open Access Article. Published on 07 February 2025. Downloaded on 19/4/2026 11:02:09 PM.
This article is licensed under a Creative Commons Attribution-NonCommercial 3.0 Unported Licence.

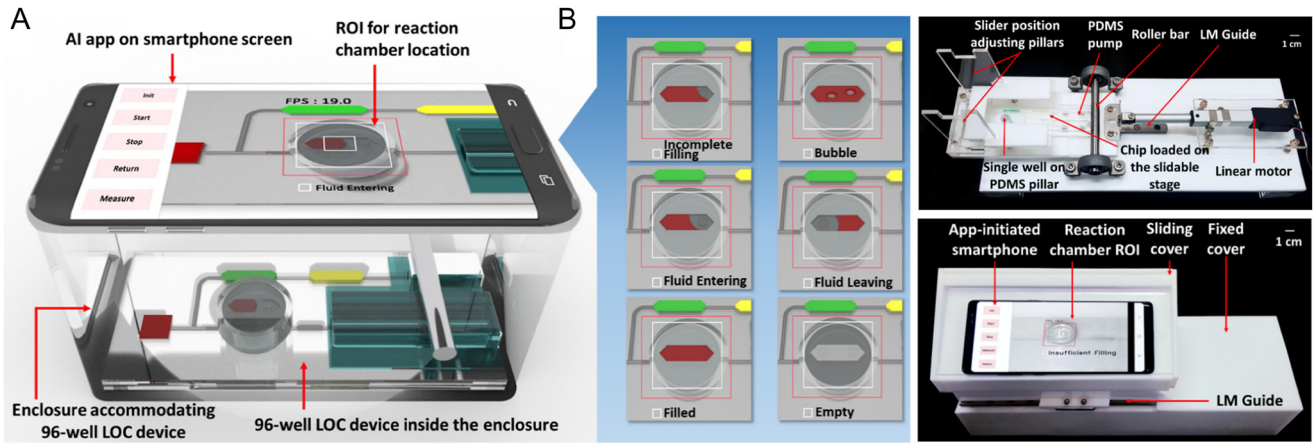

Fig. 45 Automated colorimetric ELISA executed by an AI-controlled microfluidic chip with monitoring using the smartphone camera. (A) Rendering of the smartphone-based platform and app. (B) Diagrammatic representations of the fill states (left) and photographs of the device (right). Adapted with permission from ref. 90 Copyright 2022 American Chemical Society.

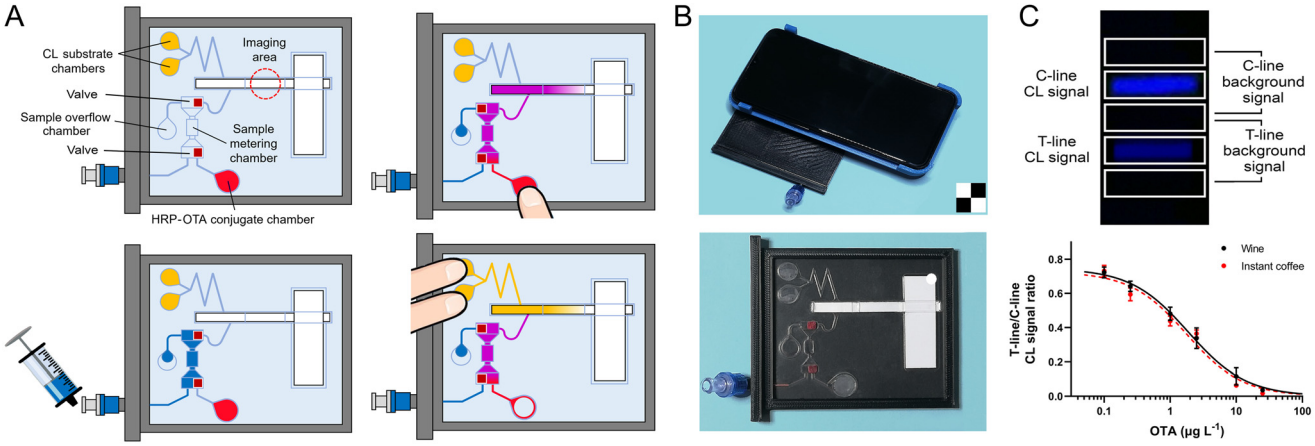

Fig. 46 LFIA-ready membrane in a cartridge with finger-actuated reagent pouches for the CL-based detection of ochratoxin A (OTA) in wine and coffee samples. (A) Schematic overview of LFIA analysis. Sample is loaded, transferred, and mixed with various reagents on-chip before being injected onto the LFIA strip. (B) Photographs of the physical device and chip. (C) Example of a smartphone-acquired CL image of the LFIA and a calibration plot for OTA obtained in wine and instant coffee. Adapted with permission from ref. 528 Copyright 2021 Elsevier B.V.

and reagents through microfluidic channels.[572] In this manner, and with assistance from an external magnet, the chip executed an immunomagnetic isolation of a pathogenic bacterium, a nucleic acid extraction and purification with a second type of magnetic nanoparticle, and on-chip amplification for detection with a smartphone.

8.2 Paper-based microfluidics

Many of the examples of smartphone-based assays highlighted in earlier sections have utilized paper as a substrate. The paper has been homogeneous in some cases, but more often has been patterned with one or more channels using wax or another method to function as a μPAD. The simplest examples of μPADs direct a single aliquot of sample to multiple test zones. The analysis of sweat is an example of such an application, where one study designed a paper microfluidic device to adhere to skin and detect pH, glucose, lactate, and uric acid through indicator dyes and chromogenic reactions with reagents and enzymes pre-deposited in the test zones (Fig. 50).[573] This format has also been used to run replicate measurements for CL detection.[532]

Other μPADs have sought to derive function beyond sample distribution. For example, a paper-based pump-free rapid mixer design was applied to the colorimetric detection of organo-phosphate pesticide.[574] Multiple assays have also extended the paper channel beyond the test zone to enable on-PAD washing steps: the fluorimetric detection of aqueous metal ions (Cd^{2+}, As^{3+}, Pb^{2+}, Hg^{2+}) *via* DNA-based probes (*e.g.* aptamers, DNAzyme, thymine-rich oligonucleotide);[575] the detection of a pesticide *via* a fluorescence recovery mechanism with dye-labeled aptamer;[576] and magnetic-based ELISA for a malaria biomarker, *Plasmodium falciparum* lactate dehydrogenase.[577] More sophisticated multi-step assay capability has been achieved through a μPAD that incorporates a mechanically actuated paper-based rotary valve system to execute a colorimetric ELISA for the β-amyloid peptide 1–42 biomarker of Alzheimer's disease

Open Access Article. Published on 07 February 2025. Downloaded on 19/4/2026 11:02:09 PM.
This article is licensed under a Creative Commons Attribution-NonCommercial 3.0 Unported Licence.

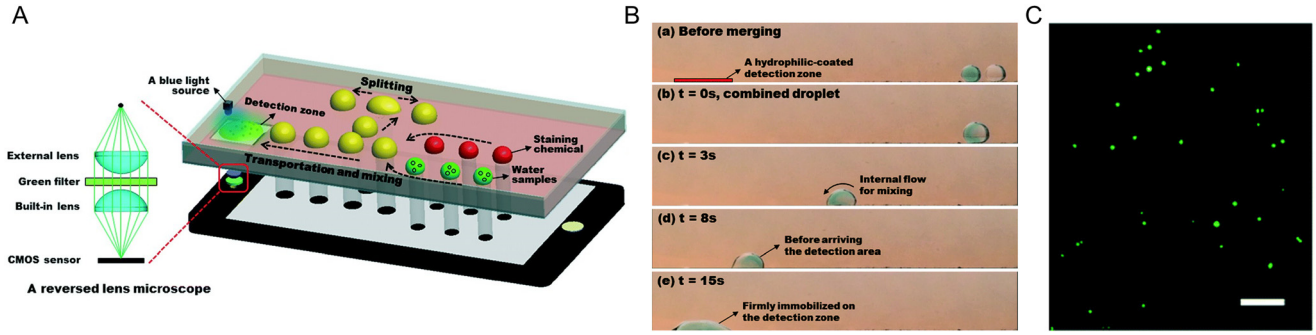

Fig. 47 Smartphone display-actuated optoelectrowetting droplet microfluidics for on-chip sample preparation and water quality detection. (A) Schematic overview of the digital microfluidic operations and (B) video frames showing these operations. (C) Smartphone-acquired fluorescent image of marine water sample showing target algae cells. The scale bar is 100 μm. Adapted from ref. 568 Copyright 2018 Royal Society of Chemistry.

(Fig. 51).[96] Reagents were pre-loaded on the μPAD, such that the user added the sample to the test zone and buffer to the inlet zone, and the rotary motion separated binding, washing, and color development steps. Manual actuation has been utilized for a multi-step assay, such as in the case of determining serum phosphate levels from a single drop of whole blood using malachite green as a colorimetric indicator.[578] Serum was isolated from blood cells *via* flow through a suitable membrane, and a mechanical mechanism dipped a serum-impregnated collection pad into reagent solution to develop a colorimetric signal.

Foldable μPADs have also been a means of executing multiple assay steps in a user-friendly format. In one example, sputum samples that were either positive or negative for infection by *Pseudomonas aeruginosa* were liquified with a bacterial catalase and hydrogen peroxide, and the liquid sample was transferred to the μPAD.[579] The μPAD was folded to bring pre-loaded AuNP-antibody conjugates into contact with the sample, the sample spot was washed, and the residual color of bound AuNPs provided a signal for the detected bacteria. A method for the detection of viral RNA was based on the release of Ag^+ (aq) ions from an oligonucleotide probe upon hybridization with target RNA, where the Ag^+ inhibited urease and prevented a pH and color change from turnover of its substrate in the presence a phenol red indicator dye (Fig. 52).[580] Sample was added to the μPAD, which was folded in sequence to separate the steps of binding with probe and the chromogenic reaction. Different regions on the device were used for multiplexed screening for MERS-CoV, SARS-CoV, and SARS-CoV-2. Similarly, another study pre-dried reagents for CL-based glucose detection (LOD 10 μM) onto a foldable μPAD. This format kept the reagents separated until needed for the assay, which reduced the required user steps to only pipetting to add sample and standard solution, a fold, and adding transport buffer.[531]

An interesting capability that has emerged with smartphone-based detection using paper test strips is quantitation by distance measurements. One report took advantage of the change in surface tension from immunoagglutination to detect SARS-CoV-2 (LOD 1–10 fg mL^{-1}) nucleocapsid *via* a change in the capillary flow velocity in a patterned paper channel, where flow was tracked using dye-doped polystyrene NPs.[581] Another report measured IL2-

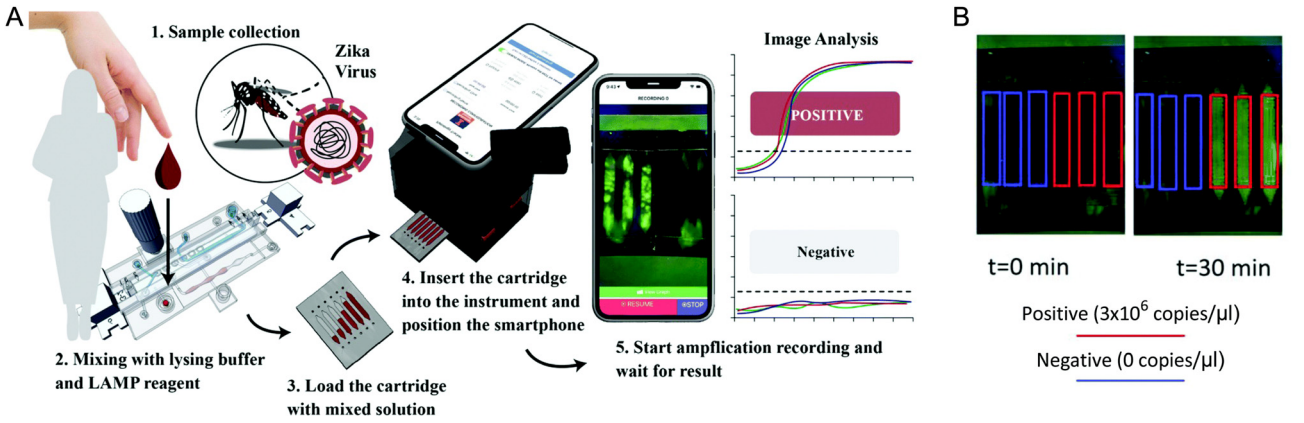

Fig. 48 Point-of-care blood testing for Zika virus with smartphone-based detection. (A) Assay workflow with a multi-stage manually actuated microfluidic chip for sample processing and transfer to a detection cartridge for smartphone-based fluorescence imaging. (B) Smartphone images for in-cartridge detection of virus spiked into whole blood. Adapted from ref. 460 Copyright 2022 The Royal Society of Chemistry.

Open Access Article. Published on 07 February 2025. Downloaded on 19/4/2026 11:02:09 PM.
This article is licensed under a Creative Commons Attribution-NonCommercial 3.0 Unported Licence.

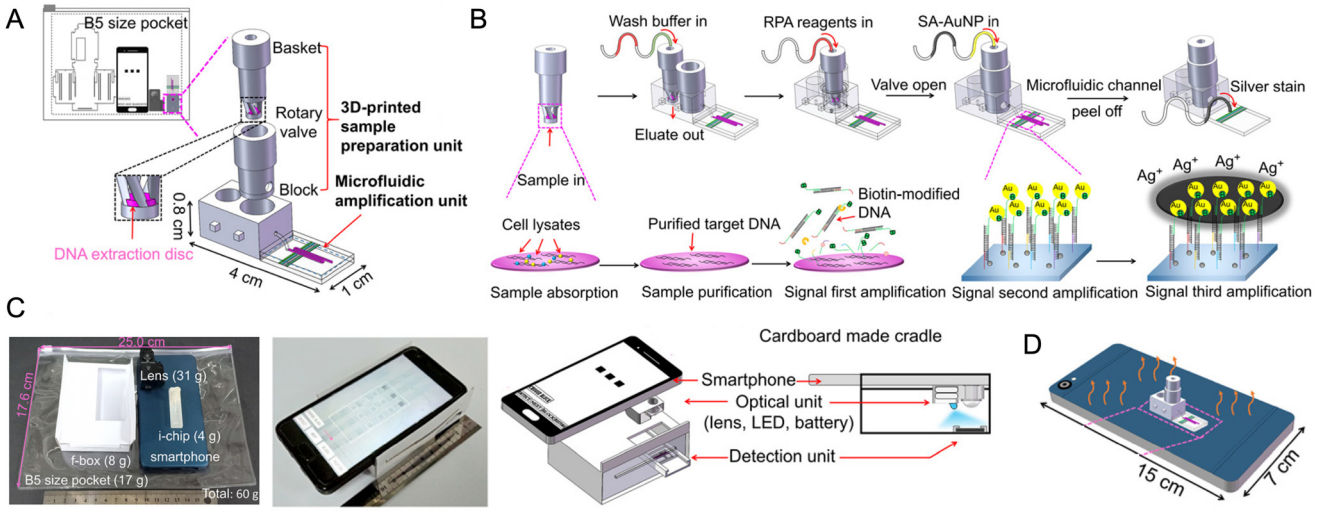

Fig. 49 Smartphone-based colorimetric detection of target DNA sequences using a pocket-sized basket-and-microfluidic system for sample preparation and assay execution with a foldable box. (A) Design of the device. (B) Assay workflow. (C) Photographs of the smartphone-based foldable-box device. (D) Illustration of how the smartphone is used to provide heat for DNA amplification. Figure adapted from ref. 571 under a Creative Commons CC BY 4.0 license.

positive and total natural killer cell concentrations in buffy coat blood samples *via* their migration distance along a paper channel. The binding of fluorescent polymer NP-antibody conjugates slowed the cell migration to a degree proportional to their CD56 level, such that the fluorescence intensity profile along the channel reflected the relative distribution of CD56 expression levels in the sample.[487] Other distance-based assays have been based on analyte depletion rather than velocity. In one case, an indicator dye was deposited in a paper channel in the pattern of a repeating QR code. The number of QR codes that appeared in a fully readable form along the length of the channel determined whether the analyte (Cu^{2+}) concentration was low, medium, or high within the dynamic range of the assay (0.4–3.2 mM).[582] In another case, a rapid blood grouping analysis was done through depletion of the relevant red blood cell type through immunocapture within a spoke pattern of paper channels with colorimetric contrast augmented by bromocresol green (Fig. 53).[161] The layout of the μPAD was such that result was readable as a QR code *via* the

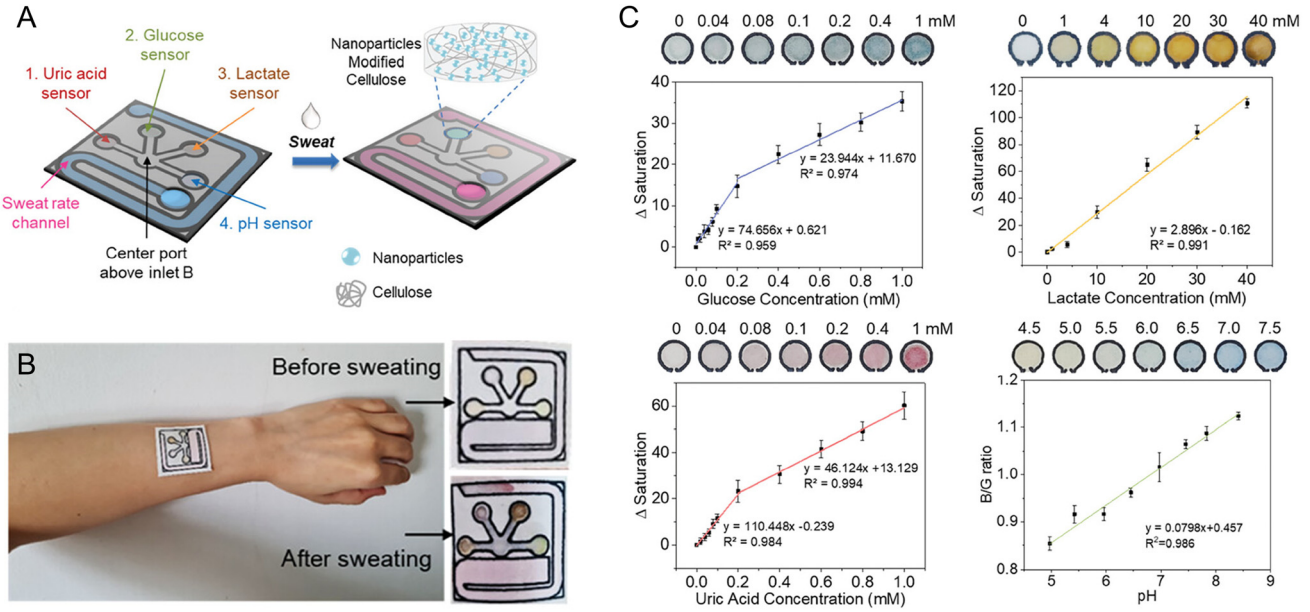

Fig. 50 Wearable μPAD for the analysis of sweat biomarkers: uric acid, glucose, lactate and pH. (A) Design of the μPAD. The NP detection region is highlighted. (B) After sweat exposure, a color change is visualized. (C) Calibration curves (based on HSV color saturation (*S*) or a B/G channel ratio) for the analytes from smartphone imaging of the μPAD. Adapted with permission from ref. 573 Copyright 2023 Wiley-VCH GmbH.

Open Access Article. Published on 07 February 2025. Downloaded on 19/4/2026 11:02:09 PM.
This article is licensed under a Creative Commons Attribution-NonCommercial 3.0 Unported Licence.

smartphone camera. Distance measurements are not unique to paper devices, as demonstrated by smartphone readout of the radial travel of DNA motor system immobilized on 5 μm beads across a DNA modified gold chip.[583] This format was able to detect SARS-CoV-2 spiked in artificial saliva and exhaled breath condensate with a sensitivity of 1000 copies per mL within 15 minutes.

9. Perspective: challenges and opportunities

As highlighted in this review, and in other recent reviews,[584–586] smartphones have clearly emerged as capable and versatile platforms for molecular analyses based on optical measurements. The built-in camera is useful for quantitative readout of changes in optical extinction, color, and luminescence induced by molecular recognition and other selective chemistries. Numerous measurements have been successfully ported from laboratory instruments to smartphone-based devices, and qualitative methods for point-of-need testing have been made quantitative. The convergence of smartphones with microfluidics, NPs, and other complementary materials and technologies holds great potential for the lab-on-a-chip concept and better democratization of chemical and biological assays. What challenges and opportunities for innovation stand between this conceptualization and its practical realization?

9.1 Pre-detection bottleneck: sample processing

About 1 in 6 smartphone-based methods and devices reported to date have been sample-to-answer approaches (Fig. 14). Most assays and devices have either been limited to proof of concept for smartphone detection or adopted one or more standard laboratory methods for processing authentic samples prior to smartphone detection. The challenge of the "world-to-chip" interface is well known in microfluidics[587] and the literature reflects an analogous challenge with smartphone-based analyses. It will be essential for processing of crude samples to be rapid and automated, simple and safe, or unnecessary for the most impactful translations of smartphone technology to authentic analytical applications. This aspect of translation is minimized or unacknowledged in much of the literature. Although studies that focus on advances in detection are important, there is a need for more studies that address the bottleneck of sample processing.

9.1.1 Minimal processing. Examples of quick and simple manual sample processing steps for non-experts are centrifugation using a portable, low-g, battery-operated device, and mixing crude sample with an equal volume of an out-of-the-box reagent cocktail. Any user manipulation of

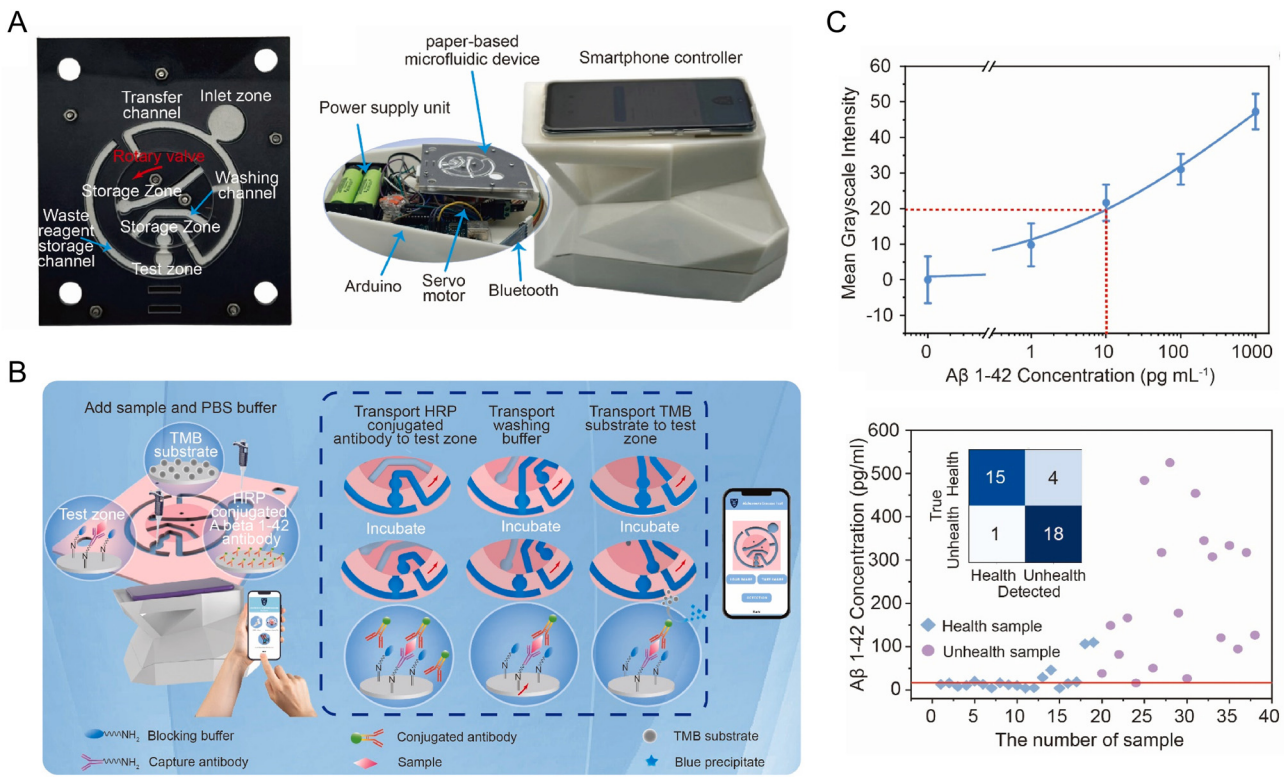

Fig. 51 Automated platform for detection of Alzheimer's disease biomarkers. (A) Design of μPAD platform (left) and the smartphone-based device (right). (B) Workflow of the colorimetric ELISA assay. (C) Calibration curve in terms of grayscale intensity *versus* Aβ 1–42 concentration (top) and comparison of the result to a traditional analytical method for artificial plasma samples (bottom). Figure adapted with permission from ref. 96 Copyright 2024 Elsevier B.V. All rights reserved.

Open Access Article. Published on 07 February 2025. Downloaded on 19/4/2026 11:02:09 PM.
This article is licensed under a Creative Commons Attribution-NonCommercial 3.0 Unported Licence.

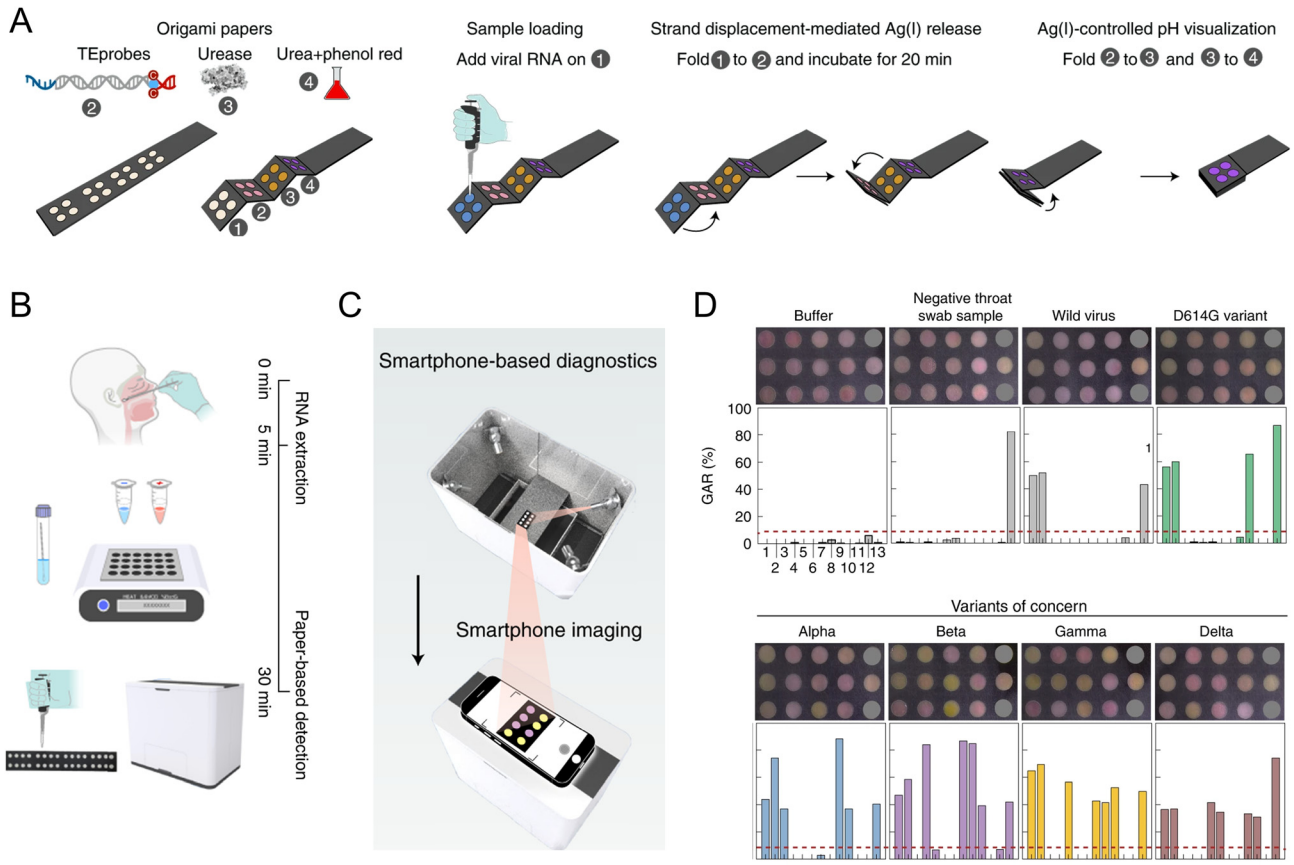

Fig. 52 Origami-based μPAD for assaying and multiplexed screening of SARS-CoV-2 variants with single-nucleotide resolution. (A and B) Design and workflow for the assay. (C) Design of the smartphone-based imaging device. (D) Examples of smartphone-acquired images and green-area-ratio values as the metric for analysis. Each dot on the device corresponds to a different targeted gene and mutation. Figure adapted with permission from ref. 580 Copyright 2022, the author(s), under exclusive license to Springer Nature Limited.

sample and solutions should have a high tolerance for imprecision between different users and between individual samples, and from the use of equipment like disposable plastic transfer pipettes and droppers rather than micropipettes or calibrated dispensers. Usability decreases markedly as steps become more numerous and require greater precision. Indeed, the ideal workflow is for an unprocessed sample to be directly analyzed in a single step, and cost and robustness are optimized with fewer components in a test strip or chip. Aside from the usual challenge of potential molecular interferents in a crude sample matrix, optical detection must be wary of interference from sample turbidity, coloration, and autofluorescence.

The above considerations provide many opportunities for innovation in stripping down laboratory assay methods to their bare minimum and enabling shortcuts through advanced optical materials, selective recognition agents, and clever optical designs. Examples include the development of chromogenic and fluorogenic reagents that have sufficient selectivity and efficiency to react with analyte in crude samples, and the development of FRET probes with fluorescent acceptors. The nanometer-scale distance dependence of FRET enables mix-and-measure protocols and ratiometric detection that will minimize the impact of inconsistent dilution and excitation intensity.[588] FRET probes based on NP materials that have high brightness,[589] exhibit upconversion PL,[590] and support time-gated measurements[591] will also mitigate challenges from sample autofluorescence. Although smartphone cameras do not support near-IR detection, the red RGB camera channel can be leveraged with similar effectiveness, and chips with integrated waveguides and short optical path lengths will facilitate optical interrogation of non-transparent samples. For crude samples that start opaque, sample chips that integrate membranes and other porous materials will ideally provide the cleanup needed for optical detection. There is also great potential in building reference markers into test strips and chips to enable compensation of variation in sample optical properties and transfer complexity from hardware to software.

9.1.2 Automated processing. For the convergence of smartphones and microfluidics to practically simplify or automate sample processing and detection, it must be implemented with mechanisms of fluid transport that are robust, low-cost, and low-power. Gravity, capillary forces,

Open Access Article. Published on 07 February 2025. Downloaded on 19/4/2026 11:02:09 PM.
This article is licensed under a Creative Commons Attribution-NonCommercial 3.0 Unported Licence.

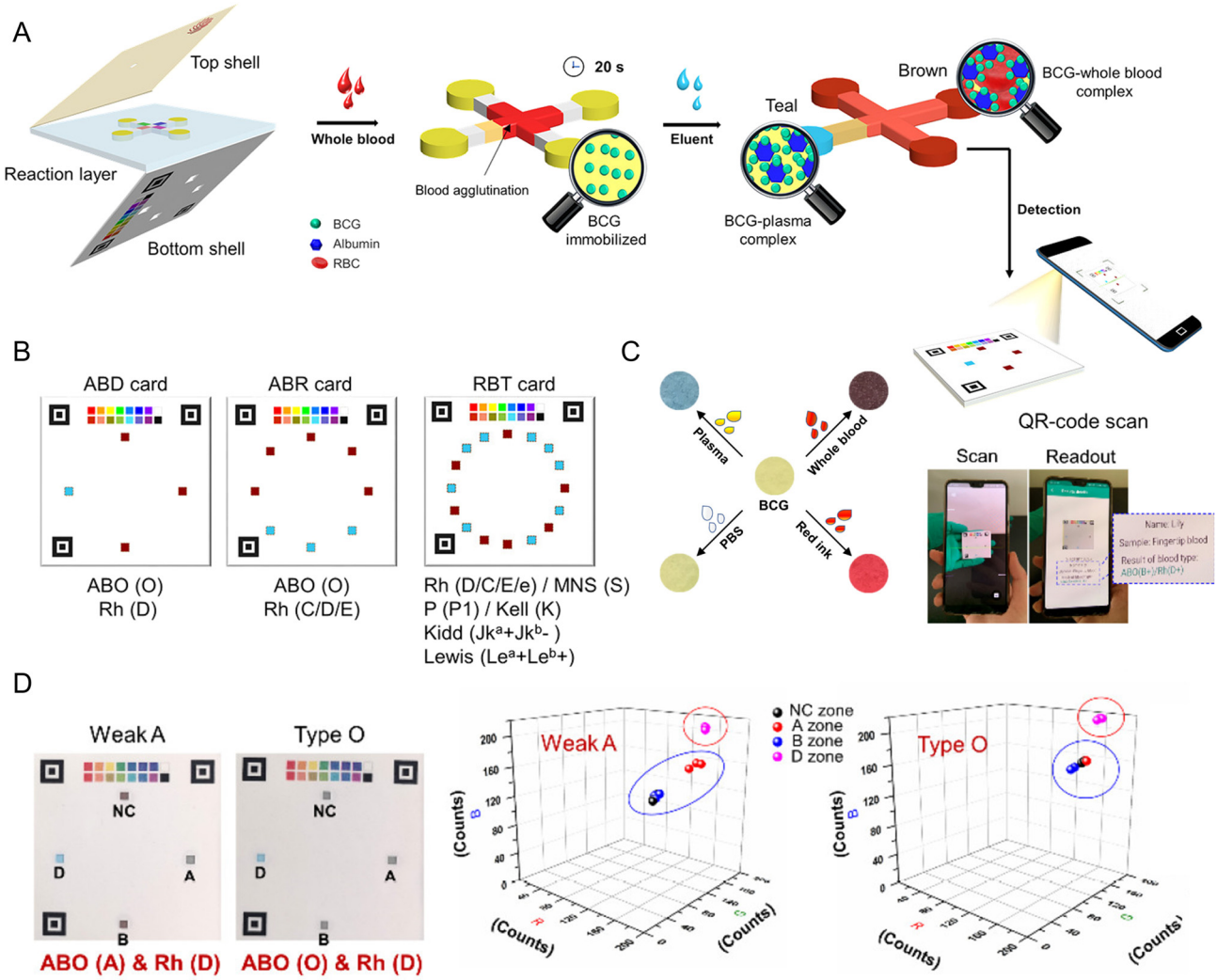

Fig. 53 Antibody-based blood typing on a μPAD *via* QR code patterns. (A) Design and workflow of the assay. (B) Different assay formats for application to different blood-typing requirements. Reference color blocks and position detection boxes ensure consistency in interpretation. (C) Bromocresol green dyes provides optical contrast for smartphone imaging. (D) Smartphone images of cards (left) and 3D plots from RGB analysis (right) for two samples of two different blood types. Adapted with permission from ref. 161 Copyright 2021 American Chemical Society.

and (opto)electrowetting mechanisms are promising candidates. Pressure and centrifugal forces are also potentially viable mechanisms if applied through device-integrated pumps and rotors that use small motors and hardware that is 3D printable or commonplace. The chips should also meter the input fluid with the assumption of imprecise transfers of sample volume by users. Waste solution will need to be safely contained, such as through surface tension, one-way valves, post-assay adhesive seals, or other approaches. The disposal of chips in a pre-existing waste management stream will also place practical limits on the size, mass, and material composition of a chip, as will regulated or unregulated incineration. Here, there is great opportunity for engineering biodegradable microfluidic chip technologies beyond paper, developing capillaric circuits for assays, and creating microfluidic chips that integrate with direct sampling tools like microneedle arrays.

Conventionally, the reuse of chips has been eschewed in point-of-need testing due to the less favorable business economics and obstacles such as sample carryover, replenishment of pre-loaded reagents, and deteriorating performance with each cycle of use. Two factors may encourage reconsideration of this aversion: the inability of disposable paper-based microfluidic devices to support the full scope of technical capabilities that will be needed to translate many assays from the bench to the field; and a future focus on sustainability and the different economics of equitable access, particularly in the case of technologies that offer high-value capability that is built on non-abundant, expensive, and non-green materials. In this scenario, the reuse of chips will require fast and reliable cleaning and decontamination using reagents that pose a minimal hazard to people and the environment. It is a prime opportunity for open chip configurations of (opto)electrowetting for digital microfluidics, both in terms of the disparate capabilities

Open Access Article. Published on 07 February 2025. Downloaded on 19/4/2026 11:02:09 PM.
This article is licensed under a Creative Commons Attribution-NonCommercial 3.0 Unported Licence.

versus paper microfluidics and the potential to be wiped clean and sterile.

9.2 Pre-detection bottleneck: calibration

Nearly all of the smartphone-based assays reported to date require calibration or training that links optical signals with the quantity or identity of an analyte. Unfortunately, calibration is a laboratory procedure that is not practical for non-laboratory users of a portable device, but quantitative capability remains important. Alternative strategies are therefore needed.

One possible strategy is to shift the onus of calibration to the production process. Such factory calibration will require reproducible manufacturing and persistence over long storage periods. It also requires excellent consistency between the readout devices used by the factory and user, and a means of compensating for variation in sample optical properties will be useful for some authentic applications. Detection based on ratio between two colors of luminescence, or on ratio of luminescence intensity between test and reference zones, is expected to provide the best tolerance of variation in sample optical properties and between readout devices. Detection based on changes from one brightfield color to another should also have more tolerance of device variability than detection that is solely based on an absolute intensity of luminescence or the tint of a color.

Digital assays,[592–594] which are an emerging trend in commercial diagnostics and in the general analytical literature, are an exciting alternative strategy. These assays count analyte molecules and are thus quantitative without requiring user calibration. Most digital assays are based on fluorescence and utilize either enzymatic amplification with fluorogenic reactions or the sophisticated and expensive hardware necessary for single-molecule detection. Enzymatic amplification adds reagents to assays with the potential challenges of cold storage, limited shelf life, special digitization chips, extra assay steps, and the associated additional costs. The typical hardware for single-molecule detection is the opposite of what is needed for a portable low-cost device. Here, there are opportunities for innovation in developing ultrabright fluorescent materials and optical configurations that will enable enzyme-free single-molecule detection with a smartphone-based device. Studies have demonstrated that such capability is a viable possibility for single fluorescent NPs and QDs,[86] multi-dye DNA origami,[29] and single dyes.[83] Remaining needs are simplification of hardware and methodology, and approaches to sampling and counting that produces results with suitable accuracy and precision.

Single-molecule detection is also not a strict necessity for quantitation by counting. Assay formats that have highly efficient mass transport of analyte to an interface with capture probes (*e.g.* microfluidic channels, microporous materials) are capable of depleting analyte from a flowing sample solution. A series of discrete clusters of capture probes along the direction of flow are then able to report on the quantity of analyte *via* the number of these clusters that have detectable luminescence or exhibit a color change. There are a myriad of unrealized opportunities for adapting binding assays to this quantitative format.

9.3 Multitasking

When the objective is to enable molecular assays outside of a laboratory, it follows that most users will not want a different smartphone-based device for every analyte or type of assay of interest. The ideal technology will be a single measurement platform that is able to utilize a variety of test strips or chips to execute multiple types of assays for a variety of analytes. This review has already highlighted how a broad scope of assays has been implemented across common test formats like clear plastic tubes, μPADs, LFIA membranes, and microfluidic chips. Assay formats have arguably been more consistent than the designs and optical configurations of the smartphone-based devices used for their readout. Here, there is great opportunity to create single devices that are reconfigurable through interchangeable modules that are matched to different test formats and different illumination configurations (Fig. 54). Smartphone-integrated devices are arguably more readymade for multitasking than linked and dongle devices because of the multitude of on-board features —including a trend of multiple camera modules with different optics—that can be accessed on-demand without bespoke reengineering.

9.4 Cost

The previous subsections outlined objectives that are important and technically challenging to achieve. Researchers must also achieve these objectives on the cheap. Integrating a smartphone into a complex device that costs thousands of dollars will largely defeat the original purpose of adopting the smartphone. Practically, the smartphone must be the most expensive component of any smartphone-based device. In this vein, we propose that the total cost of all components in a device, except the smartphone, should be a multiple, f, of the cost of the smartphone, where $0.01 < f < 0.5$. The value of f should align with the intended use case, such that non-smartphone costs ranges from \$1 to \$600 USD. Here, the opportunity is less innovation and more ingenuity: finding materials and components that are mass produced for consumers for non-scientific reasons and repurposing those things to meet a technical need in a smartphone-based device. One such example already highlighted is replacing research-grade optical filters with low-cost color films.[196,197] Indeed, one of the tenants of "frugal science" is leveraging everyday items for scientific function.[8]

The cost of the test substrate, chips, cartridges, and reagents must also be affordable. For some contexts, an affordable cost will be on the order of dollars per test; for other contexts, it will be on the order of cents per test. The simplification of test platforms is one opportunity for

 This journal is © The Royal Society of Chemistry 2025

Open Access Article. Published on 07 February 2025. Downloaded on 19/4/2026 11:02:09 PM.
This article is licensed under a Creative Commons Attribution-NonCommercial 3.0 Unported Licence.

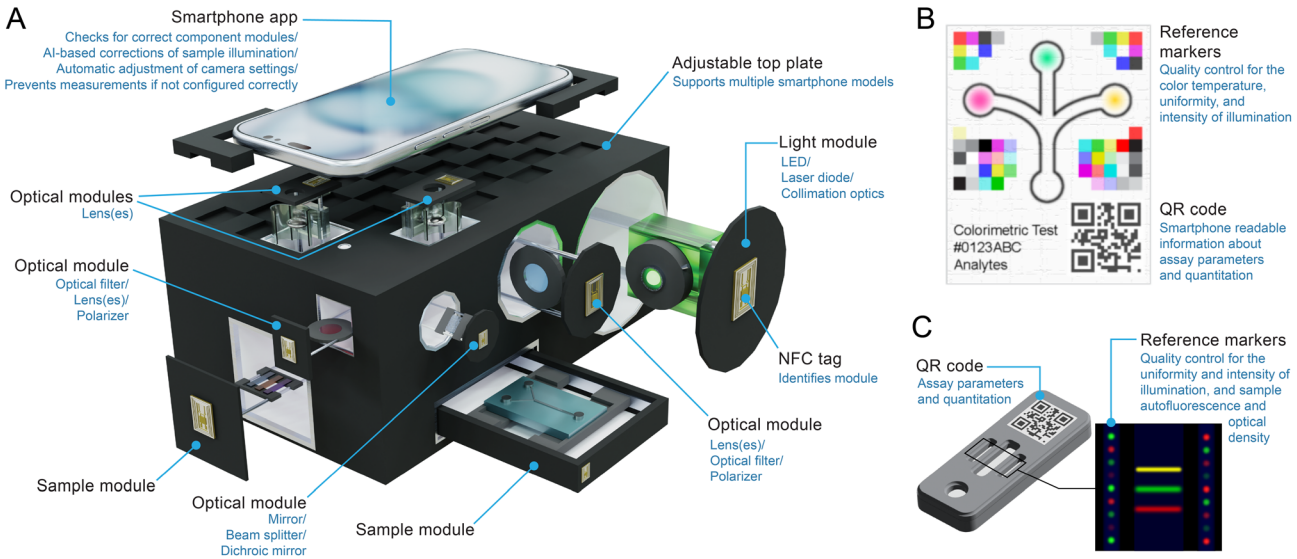

Fig. 54 Reconfigurable, smart devices and smart assays. (A) Hypothetical conceptual design of a reconfigurable smartphone-integrated device with multiple optical paths, interchangeable modules for different illumination sources and configurations, optics, and assay formats (*e.g.* microfluidic or other chips, tests strips or μPADs). (B) Concept for a smart colorimetric test (illustrated in μPAD format) that encodes assay relevant information in a QR code and includes reference markers for automated corrections from variation in illumination. (C) Concept for a smart luminescence test (illustrated in LFIA format) with similar features.

minimizing cost per test. A complete set of reagents freeze-dried or tableted[595,596] into a simple disposable tube or a single-chamber chip will be more economical than multiple reagents loaded at different sites in a multichannel or multi-chamber chip. Affinity and capture agents that can self-conjugate with optical materials and interfaces, with plug-and-play substitution of different agents for different analytes, will minimize preparatory steps and enable multiple test kits to be produced using the same workflow, both reducing costs. Tetrameric antibody complexes (TACs) with fluorescent NPs such as QDs,[597] Pdots,[598] and QD assemblies[485,486] are an example that approaches this ideal.

A reality of the need for low cost and simple operation is that some assays and applications will simply not be practically adaptable to a smartphone-integrated device for the foreseeable future. It is here that adaption of laboratory methods to portable detection is not sufficient, and that completely new methods of analysis must be developed for some analytes and samples.

9.5 Regulatory approval

For clinical applications, *in vitro* diagnostic tests and devices require regulatory approval. Laboratories that serve testing needs in clinical and many other contexts (*e.g.* food, environmental) also require or benefit from accreditations and certifications. Regulatory processes are generally slower than the pace of change in smartphone features and technical specifications, and are predicated, in part, on consistency. With an ever-changing distribution of smartphone models available for purchase and in the hands of consumers, there is natural doubt that regulatory approval of a smartphone-integrated device will be possible.

Another frequent concern is data security and privacy. Of course, challenges with the security of health data already exist with computer systems and are managed. The main difference with the smartphone is that its small size makes it easier to steal or lose. Fortunately, smartphones already support security features (*e.g.* data encryption, device tracking, remote memory wiping). At present, security patches and OS upgrades for devices are at the discretion of the manufacturer: Apple guarantees a minimum of five years, and support for Android phones varies between 2–7 years depending on the manufacturer. Given the trend of increasing consumer concern about privacy, we speculate that the industry (and legislation) will continually take steps to enhance data security. Ultimately, regulatory approval is far more likely to be a barrier to the adoption of smartphone-based devices than security and privacy concerns.

For brevity, to address the question of regulatory approval, the discussion will be limited to the context of *in vitro* diagnostic tests for health applications. We also note that the regulatory hurdle is only an unknown for devices that integrate smartphones. Linked and dongle devices bypass this challenge because the smartphone does not generate the analytical data: there is a single design of a bespoke device to be approved.

So, for a smartphone-integrated device, what are some of the possible pathways to approval?

One pathway starts from the premise that the users for smartphone-integrated diagnostic devices will be professionals and not an arbitrary consumer. For example, a primary care physician or nurse in a rural community will adopt a smartphone-based device to enable local diagnostic

Open Access Article. Published on 07 February 2025. Downloaded on 19/4/2026 11:02:09 PM.
This article is licensed under a Creative Commons Attribution-NonCommercial 3.0 Unported Licence.

capability that would otherwise only be available in a clinical lab in a city hundreds of kilometers away. The professional will also use a smartphone dedicated to diagnostic use and not their personal smartphone. In this scenario, the device can be distributed with one (or a few) specific model(s) of smartphone, providing consistency that will facilitate approval. The caveat is that the approval process may need to be repeated at multi-year intervals to enable upgrades of smartphone technology.

Other potential pathways to approval are predicated on recognition of the positive societal and global impacts of more accessible diagnostics and equitable quality of health care. For example, regulatory agencies might grant limited approval that would enable smartphone-based diagnostic testing in rural and remote communities without a clinical lab, but require that more rigorous clinical lab testing is done prior to medical interventions in the event of a disease indication. Even this limited approval would enhance health care in such communities. Likewise, with the trend of multiple camera modules per smartphone and growing interest in ethical and socially responsible smartphone technology (*e.g.* Fairphone), manufacturers might become inclined (or legislated) to include one diagnostic camera module per smartphone, which would have invariant specifications and data processing between manufacturers and models. This step would provide the consistency to facilitate regulatory approval, and the engineering challenge of accommodating different dimensions of phones is surmountable. Another scenario is that a new pandemic motivates an emergency adoption of smartphone-based methods as a rapidly deployable means of global surveillance, which then opens the door to developing a framework for approval of non-emergency use of the technology. Certainly, the two proactive scenarios are more appealing than this reactive scenario.

Another possible pathway to regulatory approval—and one over which researchers have the most control—is the development of smart tests and smart apps that identify and correct for sources of variability to yield consistent quantitative results (or declare an invalid test) regardless of smartphone model, device platform, and sample source.

9.6 Smart-tests and smart-apps for smartphones

If smartphone-integrated devices are to reach their full potential in enabling globally accessible and democratized molecular analyses, then the technology must embrace variability while also ensuring accuracy and precision in the analytical data. Reconciling this contradiction is well within the capabilities of data processing augmented by ML and AI because, to date, smartphone cameras have not advanced in ways that change their fundamental operating principles. Imagine test strips and chips that integrate reference markers for brightfield colors and tints, and for luminescence colors and intensities. Analysis of the data from these markers will enable corrections for variation in the color temperature of brightfield illumination, the intensity and uniformity of excitation light for luminescence, the intrinsic color or autofluorescence of a crude or minimally processed sample, and differences in the RGB channel responses of different smartphone cameras. QR codes printed on tests can store information about the prescribed data for the reference markers, the parameters from factory calibration of a test, and thresholds for when the smartphone should declare a test result invalid. NFC can be implemented to ensure that a reconfigurable smartphone-integrated device has the correct modules inserted for a given test. In other words, the collective ability of a smartphone camera, device, and sample to produce a reliable result from a test can be evaluated in real-time, and corrections implemented when the variable parameters fall within tolerances. As described in the review, some studies have already implemented these concepts on a more limited and individual basis. More dimensions of this concept, working in concert, will bring about smart-tests and smart-apps as another potential pathway to regulatory approval and the most globally impactful and democratized diagnostic and analytical technologies.

10. Conclusions

Smartphones have been widely adopted as optical detectors and components of prototype devices for portable molecular analyses based on colorimetry and multiple types of luminescence. These devices utilize various combinations of the smartphone camera, flash, and display in tandem with other optics and optoelectronic components, and have achieved practical detection limits in assays of ions and small molecules, immunoassays, nucleic acid amplification tests, cytometry, and more. Although molecular indicator dyes, stains, and fluorophores have been adequate or well suited to many of these methods, the potential for optically active and catalytic NPs to enhance analytical performance has also been demonstrated. For either class of material, smartphone compatible assay formats have included simple sample cells, microwell arrays, lateral flow membranes, test strips, μPADs, and multiple types of microfluidic chips. In short, smartphone-based detection is now a proven concept.

Among the next challenges and opportunities in developing smartphones as analytical tools are the elimination of sample processing for end users, achieving quantitative capability without the need for user-driven calibration, building multitasking devices, and engineering tolerance for operational variability between authentic samples, users, and devices without loss of accuracy and precision. If the field is able to address these challenges, then smartphone-based molecular analyses will be more than a passing fad in research and development and will instead evolve to be a *bona fide* tool in society and industry. Collectively, the design of digital assays and ultrabright materials, embedding smart features in test platforms and device modules, and quality-ensuring ML- and AI-powered software are a prospective route to regulatory approvals and the realization of smartphones as devices that

 This journal is © The Royal Society of Chemistry 2025

Open Access Article. Published on 07 February 2025. Downloaded on 19/4/2026 11:02:09 PM.
This article is licensed under a Creative Commons Attribution-NonCommercial 3.0 Unported Licence.

democratize chemical and biological analysis with global benefits.

Abbreviations

3D	Three-dimensional
A-GPS	Assisted (or augmented) global positioning system
ABS	Acrylonitrile butadiene styrene
AFB1	Aflatoxin B1
AgNP	Silver nanoparticle
AI	Artificial intelligence
ALS	Ambient light sensor
API	Application programming interface
AuNP	Gold nanoparticle
AuNR	Gold nanorod
B	Blue
BCG	Bromocresol green
BL	Bioluminescence
BODIPY	4,4-Difluoro-4-bora-3a,4a-diaza-*s*-indacene
BPA	Bisphenol A
BRET	Bioluminescence resonance energy transfer
Cas	CRISPR-associated protein
CD	Compact disk
CFA	Color filter array
CFU	Colony-forming unit
CIE	International Commission on Illumination
CK-MB	Creatine kinase-MB
CL	Chemiluminescence
CMOS	Complimentary metal-oxide-semiconductor
CRET	Chemiluminescence resonance energy transfer
CRISPR	Clustered regularly interspaced short palindromic repeats
Cy5	Cyanine 5
DAB	3,3′-Diaminobenzidine
DAPI	4′,6-Diamidino-2-phenylindole
DC	Direct current
DLP	Digital light processing
DNA	Deoxyribonucleic acid
DNG	Digital negative
dsDNA	Double-stranded deoxyribonucleic acid
DTNB	5,5′-Dithiobis(2-nitrobenzoic acid)
DVD	Digital versatile disk
ECL	Electrochemiluminescence
ELISA	Enzyme-linked immunosorbent assay
EphA2	Ephrin type-A receptor 2
FDM	Fused deposition modelling
FFF	Fused filament fabrication
FLFIA	Fluorescence lateral flow immunoassay
FPGA	Field programmable gate array
FPS	Frames per second
FRET	Förster resonance energy transfer
FWHM	Full width at half maximum
G	Green
GDP	Gross domestic product
GPIO	General-purpose input/output
GPS	Global positioning system
GUD	Beta-D-glucuronidase
H	Hue
HBV	Hepatitis B virus
HCA	Hierarchical cluster analysis
HCV	Hepatitis C virus
HEIC	High efficiency image container
HiLo	Hybrid illumination
HIV	Human immunodeficiency virus
HPTS	8-Hydroxypyrene-1,3,6-trisulfonic acid
HPV	Human papillomavirus
HRP	Horseradish peroxidase
HSB	Hue-saturation-brightness
HSV	Hue-saturation-value
IDE	Integrated development environment
IR	Infrared
ISO	International Organization for Standardization
JPEG	Joint Photographic Experts Group
LAMP	Loop-mediated isothermal amplification
LCD	Liquid crystal display
LDA	Linear discriminant analysis
LED	Light-emitting diode
LFA	Lateral flow assay
LFIA	Lateral flow immunosorbent assay
LiDAR	Light detection and ranging
LLC	Luminescent lanthanide complex
LM	Latex microsphere
LOC	Lab on a chip
LOD	Limit of detection
LTE	Long term evolution
MCU	Microcontroller unit
MERS-CoV	Middle East respiratory syndrome coronavirus
miRNA	Micro ribonucleic acid
ML	Machine learning
MOF	Metal–organic framework
MSLA	Masked stereolithography
NADH	Nicotinamide adenine dinucleotide
NC	Nitrocellulose
NFC	Near-field communication
NIR	Near-infrared
NN	Neural network
NP	Nanoparticle
NR	Nanorod
OLED	Organic light-emitting diode
OS	Operating system
PCA	Principal component analysis
PCR	Polymerase chain reaction
PDMS	Polydimethylsiloxane
Pdots	Semiconducting polymer dots
PES	Polyethersulfone
PL	Photoluminescence
PLA	Polylactic acid
PLNP	Persistent-luminescent nanoparticle
PMMA	Polymethyl methacrylate
PSA	Prostate-specific antigen
PTSA	1,3,6,8-Pyrenetetrasulfonic acid
QD	Quantum dot

Open Access Article. Published on 07 February 2025. Downloaded on 19/4/2026 11:02:09 PM.
This article is licensed under a Creative Commons Attribution-NonCommercial 3.0 Unported Licence.

qPCR	Quantitative polymerase chain reaction
QR	Quick response
R	Red
RAM	Random-access memory
RCA	Rolling circle amplification
RFLFIA	Ratiometric fluorescence lateral flow immunoassay
RGB	Red, green, blue
RNA	Ribonucleic acid
ROI	Region of interest
ROX	Carboxyrhodamine
RPA	Recombinase polymerase amplification
rRNA	Ribosomal ribonucleic acid
RT	Reverse transcription
RTF-EXPAR	Reverse transcription-free exponential amplification reaction
S	Saturation
SARS-CoV-2	Severe acute respiratory syndrome coronavirus 2
SBC	Single-board computer
SDK	Software development kit
SLA	Stereolithography
SPR	Surface plasmon resonance
SVM	Support vector machine
TAC	Tetrameric antibody complex
TAMRA	Carboxytetramethylrhodamine
TMB	3,3′,5,5′-Tetramethylbenzidine
TNFα	Tumor necrosis factor
ToF	Time-of-flight
TRRS	Tip-ring ring-sleeve
TTA	Triplet–triplet annihilation
UCNP	Upconversion nanoparticle
USB	Universal serial bus
USB-C	Universal serial bus type-C
USD	United states dollar
UV	Ultraviolet
UVB	Ultraviolet B
UVC	Ultraviolet C
V	Value
W	White
Y	Yellow
ZIF	Zeolitic imidazolate framework
μPAD	Micro paper analytical device

Data availability

The data supporting the meta-analysis in this review article have been uploaded as ESI† in a Microsoft Excel spreadsheet file format (.xlsx).

Author contributions

Daina V. Baker: writing – original draft preparation; formal analysis (data for Fig. 14); investigation (data for Fig. 2–5, 7); visualization (adaptation of figures from the literature, Fig. 1, 6, 13). Jasmine Bernal-Escalante: writing – original draft preparation; formal analysis (data for Fig. 14); investigation (data for Fig. 2–5, 7); visualization (adaptation of figures from the literature). Christine Traaseth: writing – original draft preparation; formal analysis (data for Fig. 14); investigation (data for Fig. 2–5, 7); visualization (adaptation of figures from the literature). Yihao Wang: writing – original draft preparation; visualization (adaptation of figures from the literature, creation of device models in Fig. 1, 9, 54A). Michael V. Tran: writing – original draft preparation. Seth Keenan: writing – original draft preparation. W. Russ Algar: conceptualization; writing – review & editing; visualization; supervision; funding acquisition.

Conflicts of interest

There are no conflicts to declare.

Acknowledgements

We thank the Natural Sciences and Engineering Research Council of Canada (NSERC), Canadian Institutes of Health Research (CIHR), Canada Foundation for Innovation (CFI), British Columbia Knowledge Development Fund (BCKDF), and the University of British Columbia (UBC) for support of our research program. JBE is grateful for a Miguel Romero Sánchez Fellowship in Chemistry from UBC. SK is grateful for an NSERC Canada Graduate Scholarship, an Ed Shuter Scholarship, and a Gladys Estella Laird Research Fellowship. We thank Zhujun Xiao and Rupsa Gupta for helpful discussion, and Ghinwa Darwish for providing the QD PL emission spectra data.

References

1 E. Samiei, M. Tabrizian and M. Hoorfar, *Lab Chip*, 2016, **16**, 2376–2396.
2 S. Surappa, P. Multani, U. Parlatan, P. D. Sinawang, J. Kaifi, D. Akin and U. Demirci, *Lab Chip*, 2023, **23**, 2942–2958.
3 N. Azizipour, R. Avazpour, D. H. Rosenzweig, M. Sawan and A. Ajji, *Micromachines*, 2020, **11**, 599.
4 V. Narayanamurthy, Z. E. Jeroish, K. S. Bhuvaneshwari, P. Bayat, R. Premkumar, F. Samsuri and M. M. Yusoff, *RSC Adv.*, 2020, **10**, 11652–11680.
5 U. A. Gurkan, D. K. Wood, D. Carranza, L. H. Herbertson, S. L. Diamond, E. Du, S. Guha, J. D. Paola, P. C. Hines, I. Papautsky, S. S. Shevkoplyas, N. J. Sniadecki, V. K. Pamula, P. Sundd, A. Rizwan, P. Qasba and W. A. Lam, *Lab Chip*, 2024, **24**, 1867–1874.
6 *68% of the world population projected to live in urban areas by 2050*, says UN, **https://www.un.org/uk/desa/68-world-population-projected-live-urban-areas-2050-says-un**, (accessed 4 November 2024).
7 *Urban Development: Overview*, **https://www.worldbank.org/en/topic/urbandevelopment/overview**, (accessed 4 November 2024).
8 G. Byagathvalli, E. J. Challita and M. S. Bhamla, *Ind. Eng. Chem. Res.*, 2021, **60**, 15874–15884.
9 M. Monteiro and A. C. Martí, *Am. J. Phys.*, 2022, **90**, 328–343.

 This journal is © The Royal Society of Chemistry 2025

Open Access Article. Published on 07 February 2025. Downloaded on 19/4/2026 11:02:09 PM.
This article is licensed under a Creative Commons Attribution-NonCommercial 3.0 Unported Licence.

10 P. Taylor, *Number of mobile (cellular) subscriptions worldwide from 1993 to 2023*, **https://www.statista.com/statistics/262950/global-mobile-subscriptions-since-1993/**, (accessed 4 November 2024).
11 F. Laricchia, *Penetration rate of smartphones in selected countries 2022*, **https://www.statista.com/statistics/539395/smartphone-penetration-worldwide-by-country/**, (accessed 4 November 2024).
12 *Smartphone owners are now the global majority*, New GSMA report reveals, **https://www.gsma.com/newsroom/press-release/smartphone-owners-are-now-the-global-majority-new-gsma-report-reveals/**, (accessed 4 November 2024).
13 P. Taylor, Mobile coverage rate worldwide from 2011 to 2029, by technology, **https://www.statista.com/statistics/1016292/mobile-coverage-by-technology-worldwide/**, (accessed 4 November 2024).
14 N. O. Theonest, K. Ngowi, E. R. Kussaga, A. Lyimo, D. Kuchaka, I. Kiwelu, D. Machuve, J.-M. Vianney, J. Reboud, B. T. Mmbaga, J. M. Cooper and J. Buza, *PLOS Digit. Health*, 2024, **3**, e0000565.
15 *The Mobile Economy 2022*, **https://www.gsma.com/solutions-and-impact/connectivity-for-good/mobile-economy/wp-content/uploads/2022/02/280222-The-Mobile-Economy-2022.pdf**, (accessed 4 November 2024).
16 F. Laricchia, *Number of smartphones sold to end users worldwide from 2007 to 2023*, **https://www.statista.com/statistics/263437/global-smartphone-sales-to-end-users-since-2007/**, (accessed 4 November 2024).
17 G. R. D. Prabhu and P. L. Urban, *Chem. Rev.*, 2020, **120**, 9482–9553.
18 G. Niezen, P. Eslambolchilar and H. Thimbleby, *BMJ Innov.*, 2016, **2**, 78–83.
19 J. M. Pearce, *Sci. Public Policy*, 2016, **43**, 192–195.
20 M. D. M. Dryden, R. Fobel, C. Fobel and A. R. Wheeler, *Anal. Chem.*, 2017, **89**, 4330–4338.
21 S. Lehtola and A. J. Karttunen, *WIREs Comput. Mol. Sci.*, 2022, **12**, e1610.
22 A. M. Chagas, *PLoS Biol.*, 2018, **16**, e3000014.
23 R. M. Sarıyer, A. D. Edwards and S. H. Needs, *Biosensors*, 2023, **13**, 948.
24 J. J. Davis, S. W. Foster and J. P. Grinias, *J. Chromatogr. A*, 2021, **1638**, 461820.
25 I. Nuñez, T. Matute, R. Herrera, J. Keymer, T. Marzullo, T. Rudge and F. Federici, *PLoS One*, 2017, **12**, e0187163.
26 S. Majumder and M. J. Deen, *ACS Sens.*, 2019, **19**, 2164.
27 Y. Xia, J. Hu, S. Zhao, L. Tao, Z. Li, T. Yue and J. Kong, *Biosens. Bioelectron.: X*, 2022, **11**, 100195.
28 S. Tominaga, S. Nishi and R. Ohtera, *ACS Sens.*, 2021, **21**, 4985.
29 C. Vietz, M. L. Schütte, Q. Wei, L. Richter, B. Lalkens, A. Ozcan, P. Tinnefeld and G. P. Acuna, *ACS Omega*, 2019, **4**, 637–642.
30 T. Krishnan, H.-N. Wang and T. Vo-Dinh, *ACS Sens.*, 2021, **21**, 8044.
31 X. Ruan, V. Hulubei, Y. Wang, Q. Shi, N. Cheng, L. Wang, Z. Lyu, W. C. Davis, J. N. Smith, Y. Lin and D. Du, *Biosens. Bioelectron.*, 2022, **208**, 114190.
32 E. V. Woodburn, K. D. Long and B. T. Cunningham, *IEEE Sens. J.*, 2019, **19**, 508–514.
33 W. Cao, Y. Deng, T. Pan, H. Hao and M. Wang, *IEEE Photonics J.*, 2019, **11**, 6802708.
34 M. Schäfer, V. Bräuler and R. Ulber, *Sens. Actuators, B*, 2018, **255**, 1902–1910.
35 A. S. Paterson, B. Raja, V. Mandadi, B. Townsend, M. Lee, A. Buell, B. Vu, J. Brgoch and R. C. Willson, *Lab Chip*, 2017, **17**, 1051–1059.
36 M. Hermann, P. Agrawal, I. Koch and R. Oleschuk, *Lab Chip*, 2019, **19**, 654–664.
37 M. R. Muir and A. Innes, *Anal. Methods*, 2024, **16**, 5571–5583.
38 E. Petryayeva and W. R. Algar, *Anal. Bioanal. Chem.*, 2016, **408**, 2913–2925.
39 R. Gupta, W. J. Peveler, K. Lix and W. R. Algar, *Anal. Chem.*, 2019, **91**, 10955–10960.
40 Y. Sekine, S. B. Kim, Y. Zhang, A. J. Bandodkar, S. Xu, J. Choi, M. Irie, T. R. Ray, P. Kohli, N. Kozai, T. Sugita, Y. Wu, K. Lee, K.-T. Lee, R. Ghaffari and J. A. Rogers, *Lab Chip*, 2018, **18**, 2178–2186.
41 F. He, X. Lv, X. Li, M. Yao, K. Li and Y. Deng, *Microchem. J.*, 2022, **179**, 107551.
42 S. Jain, A. Paliwal, V. Gupta and M. Tomar, *Biosens. Bioelectron.*, 2022, **201**, 113919.
43 Y. Liu, Q. Liu, S. Chen, F. Cheng, H. Wang and W. Peng, *Sci. Rep.*, 2015, **5**, 12864.
44 L. Lu, Z. Jiang, Y. Hu, H. Zhou, G. Liu, Y. Chen, Y. Luo and Z. Chen, *Opt. Express*, 2019, **27**, 25420–25427.
45 Q. Zhang, Y. Li, Q. Hu, R. Xie, W. Zhou, X. Liu and Y. Wang, *Lab Chip*, 2022, **22**, 4941–4949.
46 P. Preechaburana and S. Amloy, *Eur. J. Phys.*, 2021, **42**, 045302.
47 S. Kheireddine, A. S. Perumal, Z. J. Smith, D. V. Nicolau and S. Wachsmann-Hogiu, *Lab Chip*, 2019, **19**, 825–836.
48 N. Phadungcharoen, N. Pengwanput, A. Nakapan, U. Sutitaphan, P. Thanomklom, N. Jongudomsombut, A. Chinsriwongkul and T. Rojanarata, *Talanta*, 2020, **219**, 121271.
49 S. Kheireddine, Z. J. Smith, D. V. Nicolau and S. Wachsmann-Hogiu, *Biomed. Opt. Express*, 2019, **10**, 4369–4380.
50 D. Rabha, M. A. Rather, M. Mandal and P. Nath, *Opt. Lasers Eng.*, 2022, **151**, 106931.
51 J. Yu, X. Qin, D. Wang, C. Lin, X. Xian and N. Tao, *Anal. Chem.*, 2019, **91**, 6632–6637.
52 J. Chan, A. Raghunath, K. E. Michaelsen and S. Gollakota, *Proc. ACM Interact. Mob. Wearable Ubiquitous Technol.*, 2022, **6**, 1–27.
53 M. Bouazizi, C. Ye and T. Ohtsuki, *2021 IEEE Global Communications Conference*, 2021, pp. 1–6.
54 Y. Liu, G. W. Wornell, W. T. Freeman and F. Durand, *Sci. Adv.*, 2024, **10**, eadj3608.
55 D. Hatiboruah, D. Y. Devi, N. D. Namsa and P. Nath, *J. Biophotonics*, 2020, **13**, e201960159.

Open Access Article. Published on 07 February 2025. Downloaded on 19/4/2026 11:02:09 PM.
This article is licensed under a Creative Commons Attribution-NonCommercial 3.0 Unported Licence.

56 X. Chen, C. Ma, Q. Kang, Y. Chen and D. Shen, *New J. Chem.*, 2021, **45**, 2529–2535.
57 Q. Fu, C. Zhang, J. Xie, Z. Li, L. Qu, X. Cai, H. Ouyang, Y. Song, D. Du, Y. Lin and Y. Tang, *Anal. Chim. Acta*, 2019, **1092**, 126–131.
58 Y. Zhao, M. Yang, Q. Fu, H. Ouyang, W. Wen, Y. Song, C. Zhu, Y. Lin and D. Du, *Anal. Chem.*, 2018, **90**, 7391–7398.
59 L. Huang, W. Xiao, T. Xu, H. Chen, Z. Jin, Z. Zhang, Q. Song and Y. Tang, *Sens. Actuators, B*, 2021, **327**, 128893.
60 H. Xu, A. Xia, J. Luo, M. Gao, R. Liao, F. Li, Q. Zhong, W. Zhang, Y. Wang, J. Cui, W. Fu, K. Chang, M. Gan, W. Jiang and M. Chen, *Sens. Actuators, B*, 2020, **308**, 127750.
61 E. Zhang, Q. Zeng, Y. Xu, J. Lu, C. Li, K. Xiao, X. Li, J. Li, T. Li, C. Li and L. Zhang, *Lab Chip*, 2024, **24**, 4639–4648.
62 Y. Castillo-Escario, I. Ferrer-Lluis, J. M. Montserrat and R. Jané, in *2019 41st Annual International Conference of the IEEE Engineering in Medicine and Biology Society (EMBC)*, 2019, pp. 4982–4985.
63 H. Nakano, K. Hirayama, Y. Sadamitsu, A. Toshimitsu, H. Fujita, S. Shin and T. Tanigawa, *J. Clin. Sleep Med.*, 2014, **10**, 73–78.
64 L. Montanini, N. Sabino, S. Spinsante and E. Gambi, *2018 IEEE International Conference on Consumer Electronics*, 2018, pp. 1–4.
65 *Phyphox sensor database*, **https://phyphox.org/sensordb/** (accessed 15 January 2025).
66 A. Sherif, *Market share of mobile operating systems worldwide from 2009 to 2024*, by quarter, **https://www.statista.com/statistics/272698/global-market-share-held-by-mobile-operating-systems-since-2009/** (accessed 4 November 2024).
67 B. C. Gross, J. L. Erkal, S. Y. Lockwood, C. Chen and D. M. Spence, *Anal. Chem.*, 2014, **86**, 3240–3253.
68 C. Schubert, M. C. van Langeveld and L. A. Donoso, *Br. J. Ophthalmol.*, 2014, **98**, 159–161.
69 T. Rayna and L. Striukova, *Technol. Forecast. Soc. Change*, 2016, **102**, 214–224.
70 R. Su, F. Wang and M. C. McAlpine, *Lab Chip*, 2023, **23**, 1279–1299.
71 N. Bhattacharjee, A. Urrios, S. Kanga and A. Folch, *Lab Chip*, 2016, **16**, 1720–1742.
72 S. Waheed, J. M. Cabot, N. P. Macdonald, T. Lewis, R. M. Guijt, B. Paull and M. C. Breadmore, *Lab Chip*, 2016, **16**, 1993–2013.
73 G. D. Berglund and T. S. Tkaczyk, *Opt. Express*, 2019, **27**, 30405–30420.
74 N. Vaidya and O. Solgaard, *Microsyst. Nanoeng.*, 2018, **4**, 18.
75 J. Christopher, L. M. Rooney, M. Donnachie, D. Uttamchandani, G. McConnell and R. Bauer, *Biomed. Opt. Express*, 2024, **15**, 2224–2237.
76 V. R. Pereira and B. S. Hosker, *PLoS Biol.*, 2019, **17**, e3000321.
77 Y. Jung, Y. Heo, J. J. Lee, A. Deering and E. Bae, *J. Microbiol. Methods*, 2020, **168**, 105800.
78 X. Hu, L. Huang, S. Wang, R. Ahmed, P. Li, U. Demirci and Z. Zhang, *Sens. Actuators, B*, 2023, **376**, 132956.
79 J. Shin, S. Kim, T. Yoon, C. Joo and H.-I. Jung, *Biosens. Bioelectron.*, 2019, **136**, 106–111.
80 S. Li, X. Zhong, Y. Xu, Y. Zheng, X. Shi, F. Li, S. Guo and J. Yang, *Food Chem.*, 2021, **360**, 130019.
81 K. Ming, J. Kim, M. J. Biondi, A. Syed, K. Chen, A. Lam, M. Ostrowski, A. Rebbapragada, J. J. Feld and W. C. W. Chan, *ACS Nano*, 2015, **9**, 3060–3074.
82 B. Ning, T. Yu, S. Zhang, Z. Huang, D. Tian, Z. Lin, A. Niu, N. Golden, K. Hensley, B. Threeton, C. J. Lyon, X.-M. Yin, C. J. Roy, N. S. Saba, J. Rappaport, Q. Wei and T. Y. Hu, *Sci. Adv.*, 2021, **7**, eabe3703.
83 K. Trofymchuk, V. Glembockyte, L. Grabenhorst, F. Steiner, C. Vietz, C. Close, M. Pfeiffer, L. Richter, M. L. Schütte, F. Selbach, R. Yaadav, J. Zähringer, Q. Wei, A. Ozcan, B. Lalkens, G. P. Acuna and P. Tinnefeld, *Nat. Commun.*, 2021, **12**, 950.
84 M. V. Tran, K. Susumu, I. L. Medintz and W. R. Algar, *Anal. Chem.*, 2019, **91**, 11963–11971.
85 Z. Xiao, G. H. Darwish, K. Susumu, I. L. Medintz and W. R. Algar, *ACS Meas. Sci. Au*, 2022, **2**, 57–66.
86 Q. Wei, G. Acuna, S. Kim, C. Vietz, D. Tseng, J. Chae, D. Shir, W. Luo, P. Tinnefeld and A. Ozcan, *Sci. Rep.*, 2017, **7**, 2124.
87 H. K. Kondaveeti, N. K. Kumaravelu, S. D. Vanambathina, S. E. Mathe and S. Vappangi, *Comput. Sci. Rev.*, 2021, **40**, 100364.
88 J. M. Pearce, *HardwareX*, 2020, **8**, e00139.
89 K. de Haan, H. Ceylan Koydemir, Y. Rivenson, D. Tseng, E. Van Dyne, L. Bakic, D. Karinca, K. Liang, M. Ilango, E. Gumustekin and A. Ozcan, *NPJ Digit. Med.*, 2020, **3**, 1–9.
90 N. H. Bhuiyan, J. H. Hong, M. J. Uddin and J. S. Shim, *Anal. Chem.*, 2022, **94**, 3872–3880.
91 Z. Zhang, S. Zhao, L. Jiang, J. Wu, W. Zhao, X. Guo, N. Peng and F. Hu, *Analyst*, 2022, **147**, 4876–4887.
92 L. Zhu, S. Li, W. Liu, J. Chen, Q. Yu, Z. Zhang, Y. Li, J. Liu and X. Chen, *Biosens. Bioelectron.*, 2021, **187**, 113284.
93 M. A. Kabir, H. Zilouchian, M. Sher and W. Asghar, *Diagnostics*, 2020, **10**, 42.
94 T. Gou, J. Hu, W. Wu, X. Ding, S. Zhou, W. Fang and Y. Mu, *Biosens. Bioelectron.*, 2018, **120**, 144–152.
95 V. D. Nguyen, H. Q. Nguyen, K. H. Bui, Y. S. Ko, B. J. Park and T. S. Seo, *Biosens. Bioelectron.*, 2022, **195**, 113632.
96 S. Duan, T. Cai, F. Liu, Y. Li, H. Yuan, W. Yuan, K. Huang, K. Hoettges, M. Chen, E. G. Lim, C. Zhao and P. Song, *Anal. Chim. Acta*, 2024, **1308**, 342575.
97 J. J. Lee, J. Kang and C. Kim, *J. Hazard. Mater.*, 2024, **465**, 133168.
98 X. Xu, L. Cai, S. Liang, Q. Zhang, S. Lin, M. Li, Q. Yang, C. Li, Z. Han and C. Yang, *Lab Chip*, 2023, **23**, 1169–1191.
99 M. Yafia, A. Ahmadi, M. Hoorfar and H. Najjaran, *Micromachines*, 2015, **6**, 1289–1305.
100 S. K. Thio and S.-Y. Park, *Lab Chip*, 2022, **22**, 3987–4006.
101 Y. Li, S. Cai, H. Shen, Y. Chen, Z. Ge and W. Yang, *Biomicrofluidics*, 2022, **16**, 031502.
102 P. Zhang, H. Bachman, A. Ozcelik and T. J. Huang, *Annu. Rev. Anal. Chem.*, 2020, **13**, 17–43.

 This journal is © The Royal Society of Chemistry 2025

Open Access Article. Published on 07 February 2025. Downloaded on 19/4/2026 11:02:09 PM.
This article is licensed under a Creative Commons Attribution-NonCommercial 3.0 Unported Licence.

103 E. M. Khalaf, H. Sanaan Jabbar, R. Mireya Romero-Parra, G. R. L. Al-Awsi, H. S. Budi, A. S. Altamimi, M. Abdulfadhil Gatea, K. T. Falih, K. Singh and K. A. Alkhuzai, *Microchem. J.*, 2023, **190**, 108692.
104 N. Convery and N. Gadegaard, *Micro Nano Eng.*, 2019, **2**, 76–91.
105 M. N. H. Z. Alam, F. Hossain, A. Vale and A. Kouzani, *Int. J. Precis. Eng. Manuf.*, 2017, **18**, 1287–1296.
106 J. A. Cataño, S. Farthing, Z. Mascarenhas, N. Lake, P. K. D. V. Yarlagadda, Z. Li and Y.-C. Toh, *Micromachines*, 2023, **14**, 930.
107 T. Ching, J. Vasudevan, H. Y. Tan, C. T. Lim, J. Fernandez, Y.-C. Toh and M. Hashimoto, *HardwareX*, 2021, **10**, e00202.
108 S. B. Park and J. H. Shin, *HardwareX*, 2024, **19**, e00550.
109 M. R. Behrens, H. C. Fuller, E. R. Swist, J. Wu, M. M. Islam, Z. Long, W. C. Ruder and R. Steward, *Sci. Rep.*, 2020, **10**, 1543.
110 A. Jönsson, A. Toppi and M. Dufva, *HardwareX*, 2020, **8**, e00115.
111 A. S. Samokhin, *J. Anal. Chem.*, 2020, **75**, 416–421.
112 S. B. Park and J. H. Shin, *Sens. Actuators, B*, 2024, **405**, 135289.
113 S. Baas and V. Saggiomo, *HardwareX*, 2021, **10**, e00219.
114 E. Noviana, T. Ozer, C. S. Carrell, J. S. Link, C. McMahon, I. Jang and C. S. Henry, *Chem. Rev.*, 2021, **121**, 11835–11885.
115 A. Olanrewaju, M. Beaugrand, M. Yafia and D. Juncker, *Lab Chip*, 2018, **18**, 2323–2347.
116 S. Nishat, A. T. Jafry, A. W. Martinez and F. R. Awan, *Sens. Actuators, B*, 2021, **336**, 129681.
117 S. Altundemir, A. K. Uguz and K. Ulgen, *Biomicrofluidics*, 2017, **11**, 041501.
118 T. Narahari, J. Dahmer, A. Sklavounos, T. Kim, M. Satkauskas, I. Clotea, M. Ho, J. Lamanna, C. Dixon, D. G. Rackus, S. J. R. da Silva, L. Pena, K. Pardee and A. R. Wheeler, *Lab Chip*, 2022, **22**, 1748–1763.
119 X. Liu, D. Ma, H. Ye, Y. Hou, X. Bai, Y. Xing, X. Cheng, B. Lin and Y. Lu, *TrAC, Trends Anal. Chem.*, 2023, **166**, 117153.
120 E. Samiei, M. Tabrizian and M. Hoorfar, *Lab Chip*, 2016, **16**, 2376–2396.
121 S. L. S. Freire, *Sens. Actuators, A*, 2016, **250**, 15–28.
122 K. Choi, A. H. C. Ng, R. Fobel and A. R. Wheeler, *Annu. Rev. Anal. Chem.*, 2012, **5**, 413–440.
123 R. Fobel, C. Fobel and A. R. Wheeler, *Appl. Phys. Lett.*, 2013, **102**, 193513.
124 V. D. Nguyen, H. Q. Nguyen, K. H. Bui, Y. S. Ko, B. J. Park and T. S. Seo, *Biosens. Bioelectron.*, 2022, **195**, 113632.
125 H. Jiang, D. Jiang, X. Liu and J. Yang, *Sens. Actuators, B*, 2021, **349**, 130785.
126 W. Xu, M. Althumayri, A. Mohammad and H. C. Koydemir, *Biosens. Bioelectron.*, 2023, **242**, 115755.
127 L. Yang, Z. Zhang and X. Wang, *Micromachines*, 2022, **13**, 552.
128 S. Ghosh, K. Aggarwal, V. T. U., T. Nguyen, J. Han and C. H. Ahn, *Microsyst. Nanoeng.*, 2020, **6**, 1–18.
129 A. Agha, W. Waheed, N. Alamoodi, B. Mathew, F. Alnaimat, E. Abu-Nada, A. Abderrahmane and A. Alazzam, *Macromol. Mater. Eng.*, 2022, **307**, 2200053.
130 Y.-J. Juang and Y.-J. Chiu, *Polymers*, 2022, **14**, 2028.
131 W. R. Algar, M. Massey, K. Rees, R. Higgins, K. D. Krause, G. H. Darwish, W. J. Peveler, Z. Xiao, H.-Y. Tsai, R. Gupta, K. Lix, M. V. Tran and H. Kim, *Chem. Rev.*, 2021, **121**, 9243–9358.
132 L. A. Marquez and H. B. Dunford, *Biochemistry*, 1997, **36**, 9349–9355.
133 M. Taniguchi and J. S. Lindsey, *Photochem. Photobiol.*, 2018, **94**, 290–327.
134 S. K. Gupta, R. M. Kadam and P. K. Pujari, *Coord. Chem. Rev.*, 2020, **420**, 213405.
135 S. Li, Y. Zhang, Q. Wang, A. Lin and H. Wei, *Anal. Chem.*, 2022, **94**, 312–323.
136 D. Jiang, D. Ni, Z. T. Rosenkrans, P. Huang, X. Yan and W. Cai, *Chem. Soc. Rev.*, 2019, **48**, 3683–3704.
137 E. Petryayeva, W. R. Algar and I. L. Medintz, *Appl. Spectrosc.*, 2013, **67**, 215–252.
138 H. Zhong, T. Mirkovic and G. D. Scholes, in *Comprehensive Nanoscience and Technology*, ed. D. L. Andrews, G. D. Scholes and G. P. Wiederrecht, Academic Press, Amsterdam, 2011, pp. 153–201.
139 E. Petryayeva and W. R. Algar, *Anal. Chem.*, 2014, **86**, 3195–3202.
140 E. Petryayeva and W. R. Algar, *Anal. Chem.*, 2013, **85**, 8817–8825.
141 E. Petryayeva and W. R. Algar, *Analyst*, 2015, **140**, 4037–4045.
142 K. M. Tsoi, Q. Dai, B. A. Alman and W. C. W. Chan, *Acc. Chem. Res.*, 2013, **46**, 662–671.
143 C. E. Bradburne, J. B. Delehanty, K. B. Gemmill, B. C. Mei, H. Mattoussi, K. Susumu, J. B. Blanco-Canosa, P. E. Dawson and I. L. Medintz, *Bioconjugate Chem.*, 2013, **24**, 1570–1583.
144 E. Oh, R. Liu, A. Nel, K. B. Gemill, M. Bilal, Y. Cohen and I. L. Medintz, *Nat. Nanotechnol.*, 2016, **11**, 479–486.
145 R. Gupta, W. J. Peveler, K. Lix and W. R. Algar, *Anal. Chem.*, 2019, **91**, 10955–10960.
146 K. Sun, Y. Yang, H. Zhou, S. Yin, W. Qin, J. Yu, D. T. Chiu, Z. Yuan, X. Zhang and C. Wu, *ACS Nano*, 2018, **12**, 5176–5184.
147 H. Chen, J. Yu, X. Men, J. Zhang, Z. Ding, Y. Jiang, C. Wu and D. T. Chiu, *Angew. Chem., Int. Ed.*, 2021, **60**, 12007–12012.
148 F. Wang and X. Liu, *Chem. Soc. Rev.*, 2009, **38**, 976–989.
149 S. Wen, J. Zhou, K. Zheng, A. Bednarkiewicz, X. Liu and D. Jin, *Nat. Commun.*, 2018, **9**, 2415.
150 S. S. Kanani, H.-Y. Tsai and W. R. Algar, *Anal. Chem.*, 2023, **95**, 13258–13265.
151 S. Wu, Y. Li, W. Ding, L. Xu, Y. Ma and L. Zhang, *Nano-Micro Lett.*, 2020, **12**, 70.
152 Y. Yakimova, *European Parliament*, Long-awaited common charger for mobile devices will be a reality in 2024, **https://www.europarl.europa.eu/news/en/press-room/20220930IPR41928/long-awaited-common-charger-for-mobile-devices-will-be-a-reality-in-2024**, (accessed 2024/11/04).

Open Access Article. Published on 07 February 2025. Downloaded on 19/4/2026 11:02:09 PM.
This article is licensed under a Creative Commons Attribution-NonCommercial 3.0 Unported Licence.

153 J. Hou, M. Li and Y. Song, *Nano Today*, 2018, **22**, 132–144.
154 L. Hu and M. J. Serpe, *Polymers*, 2012, **4**, 134–149.
155 J. Seo, J. Kang, J. Kim, H. Han, M. Park, M. Shin and K. Lee, *ACS Biomater. Sci. Eng.*, 2024, **10**, 4035–4045.
156 G. Chen, C. Fang, H. H. Chai, Y. Zhou, W. Yun Li and L. Yu, *Sens. Actuators, B*, 2019, **281**, 253–261.
157 M. Moslemzadeh, A. Larki and K. Ghanemi, *Microchem. J.*, 2020, **159**, 105583.
158 V. A. O. P. da Silva, R. C. de Freitas, P. R. de Oliveira, R. C. Moreira, L. H. Marcolino-Júnior, M. F. Bergamini, W. K. T. Coltro and B. C. Janegitz, *Measurement*, 2020, **164**, 108085.
159 S. Apichai, N. Thunyajaroen, T. Prajongsangsri, P. Tananchai, T. Pattananandecha, F. Ogata, N. Kawasaki, K. Grudpan and C. Saenjum, *Sustainable Chem. Pharm.*, 2022, **29**, 100808.
160 A. Shahvar, D. Shamsaei and M. Saraji, *Measurement*, 2020, **150**, 107068.
161 H. Zhang, R. Liu, Q. Li, X. Hu, L. Wu, Y. Zhou, G. Qing, R. Yuan, J. Huang, W. Gu, Y. Ye, C. Qi, M. Han, X. Chen, X. Zhu, Y. Deng, L. Zhang, H. Chen, H. Zhang, W. Gao, Y. Liu and Y. Luo, *ACS Nano*, 2021, **15**, 7649–7658.
162 H. Choi, J. H. Seo and S. Weon, *J. Hazard. Mater.*, 2023, **460**, 132510.
163 K. Zhang, J. Zhang, F. Wang and D. Kong, *ACS Sens.*, 2021, **6**, 2261–2269.
164 Y. Sun, J. Wang, Q. Lu, J. Zhang, Y. Li, Y. Pang, C. Yang, Q. Wang and D. Kong, *ACS Sens.*, 2024, **9**, 1515–1524.
165 T. Taccioli, E. Ragusa, T. Pomili, P. Gastaldo and P. P. Pompa, *IEEE Sens. J.*, 2023, **23**, 29869–29876.
166 B. Berg, B. Cortazar, D. Tseng, H. Ozkan, S. Feng, Q. Wei, R. Y.-L. Chan, J. Burbano, Q. Farooqui, M. Lewinski, D. Di Carlo, O. B. Garner and A. Ozcan, *ACS Nano*, 2015, **9**, 7857–7866.
167 Z. Wu, C. Wang, B. Liu, C. Liang, J. Lu, J. Li, X. Tang, C. Li and T. Li, *ACS Sens.*, 2022, **7**, 1985–1995.
168 R. Deng, X. Chao, H. Li, X. Li, Z. Yang and H.-Z. Yu, *Analyst*, 2023, **148**, 735–741.
169 Y. Yano-Ozawa, N. Lobsiger, Y. Muto, T. Mori, K. Yoshimura, Y. Yano, W. J. Stark, M. Maeda, T. Asahi, A. Ogawa and T. Zako, *RSC Adv.*, 2021, **11**, 11984–11991.
170 X. Huang, Y. Yan, L. Zhang, L. Yuan, Y. Tang, X. Jiang, W. Zhu, Y. Yuan, J. Nie and Y. Zhang, *Anal. Bioanal. Chem.*, 2024, **416**, 1821–1832.
171 Q. Gao, J. Wan, X. Chen, X. Mo, Y. Sun, J. Zou, J. Nie and Y. Zhang, *RSC Adv.*, 2021, **11**, 39306–39310.
172 S. Chung, L. E. Breshears, A. Gonzales, C. M. Jennings, C. M. Morrison, W. Q. Betancourt, K. A. Reynolds and J.-Y. Yoon, *Nat. Protoc.*, 2021, **16**, 1452–1475.
173 T. Ghonge, H. C. Koydemir, E. Valera, J. Berger, C. Garcia, N. Nawar, J. Tiao, G. L. Damhorst, A. Ganguli, U. Hassan, A. Ozcan and R. Bashir, *Analyst*, 2019, **144**, 3925–3935.
174 M. A. Sami, M. Tayyab, P. Parikh, H. Govindaraju and U. Hassan, *Analyst*, 2021, **146**, 2531–2541.
175 L. Zhang, K. S. Chen and H.-Z. Yu, *ACS Appl. Mater. Interfaces*, 2020, **12**, 7665–7672.
176 C. Jurischka, F. Dinter, A. Efimova, R. Weiss, J. Schiebel, C. Schulz, B. Fayziev, P. Schierack, T. Fischer and S. Rödiger, *Clin. Hemorheol. Microcirc.*, 2020, **75**, 57–84.
177 A. Piruska, I. Nikcevic, S. H. Lee, C. Ahn, W. R. Heineman, P. A. Limbach and C. J. Seliskar, *Lab Chip*, 2005, **5**, 1348–1354.
178 W. E. van der Veer and D. Wolpert, *Laser Focus World*, Optics for microscopy: Fluorescence of colored-glass filters can be stronger than expected, **https://www.laserfocusworld.com/optics/article/16554918/optics-for-microscopy-fluorescence-of-colored-glass-filters-can-be-stronger-than-expected**, (accessed 2024/11/04).
179 Y. Zhang, R. Zhang, X. Yang, H. Qi and C. Zhang, *J. Pharm. Anal.*, 2018, **9**, 9–19.
180 G. Giagu, A. Fracassa, A. Fiorani, E. Villani, F. Paolucci, G. Valenti and A. Zanut, *Microchim. Acta*, 2024, **191**, 359.
181 Y. Liu, P. Li, N. Zhang, S. Chen, Z. Liu and J. Guang, *IEEE Sens. J.*, 2019, **19**, 11955–11960.
182 E. S. da Silva, L. C. de Souza and L. C. Oliveira, *IEEE Sens. J.*, 2021, **21**, 16613–16620.
183 C. Xiao, J. Eriksson, A. Suska, D. Filippini and W. C. Mak, *Anal. Chim. Acta*, 2022, **1201**, 339606.
184 S. Bhaskar and S. S. Ramamurthy, *ACS Appl. Nano Mater.*, 2019, **2**, 4613–4625.
185 S. Bhaskar, N. C. S. S. Kowshik, S. P. Chandran and S. S. Ramamurthy, *Langmuir*, 2020, **36**, 2865–2876.
186 A. Rai, S. Bhaskar, N. Reddy and S. S. Ramamurthy, *ACS Sustainable Chem. Eng.*, 2021, **9**, 14959–14974.
187 S. Bhaskar, A. Rai, K. M. Ganesh, R. Reddy, N. Reddy and S. S. Ramamurthy, *Langmuir*, 2022, **38**, 12035–12049.
188 R. Matsuda and F. Okiharu, *In Vitro Cell. Dev. Biol.: Anim.*, 2024, **60**, 740–747.
189 B. Jin, A. R. Jean, A. V. Maslov and V. N. Astratov, *Laser Photonics Rev.*, 2023, **17**, 2300146.
190 A. V. Maslov, B. Jin and V. N. Astratov, *Sci. Rep.*, 2023, **13**, 6688.
191 X. Guo, J. Chang, W. Chen, Y. Hu, N. Ma and J. Zhang, *Appl. Opt.*, 2023, **62**, 5236–5243.
192 Y. Zheng, H. Yin, C. Zhou, W. Zhou, Z. Huan and W. Ma, *Biosensors*, 2023, **13**, 978.
193 D. Sakharkar, A. Jain, A. Parakh and R. R. Khandelwal, *IEEE Sens. Lett.*, 2023, **7**, 1–4.
194 Z. Jiao, M. Pan, K. Yousaf, D. Doveiko, M. Maclean, D. Griffin, Y. Chen and D. D. U. Li, *J. Microsc.*, 2024, **296**, 10–23.
195 K. C. Lee, K. Lee, J. Jung, S. H. Lee, D. Kim and S. A. Lee, *ACS Photonics*, 2021, **8**, 1307–1315.
196 S. Kim, K. Sosnowski, D. S. Hwang and J.-Y. Yoon, *ACS ES&T Eng.*, 2024, **4**, 186–195.
197 M. A. Schaefer, H. N. Nelson, J. L. Butrum, J. R. Gronseth and J. H. Hines, *Sci. Rep.*, 2023, **13**, 2722.
198 B. Dai, Z. Jiao, L. Zheng, H. Bachman, Y. Fu, X. Wan, Y. Zhang, Y. Huang, X. Han, C. Zhao, T. J. Huang, S. Zhuang and D. Zhang, *Light: Sci. Appl.*, 2019, **8**, 75.
199 C. Song, Y. Yang, X. Tu, Z. Chen, J. Gong and C. Lin, *IEEE Sens. J.*, 2021, **21**, 1229–1235.

 This journal is © The Royal Society of Chemistry 2025

Open Access Article. Published on 07 February 2025. Downloaded on 19/4/2026 11:02:09 PM.
This article is licensed under a Creative Commons Attribution-NonCommercial 3.0 Unported Licence.

200 H. Zhang, W. Zhang, Z. Zuo and J. Yang, *Microsc. Res. Tech.*, 2024, **87**, 1521–1533.
201 R. Koohkan, M. Kaykhaii, M. Sasani and B. Paull, *ACS Omega*, 2020, **5**, 31450–31455.
202 M. Sargazi and M. Kaykhaii, *Spectrochim. Acta, Part A*, 2020, **227**, 117672.
203 F. Matinrad, M. Kompany-Zareh, N. Omidikia and M. Dadashi, *Anal. Chim. Acta*, 2020, **1129**, 98–107.
204 L. Kong, Y. Gan, T. Liang, L. Zhong, Y. Pan, D. Kirsanov, A. Legin, H. Wan and P. Wang, *Anal. Chim. Acta*, 2020, **1093**, 150–159.
205 R. O. Hassan, H. O. Othman and D. S. Ali, *Spectrochim. Acta, Part A*, 2023, **302**, 123009.
206 E. Vidal, A. S. Lorenzetti, C. D. Garcia and C. E. Domini, *Anal. Chim. Acta*, 2021, **1151**, 338249.
207 R. Bogucki, M. Greggila, P. Mallory, J. Feng, K. Siman, B. Khakipoor, H. King and A. W. Smith, *J. Chem. Educ.*, 2019, **96**, 1527–1531.
208 A. Bayram, N. Horzum, A. U. Metin, V. Kılıç and M. E. Solmaz, *IEEE Sens. J.*, 2018, **18**, 5948–5955.
209 K. D. Long, H. Yu and B. T. Cunningham, *Biomed. Opt. Express*, 2014, **5**, 3792–3806.
210 D. Jian, B. Wang, H. Huang, X. Meng, C. Liu, L. Xue, F. Liu and S. Wang, *Biosens. Bioelectron.*, 2019, **143**, 111632.
211 E. Pituła, M. Koba and M. Śmietana, *Opt. Laser Technol.*, 2021, **140**, 107067.
212 L.-J. Wang, Y.-C. Chang, R. Sun and L. Li, *Biosens. Bioelectron.*, 2017, **87**, 686–692.
213 M. A. Hossain, J. Canning, K. Cook and A. Jamalipour, *Opt. Lett.*, 2016, **41**, 2237–2240.
214 L.-J. Wang, N. Naudé, Y.-C. Chang, A. Crivaro, M. Kamoun, P. Wang and L. Li, *J. Biophotonics*, 2018, **11**, e201700382.
215 X. Hong, T. Lu, L. Fruzyna and B. Yu, *Sci. Rep.*, 2019, **9**, 15713.
216 C. B. Sánchez, R. P. D. Redondo, A. F. Vilas and A. M. S. Bermúdez, *Comput. Appl. Eng. Educ.*, 2019, **27**, 371–379.
217 S. Dhawan, *Int. J. Electron. Commun. Technol.*, 2011, **2**, 22–26.
218 A. K. Jain, *Proc. IEEE*, 1981, **69**, 349–389.
219 K. Marlapalli, R. S. B. P. Bandlamudi, R. Busi, V. Pranav and B. Madhavrao, in *Communication Software and Networks*, ed. S. C. Satapathy, V. Bhateja, M. Ramakrishna Murty, N. Gia Nhu and J. Kotti, Springer, Singapore, 2021, pp. 271–279.
220 X. Bao, S. Jiang, Y. Wang, M. Yu and J. Han, *Analyst*, 2018, **143**, 1387–1395.
221 A. Y. Mutlu, V. Kılıç, G. K. Özdemir, A. Bayram, N. Horzum and M. E. Solmaz, *Analyst*, 2017, **142**, 2434–2441.
222 P. Siribunbandal, Y.-H. Kim, T. Osotchan, Z. Zhu and R. Jaisutti, *ACS Omega*, 2022, **7**, 18714–18721.
223 G. H. Darwish, D. V. Baker and W. R. Algar, *ACS Sens.*, 2023, **8**, 4686–4695.
224 S. Duan, T. Cai, J. Zhu, X. Yang, E. G. Lim, K. Huang, K. Hoettges, Q. Zhang, H. Fu, Q. Guo, X. Liu, Z. Yang and P. Song, *Anal. Chim. Acta*, 2023, **1248**, 340868.
225 S. Mondal, S. Park, T. H. Vo, J. Choi, V. H. M. Doan, D. T. Phan, C.-S. Kim, B. Lee and J. Oh, *Mater. Chem. Phys.*, 2022, **287**, 126289.
226 E. Ghohestani, J. Tashkhourian, H. Sharifi, N. M. Bojanowski, K. Seehafer, E. Smarsly, U. H. F. Bunz and B. Hemmateenejad, *Analyst*, 2022, **147**, 4266–4274.
227 M. Adampourezare, B. Nikzad, S. Sajedi-Amin and E. Rahimpour, *BMC Chem.*, 2024, **18**, 80.
228 F. Wang, Y. Lu, J. Yang, Y. Chen, W. Jing, L. He and Y. Liu, *Analyst*, 2017, **142**, 3177–3182.
229 L. Guo, T. Wang, Z. Wu, J. Wang, M. Wang, Z. Cui, S. Ji, J. Cai, C. Xu and X. Chen, *Adv. Mater.*, 2020, **32**, 2004805.
230 Z. Wang, Y. Dong, X. Sui, X. Shao, K. Li, H. Zhang, Z. Xu and D. Zhang, *npj Flexible Electron.*, 2024, **8**, 1–11.
231 J. Cruz, R. Sáez-Hernández, S. Armenta, A. E. Morales-Rubio and M. L. Cervera, *Talanta*, 2024, **276**, 126217.
232 J.-Q. Du, W.-C. Luo, J.-T. Zhang, Q.-Y. Li, L.-N. Bao, M. Jiang, X. Yu and L. Xu, *Sens. Actuators, B*, 2024, **417**, 136173.
233 S. K. R, K. R. Ashok Kumar, K. Vijayakrishna, A. Sivaramakrishna, C. V. S. Brahmmananda Rao, N. Sivaraman and S. K. Sahoo, *Inorg. Chem.*, 2018, **57**, 15270–15279.
234 D. S. Lim, S. Y. Park, K. S. Hwang and S.-K. Chang, *Tetrahedron Lett.*, 2018, **59**, 1819–1822.
235 T. Anand and S. K. Sahoo, *Phys. Chem. Chem. Phys.*, 2019, **21**, 11839–11845.
236 L. K. Shaji, J. Jose, R. Bhaskar, R. S. Kumar, V. Vetriarasu, S. G. Bhat and S. K. A. Kumar, *Inorg. Chem. Commun.*, 2023, **147**, 110252.
237 D. Aydin, S. N. K. Elmas and F. N. Arslan, *Food Chem.*, 2023, **402**, 134439.
238 R. Kaushik, R. Sakla, N. Kumar, A. Ghosh, V. D. Ghule and D. A. Jose, *Sens. Actuators, B*, 2021, **328**, 129026.
239 X. Liu, Z. Chen, R. Gao, C. Kan and J. Xu, *Sens. Actuators, B*, 2021, **340**, 129958.
240 I. Lewińska, M. Ścibisz and Ł. Tymecki, *Anal. Chim. Acta*, 2024, **1308**, 342639.
241 L. Bokelmann, O. Nickel, T. Maricic, S. Pääbo, M. Meyer, S. Borte and S. Riesenberg, *Nat. Commun.*, 2021, **12**, 1467.
242 Q. Tang, J. Hu, S. Li, S. Lin, Y. Tu and X. Gui, *Int. J. Food Sci. Technol.*, 2022, **57**, 6867–6880.
243 K. Lee, S. Baek, D. Kim and J. Seo, *Food Packag. Shelf Life*, 2019, **19**, 40–46.
244 L. R. Magnaghi, G. Alberti, B. M. Pazzi, C. Zanoni and R. Biesuz, *New J. Chem.*, 2022, **46**, 19460–19467.
245 Y. Cao, Y. Liu, F. Li, S. Guo, Y. Shui, H. Xue and L. Wang, *Microchem. J.*, 2019, **150**, 104176.
246 K. Chayavanich, P. Thiraphibundet and A. Imyim, *Spectrochim. Acta, Part A*, 2020, **226**, 117601.
247 L. Placer, I. Lavilla, F. Pena-Pereira and C. Bendicho, *Sens. Actuators, B*, 2023, **377**, 133109.
248 N. Peamaroon, J. Jakmunee and N. Moonrungsee, *J. Anal. Test.*, 2021, **5**, 379–386.
249 M. D. Yilmaz, *Microchem. J.*, 2024, **196**, 109554.
250 H. Zhang, X. Jiang, Q. Yu, X. Cui, Y. Liu, P.-L. Tremblay and T. Zhang, *Spectrochim. Acta, Part A*, 2024, **323**, 124930.

Open Access Article. Published on 07 February 2025. Downloaded on 19/4/2026 11:02:09 PM.
This article is licensed under a Creative Commons Attribution-NonCommercial 3.0 Unported Licence.

251 S. Erdemir and S. Malkondu, *Talanta*, 2020, **207**, 120278.
252 A. Kathiravan, S. Sengottiyan, T. Puzyn, P. Gopinath, K. Ramasubramanian, P. Ayyappan Susila and M. Asha Jhonsi, *Anal. Methods*, 2022, **14**, 518–525.
253 K. Kalinowska, W. Wojnowski and M. Tobiszewski, *Anal. Methods*, 2023, **15**, 1395–1401.
254 J. Câmara Cardozo, I. D. Barbosa Segundo, E. R. V. P. Galvão, D. R. da Silva, E. V. dos Santos and C. A. Martínez-Huitle, *Sci. Rep.*, 2023, **13**, 11082.
255 A. P. Vargas, F. Gámez, J. Roales, T. Lopes-Costa and J. M. Pedrosa, *Chemosensors*, 2021, **9**, 40.
256 A. Maiti, T. Sultana, B. Rajbanshi, B. Bhaumik, N. Roy and M. Nath Roy, *Microchem. J.*, 2024, **199**, 109977.
257 A. Shen, X. Hao, L. Zhang, M. Du, M. Li, J. Yuan, X. Du, S. Ma, Y. Zhao, L. Hou, Z. Li and Y. Yang, *Dyes Pigm.*, 2022, **207**, 110674.
258 Y. Zhang, Y. Cai, F. Dong, L. Bian, H. Li, J. Wang, J. Du, X. Qi and Y. He, *Anal. Bioanal. Chem.*, 2019, **411**, 8063–8071.
259 R. Silva Lamarca, N. da Costa Luchiari, A. Francielli Bonjorno, J. Passaretti Filho, A. Alves Cardoso and P. Clairmont Feitosa de Lima Gomes, *Anal. Methods*, 2019, **11**, 3697–3705.
260 S. Jantra, L. Waiysuksri, P. Rattanamunee, P. Rashatasakhon, M. Sukwattanasinitt and S. Wacharasindhu, *Dyes Pigm.*, 2023, **214**, 111210.
261 C. Vakh, Z. Mallabaeva and M. Tobiszewski, *Spectrochim. Acta, Part A*, 2024, **315**, 124238.
262 H.-A. H. Abd-ElSalam, G. N. N. Saleh, K. G. Waked, O. A. Refaeey, K. S. Poules, H. H. Georgey and E. S. Elzanfaly, *Chem. Pap.*, 2024, **78**, 6607–6615.
263 I. Lewińska, M. Speichert, M. Granica and Ł. Tymecki, *Sens. Actuators, B*, 2021, **340**, 129915.
264 X.-X. Zhang, Y.-Z. Song, F. Fang and Z.-Y. Wu, *Anal. Bioanal. Chem.*, 2018, **410**, 2665–2669.
265 D. Merli, A. Profumo, S. Tinivella and S. Protti, *Forensic Chem.*, 2019, **14**, 100167.
266 A. Procida and K. C. Honeychurch, *J. Forensic Sci.*, 2022, **67**, 1697–1703.
267 Ö. Berfin Mercan, V. Kılıç and M. Şen, *Sens. Actuators, B*, 2021, **329**, 129037.
268 T.-T. Wang, C. Kit Lio, H. Huang, R.-Y. Wang, H. Zhou, P. Luo and L.-S. Qing, *Talanta*, 2020, **206**, 120211.
269 E. Yüzer, V. Doğan, V. Kılıç and M. Şen, *Sens. Actuators, B*, 2022, **371**, 132489.
270 M. Domínguez, D. Moraru, S. Lasso, I. Sanz-Vicente, S. de Marcos and J. Galbán, *Anal. Bioanal. Chem.*, 2024, **416**, 7317–7323.
271 Y. Jin Chi, B. Ryu, S. Ahn and W.-G. Koh, *Sens. Actuators, B*, 2023, **396**, 134601.
272 H. Wu, J. Chen, Y. Yang, W. Yu, Y. Chen, P. Lin and K. Liang, *Anal. Bioanal. Chem.*, 2022, **414**, 1759–1772.
273 D. Wang, D. Liu, H. Duan, Y. Xu, Z. Zhou and P. Wang, *J. Agric. Food Chem.*, 2020, **68**, 9252–9259.
274 L. Li, Z. Liu, H. Zhang, W. Yue, C.-W. Li and C. Yi, *Sens. Actuators, B*, 2018, **254**, 337–346.
275 N. Rafat, L. Brewer, N. Das, D. J. Trivedi, B. K. Kaszala and A. Sarkar, *ACS Sens.*, 2023, **8**, 534–542.
276 X. Wang, J. Li, D. Jian, Y. Zhang, Y. Shan, S. Wang and F. Liu, *Sens. Actuators, B*, 2021, **329**, 129173.
277 C. Chen, P.-W. Wang, Y.-C. Yen, H.-L. Lin, Y.-C. Fan, S.-M. Wu and C.-F. Chen, *Sens. Actuators, B*, 2019, **282**, 251–258.
278 L. Zhong, J. Sun, Y. Gan, S. Zhou, Z. Wan, Q. Zou, K. Su and P. Wang, *Anal. Sci.*, 2019, **35**, 133–140.
279 X. Li, Y. Cheng, R. Xu, Z. Zhang, X. Qi, L. Chen and M. Zhu, *Talanta*, 2022, **247**, 123567.
280 Y.-P. Hsu, H.-W. Yang, N.-S. Li, Y.-T. Chen, H.-H. Pang and S.-T. Pang, *ACS Sens.*, 2020, **5**, 928–935.
281 G. Papadakis, A. K. Pantazis, N. Fikas, S. Chatziioannidou, V. Tsiakalou, K. Michaelidou, V. Pogka, M. Megariti, M. Vardaki, K. Giarentis, J. Heaney, E. Nastouli, T. Karamitros, A. Mentis, A. Zafiropoulos, G. Sourvinos, S. Agelaki and E. Gizeli, *Sci. Rep.*, 2022, **12**, 3775.
282 J. Song, B. Cha, J. Moon, H. Jang, S. Kim, J. Jang, D. Yong, H.-J. Kwon, I.-C. Lee, E.-K. Lim, J. Jung, H. G. Park and T. Kang, *ACS Nano*, 2022, **16**, 11300–11314.
283 F. Li, Y. Hu, A. Zhao, Y. Xi, Z. Li and J. He, *Microchim. Acta*, 2020, **187**, 425.
284 L. Xue, N. Jin, R. Guo, S. Wang, W. Qi, Y. Liu, Y. Li and J. Lin, *ACS Sens.*, 2021, **6**, 2883–2892.
285 B. Zhang, R. Zhou, H. Zhang, D. Cai, X. Lin, Y. Lang, Y. Qiu, X. Shentu, Z. Ye and X. Yu, *Foods*, 2022, **11**, 2900.
286 J. Liu, Y. Xing, B. Xue and X. Zhou, *Biosens. Bioelectron.*, 2022, **205**, 114099.
287 X. Zhang, D. Wu, Y. Wu and G. Li, *Biosens. Bioelectron.*, 2021, **172**, 112776.
288 T. D. Tran, P. T. Nguyen, T. N. Le and M. I. Kim, *Biosens. Bioelectron.*, 2021, **182**, 113187.
289 Z. Zhu, X. Wang, N. Wang, C. Zeng, L. Zhang, J. Fan, X. Yang, P. Li, H. Yuan, Y. Feng, S. Huo and X. Lu, *Anal. Bioanal. Chem.*, 2024, **416**, 4417–4426.
290 E. Ko, W. Hur, S. E. Son, G. H. Seong and D. K. Han, *Microchim. Acta*, 2021, **188**, 382.
291 Y.-T. Zhuang, S. Chen, R. Jiang, Y.-L. Yu and J.-H. Wang, *Anal. Chem.*, 2019, **91**, 5346–5353.
292 D.-H. Park, J.-M. Heo, W. Jeong, Y. H. Yoo, B. J. Park and J.-M. Kim, *ACS Appl. Mater. Interfaces*, 2018, **10**, 5014–5021.
293 T.-T. T. Nguyen, B. T. Huy and Y.-I. Lee, *ACS Omega*, 2019, **4**, 12665–12670.
294 L. Engel, I. Benito-Altamirano, K. R. Tarantik, C. Pannek, M. Dold, J. D. Prades and J. Wöllenstein, *Sens. Actuators, B*, 2021, **330**, 129281.
295 P. Escobedo, C. E. Ramos-Lorente, A. Ejaz, M. M. Erenas, A. Martínez-Olmos, M. A. Carvajal, C. García-Núñez, I. de Orbe-Payá, L. F. Capitán-Vallvey and A. J. Palma, *Sens. Actuators, B*, 2023, **376**, 133001.
296 J. R. P. Albuquerque, C. N. Makara, V. G. Ferreira, L. C. Brazaca and E. Carrilho, *RSC Adv.*, 2024, **14**, 23392–23403.
297 F. Li, Y. Hu, Z. Li, J. Liu, L. Guo and J. He, *Anal. Bioanal. Chem.*, 2019, **411**, 6497–6508.
298 S. Chunta, P. Jarujamrus, A. Prakobkij, S. Khongwichit, N. Ditcharoen, S. Pencharee and M. Amatatongchai, *Microchim. Acta*, 2024, **191**, 402.

 This journal is © The Royal Society of Chemistry 2025

Open Access Article. Published on 07 February 2025. Downloaded on 19/4/2026 11:02:09 PM.
This article is licensed under a Creative Commons Attribution-NonCommercial 3.0 Unported Licence.

299 A. K. Yetisen, R. Moreddu, S. Seifi, N. Jiang, K. Vega, X. Dong, J. Dong, H. Butt, M. Jakobi, M. Elsner and A. W. Koch, *Angew. Chem., Int. Ed.*, 2019, **58**, 10506–10513.
300 A. T. Güntner and F. M. Schenk, *Nanoscale*, 2023, **15**, 3967–3977.
301 T. Zhao, X. Liang, X. Guo, X. Yang, J. Guo, X. Zhou, X. Huang, W. Zhang, Y. Wang, Z. Liu, Z. Jiang, H. Zhou and H. Zhou, *Food Chem.*, 2023, **404**, 134768.
302 E. M. Materón, F. R. Gómez, M. B. Almeida, F. M. Shimizu, A. Wong, K. B. R. Teodoro, F. S. R. Silva, M. J. A. Lima, M. K. S. C. Angelim, M. E. Melendez, N. Porras, P. M. Vieira, D. S. Correa, E. Carrilho, O. N. Oliveira, R. B. Azevedo and D. Goncalves, *ACS Appl. Mater. Interfaces*, 2022, **14**, 54527–54538.
303 S. Ngernpimai, S. Srijampa, P. Thongmee, S. Teerasong, T. Puangmali, W. Maleewong, A. Chompoosor and P. Tippayawat, *Bioconjugate Chem.*, 2022, **33**, 2103–2112.
304 J. Zhang, Y. Wang, X. Zhao, M. Chen, Y. Peng, J. Bai, S. Li, D. Han, S. Ren, K. Qin, S. Li, T. Han and Z. Gao, *Anal. Chem.*, 2021, **93**, 16922–16931.
305 F. Liu, R. Chen, W. Song, L. Li, C. Lei and Z. Nie, *Anal. Chem.*, 2021, **93**, 3517–3525.
306 L. Ma, L. Yin, X. Li, S. Chen, L. Peng, G. Liu, S. Ye, W. Zhang and S. Man, *Biosens. Bioelectron.*, 2022, **195**, 113646.
307 S. Tang, T. Qi, D. Xia, M. Xu, M. Xu, A. Zhu, W. Shen and H. K. Lee, *Anal. Chem.*, 2019, **91**, 5888–5895.
308 T. Qi, M. Xu, Y. Yao, W. Chen, M. Xu, S. Tang, W. Shen, D. Kong, X. Cai, H. Shi and H. K. Lee, *Talanta*, 2020, **220**, 121388.
309 N. Villarino, F. Pena-Pereira, I. Lavilla and C. Bendicho, *ACS Sens.*, 2022, **7**, 839–848.
310 Z. Li, R. Paul, T. B. Tis, A. C. Saville, J. C. Hansel, T. Yu, J. B. Ristaino and Q. Wei, *Nat. Plants*, 2019, **5**, 856–866.
311 A. W. Kahandal, L. Sharma, V. Sirdeshmukh, A. Kulkarni and C. K. Tagad, *Int. J. Environ. Sci. Technol.*, 2023, **20**, 9077–9088.
312 B.-W. Liu, P.-C. Huang and F.-Y. Wu, *Anal. Bioanal. Chem.*, 2020, **412**, 8051–8059.
313 C.-Y. Wen, Y. Chen, R.-S. Liu, J. Huang, D. Wang, Z. Cao, B. Meteku and J. Zeng, *J. Mater. Chem. C*, 2021, **9**, 4661–4669.
314 S. Bhaskar, P. Jha, C. Subramaniam and S. S. Ramamurthy, *Phys. E*, 2021, **132**, 114764.
315 H.-J. Fu, L. Luo, Y. Wang, C.-L. Wang, H. Wang, Y.-D. Shen, H.-T. Lei, N. Hildebrandt and Z.-L. Xu, *ACS Appl. Nano Mater.*, 2022, **5**, 12915–12925.
316 T. Zhang, H.-B. Wang, Z.-T. Zhong, C.-Q. Li, W. Chen, B. Liu and Y.-D. Zhao, *Microchem. J.*, 2020, **157**, 105038.
317 Y. Wu, Y. Hu, N. Jiang, R. Anantharanjit, A. K. Yetisen and M. F. Cordeiro, *Lab Chip*, 2022, **22**, 3521–3532.
318 A. Roberts, D. Prakashan, H. Dhanze, R. K. Gandham, S. Gandhi and G. T. Sharma, *Nanoscale Adv.*, 2022, **4**, 3966–3977.
319 A. Roda, S. Cavalera, F. D. Nardo, D. Calabria, S. Rosati, P. Simoni, B. Colitti, C. Baggiani, M. Roda and L. Anfossi, *Biosens. Bioelectron.*, 2021, **172**, 112765.
320 D. P. Hainsworth, A. Gangula, S. Ghoshdastidar, R. Kannan and A. Upendran, *Am. J. Ophthalmol.*, 2020, **213**, 306–319.
321 N. Yang, L.-L. Xie, C. Pan, M.-F. Yuan, Z.-H. Tao and H.-P. Mao, *J. Food Process Eng.*, 2019, **42**, e12976.
322 C. Rodriguez-Quijada, C. Lyons, M. Sanchez-Purra, C. Santamaria, B. M. Leonardo, S. Quinn, M. F. Tlusty, M. Shiaris and K. Hamad-Schifferli, *ACS Omega*, 2023, **8**, 19494–19502.
323 J. P. Devadhasan, J. Gu, P. Chen, S. Smith, B. Thomas, M. Gates-Hollingsworth, D. Hau, S. Pandit, D. AuCoin and F. Zenhausern, *Anal. Chem.*, 2021, **93**, 9337–9344.
324 Y. Uwamino, S. Tanaka, A. Shibata, T. Kurafuji, H. Ishihara, Y. Sato and H. Matsushita, *Diagn. Microbiol. Infect. Dis.*, 2024, **108**, 116166.
325 G. Yang, J. Li, S. Zhang, H. Ouyang, C. Jiang and H. Pan, *J. Immunol. Methods*, 2023, **523**, 113574.
326 S. B. Park and J. H. Shin, *BioChip J.*, 2022, **16**, 480–489.
327 T. Kosawatphat, A. Yakoh, S. Rengpipat, N. Khongchareonporn, O. Chailapakul, S. Chaiyo and N. Praphairaksit, *Anal. Lett.*, 2022, **55**, 2517–2530.
328 C. Kim, Y. K. Yoo, S. I. Han, J. Lee, D. Lee, K. Lee, K. S. Hwang, K. H. Lee, S. Chung and J. H. Lee, *Lab Chip*, 2017, **17**, 2451–2458.
329 R. Tian, J. Ji, Y. Zhou, Y. Du, X. Bian, F. Zhu, G. Liu, S. Deng, Y. Wan and J. Yan, *Biosens. Bioelectron.*, 2020, **160**, 112218.
330 H. Tong, C. Cao, M. You, S. Han, Z. Liu, Y. Xiao, W. He, C. Liu, P. Peng, Z. Xue, Y. Gong, C. Yao and F. Xu, *Biosens. Bioelectron.*, 2022, **213**, 114449.
331 R. Thakur, F. Akram, V. Rastogi, A. Mitra, R. Nawani, V. Av, S. K. Dubey and C. Shakher, *IEEE Sens. J.*, 2020, **20**, 14491–14500.
332 G.-R. Han, H. J. Koo, H. Ki and M.-G. Kim, *ACS Appl. Mater. Interfaces*, 2020, **12**, 34564–34575.
333 P. Phangwipas, B. Thangavel and J. H. Shin, *Chemosensors*, 2023, **11**, 36.
334 G. Zhao, S. Liu, G. Li, W. Fang, Y. Liao, R. Li, L. Fu and J. Wang, *Talanta*, 2023, **253**, 123925.
335 S. Lee, Y. K. Yoo, S. I. Han, D. Lee, S.-Y. Cho, C. Park, D. Lee, D. S. Yoon and J. H. Lee, *Analyst*, 2023, **148**, 6001–6010.
336 M. Colombo, L. Bezinge, A. R. Tapia, C.-J. Shih, A. J. de Mello and D. A. Richards, *Sens. Diagn.*, 2023, **2**, 100–110.
337 K. H. Foysal, S. E. Seo, M. J. Kim, O. S. Kwon and J. W. Chong, *Sensors*, 2019, **19**, 4812.
338 S. Zhang, X. Jiang, S. Lu, G. Yang, S. Wu, L. Chen and H. Pan, *Sensors*, 2023, **23**, 6401.
339 S. Lee, S. Kim, D. S. Yoon, J. S. Park, H. Woo, D. Lee, S.-Y. Cho, C. Park, Y. K. Yoo, K.-B. Lee and J. H. Lee, *Nat. Commun.*, 2023, **14**, 2361.
340 S. Kumar, T. Ko, Y. Chae, Y. Jang, I. Lee, A. Lee, S. Shin, M.-H. Nam, B. S. Kim, H. S. Jun and S. Seo, *Biosensors*, 2023, **13**, 623.
341 S. Arumugam, J. Ma, U. Macar, G. Han, K. McAulay, D. Ingram, A. Ying, H. H. Chellani, T. Chern, K. Reilly,

Open Access Article. Published on 07 February 2025. Downloaded on 19/4/2026 11:02:09 PM.
This article is licensed under a Creative Commons Attribution-NonCommercial 3.0 Unported Licence.

D. A. M. Colburn, R. Stanciu, C. Duffy, A. Williams, T. Grys, S.-F. Chang and S. K. Sia, *Commun. Med.*, 2023, **3**, 1–14.
342 N. Cheng, Y. Song, M. M. A. Zeinhom, Y.-C. Chang, L. Sheng, H. Li, D. Du, L. Li, M.-J. Zhu, Y. Luo, W. Xu and Y. Lin, *ACS Appl. Mater. Interfaces*, 2017, **9**, 40671–40680.
343 F. D. Nardo, E. Alladio, C. Baggiani, S. Cavalera, C. Giovannoli, G. Spano and L. Anfossi, *Talanta*, 2019, **192**, 288–294.
344 Z. Lu, Y. Huang, X. Xiao, Y. Luo, J. Liu, J. Yin, C. Liu, S. Shan, D. Liu and W. Lai, *Sens. Actuators, B*, 2023, **383**, 133580.
345 J. Chen, P. Luo, Z. Liu, Z. He, Y. Pang, H. Lei, Z. Xu, H. Wang and X. Li, *Anal. Chim. Acta*, 2022, **1221**, 340138.
346 D. Quesada-González, A. Sena-Torralba, W. P. Wicaksono, A. de la Escosura-Muñiz, T. A. Ivandini and A. Merkoçi, *Biosens. Bioelectron.*, 2019, **132**, 132–135.
347 F. Ghorbanizamani, H. Moulahoum and S. Timur, *IEEE Sens. J.*, 2022, **22**, 1146–1153.
348 S. Teepoo, J. Jantra, K. Panapong and D. T. Ajayi, *Anal. Chim. Acta*, 2024, **1285**, 342031.
349 G. M. S. Ross, G. I. Salentijn and M. W. F. Nielen, *Biosensors*, 2019, **9**, 143.
350 R. Shu, Y. Liang, S. Liu, L. Dou, T. Bu, S. Wang, X. Lan, D. Zhang, J. Sun, M. Zhu and J. Wang, *Biosens. Bioelectron.*, 2023, **219**, 114807.
351 M. Mao, X. Chen, Y. Cai, H. Yang, C. Zhang, Y. Zhang, Z. Wang and C. Peng, *Sens. Actuators, B*, 2023, **378**, 133148.
352 X. Zhu, J. Tang, X. Ouyang, Y. Liao, H. Feng, J. Yu, L. Chen, Y. Lu, Y. Yi and L. Tang, *J. Hazard. Mater.*, 2024, **465**, 133178.
353 Q. He, H. Yang, J. Pan, X. Cui, D. Shen, S. A. Eremin, Y. Fang and S. Zhao, *ACS Appl. Bio Mater.*, 2020, **3**, 8849–8856.
354 D. Y. Kong, N. S. Heo, J. W. Kang, J. B. Lee, H. J. Kim and M. I. Kim, *Anal. Bioanal. Chem.*, 2022, **414**, 3257–3265.
355 F. Feng, Q. Fu, F. Cao, Y. Yuan, R. Kong, D. Ji and H. Liu, *ChemBioChem*, 2024, **25**, e202300575.
356 S. Agarwal, C. Warmt, J. Henkel, L. Schrick, A. Nitsche and F. F. Bier, *Anal. Bioanal. Chem.*, 2022, **414**, 3177–3186.
357 T. Sukonta, S. Senapin, S. Taengphu, P. Hannanta-anan, M. Kitthamarat, P. Aiamsa-at and T. Chaijarasphong, *Aquaculture*, 2022, **560**, 738538.
358 P.-R. Li, Z.-X. Wang, Z.-K. Xu, J. Wang, B. Li, X. Shen and Z.-L. Xu, *J. Agric. Food Chem.*, 2024, **72**, 14000–14010.
359 M. Liu, X. Li, J. Xu, S. Zhou, L. Deng, D. Men, Y. Duan, D. Huo and C. Hou, *Microchem. J.*, 2024, **205**, 111313.
360 L. Yin, N. Duan, S. Chen, Y. Yao, J. Liu and L. Ma, *Sens. Actuators, B*, 2021, **347**, 130586.
361 S. H. Needs, H. M. I. Osborn and A. D. Edwards, *J. Microbiol. Methods*, 2021, **187**, 106199.
362 D. H. Jung, Y. Kim, H. H. Cho, B. Lee, S.-J. Suh, J. H. Heo and J. H. Lee, *Chem. Eng. J.*, 2022, **450**, 138281.
363 S. Fu, P. Zuo and B.-C. Ye, *Biotechnol. J.*, 2021, **16**, 2000126.
364 C. Chang, H. Yang, W. Bi, C. Huang and Z. Xu, *ACS Sens.*, 2023, **8**, 543–554.
365 C. Imashiro, Y. Tokuoka, K. Kikuhara, T. G. Yamada, K. Takemura and A. Funahashi, *IEEE Access*, 2020, **8**, 170033–170043.
366 D. Rabha, A. Sarmah and P. Nath, *J. Microsc.*, 2019, **276**, 13–20.
367 R. Shrestha, R. Duwal, S. Wagle, S. Pokhrel, B. Giri and B. B. Neupane, *PLoS Neglected Trop. Dis.*, 2020, **14**, e0008560.
368 M. K. Kanakasabapathy, H. J. Pandya, M. S. Draz, M. K. Chug, M. Sadasivam, S. Kumar, B. Etemad, V. Yogesh, M. Safavieh, W. Asghar, J. Z. Li, A. M. Tsibris, D. R. Kuritzkes and H. Shafiee, *Lab Chip*, 2017, **17**, 2910–2919.
369 S. Ilyas, M. Sher, E. Du and W. Asghar, *Biosens. Bioelectron.*, 2020, **165**, 112417.
370 M. K. Aslan, Y. Ding, S. Stavrakis and A. J. deMello, *Anal. Chem.*, 2023, **95**, 14526–14532.
371 M. Cesaretti, J. Gal, C. Bouveyron, A. Diaspro, E. Fontas, A. Antonini, R. Anty, A. Iannelli and S. Patouraux, *Microsc. Res. Tech.*, 2020, **83**, 1025–1031.
372 W. Sirithanaphol, N. Incharoen, U. Rompsaithong, P. Kiatsopit, S. Lumbiganon and J. Chindaprasirt, *Heliyon*, 2021, **7**, e07189.
373 A. F. Sampaio, L. Rosado and M. J. M. Vasconcelos, *IEEE Access*, 2021, **9**, 152188–152205.
374 V. Mosiichuk, A. Sampaio, P. Viana, T. Oliveira and L. Rosado, *Appl. Sci.*, 2023, **13**, 9850.
375 F. Veronese, F. Branciforti, E. Zavattaro, V. Tarantino, V. Romano, K. M. Meiburger, M. Salvi, S. Seoni and P. Savoia, *Diagnostics*, 2021, **11**, 451.
376 H. Li, Y. Liang, Y. Liu, X. Xian, Y. Xue, H. Huang, Q. Yao and W. Liu, *Comput. Electron. Agric.*, 2023, **214**, 108276.
377 P. Treepong and N. Theera-Ampornpunt, *Curr. Res. Food Sci.*, 2023, **7**, 100574.
378 M. Rolfe, S. Hayes, M. Smith, M. Owen, M. Spruth, C. McCarthy, A. Forkan, A. Banerjee and R. K. Hocking, *J. Hazard. Mater.*, 2024, **463**, 132853.
379 Y. Zhang, X. Song, J. Xie, J. Hu, J. Chen, X. Li, H. Zhang, Q. Zhou, L. Yuan, C. Kong, Y. Shen, J. Wu, L. Fang and Q. Dai, *Nat. Commun.*, 2023, **14**, 4118.
380 S. Assaad, D. Dov, R. Davis, S. Kovalsky, W. T. Lee, R. Kahmke, D. Rocke, J. Cohen, R. Henao, L. Carin and D. E. Range, *Mod. Pathol.*, 2023, **36**, 100129.
381 M. Y. Lu, D. F. K. Williamson, T. Y. Chen, R. J. Chen, M. Barbieri and F. Mahmood, *Nat. Biomed. Eng.*, 2021, **5**, 555–570.
382 M. K. Kanakasabapathy, P. Thirumalaraju, C. L. Bormann, H. Kandula, I. Dimitriadis, I. Souter, V. Yogesh, S. K. S. Pavan, D. Yarravarapu, R. Gupta, R. Pooniwala and H. Shafiee, *Lab Chip*, 2019, **19**, 4139–4145.
383 J. S. Prusty and A. Kumar, *Rend. Fis. Acc. Lincei.*, 2021, **32**, 163–180.
384 A. Jamir, S. Longkumer, V. K. Roy, R. K. Kharwar and P. P. Pankaj, *Multimed. Tools Appl.*, 2024, **83**, 16197–16203.
385 M. Ren, Y. Dong, J. Wang, J. Lin, L. Qu, Y. Zhou and Y. Chen, *Anal. Chim. Acta*, 2023, **1278**, 341687.

 This journal is © The Royal Society of Chemistry 2025

Open Access Article. Published on 07 February 2025. Downloaded on 19/4/2026 11:02:09 PM.
This article is licensed under a Creative Commons Attribution-NonCommercial 3.0 Unported Licence.

386 G. M. e Silva, J. A. Garcia, J. de A. Garitta, D. G. F. Cunha, N. R. Finkler, E. M. Mendiondo and F. Ghiglieno, *J. Environ. Manage.*, 2022, **323**, 116214.
387 W. Xiao, Z. Deng, J. Huang, Z. Huang, M. Zhuang, Y. Yuan, J. Nie and Y. Zhang, *Anal. Chem.*, 2019, **91**, 15114–15122.
388 K. Yuan, Y. Sun, F. Liang, F. Pan, M. Hu, F. Hua, Y. Yuan, J. Nie and Y. Zhang, *RSC Adv.*, 2022, **12**, 23379–23386.
389 F. Pan, F. Hua, Y. Yan, X. Huang, L. Yuan, Y. Tang, Y. Yuan, J. Nie and Y. Zhang, *Microchem. J.*, 2023, **190**, 108707.
390 X. Mo, J. Huang, Y. Sun, X. Chen, Y. Deng, C. Liu, W. Jin, J. Nie and Y. Zhang, *Microchem. J.*, 2022, **174**, 107075.
391 J. Huang, X. Mo, H. Fu, Y. Sun, Q. Gao, X. Chen, J. Zou, Y. Yuan, J. Nie and Y. Zhang, *Sens. Actuators, B*, 2021, **344**, 130218.
392 Y. Sun, K. Yuan, X. Mo, X. Chen, Y. Deng, C. Liu, Y. Yuan, J. Nie and Y. Zhang, *Talanta*, 2022, **238**, 122999.
393 M. Hu, W. Xiao, Y. Chen, Q. He, K. Yuan, X. Huang, W. Jin, J. Nie and Y. Zhang, *Photochem. Photobiol. Sci.*, 2023, **22**, 631–640.
394 F. Hua, F. Pan, J. Yang, Y. Yan, X. Huang, Y. Yuan, J. Nie, H. Wang and Y. Zhang, *Anal. Bioanal. Chem.*, 2023, **415**, 2705–2713.
395 X. Chen, Y. Sun, X. Mo, Q. Gao, Y. Deng, M. Hu, J. Zou, J. Nie and Y. Zhang, *RSC Adv.*, 2021, **11**, 36859–36865.
396 F.-J. Cao, H.-H. Cheng, S.-X. Ma, F. Jiao and D.-M. Dong, *Sens. Biosensing Res.*, 2022, **38**, 100533.
397 S. İ. Dönmez, S. H. Needs, H. M. I. Osborn and A. D. Edwards, *Sens. Actuators, B*, 2020, **323**, 128645.
398 A. S. Day, T.-H. Ulep, B. Safavinia, T. Hertenstein, E. Budiman, L. Dieckhaus and J.-Y. Yoon, *Biosens. Bioelectron.*, 2021, **179**, 113099.
399 I.-J. Doh, B. Dowden, V. Patsekin, B. Rajwa, J. P. Robinson and E. Bae, *Sensors*, 2022, **22**, 2646.
400 M. Fang, Y. Wang, T. Yang, J. Zhang, H. Yu, Z. Luo, B. Su and X. Lin, *ACS Sens.*, 2024, **9**, 2010–2019.
401 H. Nguyen, I. Misbah and W.-C. Shih, *IEEE Sens. J.*, 2020, **20**, 6685–6691.
402 W. Lu, C. Lin, J. Yang, X. Wang, B. Yao and M. Wang, *Anal. Bioanal. Chem.*, 2019, **411**, 5383–5391.
403 M. Li, Y. Gao, Y. Zhang, S. Gong, X. Tian, Y. Yang, X. Xu, Z. Wang and S. Wang, *Spectrochim. Acta. Part A*, 2021, **262**, 120135.
404 Y. Li, X. Jiang, Y. Li, X. Yan, L. Tang, X. Sun, K. Zhong, X. Li and J. Li, *Food Chem.*, 2024, **458**, 140239.
405 E. Garrido, G. Hernández-Sigüenza, E. Climent, M. D. Marcos, K. Rurack, P. Gaviña, M. Parra, F. Sancenón, V. Martí-Centelles and R. Martínez-Máñez, *Sens. Actuators, B*, 2023, **377**, 133043.
406 Z. Jiao, Z. Guo, X. Huang, J. Yang, J. Huang, Y. Liu, G. Liu, P. Zhang, C. Song and B. Z. Tang, *ACS Sens.*, 2021, **6**, 2845–2850.
407 M. Xu, W. Huang, D. Lu, C. Huang, J. Deng and T. Zhou, *Anal. Methods*, 2019, **11**, 4267–4273.
408 E. Teknikel, *Spectrochim. Acta. Part A*, 2024, **322**, 124807.
409 W.-Y. Zhang, T. Tian, L.-J. Peng, H.-Y. Zhou, H. Zhang, H. Chen and F.-Q. Yang, *Biosensors*, 2022, **12**, 893.
410 Y. Zhu, J. Zhang, J. Song, J. Yang, Z. Du, W. Zhao, H. Guo, C. Wen, Q. Li, X. Sui and L. Zhang, *Adv. Funct. Mater.*, 2020, **30**, 1905493.
411 Nandini and D. A. Jose, *Sens. Actuators, B*, 2024, **417**, 136070.
412 D. Hatiboruah, T. Das, N. Chamuah, D. Rabha, B. Talukdar, U. Bora, K. U. Ahamad and P. Nath, *Measurement*, 2020, **154**, 107507.
413 C. Zhang, J. P. Kim, M. Creer, J. Yang and Z. Liu, *Biosens. Bioelectron.*, 2017, **97**, 164–168.
414 Y. Sun, M. Wei, R. Liu, H. Wang, H. Li, Q. Kang and D. Shen, *Talanta*, 2019, **194**, 452–460.
415 Z. Lu, M. Chen, T. Liu, C. Wu, M. Sun, G. Su, X. Wang, Y. Wang, H. Yin, X. Zhou, J. Ye, Y. Shen and H. Rao, *ACS Appl. Mater. Interfaces*, 2023, **15**, 9800–9812.
416 L. Luo, J. Li, X. Bi, P. Jiang, L. Li, G. Qiao and T. You, *J. Hazard. Mater.*, 2024, **476**, 134967.
417 R. Gu, X. Li, Y. Meng, Z. Li, H. Nie, X. Wang and D. Xiao, *Analyst*, 2022, **147**, 4228–4236.
418 P. Jia, Q. Wu, B. Sun and L. Wang, *Small*, 2023, **19**, 2304096.
419 F. Liu, T. Lei, Y. Zhang, Y. Wang and Y. He, *Anal. Chim. Acta*, 2021, **1184**, 339026.
420 W. Yang, L. Ye, Y. Wu, X. Wang, S. Ye, Y. Deng, K. Huang, H. Luo, J. Zhang and C. Zheng, *J. Hazard. Mater.*, 2024, **470**, 134038.
421 K. G. Shah, V. Singh, P. C. Kauffman, K. Abe and P. Yager, *Anal. Chem.*, 2018, **90**, 6967–6974.
422 P. Preechakasedkit, K. Osada, Y. Katayama, N. Ruecha, K. Suzuki, O. Chailapakul and D. Citterio, *Analyst*, 2018, **143**, 564–570.
423 J. Wang, C. Jiang, J. Yuan, L. Tong, Y. Wang, D. Zhuo, L. Huang, W. Ni, J. Zhang, M. Huang, D. Li, B. Su and J. Hu, *Anal. Chem.*, 2022, **94**, 10865–10873.
424 B. Peng, J. Liang, Y. Wang, G. He, X. Zhang, C. Lu, Q. Song, Y. Zhang, G. Li, Y. Hao and Y. Tang, *Sens. Actuators, B*, 2022, **369**, 132376.
425 Y. Wu, Y. Zhang, Y. Hu, N. Jiang, R. P. Patel, A. K. Yetisen and M. F. Cordeiro, *Adv. Mater. Technol.*, 2024, **9**, 2400238.
426 C. Lee, J. Noh, S. E. O'Neal, A. E. Gonzalez, H. H. Garcia and S. Handali, *PLoS Neglected Trop. Dis.*, 2019, **13**, e0007746.
427 S. Bock, H.-M. Kim, J. Kim, J. An, Y.-S. Choi, X.-H. Pham, A. Jo, K. Ham, H. Song, J.-W. Kim, E. Hahm, W.-Y. Rho, S. H. Lee, S. Park, S. Lee, D. H. Jeong, H.-Y. Lee and B.-H. Jun, *Nanomaterials*, 2021, **12**, 33.
428 T. Zhong, J. Li, S. Zhang and H. Pan, *Appl. Biochem. Microbiol.*, 2023, **59**, 946–958.
429 J. Liu, B. Wang, H. Huang, D. Jian, Y. Lu, Y. Shan, S. Wang and F. Liu, *Food Chem.*, 2021, **335**, 127596.
430 Z. Rong, Q. Wang, N. Sun, X. Jia, K. Wang, R. Xiao and S. Wang, *Anal. Chim. Acta*, 2019, **1055**, 140–147.
431 H. Chen, Y. Ding, J. Li, L. Huang, G. González-Sapienza, B. D. Hammock, M. Wang and X. Hua, *Anal. Chem.*, 2022, **94**, 7358–7367.
432 J. Wang, C. Jiang, J. Jin, L. Huang, W. Yu, B. Su and J. Hu, *Angew. Chem., Int. Ed.*, 2021, **133**, 13152–13159.

Open Access Article. Published on 07 February 2025. Downloaded on 19/4/2026 11:02:09 PM.
This article is licensed under a Creative Commons Attribution-NonCommercial 3.0 Unported Licence.

433 Y. Zhu, L. Ao, S. Chu, Y. Liao, J. Wang, J. Hu and L. Huang, *Adv. Funct. Mater.*, 2024, **34**, 2316147.
434 L. Huang, Z. Shi, D. Li, C. Jiang, X. Wang, M. Huang, J. Wang and B. Su, *ACS Appl. Nano Mater.*, 2022, **6**, 86–95.
435 V. K. Rajendran, P. Bakthavathsalam, P. L. Bergquist and A. Sunna, *Sens. Actuators, B*, 2019, **298**, 126849.
436 Z. Rong, Z. Bai, J. Li, H. Tang, T. Shen, Q. Wang, C. Wang, R. Xiao and S. Wang, *Biosens. Bioelectron.*, 2019, **145**, 111719.
437 C. Lu, W. Xiao, Y. Su, X. Zhang, Y. Chen, K. Lu, P. Teng, J. Liang, H. Yang, Q. Song, Y. Tang and D. Cao, *ACS Sens.*, 2023, **8**, 1950–1959.
438 Y. Tian, X. Hu, J. Jiang, X. Tang, Z. Tian, Z. Zhang and P. Li, *Foods*, 2023, **12**, 431.
439 H. Jiang, D. Wu, L. Song, Q. Yuan, S. Ge, X. Min, N. Xia, S. Qian and X. Qiu, *SLAS Technol.*, 2017, **22**, 122–129.
440 Z. Liu, Q. Hua, J. Wang, Z. Liang, J. Li, J. Wu, X. Shen, H. Lei and X. Li, *Biosens. Bioelectron.*, 2020, **158**, 112178.
441 Y. Gong, Y. Zheng, B. Jin, M. You, J. Wang, X. Li, M. Lin, F. Xu and F. Li, *Talanta*, 2019, **201**, 126–133.
442 J. Guo, S. Chen, S. Tian, K. Liu, X. Ma and J. Guo, *Talanta*, 2021, **230**, 122335.
443 H. He, B. Liu, S. Wen, J. Liao, G. Lin, J. Zhou and D. Jin, *Anal. Chem.*, 2018, **90**, 12356–12360.
444 M. You, M. Lin, Y. Gong, S. Wang, A. Li, L. Ji, H. Zhao, K. Ling, T. Wen, Y. Huang, D. Gao, Q. Ma, T. Wang, A. Ma, X. Li and F. Xu, *ACS Nano*, 2017, **11**, 6261–6270.
445 Y. Zhang, L. Wang, W.-L. Wang, C. Yang, Y. Feng and X. Shi, *Talanta*, 2021, **232**, 122427.
446 Y. Cao, T. Bu, H. Wu, J. Xi, Y. Wang, C. Xuan, P. Jia, B. Zheng, J. Zhao, Y. Zhuang and L. Wang, *Anal. Chem.*, 2023, **95**, 16585–16592.
447 A. N. Danthanarayana, E. Finley, B. Vu, K. Kourentzi, R. C. Willson and J. Brgoch, *Anal. Methods*, 2020, **12**, 272–280.
448 S. Zhang, J. Xiong, S. Wang, Z. Li, L. Qin, B. Sun, Z. Wang, X. Liu, Y. Zheng and H. Jiang, *J. Hazard. Mater.*, 2024, **469**, 134068.
449 W. Wu, Y. Li, P. Song, Q. Xu, D. Lei, J. Wang, B. Fu and W. Kong, *J. Hazard. Mater.*, 2024, **465**, 133103.
450 R. Paul, E. Ostermann, Y. Chen, A. C. Saville, Y. Yang, Z. Gu, A. E. Whitfield, J. B. Ristaino and Q. Wei, *Biosens. Bioelectron.*, 2021, **187**, 113312.
451 P. Teengam, N. Nisab, N. Chuaypen, P. Tangkijvanich, T. Vilaivan and O. Chailapakul, *Biosens. Bioelectron.*, 2021, **189**, 113381.
452 V. K. Rajendran, P. Bakthavathsalam, P. L. Bergquist and A. Sunna, *Biosens. Bioelectron.*, 2019, **134**, 68–75.
453 X. Qiu, J. I. Shu, O. Baysal, J. Wu, S. Qian, S. Ge, K. Li, X. Ye, N. Xia and D. Yu, *Microfluid. Nanofluid.*, 2019, **23**, 1–8.
454 B. Shi, Y. Li, D. Wu and W. Wu, *Analyst*, 2020, **145**, 2767–2773.
455 W. Chen, H. Yu, F. Sun, A. Ornob, R. Brisbin, A. Ganguli, V. Vemuri, P. Strzebonski, G. Cui, K. J. Allen, S. A. Desai, W. Lin, D. M. Nash, D. L. Hirschberg, I. Brooks, R. Bashir and B. T. Cunningham, *Anal. Chem.*, 2017, **89**, 11219–11226.
456 R. R. G. Soares, A. S. Akhtar, I. F. Pinto, N. Lapins, D. Barrett, G. Sandh, X. Yin, V. Pelechano and A. Russom, *Lab Chip*, 2021, **21**, 2932–2944.
457 J. Wang, G. Jing, W. Huang, L. Xin, J. Du, X. Cai, Y. Xu, X. Lu and W. Chen, *Anal. Chem.*, 2022, **94**, 18083–18091.
458 P. Mao, L. Cao, Z. Li, M. You, B. Gao, X. Xie, Z. Xue, P. Peng, C. Yao and F. Xu, *Analyst*, 2021, **146**, 6960–6969.
459 B. P. Sullivan, Y.-S. Chou, A. T. Bender, C. D. Martin, Z. G. Kaputa, H. March, M. Song and J. D. Posner, *Lab Chip*, 2022, **22**, 2352–2363.
460 A. M. Jankelow, H. Lee, W. Wang, T.-H. Hoang, A. Bacon, F. Sun, S. Chae, V. Kindratenko, K. Koprowski, R. A. Stavins, D. D. Ceriani, Z. W. Engelder, W. P. King, M. N. Do, R. Bashir, E. Valera and B. T. Cunningham, *Analyst*, 2022, **147**, 3838–3853.
461 X. Zhu, J. Zhao, A. Hu, J. Pan, G. Deng, C. Hua, C. Zhu, Y. Liu, K. Yang and L. Zhu, *Micromachines*, 2020, **11**, 186.
462 S.-A. Hsieh, D. Shamsaei, D. R. Eitzmann and J. L. Anderson, *Anal. Chem.*, 2022, **94**, 11949–11956.
463 M. Moazeni, P. Berger and C. Padeste, *Micro Nano Eng.*, 2023, **19**, 100184.
464 Y. Zhu, X. Gu, Q. Tang, W. Jiang, R. Xia, J. Zhang, H. Ji, Y. Qin and L. Wu, *Anal. Chem.*, 2024, **96**, 14116–14124.
465 B. Jin, C. Ma, C. Zhang, H. Yin, G. Zhao, J. Hu and Z. Li, *Microchim. Acta*, 2024, **191**, 177.
466 T. Tian, Z. Qiu, Y. Jiang, D. Zhu and X. Zhou, *Biosens. Bioelectron.*, 2022, **196**, 113701.
467 M. Lin, H. Yue, T. Tian, E. Xiong, D. Zhu, Y. Jiang and X. Zhou, *Anal. Chem.*, 2022, **94**, 8277–8284.
468 Z. Lei, L. Lian, L. Zhang, C. Liu, S. Zhai, X. Yuan, J. Wei, H. Liu, Y. Liu, Z. Du, I. Gul, H. Zhang, Z. Qin, S. Zeng, P. Jia, K. Du, L. Deng, D. Yu, Q. He and P. Qin, *ACS Omega*, 2023, **8**, 32555–32564.
469 P. Fozouni, S. Son, M. D. de L. Derby, G. J. Knott, C. N. Gray, M. V. D'Ambrosio, C. Zhao, N. A. Switz, G. R. Kumar, S. I. Stephens, D. Boehm, C.-L. Tsou, J. Shu, A. Bhuiya, M. Armstrong, A. R. Harris, P.-Y. Chen, J. M. Osterloh, A. Meyer-Franke, B. Joehnk, K. Walcott, A. Sil, C. Langelier, K. S. Pollard, E. D. Crawford, A. S. Puschnik, M. Phelps, A. Kistler, J. L. DeRisi, J. A. Doudna, D. A. Fletcher and M. Ott, *Cell*, 2021, **184**, 323–333.
470 H. De Puig, R. A. Lee, D. Najjar, X. Tan, L. R. Soenksen, N. M. Angenent-Mari, N. M. Donghia, N. E. Weckman, A. Ory, C. F. Ng, P. Q. Nguyen, A. S. Mao, T. C. Ferrante, G. Lansberry, H. Sallum, J. Niemi and J. J. Collins, *Sci. Adv.*, 2021, **7**, eabh2944.
471 J. Arizti-Sanz, C. A. Freije, A. C. Stanton, B. A. Petros, C. K. Boehm, S. Siddiqui, B. M. Shaw, G. Adams, T.-S. F. Kosoko-Thoroddsen, M. E. Kemball, J. N. Uwanibe, F. V. Ajogbasile, P. E. Eromon, R. Gross, L. Wronka, K. Caviness, L. E. Hensley, N. H. Bergman, B. L. MacInnis, C. T. Happi, J. E. Lemieux, P. C. Sabeti and C. Myhrvold, *Nat. Commun.*, 2020, **11**, 5921.

 This journal is © The Royal Society of Chemistry 2025

Open Access Article. Published on 07 February 2025. Downloaded on 19/4/2026 11:02:09 PM.
This article is licensed under a Creative Commons Attribution-NonCommercial 3.0 Unported Licence.

472 J. Liu, N. Li, L. Zhang, Y. Lu, M. Shen, Y. Zhang, L. Feng, J. Jing, J. Cheng and Y. Xu, *Small Methods*, 2024, **8**, 2400030.
473 T. Yu, S. Zhang, R. Matei, W. Marx, C. L. Beisel and Q. Wei, *AIChE J.*, 2021, **67**, e17365.
474 Y. Zhu, J. Wang, H. Xie, H. Liu, S. Liu, D. He, P. Mi, S. He, J. Wang and Y. Sun, *ACS Appl. Mater. Interfaces*, 2022, **14**, 10212–10226.
475 X. Peng, X. Mei, X. Liu, G. Zhang and Y. Li, *Anal. Chem.*, 2024, **96**, 13252–13259.
476 C. M. Green, J. Spangler, K. Susumu, D. A. Stenger, I. L. Medintz and S. A. Díaz, *ACS Nano*, 2022, **16**, 20693–20704.
477 T. Treebupachatsakul, C. Lochotinunt, T. Teechot, N. Pensupa and S. Pechprasarn, *IEEE Sens. J.*, 2022, **22**, 12473–12484.
478 S. Hong, D.-W. Zheng, Q.-L. Zhang, W.-W. Deng, W.-F. Song, S.-X. Cheng, Z.-J. Sun and X.-Z. Zhang, *Chem. Sci.*, 2020, **11**, 4403–4409.
479 M. N. Tahir, Y. Xie, M. A. Sami, R. Punde and U. Hassan, *IEEE Sens. Lett.*, 2024, **8**, 1–4.
480 M. V. Bills, B. T. Nguyen and J.-Y. Yoon, *IEEE Sens. J.*, 2019, **19**, 7822–7828.
481 J. W. Snow, H. C. Koydemir, D. K. Karinca, K. Liang, D. Tseng and A. Ozcan, *Lab Chip*, 2019, **19**, 789–797.
482 C. Goenka, W. Lewis, L. R. Chevres-Fernández, A. Ortega-Martínez, E. Ibarra-Silva, M. Williams and W. Franco, *Lasers Surg. Med.*, 2019, **51**, 201–207.
483 Y. Liu, A. M. Rollins, R. M. Levenson, F. Fereidouni and M. W. Jenkins, *Commun. Biol.*, 2021, **4**, 1–14.
484 O. Ormachea, A. Villazón, P. Rodriguez and M. Zimic, *Biosensors*, 2022, **12**, 960.
485 G. H. Darwish, J. Asselin, M. V. Tran, R. Gupta, H. Kim, D. Boudreau and W. R. Algar, *ACS Appl. Mater. Interfaces*, 2020, **12**, 33530–33540.
486 K. Rees, G. H. Darwish and W. R. Algar, *ACS Appl. Mater. Interfaces*, 2023, **15**, 18672–18684.
487 R. Zenhausern, A. S. Day, B. Safavinia, S. Han, P. E. Rudy, Y.-W. Won and J.-Y. Yoon, *Biosens. Bioelectron.*, 2022, **200**, 113916.
488 S. Kim, A. Romero-Lozano, D. S. Hwang and J.-Y. Yoon, *J. Hazard. Mater.*, 2021, **413**, 125338.
489 S. Chung, L. E. Breshears, S. Perea, C. M. Morrison, W. Q. Betancourt, K. A. Reynolds and J.-Y. Yoon, *ACS Omega*, 2019, **4**, 11180–11188.
490 T.-H. Ulep, R. Zenhausern, A. Gonzales, D. S. Knoff, P. A. Lengerke Diaz, J. E. Castro and J.-Y. Yoon, *Biosens. Bioelectron.*, 2020, **153**, 112042.
491 S. Kim, P. Akarapipad, B. T. Nguyen, L. E. Breshears, K. Sosnowski, J. Baker, J. L. Uhrlaub, J. Nikolich-Žugich and J.-Y. Yoon, *Biosens. Bioelectron.*, 2022, **200**, 113912.
492 Y. Liang, A. Zhou, C. S. Bever, L. W. Cheng and J.-Y. Yoon, *Microchim. Acta*, 2022, **189**, 322.
493 Y. Liang, A. Zhou and J.-Y. Yoon, *ACS Omega*, 2022, **7**, 30064–30073.
494 S. Kim, K. Samanta, B. T. Nguyen, S. Mata-Robles, L. Richer, J.-Y. Yoon and M. Gomes-Solecki, *Sci. Rep.*, 2023, **13**, 7546.
495 Q. Deng, Z. Lan, L. Xu, Z. Zhu and X. Shu, *Sens. Actuators, B*, 2021, **343**, 130086.
496 J. Luo and Z. Zhu, *Anal. Chem.*, 2024, **96**, 11115–11120.
497 C.-H. Huang, Y. I. Park, H.-Y. Lin, D. Pathania, K. S. Park, M. Avila-Wallace, C. M. Castro, R. Weissleder and H. Lee, *ACS Nano*, 2019, **13**, 11698–11706.
498 Y. Wang, S. Sadeghi, A. Velayati, R. Paul, Z. Hetzler, E. Danilov, F. S. Ligler and Q. Wei, *PNAS Nexus*, 2023, **2**, pgad313.
499 B. Bruininks and L. B. F. Juurlink, *J. Chem. Educ.*, 2022, **99**, 2168–2174.
500 M. Xiao, N. Xu, A. He, Z. Yu, B. Chen, B. Jin, L. Jiang and C. Yi, *iScience*, 2023, **26**, 106553.
501 H. Yu, Y. Tan and B. T. Cunningham, *Anal. Chem.*, 2014, **86**, 8805–8813.
502 M. A. Hossain, J. Canning, S. Ast, K. Cook, P. J. Rutledge and A. Jamalipour, *Opt. Lett.*, 2015, **40**, 1737–1740.
503 D. Hatiboruah, S. Biswas, D. Sarma and P. Nath, *Sens. Actuators, A*, 2022, **341**, 113586.
504 S. Shukla, A. N. Sah, D. Hatiboruah, S. Ahirwar, P. Nath and A. Pradhan, *Sci. Rep.*, 2022, **12**, 11192.
505 Q. Deng, Y. Liu, Z. Zhu and X. Shu, *Opt. Lett.*, 2022, **47**, 3427–3430.
506 S. Shukla, B. S. Deo, C. Vishwakarma, S. Mishra, S. Ahirwar, A. N. Sah, K. Pandey, S. Singh, S. N. Prasad, A. K. Padhi, M. Pal, P. K. Panigrahi and A. Pradhan, *J. Biophotonics*, 2024, **17**, e202300468.
507 Y. Sun, L. Shi, Q. Wang, L. Mi and T. Li, *Anal. Chem.*, 2019, **91**, 3652–3658.
508 L. Shi, Y. Sun, L. Mi and T. Li, *ACS Sens.*, 2019, **4**, 3219–3226.
509 L. Mi, Y. Sun, L. Shi and T. Li, *ACS Appl. Mater. Interfaces*, 2020, **12**, 7879–7887.
510 Y. Zhou, S. Xie, B. Liu, C. Wang, Y. Huang, X. Zhang and S. Zhang, *Anal. Chem.*, 2023, **95**, 3332–3339.
511 P. M. Kalligosfyri, A. Sevastou, I. K. Kyriakou, S. S. Tragoulias, D. P. Kalogianni and T. K. Christopoulos, *Anal. Chim. Acta*, 2019, **1088**, 123–130.
512 H. Chen, Y. Feng, F. Liu, C. Tan, N. Xu, Y. Jiang and Y. Tan, *Biosens. Bioelectron.*, 2024, **247**, 115929.
513 X. Chen, Y. Ning, S. Pan, B. Liu, Y. Chang, W. Pang and X. Duan, *ACS Sens.*, 2021, **6**, 2386–2394.
514 D. Liu, C. Ju, C. Han, R. Shi, X. Chen, D. Duan, J. Yan and X. Yan, *Biosens. Bioelectron.*, 2021, **173**, 112817.
515 F. Li, L. Guo, Z. Li, J. He and H. Cui, *Anal. Chem.*, 2020, **92**, 6827–6831.
516 S. Wang, F. Qu, R. Zhang, T. Jin, T. Zheng, J. Shu and H. Cui, *Anal. Chem.*, 2023, **95**, 12497–12504.
517 Y. Lai, J. Huang, D. Tang, X. Chen, L. Hou, S. Zhao and T. Lin, *Biosens. Bioelectron.*, 2024, **263**, 116602.
518 H. Chen, Z. Zhuang, N. Xu, Y. Feng, K. Fang, C. Tan and Y. Tan, *Biosensors*, 2024, **14**, 135.
519 X. Yu, Y. Ma, S. Liu, C. Qi, W. Zhang, W. Xiang, Z. Li, K. Yang, S. Duan, X. Du, J. Yu, Y. Xie, Z. Wang, W.

Open Access Article. Published on 07 February 2025. Downloaded on 19/4/2026 11:02:09 PM.
This article is licensed under a Creative Commons Attribution-NonCommercial 3.0 Unported Licence.

Jiang, L. Zhang and X. Lin, *Anal. Chim. Acta*, 2023, **1281**, 341899.
520 H. Wu, Y. Fang, L. Tian, X. Liu, X. Zhou, X. Chen, H. Gao, H. Qin and Y. Liu, *ACS Sens.*, 2023, **8**, 3205–3214.
521 X. Tao, L. Yue, T. Tian, Y. Zhang, X. Zhou and E. Song, *Anal. Chem.*, 2024, **96**, 9270–9277.
522 A. Sevastou, S. S. Tragoulias, D. P. Kalogianni and T. K. Christopoulos, *Anal. Bioanal. Chem.*, 2020, **412**, 5663–5669.
523 A. Shahvar, M. Saraji and D. Shamsaei, *Sens. Actuators, B*, 2018, **255**, 891–894.
524 M. J. Juachon, J. G. Regala, J. M. Marquez and M. X. Bailon, *Open Chem.*, 2019, **17**, 270–278.
525 C. Wang, Z. Wu, M. Hao, B. Chen, J. Zhu, X. Cui and T. Wang, *Sens. Actuators, B*, 2023, **388**, 133840.
526 R. S. Rafee, H. R. Pouretedal and S. Damiri, *Luminescence*, 2024, **39**, e4775.
527 H. A. J. Al Lawati, J. Hassanzadeh, N. Bagheri and I. Al Lawati, *Talanta*, 2021, **234**, 122648.
528 M. Zangheri, F. Di Nardo, D. Calabria, E. Marchegiani, L. Anfossi, M. Guardigli, M. Mirasoli, C. Baggiani and A. Roda, *Anal. Chim. Acta*, 2021, **1163**, 338515.
529 J. Ma, Y. Guan, F. Xing, Y. Wang, X. Li, Q. Yu and X. Yu, *Food Chem.*, 2023, **413**, 135654.
530 Z. Li, Y. Xi, A. Zhao, J. Jiang, B. Li, X. Yang, J. He and F. Li, *Anal. Bioanal. Chem.*, 2021, **413**, 3541–3550.
531 D. Calabria, M. Zangheri, I. Trozzi, E. Lazzarini, A. Pace, M. Mirasoli and M. Guardigli, *Biosensors*, 2021, **11**, 381.
532 S. Rink, A. Duerkop and A. J. Baeumner, *Anal. Sens.*, 2023, **3**, e202200111.
533 J. Hassanzadeh, H. A. J. Al Lawati and N. Bagheri, *Talanta*, 2024, **276**, 126219.
534 K. Kourentzi, K. Brosamer, B. Vu and R. C. Willson, *Acc. Chem. Res.*, 2024, **57**, 1372–1383.
535 M. Chabi, B. Vu, K. Brosamer, M. Smith, D. Chavan, J. C. Conrad, R. C. Willson and K. Kourentzi, *Analyst*, 2023, **148**, 839–848.
536 Y. Li, L. Zhou, W. Ni, Q. Luo, C. Zhu and Y. Wu, *Anal. Chem.*, 2019, **91**, 14838–14841.
537 D. Chang, K. T. Kim, E. Lindberg and N. Winssinger, *ACS Sens.*, 2020, **5**, 807–813.
538 L. Zhou, L. Zhang, L. Yang, W. Ni, Y. Li and Y. Wu, *Biosens. Bioelectron.*, 2021, **173**, 112824.
539 M. Hattori, N. Sugiura, T. Wazawa, T. Matsuda and T. Nagai, *Anal. Chem.*, 2021, **93**, 13520–13526.
540 Y. Li, P. Yang, N. Lei, Y. Ma, Y. Ji, C. Zhu and Y. Wu, *Anal. Chem.*, 2018, **90**, 11495–11502.
541 K. Tomimuro, K. Tenda, Y. Ni, Y. Hiruta, M. Merkx and D. Citterio, *ACS Sens.*, 2020, **5**, 1786–1794.
542 M. M. Calabretta, D. Gregucci, M. Guardigli and E. Michelini, *Biosens. Bioelectron.*, 2024, **261**, 116454.
543 Y. Ding, X. Hua, H. Chen, F. Liu, G. González-Sapien and M. Wang, *Anal. Chem.*, 2018, **90**, 2230–2237.
544 J. Li, N. Wang, M. Xiong, M. Dai, C. Xie, Q. Wang, K. Quan, Y. Zhou and Z. Qing, *Anal. Chem.*, 2023, **95**, 7142–7149.
545 M.-Y. Lu, W.-C. Kao, S. Belkin and J.-Y. Cheng, *Sensors*, 2019, **19**, 3882.
546 R. Zhang, Y. Wang, H. Deng, S. Zhou, Y. Wu and Y. Li, *Anal. Chim. Acta*, 2023, **1273**, 341538.
547 Y. Itoh, M. Hattori, T. Wazawa, Y. Arai and T. Nagai, *ACS Sens.*, 2021, **6**, 889–895.
548 M. M. Calabretta, R. Álvarez-Diduk, E. Michelini, A. Roda and A. Merkoçi, *Biosens. Bioelectron.*, 2020, **150**, 111902.
549 A. Lopreside, L. Montali, B. Wang, A. Tassoni, M. Ferri, M. M. Calabretta and E. Michelini, *Biosens. Bioelectron.*, 2021, **194**, 113569.
550 M. N. Hossain, R. Ishida, M. Hattori, T. Matsuda and T. Nagai, *Sensors*, 2020, **20**, 3164.
551 E. Michelini, M. M. Calabretta, L. Cevenini, A. Lopreside, T. Southworth, D. M. Fontaine, P. Simoni, B. R. Branchini and A. Roda, *Biosens. Bioelectron.*, 2019, **123**, 269–277.
552 A. Lopreside, M. M. Calabretta, L. Montali, M. Ferri, A. Tassoni, B. R. Branchini, T. Southworth, M. D'Elia, A. Roda and E. Michelini, *Anal. Bioanal. Chem.*, 2019, **411**, 4937–4949.
553 M. Bhaiyya, P. K. Pattnaik and S. Goel, *Microchim. Acta*, 2022, **189**, 79.
554 D. Calabria, E. Lazzarini, A. Pace, I. Trozzi, M. Zangheri, S. Cinti, M. Difonzo, G. Valenti, M. Guardigli, F. Paolucci and M. Mirasoli, *Biosens. Bioelectron.*, 2023, **227**, 115146.
555 S. Li, J. Liu, Z. Chen, Y. Lu, S. S. Low, L. Zhu, C. Cheng, Y. He, Q. Chen, B. Su and Q. Liu, *Sens. Actuators, B*, 2019, **297**, 126811.
556 J. Totoricaguena-Gorriño, M. Dei, A. F. Alba, N. Peřinka, L.-R. Rubio, J. L. Vilas-Vilela and F. J. del Campo, *ACS Sens.*, 2022, **7**, 1544–1554.
557 Z. Fan, Z. Geng, W. Fang, X. Lv, Y. Su, S. Wang and H. Chen, *Sensors*, 2020, **20**, 446.
558 P. Dutta, T.-Y. Su, A.-Y. Fu, M.-C. Chang, Y.-J. Guo, I.-J. Tsai, P.-K. Wei, Y.-S. Chang, C.-Y. Lin and Y.-J. Fan, *Chem. Eng. J.*, 2022, **434**, 133864.
559 Y. Zhou, A. Cui, D. Xiang, Y. Luan, Q. Wang, J. Huang, J. Liu, X. Yang and K. Wang, *Sens. Actuators, B*, 2024, **398**, 134734.
560 Y. Xia, Y. Chen, Y. Tang, G. Cheng, X. Yu, H. He, G. Cao, H. Lu, Z. Liu and S.-Y. Zheng, *ACS Sens.*, 2019, **4**, 3298–3307.
561 M. Armstrong, A. R. Harris, M. V. D'Ambrosio, J. T. Coulibaly, S. Essien-Baidoo, R. K. D. Ephraim, J. R. Andrews, I. I. Bogoch and D. A. Fletcher, *Am. J. Trop. Med. Hyg.*, 2022, **106**, 1442–1449.
562 X. Zeng, L. Wang, C. Liu, J. Zhang, H.-W. Shi, W. Shen, D. Kong, C. Huang, H. K. Lee and S. Tang, *Talanta*, 2024, **272**, 125838.
563 Y. Man, M. Ban, A. Li, X. Jin, Y. Du and L. Pan, *Food Chem.*, 2021, **354**, 129578.
564 F. Li, Y. Zheng, J. Wu, L. Zhao, L. Shui, Q. Pu and S. Liu, *Talanta*, 2019, **203**, 83–89.
565 N. M. Reis, S. H. Needs, S. M. Jegouic, K. K. Gill, S. Sirivisoot, S. Howard, J. Kempe, S. Bola, K. Al-Hakeem, I. M. Jones, T. Prommool, P. Luangaram, P. Avirutnan, C. Puttikhunt and A. D. Edwards, *ACS Sens.*, 2021, **6**, 4338–4348.

 This journal is © The Royal Society of Chemistry 2025

Open Access Article. Published on 07 February 2025. Downloaded on 19/4/2026 11:02:09 PM.
This article is licensed under a Creative Commons Attribution-NonCommercial 3.0 Unported Licence.

566 X.-L. Guo, Y. Chen, H.-L. Jiang, X.-B. Qiu and D.-L. Yu, *Sensors*, 2018, **18**, 3141.
567 T. Li, N. Yang, X. Pan, X. Zhang and L. Xu, *Biosens. Bioelectron.*, 2024, **244**, 115794.
568 D. Jiang, S. Lee, S. W. Bae and S.-Y. Park, *Lab Chip*, 2018, **18**, 532–539.
569 E. Ditchendorf, I. Ahmed, J. Sepate and A. Priye, *Sensors*, 2023, **23**, 8310.
570 F. Sun, A. Ganguli, J. Nguyen, R. Brisbin, K. Shanmugam, D. L. Hirschberg, M. B. Wheeler, R. Bashir, D. M. Nash and B. T. Cunningham, *Lab Chip*, 2020, **20**, 1621–1627.
571 H. Xu, A. Xia, D. Wang, Y. Zhang, S. Deng, W. Lu, J. Luo, Q. Zhong, F. Zhang, L. Zhou, W. Zhang, Y. Wang, C. Yang, K. Chang, W. Fu, J. Cui, M. Gan, D. Luo and M. Chen, *Sci. Adv.*, 2020, **6**, eaaz7445.
572 Y. Shang, G. Xing, X. Liu, H. Lin and J.-M. Lin, *Anal. Chem.*, 2022, **94**, 16787–16795.
573 X. T. Zheng, W. P. Goh, Y. Yu, L. Sutarlie, D. Y. Chen, S. C. L. Tan, C. Jiang, M. Zhao, T. Ba, H. Li, X. Su and L. Yang, *Adv. Healthcare Mater.*, 2024, **13**, 2302173.
574 I. Jang, D. B. Carrão, R. F. Menger, A. R. Moraes de Oliveira and C. S. Henry, *ACS Sens.*, 2020, **5**, 2230–2238.
575 M. Yuan, C. Li, Y. Zheng, H. Cao, T. Ye, X. Wu, L. Hao, F. Yin, J. Yu and F. Xu, *Talanta*, 2024, **266**, 125112.
576 S. Liu, J. Zhao, J. Wu, L. Wang, C. Yao, J. Hu and H. Zhang, *Food Chem.*, 2025, **463**, 141205.
577 K. Arias-Alpízar, A. Sánchez-Cano, J. Prat-Trunas, E. Sulleiro, P. Bosch-Nicolau, F. Salvador, I. Oliveira, I. Molina, A. Sánchez-Montalvá and E. Baldrich, *Biosensors*, 2022, **12**, 680.
578 A. Ray, S. Esparza, D. Wu, M. R. Hanudel, H.-A. Joung, B. Gales, D. Tseng, I. B. Salusky and A. Ozcan, *Analyst*, 2020, **145**, 1841–1848.
579 A. Clemente, A. Alba-Patiño, E. Rojo-Molinero, S. M. Russell, M. Borges, A. Oliver and R. de la Rica, *ACS Sens.*, 2020, **5**, 3956–3963.
580 T. Zhang, R. Deng, Y. Wang, C. Wu, K. Zhang, C. Wang, N. Gong, R. Ledesma-Amaro, X. Teng, C. Yang, T. Xue, Y. Zhang, Y. Hu, Q. He, W. Li and J. Li, *Nat. Biomed. Eng.*, 2022, **6**, 957–967.
581 P. Akarapipad, K. Kaarj, L. E. Breshears, K. Sosnowski, J. Baker, B. T. Nguyen, C. Eades, J. L. Uhrlaub, G. Quirk, J. Nikolich-Žugich, M. Worobey and J.-Y. Yoon, *Biosens. Bioelectron.*, 2022, **207**, 114192.
582 A. Katoh, K. Maejima, Y. Hiruta and D. Citterio, *Analyst*, 2020, **145**, 6071–6078.
583 S. Piranej, L. Zhang, A. Bazrafshan, M. Marin, G. B. Melikian and K. Salaita, *ACS Cent. Sci.*, 2024, **10**, 1332–1347.
584 S. Banik, S. K. Melanthota, Arbaaz, J. M. Vaz, V. M. Kadambalithaya, I. Hussain, S. Dutta and N. Mazumder, *Anal. Bioanal. Chem.*, 2021, **413**, 2389–2406.
585 I. Hussain and A. K. Bowden, *Biomed. Opt. Express*, 2021, **12**, 1974–1998.
586 C. S. Wood, M. R. Thomas, J. Budd, T. P. Mashamba-Thompson, K. Herbst, D. Pillay, R. W. Peeling, A. M. Johnson, R. A. McKendry and M. M. Stevens, *Nature*, 2019, **566**, 467–474.
587 M. L. Cunha, S. S. da Silva, M. C. Stracke, D. L. Zanette, M. N. Aoki and L. Blanes, *Anal. Chem.*, 2022, **94**, 41–58.
588 W. R. Algar, N. Hildebrandt, S. S. Vogel and I. L. Medintz, *Nat. Methods*, 2019, **16**, 815–829.
589 N. Hildebrandt, C. M. Spillmann, W. R. Algar, T. Pons, M. H. Stewart, E. Oh, K. Susumu, S. A. Díaz, J. B. Delehanty and I. L. Medintz, *Chem. Rev.*, 2017, **117**, 536–711.
590 Z. Li, H. Yuan, W. Yuan, Q. Su and F. Li, *Coord. Chem. Rev.*, 2018, **354**, 155–168.
591 X. Qiu, J. Xu, M. Cardoso Dos Santos and N. Hildebrandt, *Acc. Chem. Res.*, 2022, **55**, 551–564.
592 C.-W. Kuo and A. M. Smith, *Acc. Chem. Res.*, 2023, **56**, 1031–1042.
593 D. C. Duffy, *Lab Chip*, 2023, **23**, 818–847.
594 W. Yin, J. Zhuang, J. Li, L. Xia, K. Hu, J. Yin and Y. Mu, *Small*, 2023, **19**, 2303398.
595 V. Y. C. Li, B. Udugama, P. Kadhiresan and W. C. W. Chan, *Anal. Chem.*, 2022, **94**, 17102–17111.
596 B. Udugama, P. Kadhiresan, A. Samarakoon and W. C. W. Chan, *J. Am. Chem. Soc.*, 2017, **139**, 17341–17349.
597 K. Rees, M. V. Tran, M. Massey, H. Kim, K. D. Krause and W. R. Algar, *Bioconjugate Chem.*, 2020, **31**, 861–874.
598 K. Lix, M. V. Tran, M. Massey, K. Rees, E. R. Sauve, Z. M. Hudson and W. R. Algar, *ACS Appl. Bio Mater.*, 2020, **3**, 432–440.